Electronic Structure of Solid-State Dye-Sensitized Solar Cells: Synchrotron Induced Photoelectron Spectroscopy on Nanocrystalline TiO_2, Newly Developed Dyes and Spiro-MeOTAD

Zur Erlangung des akademischen Grades Doktor-Ingenieur (Dr.-Ing.)
genehmigte Dissertation von Dipl.-Ing. René Pekkola aus Erlenbach am Main
Juni 2014 — Darmstadt — D 17

TECHNISCHE UNIVERSITÄT DARMSTADT

Fachbereich Material- und Geowissenschaften
Oberflächenforschung

Electronic Structure of Solid-State Dye-Sensitized Solar Cells: Synchrotron Induced Photoelectron Spectroscopy on Nanocrystalline TiO_2, Newly Developed Dyes and Spiro-MeOTAD

Genehmigte Dissertation von Dipl.-Ing. René Pekkola aus Erlenbach am Main

1. Gutachten: Prof. Dr. Wolfram Jaegermann
2. Gutachten: Prof. Dr.-Ing. Heinz von Seggern

Tag der Einreichung: 07. Februar 2014
Tag der Prüfung: 09. April 2014

Darmstadt — D 17

Erklärung zur Dissertation

Hiermit versichere ich, die vorliegende Dissertation ohne Hilfe Dritter nur mit den angegebenen Quellen und Hilfsmitteln angefertigt zu haben. Alle Stellen, die aus Quellen entnommen wurden, sind als solche kenntlich gemacht. Diese Arbeit hat in gleicher oder ähnlicher Form noch keiner Prüfungsbehörde vorgelegen.

Darmstadt, den 09. April 2014

_____

(René Pekkola)

Contents

1 Introduction

Because the energy consumption of the world's population is steadily increasing (Figure 1.1) and fossil energy resources are limited, the urge to find new, economical concepts and ways to satisfy the global energy demand is increasing. Renewable energy means the conversion of wind, solar and other renewable energies into electrical energy. The big advantage of these techniques is the unlimited availability combined with the lack of material input in contrast to coal and nuclear energy, for example.

Beside wind energy, which is one of the biggest supplier of green energy today, solar energy has been one of the most upcoming and evolving energy sources in the last decades. One reason for this is the gigantic energy supply from the sun to the earth ($3 \cdot 10^{24}$ joules a year), which is about 10000 times more than the global energy consumption today [1]. Additionally, a big advantage of photovoltaic is that solar energy can be harvested at any point in the world without nearly any further cost. Therefore, photovoltaic is also interesting for underdeveloped countries with a insufficient electrical grid infrastructure.

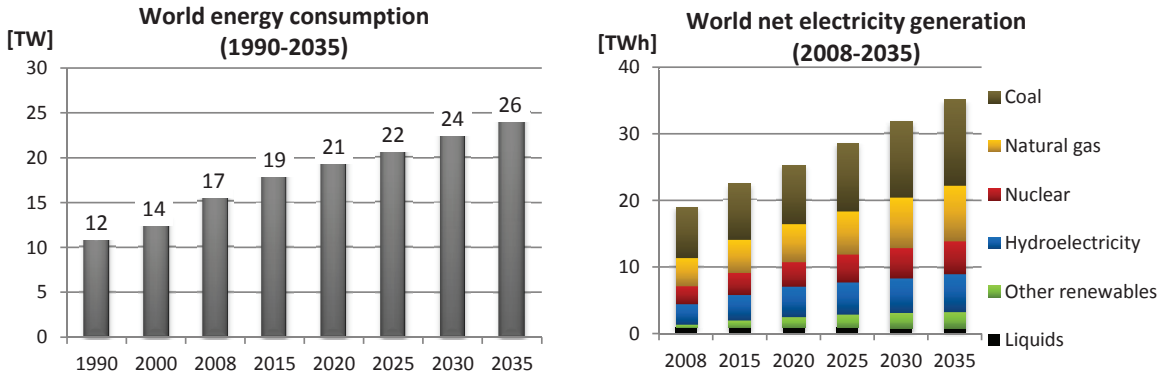

Figure 1.1.: The world energy consumption and the world net electricity generation (prediction) [http://www.eia.gov/forecasts/ieo/more_highlights.cfm#world].

Today's solar energy production is mainly based on silicon solar cells, the so called first generation solar cells. These cells are based on crystalline silicon wafers and yield efficiencies of up to 22.9% per module [2]. However, one of the biggest disadvantages of conventional photovoltaic devices compared to other energy sources is the production cost of the solar cells, which increases the price per kilowatt hour drastically. Because the silicon has to be very pure and the wafer relatively thick compared to later generations of solar cells, the production of first generation silicon solar cells is very energy and material intensive and thus expensive.

Beside improvements in the production to reduce the costs of first generation solar cells, new concepts of solar cells were developed. The so-called second generation solar cells include thin film solar cells, like CdTe and CIGS, which have proven to be less material-intensive and more cost-effective. In order to avoid the use of wafers, the energy converting layers are deposited by thin film technologies, like physical vapor deposition. Nevertheless, those concepts suffer from some disadvantages. The efficiencies of the second generation cells are lower (up to 19.6% for CIGS and up to 16.7% for CdTe cells [2]) than those of the first generation solar cells. More important, the low abundance of the materials used for these cells, like indium and tellurium, complicates the use for mass application.

Organic or inorganic-organic hybride solar cells, like organic thin film solar cells and dye-sensitized solar cells (DSSC), are counted to the third generation of solar cells. These types of cells combine the advantages of thin film technologies with the abundance of organic materials. They are promising for the further reduction of the energy input and the simplification of the production, as the materials can be deposited by conventional roll-printing techniques. So far, the biggest problems of organic solar cells are their long term stability and their low efficiencies (up to 11.0% for DSSC and up to 10.0% for organic thin film modules [2]). Hereby, organic thin film solar cells suffer from the degrading of the energy converting materials, whereas the main challenge of the DSSCs is the evaporation of their liquid electrolyte.

In general, the interest in organic electronics has increased rapidly over the last decade. It is mostly driven by the hope for easily processable and cheap materials and thus cheap devices. Printing technologies and wet chemical processing methods are already used for various applications, such as the silver busbars in silicon solar cells. Nevertheless, one of the major disadvantages of organic electronics is the lower performance and stability compared to inorganic counterparts.
Within the project 'Organische Photovoltaik zur integrierbaren Energieversorgung' (OPEG 2010) of the German Federal Ministry of Education and Research in cooporation with BASF and Bosch, organic thin film and dye-sensitized solar cells were investigated. This PhD thesis was part of this project and focused on dye-sensitized solar cells.

Part I.
Fundamentals

2 Dye-sensitized solar cells

In 1991 Grätzel and coworkers presented a dye-sensitized solar cell (DSSC) with an efficiency of 7.1% based on a nanocrystalline TiO_2 substrate (nc-TiO_2) and the ruthenium dye Ru^{II}(2,2'-bipyridine-4,4'-dicarboxylate)$_2$(NCS)$_2$, also known as N3 [3]. This was a breakthrough for this kind of solar cell. With the highly increased surface area, it was possible to adsorb much more dye than on a flat surface of the same substrate size and thus to increase the light harvesting drastically. The principle of sensitization goes back to Moser, who sensitized a solid silver halide electrode with erythrosine in 1887 [4]. However, the first highly efficient sensitization of TiO_2 was reported in 1985 by Desilvestro, who achieved a 44% incident photon to current conversion efficiency with tris(2,2'-bipyridyl-4,4'-dicarboxylate) ruthenium(II) dichloride as the senitizer [5].
An advantage of the DSSC compared to other solar cell concepts is its efficiency which is very insensitive to temperature changes. In contrast to conventional silicon cells, for example, which exhibit a decline in efficiency of about 20% in a temperature range from 20 to 60 °C, the efficiency of the DSSC stays unaltered. Furthermore, DSSCs generate more energy than conventional solar cells in diffuse lighting conditions, both indoors and outdoors, do not suffer from angular dependence of sunlight and their structure allow flexible, thin and lightweight modules. Companies, like G24i and Dyesol, offer modules for different applications: for example, flexible modules which can be implemented in backpacks or modules for house fronts or windows whose transparency and color are tunable.

2.1 Structure and working principle

Similarly to thin film solar cells, the dye-sensitized solar cell consists of different functional layers. The nanocrystalline mesoporous TiO_2 electrode is deposited on top of a glass / transparent oxide substrate. The dye which absorbs the incident light is adsorbed on the TiO_2. Usually, the TiO_2 substrate is put into a solution of dissolved dye so that by capillary forces the dye solution is soaked into the mesoporous structure. Inbetween the platinized counter electrode and the TiO_2 electrode, the liquid electrolyte I_3^-/I^- completes the solar cell.

The function of the dye-sensitized solar cell is based on the sensitization of the semiconductor TiO_2 [6]. The band gap of TiO_2 is 3.2 eV [1, 7] and thus too high to absorb most photons of the visible light. Therefore, in the dye-sensitized solar cell, organic dyes, which have a band gap of ca. 2 eV and which can harvest light efficiently due to their extended π-systems, are employed [8–10].
In the first step, a photon which is absorbed by the dye (step ① in Figure 2.1) excites an electron from the highest occupied molecular orbital (HOMO) to the lowest unoccupied molecular orbital (LUMO) of the dye. The excited electron is then transferred from the LUMO of the dye to the conduction band of the nanocrystalline TiO_2 (step ②). The transferred electron diffuses through the TiO_2 layer to the FTO working electrode (step ④) and contributes in this way to the electric circuit (step ⑤). As the dimensions of the grains of the nanocrystalline TiO_2 (10 - 50 nm) are too small that a space charge region and hence a built in field can form, the electron transport in TiO_2 is of diffusional type.

In between step ② and step ④, the dye is regenerated meaning reduced again (step ③). Since the first version of the cell which O´Regan and Grätzel came up with in 1991 [3] an I_3^-/I^- electrolyte couple is commonly used. The counter electrode consisted of platinum clusters on a glass which act as a catalyst for the reduction of triiodide. The dye regeneration itself is a two-step process [12, 13]. In the first step, the actual regeneration process takes place. In this process, an intermediate product ($I_2^{-\cdot}$) is created and

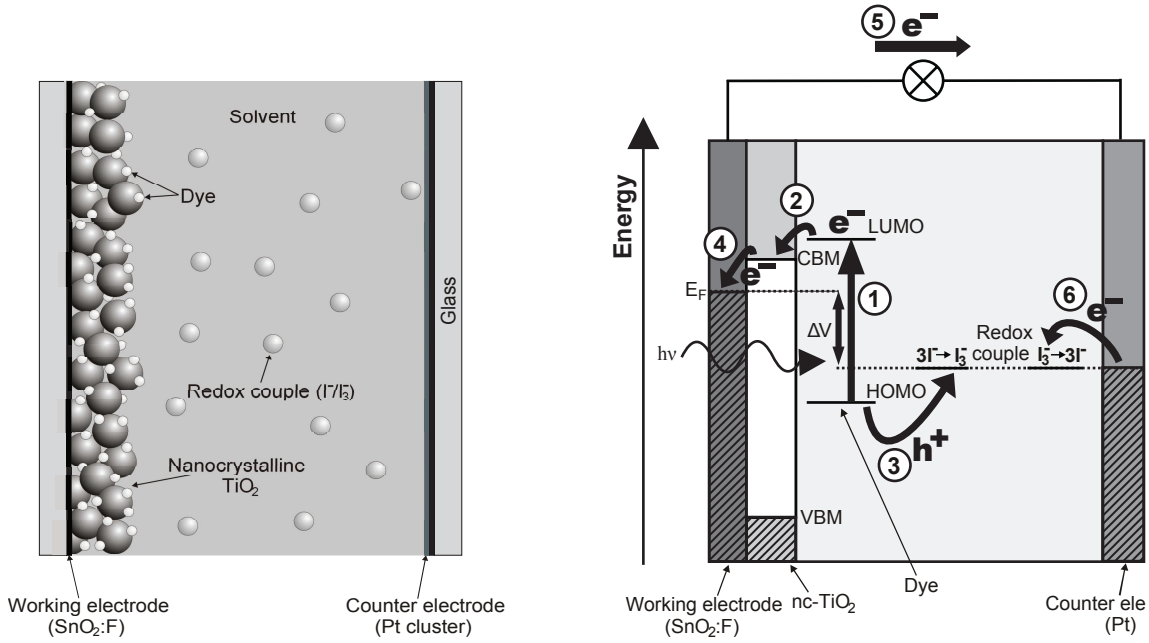

Figure 2.1.: The structure (left) and the function of as well as the energetic positions within a dye-sensitized solar cell (right). The pictures are taken from [11] and modified.

the oxidized dye (D^+) is regenerated [14]. The overpotential to drive this reaction is equal to the offset between the highest occupied molecular orbital (HOMO) of the dye and the $I_2^{-\cdot}/I^-$ potential.

$$D^+ + 2I^- \rightarrow D + I_2^{-\cdot} \tag{2.1}$$

This step is followed by the disproportonation of two intermediate species into I_3^- and I^-.

$$2I_2^{-\cdot} \rightarrow I_3^- + I^- \tag{2.2}$$

Subsequently, the I_3^- diffuses to the Pt counter electrode and is reduced to three I^- species (step ⑥):

$$I_3^- \rightarrow 3I^-. \tag{2.3}$$

The generated voltage under illumination, labeled as ΔV in Figure 2.1, corresponds to the difference between the quasi-Fermi level of the electrons in the TiO_2 and the equilibrium redox potential of the electrolyte, I_3^-/I^- [6]. Hereby, one of the biggest losses in the dye-sensitized solar cell is the regeneration process. It requires an overpotential of ca. 0.2-0.3 eV to drive the electrolyte oxidation. Another big loss is the potential drop of around 0.3 eV for the second regeneration step, which is the potential difference between $I_2^{-\cdot}/I^-$ and I_3^-/I^-. A typical DSSC has a loss-in-potential of around 0.8 eV [15].

After electron injection, electron transport to the electrode and dye regeneration compete with interfacial recombination. Due to the much faster reaction speed of dye regeneration (in the ns- to ps-range) as well as electron injection (<100 fs [16, 17]) and transport (in the order of microseconds to miliseconds [18]), the recombination at the interface between the injected electron in TiO_2 and the oxidized dye (in the order of microseconds to miliseconds [19, 20]) is outpaced (Figure 2.2). For an efficient charge separation, the regneration of the dye, which is the electron transfer from I^- to the oxidized dye, must be much faster than the charge recombination process.

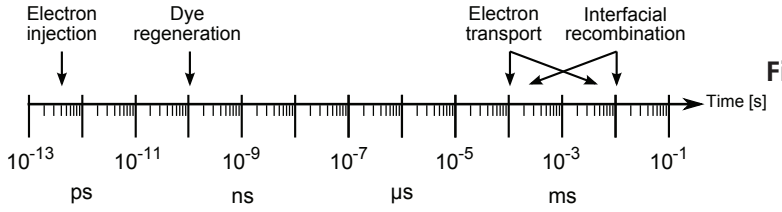

Figure 2.2: The comparison of reaction speeds of the most important reactions occuring during the operation of a DSSC.

2.2 State of the art dye-sensitized solar cells

As mentioned in the previous section, the voltage generated under illumination corresponds to the difference between the quasi-Fermi level of the electrons in the TiO_2 and the equilibrium redox potential of the electrolyte [21]. Hence, researchers are searching for other redox couples with higher redox potentials, which increase the open circuit voltage (V_{OC}). So far, I_3^-/I^- has been the most suitable redox couple, as its oxidized form, I_3^-, can persist for more than 1 ms allowing it to diffuse to the counter-electrode for reduction. Additionally, I_3^- is not readily reduced by the TiO_2 surface, which would be an unwanted recombination process [22]. Other redox couples with better redox potentials than I_3^-/I^- have typically suffered from high recombination rates and lower open-circuit voltages leading to poor efficiencies. In 2010 Feldt et al. presented a iodide-free dye-sensitized solar cell with a cobalt complex electrolyte and an efficiency of 6.7% [23]. The Co complex (redox potential of 0.6 V vs. NHE) has an advantage in the potential over the I_3^-/I^- (potential of 0.35 V) which is shown in Figure 2.3. In 2011 Yella et al. came up with a new donor-π-bridge-acceptor, a zinc porphyrin dye which in conjunction with the Co complex redox electrolyte lead to an efficiency of 12.3%. So far, this is the record for a single cell dye-sensitized solar cell [24].

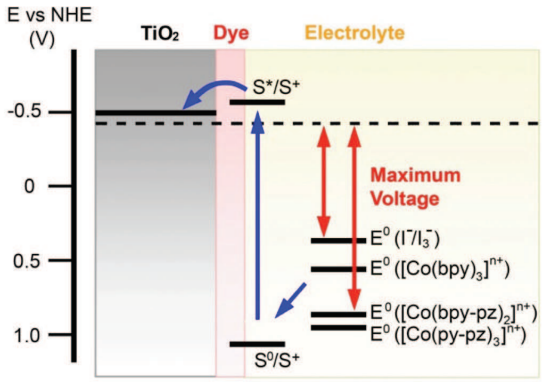

Figure 2.3: The energy level diagram plotted vs. NHE of a DSSC: the redox potentials, ground and excited state, for a typical sensitizer, for the iodide/triiodide redox couple as well as for a series of cobalt complexes are shown. The maximum achievable voltage is indicated. The figure is taken from [25].

Another aim of the current research on dye-sensitized solar cells is the scale up of these cells. Two of their biggest problems are imperfect sealing, which causes electrolyte evaporation and thus decreases the long-term stability of the cell, and the cost and the abundance of platinum and ruthenium. Recently, Wang et al. demonstrated a 6.5% cell with an amphiphilic ruthenium polypyridyl photosensitizer, an eutectic melt, which is a solvent-free ionic liquid electrolyte, and a CoS counter electrode as a replacement for the platinum electrode [26]. Although I_3^-/I^- redox couples work quite efficiently in the dye-sensitized solar cell, they suffer from two major disadvantages in addition to the imperfect redox potential. Electrolytes that contain I_3^-/I^- corrode electrical contacts made of silver and triiodide partially absorbs visible light [27]. Furthermore, a big effort is made on inventing ruthenium-free dyes, as for example perylene derivates as shown by Li et al. [28].
Another approach to circumvent the problems related to liquid electrolytes is the use of solid-state hole conducting molecules. One of the most promising molecules is Spiro-MeOTAD, which was first synthesized by Salaneck et al. [29, 30] and which was first used in a cell by Bach et al. in 1998 [31]. This type of cell is subject of this work. The best efficiency of the solid-state dye-sensitized solar cell obtained so far

is 4 to 5% [32–36] and so less than half of the best single cell dye-sensitized solar cell. For comparison, the best efficiency obtained for a organic thin film solar cell is ca. 10% [2] and for a silicon crystalline cell ca. 25% [2].

2.3 Solid-state dye-sensitized solar cells (solid-state DSSC)

In a solid-state dye-sensitized solar cell (solid-state DSSC), in comparison to a conventional dye-sensitized solar cell, the liquid electrolyte is replaced by a solid-state hole conducting organic molecule. Commonly used molecules are spiro-linked molecules such as Spiro-MeOTAD which are deposited by spin-coating and which can penetrate the mesoporous TiO_2 structure [31]. Because the charge carrier density of the hole conductor is lower than the density of the electrolyte, the space charge region of the organic molecule is much wider than the Helmholtz layer of the electrolyte. In order to avoid an ohmic contact between Spiro-MeOTAD and the FTO electrode, which would cause charge carrier recombination at the interface [37], a dense TiO_2 blocking layer (BL-TiO_2) is added between the FTO film and the nc-TiO_2 film [31, 37, 38].

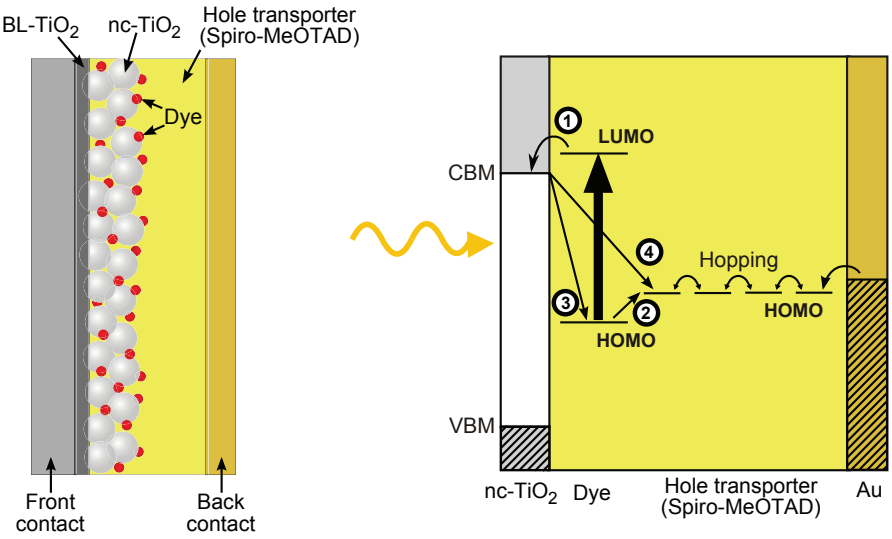

Figure 2.4.: The build-up (left), the function and the charge-transfer processes (right) of the solid-state dye-sensitized solar cell: reaction 1 and 2 are the electron and hole injection from the dye into the TiO_2 and hole conductor, respectively. Reactions 3 and 4 are direct recombination with the dye cations and with the hole conductor, respectively.

The operation principle of a solid-state DSSC is illustrated in 2.4. The light harvesting in the dye monolayer, electron injection (reaction ①) and transport in the nc-TiO_2 are the same processes in the solid-state DSSC and the DSSC. The biggest differences are the dye reduction and the hole transport in the hole conductor. In a solid-state DSSC, after hole injection (reaction ②), the hole is travelling through the hole conducting layer via a hopping process [39]. This is a one step process instead of a two step redox reaction as for the I_3^-/I^- electrolyte (see Section 2.1).

The nc-TiO_2 thickness of an optimized solid-state dye-sensitized solar cell is $2\,\mu m$ [40] which is much lower than the thickness of about $10\,\mu m$ that is used for DSSCs [6] and hence reduces the absorption of light due to the smaller amount of adsorbed dye. There are two factors that limit the efficiency of solid-state DSSCs with higher TiO_2 thicknesses: incomplete pore filling of the mesoporous nc-TiO_2 films with the hole conductor, which is between 60-70% for TiO_2 thicknesses below $3\,\mu m$ and decreases for higher thicknesses [35, 41], and electron-hole recombination [32, 42].

The charge transfer rate for dye regeneration depends on the HOMO energy offset between the dye and hole conductor [43]. Hence, the interfacial charge transfer process is controlled thermodynamically but not kinetically [32, 44]. In order to achieve a charge transfer yield of 85%, the energy difference between the HOMO of the dye and the hole conductor must be at least 0.2 eV.
Recombination in solid-state DSSCs is two orders of magnitude faster than in liquid DSSCs [45]. Two possible recombination pathways are indicated in Figure 2.4: the excited electron can either recombine with a hole in the excited dye (reaction ③) or with a hole in the hole conductor (reaction ④). An indicator of the recombination rate is the electron diffuson length (L_D), which is a function of the electron lifetime τ and the diffusion coefficient D.

$$L_n = (D\tau)^{1/2} \tag{2.4}$$

In mesoporous nanocrystalline TiO_2, L_D is $6\,\mu m$, which is much larger than the optimized $2\,\mu m$ film thickness [46, 47]. However, Snaith et al. calculated that the diffusion length in solid-state DSSCs is light dependent and reduces as much as to $0.6\,\mu m$ under standard solar illumination intensities ($100\,mWcm^{-2}$) [48], which indicates a shorter electron lifetime and more losses in the electron collection efficiency.

Generally, other loss mechanisms in a dye-sensitized solar cell include: incomplete light harvesting of the dye, inefficient photoinduced electron transfer due to a direct loss of absorbed photons to non-injecting channels and relaxation of the excited dye, which results in a formation of a relaxed exciton at a lower energy. Furthermore, resistivity losses during the charge transport through the solar cell and resisitvity losses as well as potential barriers at the electrodes reduce the attainable V_{OC} and fill factor.

3 Materials

The requirements for the materials used for the different parts of the solid-state dye-sensitized solar cell vary significantly. The properties of those materials range from a high surface area and a good electron mobility required for the nc-TiO_2 substrate to a high absorbtivity for the organic dyes and a high hole mobility for the organic hole conductor. As the main focus of this work lies on the investigation of electronic properties like the energetical lineup of the materials at the interface the materials are introduced especially in terms of electronic properties in the following. In the beginning, a short comparison of organic and inorganic semiconductors, which are the materials mainly investigated in this work, is given. Furthermore, titanium dioxide (TiO_2) as the photoelectrode, the hole conductor Spiro-MeOTAD with its dotants Li-TFSI and WO_3 and ruthenium and ruthenium-free dyes are introduced.

3.1 Organic vs. inorganic semiconductors

Comparing inorganic and organic semiconductors, one of the largest differences are the very dissimilar conductivities (Figure 3.1). Organic molecular crystals, solids and amorphous solids with conjugated π-systems are insolators at room temperature and below in thermal equilibrium without any applied electric field strength and any irradiation with light, electrons etc. The conductivity of inorganic semiconductors are between isolators and metals ($\sim 10^{-7}$-10^{2} S/cm), whereas the transitions are not sharp but smooth.
There are two ways how organic semiconductors can become conducting. Firstly, excess charge carriers can be either injected by an external field or created by the internal photoelectric effect. Secondly, the semiconductor can be doped by defects, contaminations and dopants which can be atoms or molecules. On one hand, these impurities can be ionized thermally and create movable charge carriers and hence increase the conductivity. On the other hand, defects can also act as traps for excess charge carriers and therefore lead to a reduced conductivity.

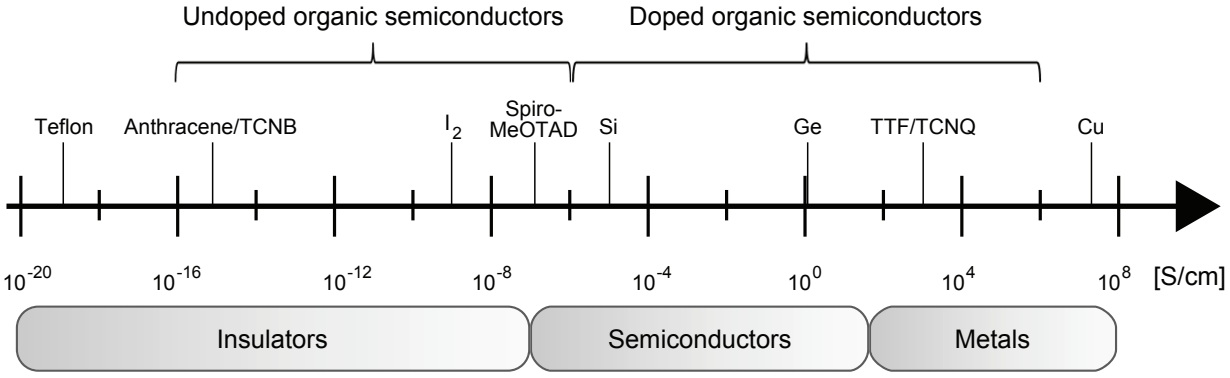

Figure 3.1.: The conductivity of various insulating, semiconducting and metallic materials: undoped organic materials are classified as insulators, unless they are doped, which increases the conductivity. Values are taken from references [10, 49].

Organic semiconductors are carbon based molecules with conjugated π-bonds which are part of double bonds between two carbon atoms. In those double bonds, σ bonds result due the overlap of two sp^2 hybridized orbitals and π bonds due to the overlap of two p orbitals. The electrons of conjugated π bonds are delocalized all over the π system. By the combination of orbitals, binding and antibinding

orbitals are created within a molecule. The highest occupied molecular orbital (HOMO) consists of the binding π orbitals and the lowest unoccupied molecular orbital (LUMO) of the antibinding π^* orbitals. The exchange interaction between the hybrid orbitals is strong, which leads to a large split-up of the states. By contrast, the intermolecular interaction of Van der Waals type which is determined by the easily polarizable and excitable π electrons is weak and hence the split-up of the HOMO und LUMO states of the individual molecules by the interaction of the molecules is low. The resulting bandwidth in organic semiconductors is 4-300 meV, which is much smaller than the bandwith of inorganic semiconductors of 2-8 eV. In contrast to inorganic semiconductors, the valence electrons of organic semiconductors are also delocalized, but only on the respective molecule.
In inorganic semiconductors, the superposition and exchange interaction of atomic orbitals cause the discrete states of the individual atoms to form continuous bands of atoms ordered in a periodic lattice which is described in the so called energy band model. The highest occupied band is called valence band (VB) and the lowest unoccupied band conduction band (CB). The gap between valence and conduction band is called bandgap. The transport of electrons and holes in the conduction band and valence band, respectively, is described by the energy band model and is influenced by crystal imperfections, impurities, doping and temperature.

Because of the strong localization on single molecules of the charge carriers in organic semiconductors, charge carrier transport between the molecules cannot be described by the energy band model. In organic semiconductors the charge carrier transport is highly dependant on the chemical structure and the morphology of the material [50, 51]. Therefore, the transport cannot be described by a single model that applies for all materials. In amorphous materials the commonly accepted model is a hopping mechanism which is a thermally promoted tunneling process between strongly localized states. In amorphous organic semiconductors, the distances between the single molecules and therefore the intermolecular interaction vary strongly. The resulting distribution of the HOMO and LUMO states can be described by a Gaussian distribution (Figure 3.2).

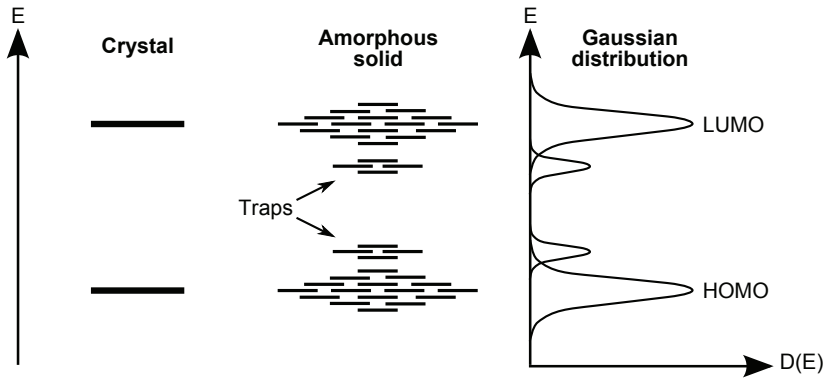

Figure 3.2.: The distribution of the HOMO and LUMO states in an organic crystal and amorphous solid.

As stated by Kaake et al., grain boundaries between amorphous and crystalline phases act as intrinsic charge carrier traps which hinder charge carrier transport [52]. Similarly, grain boundaries in polycrystalline films function as trap states and lead to spatial inhomogeneity of the transport properties. Hereby, electrostatic interactions cause the trapping of electrons by grain boundaries. Thus, the aim for amorphous materials is to supress the crystallinization of the organic semiconductors, for example by introducing a spiro connection between two defined π-systems. One example of this concept is the hole conductor Spiro-MeOTAD which is used in the solid-state dye-sensitized solar cell [29, 53, 54].

3.2 TiO_2

Titanium dioxide (TiO_2) which is abundant and a low cost material is one of the most commonly used inorganic semiconductors for photoelectrochemical applications [1, 7, 55–57]. Because of its energetic properties, stability and the Lewis acidity of the surface, which enables the adsorbtion of dyes, it is favored over other materials for the photoelectrode in DSSCs.
In the DSSC, mesoporous TiO_2 is used as the photoelectrode. For this purpose, TiO_2 is often deposited by the sol-gel method and subsequent calzination at ca. 450 °C [11]. As the surface area is up to 1000-fold higher than of a dense flat TiO_2 electrode [48, 58], more dye can be adsorbed, which leads to a higher light absorbtion. A standard, mesoporous TiO_2 film shows a pore volume of about 60% [58] and an average pore size of about 15 nm [6]. The standard dye N719 used in the DSSC has a diameter of ca. 1-2 nm [59]. Therefore, the pores of TiO_2 are big enough to enable the dye to penetrate the mesoporous structure. In addition to the mesoporous TiO_2, a dense and pinhole-free and flat layer called the blocking layer is employed in the solid-state DSSC in order to prevent an ohmic contact between the hole conductor and the FTO front contact. This layer is usually prepared by spray-pyrolysis [60].

Structural properties

In nature, TiO_2 exists in two tetragonal forms, rutile and anatase, and in one rhombic form, brookite. For applications, rutile and anatase are favored over brookite, as they are easier to synthesize. Therefore, in the following, only the properties of these two phases are discussed.
Both anatase and rutile have a tetragonal symmetry and belong to the same point group, but have different space groups, $I4_1/amd$ and $P4_2/mnm$, respectively. The unit cells of anatase and rutile contain 6 and 12 atoms, respectively. In both cases, the lattice is built up by distorted $[TiO_6]^{2-}$ octahedra (Figure 3.3), in which one titanium atom is coordinated to six oxygen atoms, two Ti-O bonds are slightly larger than the other four and some of the O-Ti-O bond angles deviate from 90° (see Table 3.1) [61]. The distortion of the octahedra is slightly higher for anatase than for rutile, which explains the lower density of anatase. In anatase and rutile, each octahedra shares four and two edges, respectively. In literature, nanocrystalline TiO_2 is reported to have the same Raman active modes as single crystals [62, 63]. Anatase (D_{4h}^{19}) with its two formula units per unit cell has six Raman active modes ($A_{1g}+2B_{1g}+3E_g$) and rutile (D_{4h}^{14}) with its two units four Raman active modes ($A_{1g}+B_{1g}+B_{2g}+E_g$).

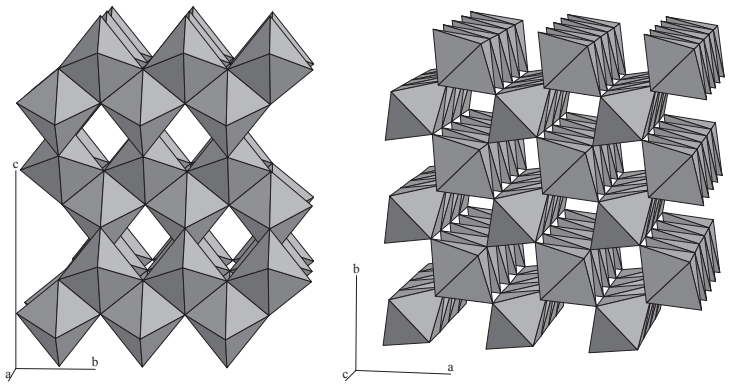

(a) Anatase (b) Rutile

Figure 3.3.: The anatase (a) and rutile (b) polytypes of TiO_2 with its crystal structures: the basic build up units are distorted $[TiO_6]^{2-}$ octahedra.

Table 3.1.: The crystal structure data of anatase and rutile [56, 61, 64].

		Anatase	Rutile
Crystal structure		tetragonal	tetragonal
Space group		D_{4h}^{19}-$I4_1/amd$	D_{4h}^{14}-$P4_2/mnm$
Lattice constants	a=b	3.784 Å	4.594 Å
	c	9.515 Å	2.959 Å
Ti-O bond length [Å]		1.937 1.965	1.949 1.980
O-Ti-O bond angle [°]		77.7 92.6	81.2 90.0
Density [g/cm^3]		3.79	4.13
Bandgap [eV]		3.2 (indirect)	3.0 (direct), 3.1 (indirect)

For the application in dye-sensitized solar cells, TiO_2 in the anatase crystal modification is preferred over rutile, as the electron mobility in anatase ($\mu = 10\,cm^2/Vs$) is higher than in rutile ($\mu = 1\,cm^2/Vs$) [64, 65]. Moreover, the diffusion coefficient of conduction band electrons in rutile is significantly smaller than that in anatase [66]. As the bandgap of anatase is 3.2 eV which is slightly higher than the bandgap of rutile ($E_g = 3.0\,eV$) [56, 64], it is transparent for the largest part of the visible spectrum. Nevertheless, a larger maximum photovoltage can be achieved with an anatase instead of a rutile photoelectrode because the conduction band edge of anatase is 0.2 eV higher than that of rutile [56, 67]. Because of the small particle size of the nanocrystalline TiO_2 which does not allow the formation of a band bending, electron transport in TiO_2 is dominated by diffusion [47, 68].
However, Park and co-workers found that the photocurrent-voltage responses of dye-sensitized rutile and anatase films were remarkably close [69]. In their study, the open-circuit voltage was essentially the same for the two cells, whereas the short-circuit photocurrent of the rutile based cell was only about 30% lower than that of the anatase based cell. The researchers attributed the lower photocurrent of the rutile based cell to a smaller amount of adsorbed dye due to a smaller surface area per unit volume compared with that of the anatase based cell [69]. Li et al. prepared and investigated DSSCs based on TiO_2 electrodes which consisted of anatase/rutile phase mixtures [70]. Up to a rutile weight percentage of 13 wt% the photocurrent of those cells were significantly enhanced, which is, as the authors claim, due to the additional electron injection from the rutile phase.

Electronical properties

In Figure 3.4, the calculated molecular orbital structures of anatase and rutile are shown [71, 72]. In both cases, due to the ionic character of the Ti-O bond, the valence band which is ca. 6 eV wide consists mainly of O2p states and the conduction band mainly of Ti3d states. The lower valence bands are predominantly formed of O2p orbitals, whereas the upper valence bands show a strong hybridization between O2p and Ti3d electrons. The states of lower binding energies (around 5 eV in reference to the Fermi level) are assigned mainly to Ti3d-O2p π-bonding states and the states at around 8 eV mainly to O2p-Ti3d σ-bonding states. In contrast to that, the lower conduction bands consist mainly of Ti3d states and the bands above show mainly s and p character. Thomas et al., who investigated rutile (110), anatase (101) and anatase (001) TiO_2 single-crystal surfaces by resonant photoemission spectroscopy and X-ray absorption spectroscopy, determined the valence band maximum for all the investigated surfaces to be at 3.0 eV [72].

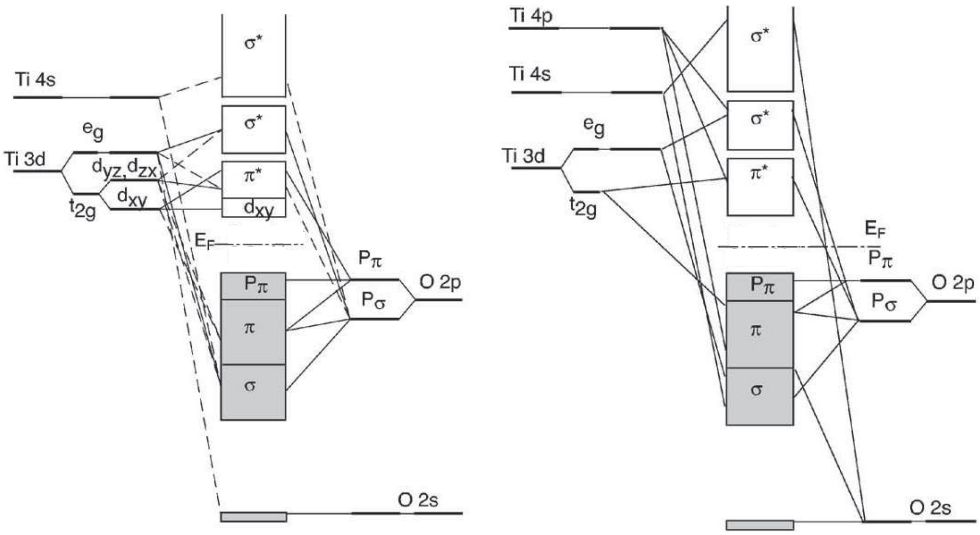

(a) Anatase (b) Rutile

Figure 3.4.: The molecular-orbital bonding diagram of anatase and rutile: the figures show the atomic levels, the crystal-field split levels and the final interaction states.[71, 72].

Defects and gap-states: Bulk defects in TiO_2 originate from the reduction of TiO_2 [64]. As the titanium-oxygen phase diagram shows a great variety of stable phases with a variety of crystal structures (Figure 3.5), TiO_2 can be reduced easily. The resulting defects act as color centers which change the color of TiO_2 from transparent over light to dark blue. These intrinsic defects are the reason for the intrinsic n-type doping of TiO_2 and its high conductivity.

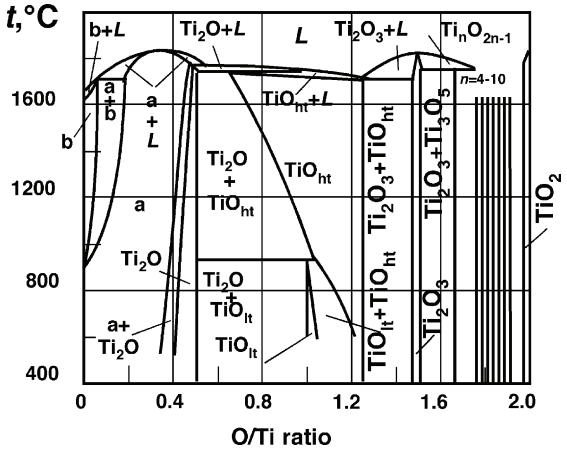

Figure 3.5: The Ti-O phase diagram taken from [64]: the region Ti_2O_3-TiO_2 contains Ti_2O_3, Ti_3O_5, seven discrete phases of the homologeous series Ti_nO_{2n-1} (Magneli phases) and TiO_2.

Two kind of surface defects can be observed in photoelectron spectroscopy spectra: oxygen vacancies (V_O) and additional band gap-states just below the Fermi level that are referred to as Ti3d$<E_F$ in this work. As clarified by calculations and resonant photoemission spectroscopy measurments on different TiO_2 surfaces, the oxygen vacancies can be attributed to Ti3d states [72–75]. The oxygen vacancy forms as a consequence of the removal of a neutral oxygen atom from the surface, which leaves two electrons behind. Those electrons previously occupied O2p levels in the valence band, which are no longer available, and must therefore go into the bottom Ti3d states of the conduction band [76, 77]. In addition, reduced Ti^{3+} states in the Ti2p core level and an oxidized oxygen species form. All three, the V_O gap-state, the reduced Ti^{3+} component and an oxidized species, are observed in sputter experiments. For example, Liu et al. compared X-ray photoemission spectroscopy and ultraviolet photoemission spectroscopy measurements of unsputtered and sputtered TiO_2 [78]. As shown in Figure 3.6, with increasing

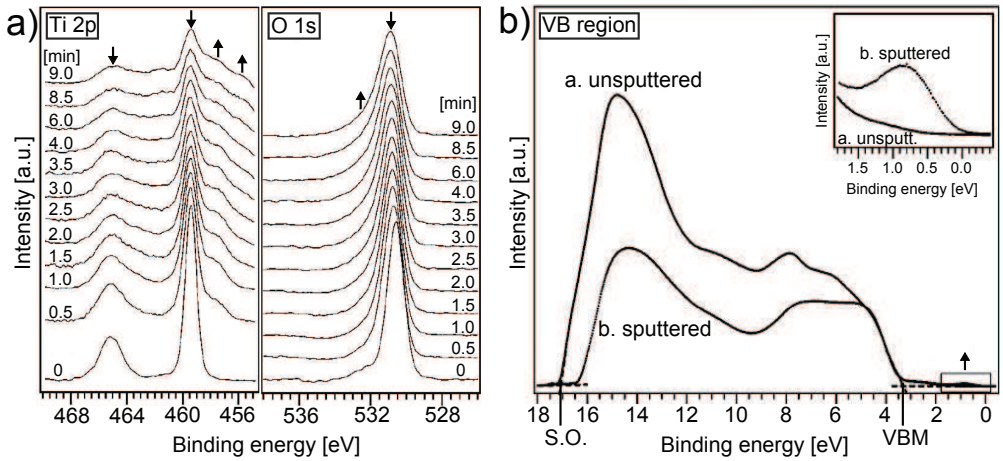

Figure 3.6.: X-ray photoemission spectroscopy (left) and ultraviolet photoemission spectroscopy (right) spectra of nanocrystalline TiO_2 recorded during sputtering: with increasing sputtering time the intensity of the reduced Ti2p species and the oxidized O1s species increase, whereas the relative intensity of the Ti2p and O1s emission lines decrease. After sputtering, the valence band of the sputtered TiO_2 shows gap-states at ca. 0.8 eV which can, hence, be correlated to oxygen vacancies. The spectra are taken from [78]

sputter time the reduced Ti2p species and the oxidized O1s species increase, whereas the relative intensity of the O1s emission line decreases. Consequently, the preferential removing of oxygen from the TiO_2 surface is assumed. After sputtering, the valence band of the sputtered TiO_2 shows gap-states at ca. 0.8 eV, which can therefore be correlated to oxygen vacancies.
The second surface defect Ti3d$<E_F$ which is not observed on single crystalline anatase [79] occurs just below the Fermi level. This gap-state was described by Westermark and Schwanitz in detail [11, 80–82]. The origin of this gap-state is still under discussion but, according to Schwanitz, could arise from non-hybridized Ti d_{xy} orbitals. Another explanation could give the work of Nunzi et al. who used quantum mechanical calculations based on DFT and DFTB methods to investigate electronic trap states in nanocrystalline TiO_2 [83]. They found states of titanium t_{2g} character at ca. 0.3-0.4 eV below the conduction band, which would appear approximately at the same energetic position as the Ti3d$<E_F$ gap states in the X-ray photoemission spectroscopy spectra. The authors state that the conduction band states originate from 4-fold, instead of 6-fold, coordinated surface Ti atoms lying mainly at the edges between the (100) and (101) facets of TiO_2.

The influence of the TiO_2 gap-states on the function of the dye-sensitized solar cell is still under discussion. In literature, by adsorbing of 4-*tert*-butyl pyridine (*t*-BP), which is often added to the I_3^-/I^- electrolyte, an increase of the open-circuit voltage is achieved [42, 84]. Yu et al. claim that the increase is due to the healing of the surface oxygen vacancies of TiO_2 and the removal of gap-state electrons through donation into empty π^* orbitals of the pyridine ring of *t*-BP [85]. The authors investigated the bonding of *t*-BP to TiO_2 by photoelectron spectroscopy and density functional theory calculations. The molecules preferentially adsorb over oxygen vacancies, which induces a band shift of ca. 0.2 eV to lower binding energies in the TiO_2 and thus increases the open-circuit voltage. Furthermore, some authors state that TiO_2 gap-states at the surface act as recombination sides and trap centers, which hinders the charge transport [84, 86, 87].

3.3 Spiro-MeOTAD

The hole transport material (HTM) in the solid-state DSSC has to fulfill a variety of requirements. This includes a sufficient offset of the HOMO of the HTM from that of the dye molecule, high hole mobility, good pore filling, good wetting ability of the TiO_2 surface, processable from solution and low crystallization rate (for the formation of smoth amorphous films) [43].
As seen in Chapter 2, the offset between the HTM and dye HOMO levels plays an important role for the reduction of the dye and thus for the working principle of the dye-sensitized solar cell. Good pore filling as well as wetting of the TiO_2 structure improve the efficiency of the cell. Furthermore, solution processability makes production easier and more cost effective as simpler and cheaper equipment like spin-coaters can be used compared to the expensive and complicated UHV-chambers used for thin-film solar cell production, for example. Unlike organic semiconductors used in applications such as organic field effect transistors, the desired state of the HTM in the solid-state DSSC is the amorphous glass state. Therefore, sufficiently high hole mobility is necessary as the charge mobility decreases with increasing disorder. Grain boundaries in polycrystalline films act as trap states and lead to spatial inhomogeneity of the transport properties [52]. While single crystal materials introduce birefringence and polycrystals lead to a large amount of scattering, the optical properties of amorphous materials are isotropic [88, 89]. The glass-transition temperature T_G at which the amorphous phase transforms into the crystalline phase is a good indicator of the stability of the amorphous glass state. A high T_G can be achieved by molecules with a symmetric globular structure, large molecular weight and small intermolecular cohesion [90, 91].

Spiro concept

A different concept to improve the morphological stability of low mass materials is spiro-linked molecules. The spiro center is the tetrahedrally coordinated, sp^3-hybridized C-atom which combines two π-systems (Figure 3.7) which can have the same or different function with respect to emission or charge transport. The perpendicular cross-shaped structure of the spiro-linked molecules minimizes the intermolecular interactions responsible for aggregation in the solid state, causes entanglement in the amorphous state and therefore hinders recrystallization and improves the solubility compared to the non-spiro parent compounds [92]. Furthermore, it enhances the temperature and thus the long-term stability of the amorphous phase without disturbing the charge transport considerably [93]. Because of the perpendicular arrangement of the π-systems and the spectroscopic transition moments, the resulting coupling between the branches is weak and, thus, most of the electronic and optical properties of the isolated branches are preserved in the molecule [88].

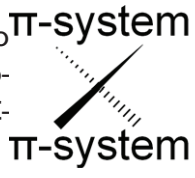

Figure 3.7: A schematic drawing of two π-systems connected by the spiro-center, which is a sp^3-hybridized C-atom.

However, in literature, the so-called "spiroconjugation" model describes interactions between the two branches [53, 94]. In the ground state, the only nodal plane of the highest occupied π-molecular orbital is the plane of each branch. Due to the symmetric mismatch of the wavefunctions, interaction is prevented. Nevertheless, in an excited state, higher π-orbitals may exhibit a second nodal plane which is perpendicular to the first plane but parallel to the nodal plane of the other branch. Other mechanisms leading to interactions are vibronic coupling and coupling due to non-perpendicular transition moments [95–99].

Spiro-MeOTAD: The solid-state hole conducting material 2,2',7,7'-tetrakis(*N*,*N*-di-p-methoxypheny-amine)-9,9'-spirobifluorene (Spiro-MeOTAD), which is shown in Figure 3.8, is currently under investigation as a replacement of the liquid triiodide/iodide electrolyte employed in the DSSC [31]. The properties of Spiro-MeOTAD are listed in Table 3.2.

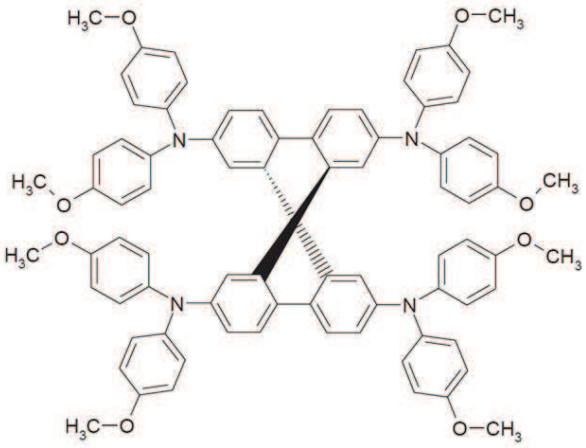

Figure 3.8: The structural formula of 2,2',7,7'-tetrakis(*N*,*N*-di-p-methoxypheny-amine)-9,9'-spirobifluorene (Spiro-MeOTAD).

Table 3.2.: The properties of Spiro-MeOTAD [49, 88, 100].

Properties	Spiro-MeOTAD
Glass transition temperature T_g [°C]	121
Melting point T_m [°C]	246
Decomposition temperature T_g [°C]	440
Absorption maxima [nm]	383, 365, 305
Fluorescence maximum [nm]	424
Absorption coefficient α [cm^{-1}]	10^5
Dielectric constant ϵ	3
Hole mobility [cm^2/Vs][1]	$2{\cdot}10^{-4}$
Conductivity [Scm^{-1}]	$2.5{\cdot}10^{-7}$

[1] At an electric field of $2.6{\cdot}10^5$ V/cm and a temperature of 300 K.

Poplavsky and Nelson investigated the temperature-field behavior of the time of flight mobility of spin-coated Spiro-MeOTAD and evaporated Spiro-TAD thin films [100]. Within the Gaussian disorder model proposed by Bässler et al. [101] a higher mobility prefactor μ_0 for the methoxy-substituted Spiro-MeoTAD was found. The authors claim that the attached methoxy side groups increase the negative charge density at the HOMO, which decreases its binding energy and results in a higher effective spatial extension of this orbital. Compared to spin-coated Spiro-MeOTAD, evaporated Spiro-MeOTAD shows a lower mobility prefactor μ_0 (0.047 for spin-coated and 0.0147 cm^2/Vs for evaporated), a lower energetic disorder parameter σ (0.101 and 0.088 eV) and a higher positional disorder parameter $\sum$ (2.7 and 3.35) [102]. From the positional and energetic disorder values it can be concluded that the evaporated film is higher ordered than the spin-coated.

In general, thin films of Spiro-MeOTAD can be either solution processed or thermally evaporated. Because spin-coating is a cheaper technique than PVD and evaporated Spiro-MeOTAD films are too highly ordered for conduction [93, 100], Spiro-MeOTAD is commonly spin-coated for the application in DSSCs. Furthermore, the conductivity of pure Spiro-MeOTAD (see Table 3.2) is not sufficient enough and the material is therefore doped to enhance its conductivity. Different additives are used in the DSSC, such as 4-tert-butylpyridine (*t*-BP) and lithium bis(trifluoromethylsulfonyl) amine lithium salt (Li-TFSI) which is investigated in this work. As seen in Section 3.2, *t*-BP increases the open-circuit voltage of a cell by ca. 0.2 eV, which is explained by the healing of the surface oxygen vacancies of TiO_2 and the removal of gap-state electrons through donation into empty π^* orbitals of the pyridine ring of *t*-BP.

3.4 Doping

In general the concept of doping is not only employed for inorganic semiconductors but becomes more and more important in the field of organic electronics. For example, relative positions of molecular levels across interfaces can be realigned by doping [103, 104]. As a consequence, energy barriers which define carrier injection and transport between layers and have thus a direct impact on the performance of organic based devices like organic photovoltaic cells, but also OLEDs and OFETs, can be engineered. In this way, doping has lead to improvements in the power conversion efficiencies of heterojunction solar cells which consist of copper phtalocyanine as the donor and undoped as well as doped carbon-60 fullerene as the acceptor by a factor of nearly 2 [105], for example. One of the concepts is p-type doping of organic molecules by metal oxides with high work functions. In this work, the doping of Spiro-MeOTAD with tungsten oxide (WO_3) was investigated.
In DSSCs various dopants are already used to enhance the properties of the materials and interfaces and hence the performance of the photovoltaic cell. One of those dopants is lithium bis(trifluoromethylsulfonyl) amine lithium salt (Li-TFSI) which is investigated in this work and introduced in the following subsection.

3.4.1 Li-TFSI dopant

In solid-state DSSCs, Li-TFSI, among other dopants, is usually added to Spiro-MeOTAD to enhance its intrinsically poor conductivity and thus the efficiency of the DSSC. Snaith et al. showed that Li-TFSI improves the hole mobility of Spiro-MeOTAD from $2{\cdot}10^{-4}$ to $1.6{\cdot}10^{-3}\,cm^2/Vs$ [49]. Similarly, the conductivity increases from $2.5{\cdot}10^{-7}$ to $2.0{\cdot}10^{-5}\,Scm^{-1}$ after adding 12% Li-TFSI. The authors claim that the ionic dopant reduces the potential barrier between neighboring Spiro-MeOTAD anions and thus increases the hole mobility. For 12 mol% TFSI-Li, the authors calculate a minimum anion-anion separation of 2.6 nm resulting in a significant overlap between the potential wells and therefore a reduction of the barrier height by up to 0.7 eV. Another contribution to the increase of hole mobility may arise from the increase of the polarizability of the matrix, which may result in a reduction of the polaron binding energy. The structure of Li-TFSI is presented in Figure 3.9.

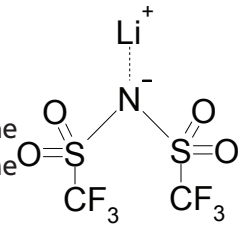

Figure 3.9: The structural formula of the lithium bis(trifluoromethylsulfonyl) amine lithium salt (Li-TFSI).

However, the precise role of Li-TFSI has not been clarified yet. Lithium ions are reported either to intercalate or to adsorb to the surface of TiO_2 inducing a shift of the surface potential of the TiO_2 to more positive values [106–108]. In dye-sensitized solar cells using the liquid I_3^-/I^- electrolyte, Koops et al. state that Li-TFSI is strongly influencing the injection kinetics [109]. By time-resolved single photon counting and varying the amount of Li-TFSI and *t*-BP in the elctrolyte, the observed injection half-time increased from less than 60 ps for 0.1 M Li-TFSI/0 M *t*-BP to 550 ps for 0 M Li-TFSI/0.1 M *t*-BP. However, the open circuit voltage was much smaller for the electrolyte with 0.1 M Li-TFSI/0 M *t*-BP, which makes a counterbalance between both additives necessary for optimized performance.

3.4.2 Tungsten(VI) oxide (WO_3) dopant

In literature, tungsten(VI) oxide (WO_3) which has a melting point of 1474 °C [110] is reported to undergo a series of phase transitions upon heating: from monoclinic (ϵ-WO_3), triclinic (δ-WO_3), monoclinic (γ-WO_3), orthorombic (β-WO_3) to tetragonal (α-WO_3) [111]. All polymorphs can be derived from the cubic ReO_3 structure [112]. At room temperature, WO_3 exists in the monoclinic form (a=7.30 Å, b=7.53 Å, c=3.85 Å, $\alpha=\gamma=90°$, $\beta=90.88°$) [113] and has a density of 7.16 g/cm^3 as a thin film [114]. Similar to TiO_2, the lattice is built up by distorted WO_6 octahedras, in which one tungsten atom is coordinated to 6 oxygen atoms and which are connected at the edges.

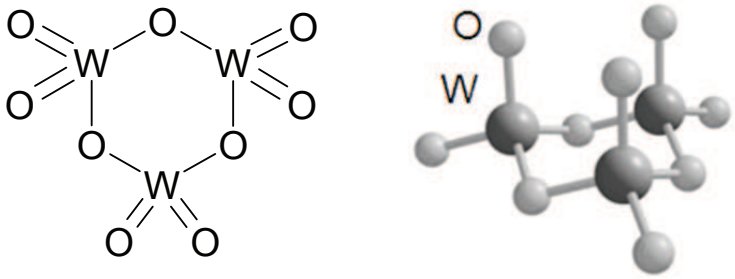

Figure 3.10.: W_3O_9 cluster

Within the gas phase in the physical vapor deposition (PVD) process, W_3O_9 clusters (Figure 3.10) are the dominant species [110, 115]. During the initial stages of growth on SiO_2, Ottaviano et al. found WO_3 in the form of clusters on the substrate proving the previous statement [116]. Furthermore, for substrate temperatures below 450 eV, thermal evaporation leads to amorphous films [117, 118]. Therefore, the growth of the WO_3 thin films which were deposited by PVD on unheated substrates with a crucible temperature in the range from 1000 to 1100 °C in this work is considered to be amorphous with possible polycrystalline parts [119, 120]. The basic build up unit is considered to be W_3O_9 clusters as was mentioned above. Because the band gap of WO_3 is also dependent on the morphology, the value of amorphous WO_3 of 3.26 eV [119, 121] is used here. For crystalline WO_3 the band gap can decrease to 2.6 eV [114, 122].
Similar to TiO_2, the valence band of WO_3 consists mainly of O2p states with an admixture of W5d states at the bottom of the band, whereas the bottom of the conduction band is a mixture of W5d and W6s states [123]. WO_3 surfaces also show gap-states which were identified as W5d states induced by oxygen deficiency [124]. In literature, gap-states and core level emissions were measured on WO_3(001) surfaces by X-ray photoemission spectroscopy and synchrotron-induced photoemission spectroscopy [124–126]. The gap-states were related to oxygen defects causing occupation of the W5d orbital of neighbor W atoms, which induces a reduced W^{5+} component in the W4f emission.
Time-dependent DFT calculations on tri-tungsten oxide clusters (W_3O_n and $W_3O_n^{-1}$) were carried out by Huang et al. [127, 128]. The authors suggest a D_{3h} structure for W_3O_9 in which each W atom is tetrahedrally coordinated to two bridging O atoms and two terminal O atoms. The extra electron of the $W_3O_9^{-1}$ cluster which for instance is assumed in this work to form after a charge transfer in an organic/WO_3 composite enters the $10a_1{}'$ LUMO orbital of W_3O_9, which is equally shared by the three W atoms (3.11).

The internal interface charge transfer model

P-type doping of organic semiconductors by metal oxides, such as WO_3, was already shown for different semiconducting molecules [129–132]. Under discussion as a possible doping mechanism is an energetically favored electron transfer from the HOMO of the organic molecule to the unoccupied states of the oxide, namely the conduction band.

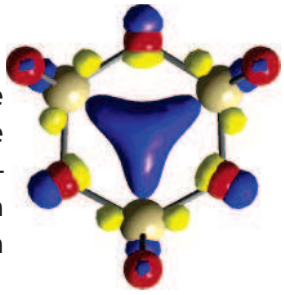

Figure 3.11: The HOMO picture of the charged $W_3O_9^-$ cluster, as present in the organic/WO_3 composite: the extra electron is equally shared by the three tungsten atoms (light green). Picture taken from [127].

In the common doping model, in the case of p-doping, the matrix molecules transfer electrons from their HOMO to the LUMO of the acceptor molecules [133]. This process which is described in the integer electron transfer model for interfaces with negligible hybridization of π-electronic molecular orbitals and substrate wave functions [134] is enegetically favorable and leads to a full ionization of the dopant. However, Mayer, Hein and coworkers, who investigated the doping of CuPc with WO_3, showed by high-resolution transmission electron microscopy that WO_3 precipitates within the organic/WO_3 composites lead to a lower doping efficiency than expected [135]. Therefore, they introduced the internal interface charge transfer model which is employed and developed further in this work.
In the model, a charge transfer and an interface dipole between the organic matrix and the precipitated dopant are discussed (Figure 3.12). Hereby, the charge transfer is thermodynamically driven by the equalization of the Fermi levels of both materials at the internal interfaces. The equalization may be discussed as a three step process. In the first step, the vacuum levels of matrix and dopant equalize according to the Anderson model. The absolute shift is equal to the initial Fermi level difference $\Delta\Phi$ of both materials. Subsequently, a dipole δ is forming at the interface, which reduces the Fermi level difference. In order to completely equalize the Fermi level difference, a charge carrier transfer takes place. As a consequence, a more or less developed band bending is forming in the materials depending on the density of states: a large band bending is formed in materials with low density of states, such as organic semiconductors, and vice versa. For small dimensions compared to the extension of the space charge region, band bending can be neglected. Transmission electron micrographs of codeposited organic semiconductor/WO_3 films performed by Mayer et al. show WO_3 precipitates of ca. 5 nm within the films [135], which is small compared to the width of a space charge region (typically in the order of 100 nm) in an organic layer of an organic/metal interface [136]. Cluster formation was also found in organic composites with MoO_3 and ReO_3 whose structural properties are comparable to WO_3 [137]. In Figure 3.12 different dipoles for different surfaces and morphologies, band bending as well as Fermi level pinning due to gap-states are neglected.

For this simplified situation, Equation 3.1 is valid:

$$\Delta E_F^M = \Delta\Phi - \delta - \Delta E_F^D, \tag{3.1}$$

where ΔE_F^M is the band bending of the matrix and ΔE_F^D that of the dopant. Assuming that the dipole at the internal interfaces is the same as for a bilayer, the Fermi level shifts of matrix ΔE_F^M and dopant ΔE_F^D in the composite are equal to the maximum band bending eV_{bb} of the matrix/dopant bilayer interface:

$$\Delta E_F^M = eV_{bb}^M \tag{3.2}$$

$$\Delta E_F^D = eV_{bb}^D. \tag{3.3}$$

In this way, all values of Equation 3.1 can be determined from X-ray photoemission spectroscopy measurments of matrix/dopant bilayer experiments.

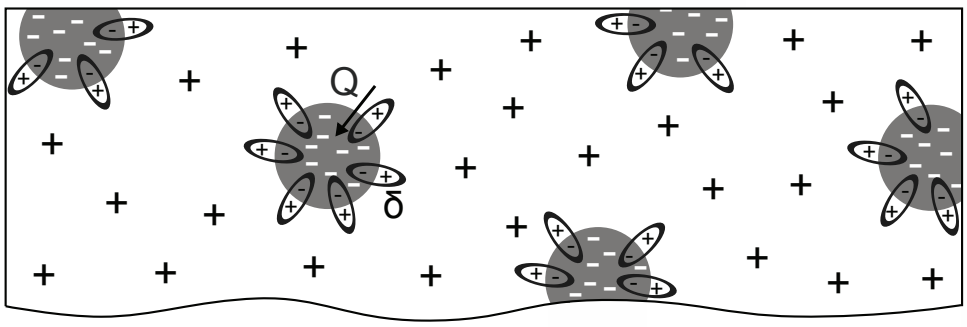

(a) Sketch of an organic/WO_3 composite.

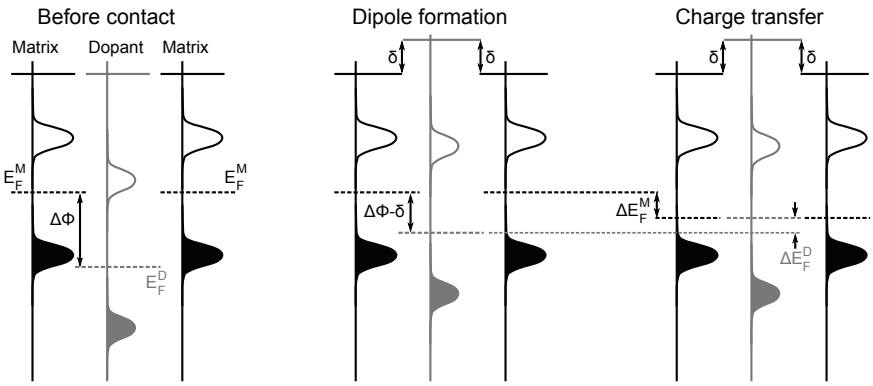

(b) Development of the band energy diagram.

Figure 3.12.: Sketch of an organic/WO_3 composite with WO_3 clusters (a) and the development of the corresponding band energy diagram (b). According to internal interface charge transfer model, the work function difference between the matrix material and the dopant precipitates is compensated by the formation of an interface dipole potential δ and the charge transfer Q between the two phases, which leads to a Fermi level shift ΔE_F^M in the matrix and ΔE_F^D in the dopant.

3.5 Dyes

The dye plays an important role for the operation of the dye-sensitized solar cell. As much incoming light as possible has to be absorbed by the dye which is adsorbed on the TiO_2. Within the dye, the absorbed photons excite electrons from the HOMO of the dye to the LUMO and create electron-hole pairs, namely excitons. Subsequently, those pairs have to be separated and transported to the respective electrode. Therefore, the dye has to fulfill various requirements: the absorption spectra and the extinction coefficient of the dye have to be adjusted to absorb a majority of the incoming visible light. On one hand, the HOMO of the dye has to be energetically localized under the HOMO of the hole conducting material to guarantee an efficient reduction of the oxidized dye. On the other hand, the LUMO has to be localized close to the anchoring group where the dye is connected to the TiO_2 and has to be energetically over the conduction band of TiO_2 to guarantee an efficient electron injection into the anode. In order to prohibit a nonradiative recombination of excitons, the aggregation of the dye should be avoided. Additionally, one of the most important properties of the dye is its long term stability to withstand the great number of oxidation and reduction cycles during operation.

Furthermore, the impact of the standard solvent acetonitrile and the adsorption geometry of the dyes on the dye performance are still under discussion. Schwanitz et al. state that the choice of the solvent has an direct influence on the orientation of the dye [82]. The authors compared synchrotron-induced photoemission spectroscopy measurements of two coadsorbed solvents, the polar acetonitrile and the unpolar benzene, on the dye N3. The measurements showed that acetonitrile can penetrate the dye layer and force the dye molecules apart standing upright. In this way, the NCS groups, on which the HOMO of the dye is mainly located, points away from the TiO_2 substrate and towards the electrolyte. The LUMO, which is mainly located over the π electron system of the bipyridine ligands, is close to the substrate. In this way, the vectorial charge transfer of the photo-induced hole to the electrolyte is promoted and a direct recombination path between the HOMO of the dye and the substrate due to the direct contact avoided. In contrast to that, the effect was not observed for unpolar benzene. A similar effect was found for the ruthenium dye C101, [NaRu(4,4'-bis(5-hexylthiophene-2-yl)-2,2'-bipyridine)(4-carboxylic acid-4'-carboxylate-2,2'-bipyridine)$(NCS)_2$] [138]. Due to different adsorption geometries and therefore different HOMO-TiO_2 distances the recombination rate which was calculated by time-dependent DFT was smaller for the shorter distance.

Ruthenium complexes

The ruthenium-complexe Ru^{II}(2,2'-bipyridine-4,4'-dicarboxylate)$_2(NCS)_2$ (N3) is one of the first used and still one of the most common dyes for dye-sensitized solar cells [139]. Since then, substantial amount of of effort has been spent on developing new dyes with different central atoms and different ligands to improve the incident photon to current efficiency (IPCE) [140, 141]. The IPCE is defined as the amount of electrons created by the incoming light divided by the amount of incident photons:

$$IPCE\,(\lambda) = \frac{1240 \cdot I_{SC}}{\lambda \phi}\,, \tag{3.4}$$

where I_{SC} is the short-circuit current, λ the wavelength and ϕ the energy flux density. In Figure 3.13, the IPCEs plotted as a function of the excitation wavelength of a DSSC sensitized with N3 ($RuL'(NCS)_3$) and N719 ($RuL_2(NCS)_2$), also called black dye, are shown. The response of the black dye extends 100 nm further into the IR than that of N3 [6].

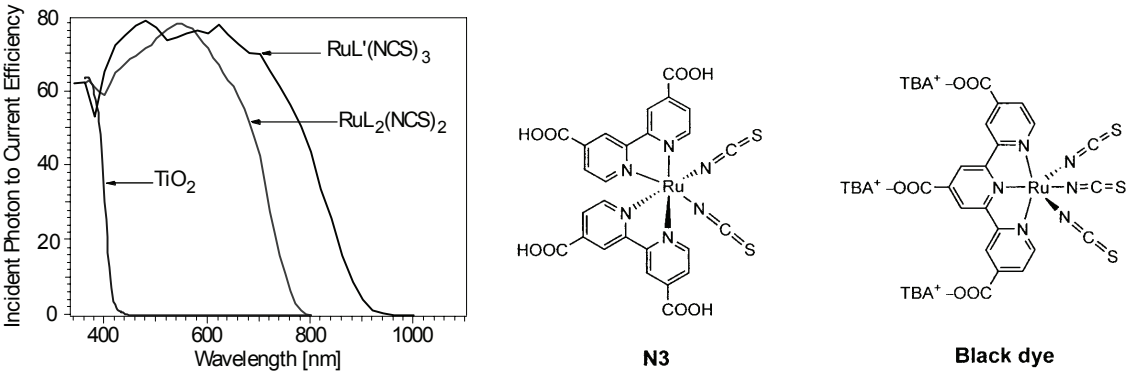

Figure 3.13.: The IPCE of DSSCs with N3 ($RuL'(NCS)_3$) and black dye ($RuL_2(NCS)_2$) as the sensitizer and bare TiO_2. The IPCE measurements are taken from [6] and the structural formula from [142].

Metal-free dyes

Besides ruthenium(II) complexes, like N3 and N719, metal-free organic dyes are currently under investigation as an alternative for the application in DSSCs. These dyes do not contain expensive ruthenium, additionally their production is most often easier and more cost-effective and their absorption and electrochemical properties are easier tunable compared with the Ruthenium complexes [142]. Due to the design of metal-free dyes, it is possible to integrate units into their structure which enlarge the absorption of the dye in a broad part of the spectrum and increase hence the extinction coefficient. Nowadays, the efficiencies of DSSCs with metal-free sensitizers reach values of up to 9% [143–145].
In this work, three metal-free perylene dyes, ID94, ID224 and ID504 together with its additive ID662, obtained from the cooperation partner BASF were investigated. The structures are shown in Figure 3.14. All three dyes have the same basic structure, perylene. The dyes ID224 and ID504 have the same anchoring group but different ligands. The dye ID94 which is the same except the anchoring group as the dye ID224 yields efficiencies of 6.8% and 1.8% in a dye-sensitized solar cell and a solid-state dye-sensitized solar cell, respectively [28]. Hereby, the IPCE value of 87% for the DSSC is remarkably high compared to cells with other metal-free sensitizers. So far, no efficiencies of DSSCs prepared with the other dyes (ID224 and ID504) have been published.

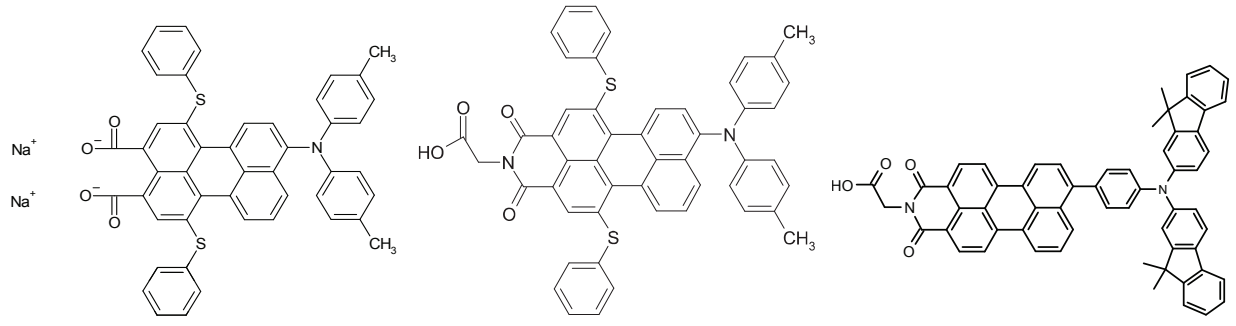

(a) ID94 (b) ID224 (c) ID504

Figure 3.14.: The structural formula of the perylene dyes ID94, ID224 and ID504.

Part II.
Experimental

4 Preparation methods

In the following, the preparation setup and the deposition methods are introduced and explained. In particular, this chapter covers the solid-liquid interface analysis system (SoLIAS) and the interface preparation methods, physical vapor deposition (PVD) and drop-casting, which were employed to deposit thin films of the materials discussed in the previous chapter.

4.1 Solid-Liquid Analysis System (SoLIAS)

The Solid-Liquid Interface Analysis System (SoLIAS) at the Berlin synchrotron radiation source BESSY II is dedicated to wet chemical experiments, such as drop-casting, and solid interface experiments, such as physical vapor deposition (PVD) [146]. A sketch of the system which consists of three levels is shown in Figure 4.1.

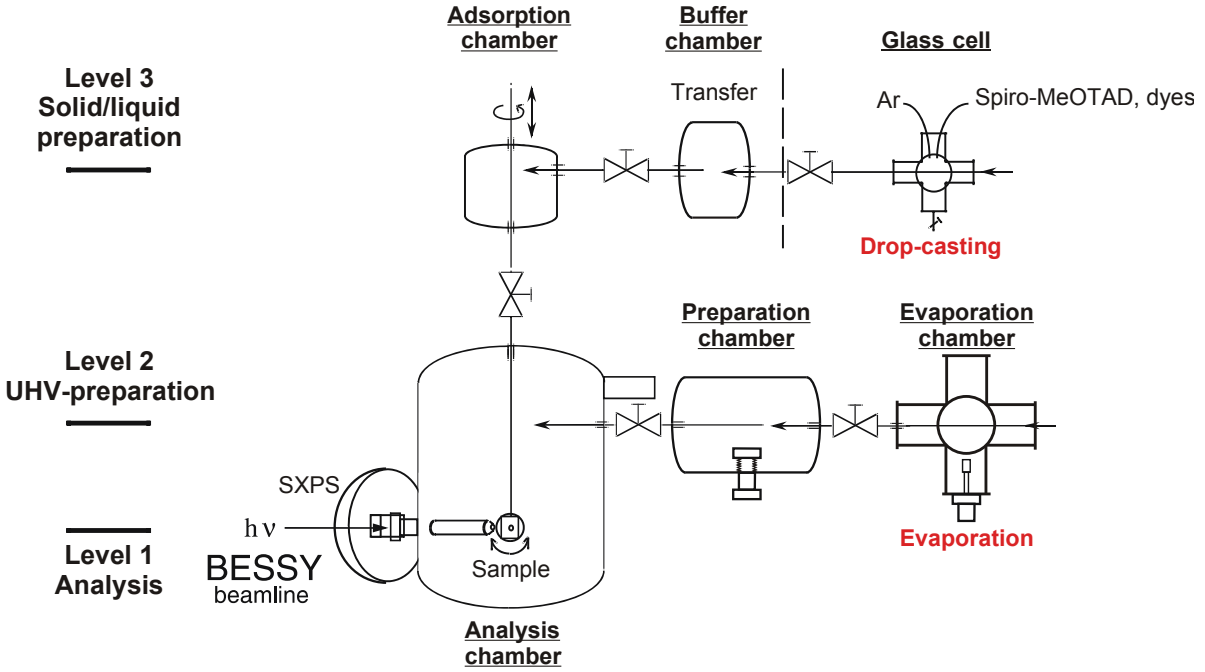

Figure 4.1.: A sketch of the Solid-Liquid Interface Analysis System (SoLIAS) at the Berlin synchrotron radiation source: the system is divided into three levels, which are shown in the sketch.

The first level is the analyzing level where samples are probed. The transfer rod with the sample holder is aligned to the incoming light so that the analyzing position is in the focus of the beamline. The second level includes opportunities for UHV-preparation, LEED and the load lock. In the third level, organic molecule and solvent adsorption experiments can be performed. This level includes a transfer system with which the samples can be cooled permantly with liquid nitrogen and a buffer chamber/glass cell combination which provides the possibility for wet chemical experiments without contact to ambient air. For this, the integrated glass cell is permantly rinsed with pure argon (purity of 5.0) and attached to the buffer chamber which can be also flooded with pure argon for transferring. As transferring can be done without breaking and leaving the vacuum, experiments which ask for different preparation methods for different materials can be performed as well.

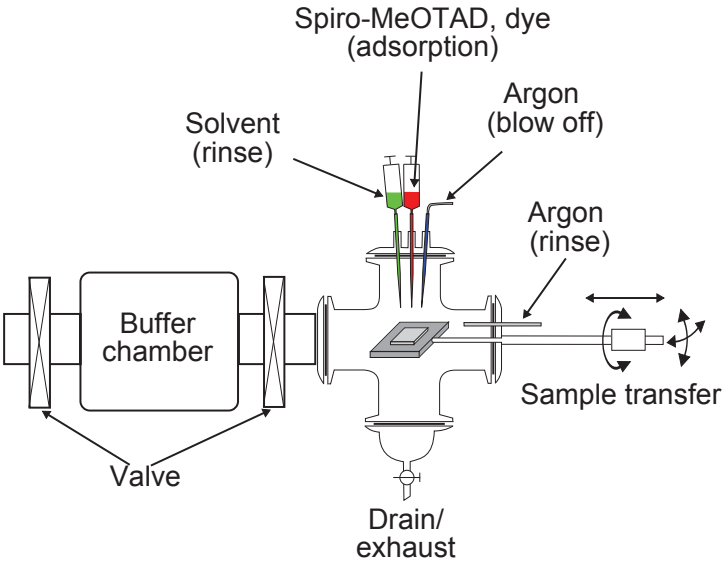

Figure 4.2.: A detailed sketch of the glass cell which is attached to the SoLIAS and is used for wet chemical experiments.

4.2 Physical vapor deposition (PVD)

In this work, physical vapor deposition (PVD) was used to deposit Spiro-MeOTAD onto different kind of substrates in order to perform interface experiments. The method utilizes the volatility of materials upon heating. This requires materials which do not decompose during heating and evaporation.
Self-made evaporation cells attached to the UHV-chamber which is labeled "Evaporation" in Figure 4.1 were used for evaporation of the powder materials. For that, Al_2O_3 crucibles were heated resistively by tantalum wires wrapped around the crucible. The temperature was controlled by a Ni/Cr-Ni thermocouple attached to the crucible. The parameters which mainly influence the deposition rates are the distance between crucible and sample, the source temperature and the pressure in the deposition chamber. In this work, the rate was determined individually for each experiment.

4.3 Drop-casting

Drop-casting is a method which is similar to printing and in a simplified way to spin-coating. Printing and spin-coating are employed in industry for cost-effective production of organic electronics. For the investigation by synchrotron-induced photoemission spectroscopy, the dyes and some Spiro-MeOTAD films were drop-casted. Drop-casting experiments on the dyes and Spiro-MeOTAD were performed in the buffer chamber/glass cell combination of the SoLIAS which is shown in Figure 4.2. For this, the molecules were dissolved in organic solvents. Afterwards, the dissolved materials were dropped with a glass pipette onto the substrate. Before transferring the sample into the buffer chamber, the residual solvent was blown off with pure argon.

5 Experimental characterization methods

In this chapter, the characterization methods photoelectron spectroscopy, including synchrotron-induced photoemission spectroscopy (SXPS) and resonant photoemission spectroscopy (RPES), scanning electron microscopy (SEM), atomic force microscopy (AFM) and grazing incidence X-ray diffraction (GIXRD) are introduced and explained.

5.1 Photoelectron spectroscopy (PES)

In general, photoelectron spectroscopy is a powerful tool to characterize the chemical state, the elemental composition and empirical stochiometry of elements in a material. The basic principle of this method is the photoelectric effect discovered by Hertz in 1886 [147] and theoretically described by Einstein in 1905 [148]. In the late fifties, Siegbahn developed the electron spectroscopy for chemical analysis (ESCA) [149–151].

Working principle

During the exposure of material to high-energetic radiation, electrons are excited from their orbitals into the vacuum level and thus emitted from the material (Figure 5.1). Depending on the excitation energy of the electromagnetic radiation, one distinguishes between X-ray photoemission spectroscopy (XPS) and ultraviolet photoemission spectroscopy (UPS). The kinetic energy of the emitted electrons E_{Kin} depends on the excitation energy $h\nu$, the work function of the sample Φ_{Sample} and the binding energy E_B of the electrons in their respective orbitals:

$$E_{Kin} = h\nu - E_B - \Phi_{Sample} \,. \tag{5.1}$$

Therefore, for the excitation of an electron from its orbital, an exitation energy larger than the respective binding energy of the electron is necessary.

Detection and chemical analysis

The emitted photoelectrons are detected with respect to the Fermi level. Due to the electrical contact between the sample and the spectrometer the Fermi levels of both equalize. Between the photoelectron generation in the sample and the detection in the spectrometer, the electron has to overcome the contact potential difference between sample and spectrometer Φ_{Sample}-$\Phi_{Analyzer}$. The kinetic energy of the electrons at the detector is given by the following equation:

$$E_{Kin} = h\nu - E_B - \Phi_{Sample} + (\Phi_{Sample} - \Phi_{Analyzer}) = h\nu - E_B - \Phi_{Analyzer} \,. \tag{5.2}$$

The binding energy of the photoelectrons in respect to the Fermi level is obtained by reorganizing Equation 5.2:

$$E_B = h\nu - E_{Kin} - \Phi_{Analyzer} \,. \tag{5.3}$$

Hence, the binding energy of the photoelectrons (PE) at the spectrometer is independent on the work function of the sample. The work function of the analyzer is determined by a calibration measurement with a metal standard and is set per definition so that the zero point of the PE spectra is the Fermi level.

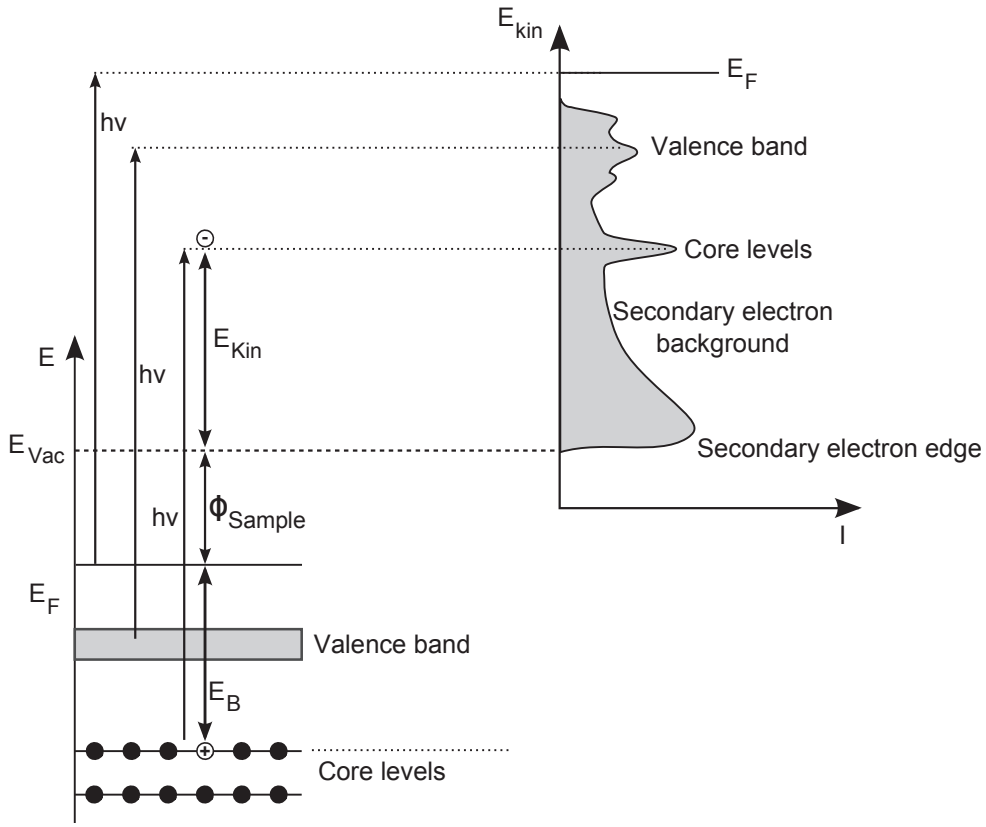

Figure 5.1.: The energy scheme of the photoemission process. In the photoelectrical effect, a photon excites an electron to the vacuum level (left). The detected kinetic energy E_{Kin} of the photoelectron is dependent on the excitation energy $h\nu$ and the binding energy E_B of the electron. The PE spectrum consists of photoelectrons from the different atomic levels as well as of secondary electrons which form the background (right).

Beside photoelectrons, Auger electrons with defined kinetic energy leave the sample and are detected in the PE spectra. The Auger process is a follow-up process of the photoelectric effect and is in competition with the emission of a X-ray quantum. The photohole which is created in the photoelectric effect is filled with an electron from a higher level (Figure 5.2). Subsequently, the energy which becomes available during this process is transferred to another electron which is excited above the vacuum level. Because of its creation mechanism the kinetic energy of an Auger electron is independent on the excitation energy.

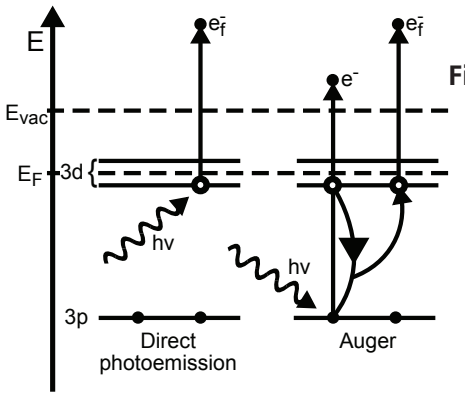

Figure 5.2: The direct photoemission process (left) and the follow-up Auger process (right): the photohole which is created during the photoelectric effect is filled with an electron of a higher level. Subsequently, the energy which becomes available during this process is transferred to another electron which is excited above the vacuum level.

Element identification, chemical shift and quantitative analysis: The individual elements of a sample are identified by comparing the measured spectra to reference spectra and tables [152] which contain all emissions of the different orbitals of each element. The emissions are unique for each element. For the identification of an element, usually all emissions of an element are used.
Moreover, the different oxidation states and different binding partners, if the electronegativity difference is larger than 0, can be distinguished with PES. As the local electron density distribution varies, the measured binding energy is also changing. Due to this, the photoelectrons appear at a higher/lower binding energy in the PE-spectra, which is called chemical shift for bonding to more electronegative/electropositive. Bonds with different partial charges of the bond partners, as it can occur in organic molecules with elements with different electronegativities, also show a chemical shift compared to a bond with the same elements. In this way, the shape of the C1s emission line is a fingerprint for organic molecules. This effect was used in this work to determine the differently bonded carbon atoms in the organic hole conductor Spiro-MeOTAD (see Subsection 8.1.3).
By integrating and comparing the intensities of the emissions of the different elements, a quantitative analysis of the surface can be performed. According to Fermi´s golden rule, the detected intensity is quantum mechanically defined as the transition probability between an initial state (i) and a final state (f) [153]:

$$I \propto W_{fi} \propto \left| < \psi_f | \hat{H}' | \psi_i > \right|^2 \cdot \delta(E_f - E_i - h\nu) \, . \tag{5.4}$$

Hereby, the delta function preserves the conservation of energy, whereas the Bracket-expression implies the overlap of both wave functions, which is equivalent to the photoionization cross section σ and contains the conservation of momentum, number of elements and symmetry. The measured intensity I_A of an emission line of an element A is given by:

$$I_A \propto \sigma_A \int_A N_A(x,y,z) \, \exp\left(-\frac{z}{\lambda_e \cos\theta} \right) dz \, , \tag{5.5}$$

where σ_A is the photoionization cross section of the element A, N_A(x,y,z) the density of atoms of the element A at the position (x,y,z), λ_e the mean free path of the photoelectrons and θ the angle between the surface normal in z-direction and the entrance slit of the analyzer.

In addition, the intensity which is measured by the spectrometer is dependent on device parameters, like the function of the transmission of the analyzer. For XPS systems, those parameters are usually combined in the atomic sensitivity factors ASF which are specific for each element and each XPS system. Hence, the concentration n_A of an element A with the intensity I_A of its emission line can be calculated in relation to an element B with the intensity I_B of its emission line by the following equation:

$$\frac{n_A}{n_B} = \frac{I_A \cdot ASF_B}{I_B \cdot ASF_A} . \tag{5.6}$$

Background and work function determintation

Beside photoelectrons and Auger electrons with defined kinetic energies, inelastic scattered electrons leave the sample. Inelastic scattering processes in the sample lead to a large amount of low-energetic electrons called secondary electrons which contribute to the background of the photoemission spectrum. The amount of electrons rises strongly with decreasing kinetic energy and drops drastically at a kinetic energy of 0, which is called the secondary electron edge. At a given excitation energy, the secondary electron edge is the maximum binding energy at which electrons still posses enough energy to exit the sample. In order to yield a higher electron counting rate and to discriminate the work function of the sample and the spectrometer, a bias voltage is applied. Therefore, the work function of the sample Φ is given by the excitation energy $h\nu$, the position of the secondary electron edge E_{Sec} and the bias voltage Φ_{bias}:

$$\Phi = h\nu - E_{Sec} - \Phi_{bias} . \tag{5.7}$$

Determination of the Film thickness and the deposition rate

The thickness of a deposited, thin film can be determined by the damping of the integrated intensity of a substrate emission line measured with PES. For this, the intensity of the substrate emission before deposition I^0_{Sub} and after deposition I^d_{Sub} is measured. Therefore, the thickness of the film must be low enough so that the substrate signal is still observable in the PE spectra after deposition. With increasing film thickness d, the intensity of the substrate signal is decreasing exponentially. As a consequence of Equation 5.5, the ratio of both integrated ratios is given as follows:

$$\frac{I^d_{Sub}}{I^0_{Sub}} = \exp\left(-\frac{d}{\lambda_e \cos\theta}\right), \tag{5.8}$$

where θ is the angle between the sample surface and the analyzer. As the mean free path λ_e of the electrons is dependent on the kinetic energy of the electrons and the investigated material, the mean free paths of electrons for the different investigated materials were calculated separately by a tool of the "NIST ELECCTRON INELASTIC-MEAN-FREE-PATH DATABASE" of the National Institute for Standards and Technology (NIST) with the equations of Tanuma, Powell and Penn [154].
For the interface experiments conducted in this work, the materials were deposited stepwise and the film thickness of each deposition step was calculated according to Equation 5.8. By plotting the film thickness versus the deposition time, the deposition rate is obtained as the slope of the resulting line. Because the rate depends not only on the material, but also on other parameters like the source temperature and the pressure inside the deposition chamber which can vary from experiment to experiment, it was calculated individually for each deposition.

Satellites

Shake-up and shake-off satellites are two electron processes and two examples of final-state effects. If an electron transfers some of its energy to another electron during excitation by the incident radiation and this second electron is also excited into a higher energy state, the kinetic energy of the photoelectron is reduced by that amount. This results in a higher measured binding energy of the photoelectron. In

case the second electron is excited to the vacuum, the process is called shake-off, whereas in the case that the second electron is excited to a higher energy state, the process is called shake-up (Figure 5.3). For organic materials, the energy the photoelectron loses in the shake-up process corresponds approximately to the energy gap. Rocco et al. showed that the HOMO-LUMO shake-up increases in intensity and moves closer toward the C1s main emission with the increasing size of the aromatic system [155]. The authors compared the shake-up spectra of benzene, naphthalene, anthracene, tetracene, and pentacene in the condensed phase and explaned this effect with a higher delocalization of the aromatic system and its capability in screening the photogenerated core hole.

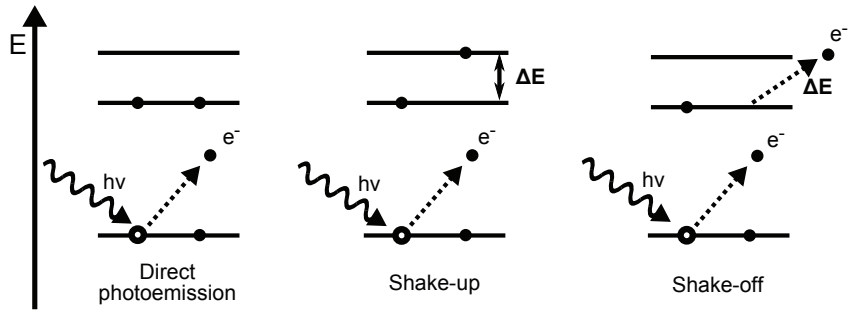

Figure 5.3.: Scheme of the direct photoemission and the final-state effects shake-up and shake-off.

5.1.1 Synchrotron-induced photoemission spectroscopy (SXPS)

Radiation sources with tunable excitation energies hν, like the synchrotron light source BESSY II in Berlin, have considerable advantages over conventional X-ray sources and provide a large number of possible applications. Beside the various excellent properties of the synchrotron light itself, like a small divergence and source size, a linear and circular polarization, a pulsed time structure and a high brillance, flux and stability, the experimentalist can select a wavelength from a broad spectrum which ranges from microwaves to hard X-rays.

The high surface sensitivity of the synchrotron-induced photoemission spectroscopy (as well as of the X-ray photoemission spectroscopy) results from the energy loss of the emitted photoelectrons during their way out of the sample. A measure for this is the mean free path of electrons which is the distance orthogonal to the surface in which the intensity is attenuated to $1/e$. As the mean free path depends on the kinetic energy of the electrons the information depths can be tuned by choosing appropriate photon energies.

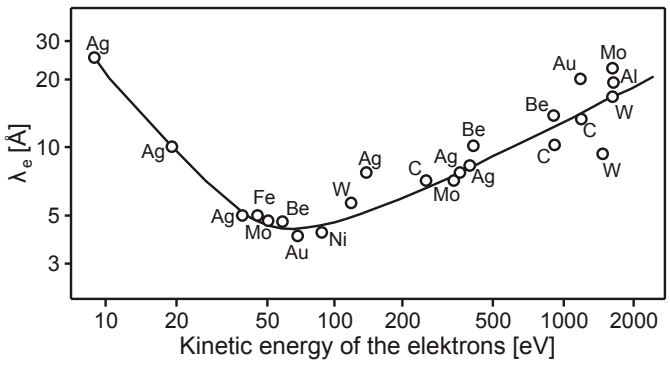

Figure 5.4.: The inelastic mean free path of electrons λ_e versus the kinetic energy of electrons for several metals. The graphic is taken from [156].

In Figure 5.4 the so called "bathtube curve", the mean free path of various metals λ_e is plotted versus the kinetic energy of the photoelectrons. The mean free path is typically in the range from 5 to 30 Å and has a minimum at ca. 50 eV. Electrons with higher kinetic energies (higher than 50 eV) have a longer range and the mean free path rises according to a square function. For energies smaller than 50 eV, the mean free path also rises due to too low energies to excite plasmons within the metals. As a consequence of the different binding energies of electrons from different orbitals and their resulting kinetic energies, the surface sensitivities are different for a fixed excitation energy.
Secondly, also the cross sections of the orbitals are dependent on the photon energy. Yeh and Lindau calculated energy dependent cross sections for the different elements and orbitals [157] which were used in this work to choose photon energies which result in a high surface sensitivity and intensity for the respective element. Two examples which employ this effect and which are shown in this work are the features of the TiO_2 valence band which react differently to different photon energies and the resonant photoemission spectroscopy which is explained in the following Subsection.

5.1.2 Resonant photoemission spectroscopy (RPES)

The resonant photoemission spectroscopy (RPES) is often used to investigate 3d metals, such as copper and zinc, and their contribution to the valence band in various systems [158–162]. Hereby, one utilizes the resonant enhancement of a feature by an autionization process (Figure 5.5). In this process, an electron is excited to an unoccupied state that subsequently relaxes back to its ground state. The available energy is then transferred to another electron which is ejected from the solid, can be detected and increases the counting rate. The Ti3d gap-states in TiO_2 are investigated by RPES to enhance their low

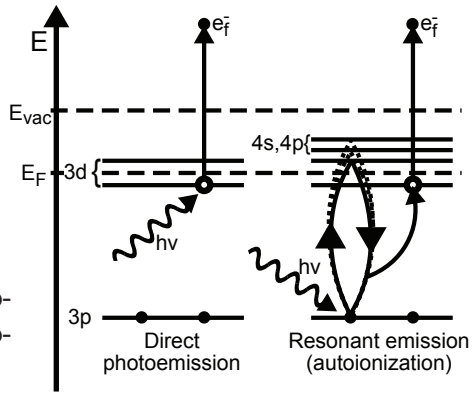

Figure 5.5: The direct photoemission process and the autoionization of the resonant photoemission.

intensities in PE spectra [72, 79]. For RPES, the excitation energy is scanned over the transition of a core level to a valence level in order to find an optimum energy. In the case of TiO_2, the excitation energy is approximately 47 eV for the Ti3p to Ti3d transition [72]) and approximately 465 eV for the Ti2p to Ti3d transition [163]). It has to be mentioned that the transitions in both cases can also take place to the Ti4s level. The direct Ti3p photoemission process is given by:

$$3p^6 3d^n + h\nu \rightarrow 3p^6 3d^{n-1} + e_f^- \,. \tag{5.9}$$

At the Ti3p→Ti3d transition, a resonance is observed due to the interference between the direct photoemission process and the excitation of electrons from the Ti3p to the Ti3d orbital followed by a decay into the same final state. These steps can be summarized by:

$$3p^6 3d^n + h\nu \rightarrow [3p^5 3d^{n+1}]^* \rightarrow 3p^6 3d^{n-1} + e_f^- \,, \tag{5.10}$$

where the asterisk denotes an excited state.

Although the Ti3d level (the same is true for the transition to the Ti4s level) in TiO_2 is unoccupied and no resonance would therefore be expected, the resonance occurs via an interatomic process due to the hybridization of Ti3d and O2p levels [164]. The resonant excitation process (for 3d orbitals) occurs initially as in Equation 5.10, but the decay channel is via the O2p orbitals and given by

$$[Ti3p^5 3d^{n+1}]^* + O2p^6 \rightarrow Ti3p^6 3d^n + O2p^5 + e_f^- \,. \tag{5.11}$$

In Figure 5.6, two series of RPES measurements performed by Schwanitz with different excitation energies for the Ti3p→Ti3d and the Ti2p→Ti3d resonances are shown [11]. The maximum intensities are obtained at an exitation energy of 47 eV and 465 eV, respectively. Therefore, those energies were also chosen in this work to perform RPES measurements on TiO_2.

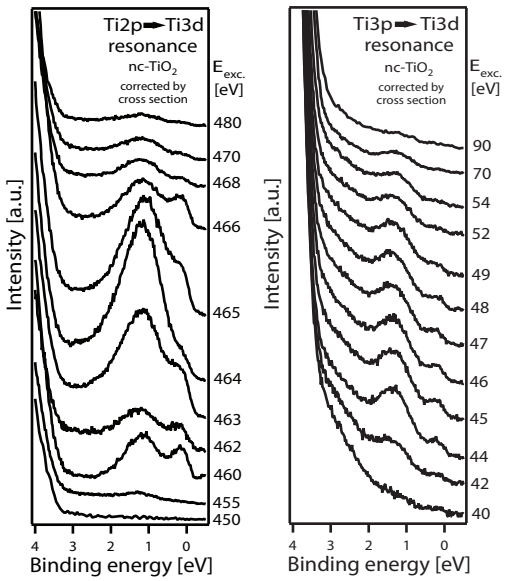

Figure 5.6: Series of RPES measurements of the gap region with different excitation energies for the Ti3p→Ti3d (left) and the Ti2p→Ti3d (right) resonances: the maximum intensities are obtained at an exitation energy of 47 eV and 465 eV, respectively. The graphs are taken from [11].

5.2 Raman spectroscopy

The Raman spectroscopy employs the inelastic scattering of light in molecules and solids. This effect called Raman effect was described first by Raman and Krishnan in 1928 [165]. For this, the sample is probed with monochromized light, usually with a laser in the visible, near infrared or near ultraviolet range. Hereby, the polarizability of the electron shell of the molecule must change during an oscillation for the occurance of a Raman line.

Due to the interaction of the light with vibrational, rotational or phonon modes of the sample, the Raman spectra shows beside the frequency of the elastically scattered light (Rayleigh scattering) also frequencies shifted to higher (Anti-Stokes Raman scattering) or lower frequencies (Stokes Raman scattering) which can be assigned to the characteristical energy modes of the investigated material. As shown in Figure 5.7, the molecules are excited from a vibrational state into a virtual energy state and then relax back. On one hand, in the case of elastic scattering, the initial and final states are the same and, hence, no shift is observed. On the other hand, whether the incident light gains or loses energy in the inelastical scattering process depends on the interaction of the incident light with the material. For the Stokes Raman scattering, the cross section of which is usually orders of magnitude lower than for the Rayleigh scattering process [166], the photon loses energy to the material which is initially in the ground state and ends up in an excited state. In the Anti-Stokes Raman process which has a lower probability than the Stokes Raman process, the photon gains energy from the material which is initially in an excited state and relaxes back to the ground state. In the spectra, Stokes and Anti-Stokes shifts are observed in the same distance from the incident frequency which is the Rayleigh frequency. Raman spectroscopy

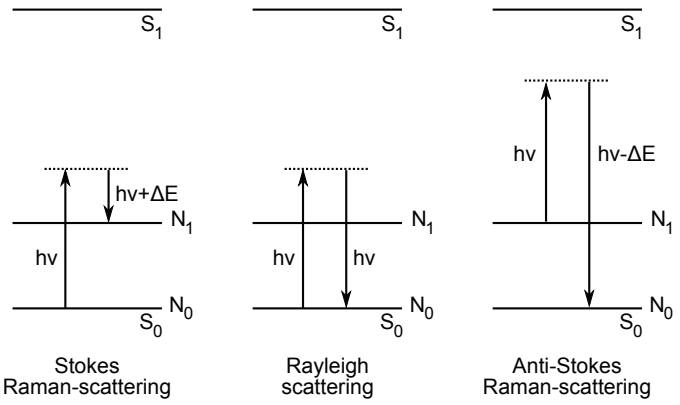

Figure 5.7.: The energetic scheme of the Rayleigh and Raman scattering: in the case of elastic scattering the frequency is the same for the incoming and the scattered light (Rayleigh scattering); in the case of inelasting scattering the frequency of the scattered light is either shifted to lower frequencies (Stokes Raman scattering) or to higher frequencies (Anti-Stokes Raman scattering). S_0, N_0 are the electronical and vibronical ground states and S_1, N_1 the electronical and vibronical excited states, respectively.

is commonly used to investigate the cristallinity, crystal orientation, composition and lattice strain of a sample which can be solid or liquid. As the vibrational information is specific for the chemical bonds and the symmetry of a molecule, Raman spectroscopy also provides a fingerprint spectrum of a material and its phases. In this work, Raman spectroscopy was used to investigate the crystal phases of the TiO_2 substrates before and after heat treatment.

5.3 Scanning Electron Microscope (SEM)

The scanning electron microscope (SEM) produces images with a magnification of up to 10^6 by scanning the sample with a focused electron beam. The electron beam which is emitted from an electron gun which usually consists of a tungsten or lanthanum hexaboride (LaB_6) cathode is focused and scanned over the sample by different electromagnetic lenses in the electron optical column. Therefore, the electro optical column has to be pumped to ultra-high vacuum conditions to minimize the interactions of the electrons with residual gas molecules in the column.

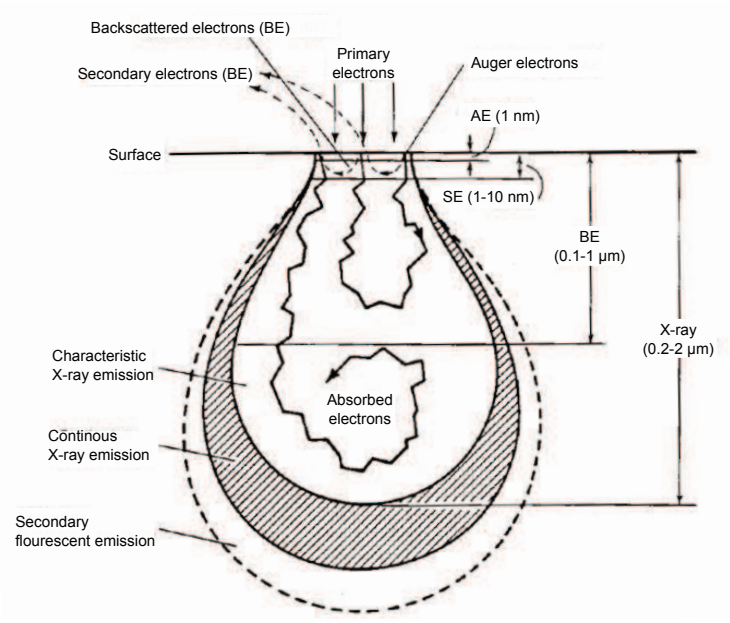

Figure 5.8: Areas of interaction of the electrons with the matter and the information depth of the detected radiation and electrons, respectively. The figure is taken from [167].

Inelastic scattering in the sample leads to ionization of the atoms. Because this so called secondary electrons (SE) have an energy of less than 50 eV, only electrons in a region less than 10 nm under the surface of the specimen are detected. A high topological contrast can be achieved by secondary electrons as the intensity of the SE varies strongly depending on the geometry of the specimen. For example, in a small particle and at a edge, more secondary electrons can leave the sample and be detected than on a flat structure, whereas, for example by tilting, certain regions of the sample can be shadowed by features which stand out. SEM pictures taken in this work are mainly recorded by secondary electrons.

Another type of signal are backscattered electrons (BSE). These are primary electrons which are scattered elastically before leaving the sample. Depending on the losses due to the scattering processes within the specimen, their energy can reach the energy of the primary electrons. As the intensity of the BSE are strongly dependent on the atomic number of the specimen, an image can be created which mirrors the distribution of different elements in the sample.

Beside SE and BSE, characteristic X-radiation can be used to characterize the sample. Similar to BSE, X-radiation originates from a larger volume than SE and is used to identify and map elements on the surface of a sample. Hereby, the incident electron beam ejects an electron from the sample atoms. Subsequently, characteristic X-ray radiation is emitted when an electron from an outer shell fills the vacancy of the ejected electron in one of the inner shells.

5.4 Atomic Force Microscope (AFM)

The atomic force microscope (AFM) belongs to the group of scanning probe microscopes. In contrast to the scanning tunneling microscope which was developed before the AFM, insulating samples can be measured as well. Instead of an electric tunneling current, the force between the tip and the sample is measured in the AFM (5.9). The sharp tip with a radius of ca. 10 nm on a cantilever is mounted to a Piezoelectric actuator which moves the sample under the tip and thus scans the sample. During the scan of a sample, a laser beam is directed on the cantilever and is reflected onto a position sensitive photodetector. The detector converts the change of position of the laser beam on the detector in an electrical signal.

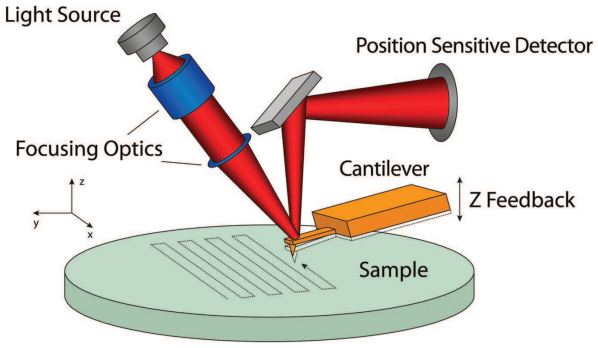

Figure 5.9.: The working principle of the AFM. The graphic is taken from [168].

The bending of the cantilever is due to the interaction of the tip and the sample and can be described in good approximation by the Lennart-Jones potential (5.10). The interaction consists of a long-ranged attractive force (up to 100 nm) like the van der Waals forces and a short-ranged repulsive force (few Ångströms). The overlap of the atomic electron shells of tip and sample causes a repulsive force which is caused by the Pauli principle.

Depending on the imaging mode of the AFM, different interatomic forces are employed to gain the topography of the sample. In the contact mode, the tip and the sample are in direct contact to each other. Hence, the repulsive forces in Figure 5.10 are detected. For smooth samples, the height of the cantilever is kept constant (constant height mode) and the repulsive force is measured directly, whereas for rough samples the force on the cantilever which is the bending of the cantilever is kept constant by adjusting the height of the sample (constant force mode).
In the non-contact mode, the tip and the sample are not in direct contact and, hence, the attractive forces are detected. Hereby, the cantilever oscillates in its resonance frequency and the deviation of its resonance frequency or the oscillation amplitude is detected. A disadvantage of this mode is its lower lateral resolution compared to the other modes.
Both modes are combined in the tapping mode. In this mode, the cantilever oscillates in its resonance frequency close to the sample touching it at the maximum deflection of the cantilever. The interactions are mainly attractive and, therefore, weaker than in the contact modus. In this way, very soft samples can be investigated.

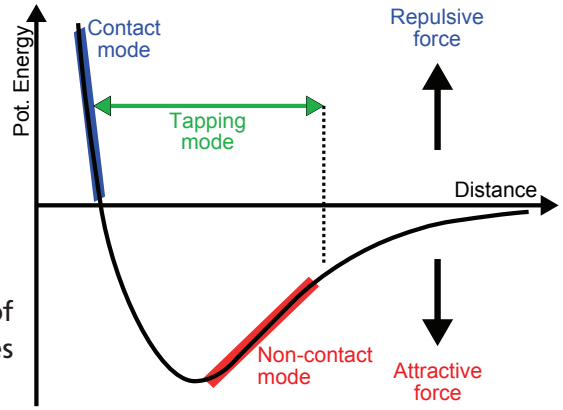

Figure 5.10: The different imaging modi of the AFM indicatet in the Lennard-Jones potential.

5.5 X-ray Diffraction (XRD)

X-ray diffraction (XRD) is a non-destructive analysis technique. It provides information about the crystallographic structure and the chemical composition of powders and thin films. The technique is based on elastically scattered X-rays (Figure 5.11) according to Bragg´s law [169]:

$$n \cdot \lambda = 2d \cdot \sin\theta \ , \tag{5.12}$$

where n is an integer, λ the wavelength of the incident X-rays, d the spacing between the planes in the atomic lattice and θ the angle between the incident X-ray and the planes.
Because the spacing between the planes is in the range of the incident X-rays which are typically in the range from 0.03 to 0.5 nm, the incident X-rays are diffracted and not refracted or scattered. The physical reason for this is that the electrons of the sample diffract the electromagnetic X-rays according to the Huygens-Fresnel principle: the electrons oscillate in the electromagnetic field of the X-ray and emitt a secondary wave with the same frequency and wavelength as the primary wave.
Depending on the angle between the incident X-rays and the planes the path difference of the X-rays which are diffracted in the atomic planes is different. Only with a path differences of nλ the diffracted X-rays are interfering constructively, otherwise destructively, which is dominant. Therefore, the X-rays have to be parallel and monochromated. In this way, the metric of the atomic lattice determines the angle of the reflections in the XRD-spectra. Therefore, the reflections in the spectra can be used to determine the crystal phase of the investigated material, for example. This was done in this work for the crystal phase of the TiO_2 substrates.

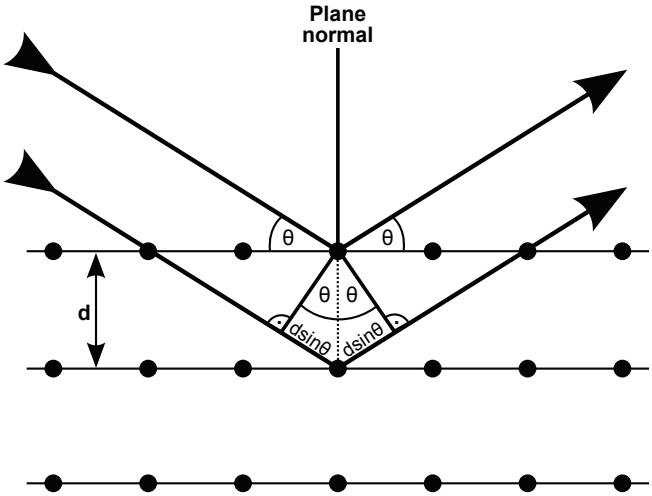

Figure 5.11.: X-ray diffraction on an atomic lattice according to Bragg´s law.

Part III.
Results and discussion

6 The goal of this work

The goal of this work was to investigate the solid-state dye-sensitized solar cell. The work was intended to contribute to the basic understanding of the function of this type of solar cell. This included a better understanding of the materials used in the solid-state DSSC and their processing. Moreover, different factors influencing the efficiency of the solid-state DSSC were investigated. The issues were coordinated with the cooporation partners BASF and Bosch.

The main part of this work was to investigate the organic hole conductor Spiro-MeOTAD by photoemission spectroscopy. Spiro-MeOTAD is used as a substitution for the liquid iodide/triiodide redox couple in solid-state dye-sensitized solar cells. For the in-situ preparation and measurement in the SoLIAS (see Section 4.1), drop-casting was used to deposit Spiro-MeOTAD wet chemically. Drop-casting is a method close to spin-coating which is normally used in industry. Because interface experiments can hardly be performed with drop-casting, PVD as a method which is suitable for interface experiments was applied. In order to investigate the equality of both methods, drop-casting and PVD were compared. Furthermore, the poor conductivity of Spiro-MeOTAD makes it necessary to dope the hole conductor. Therefore, the doping mechanisms of the dopants Li-TFSI and WO_3 were investigated. Li-TFSI is a dopant widely used for Spiro-MeOTAD in solid-state DSSCs and WO_3 was chosen as a model system. Furhermore, the interfaces of Spiro-MeOTAD to the substrate TiO_2, different dyes and gold which is used as the back-contact in solid-state DSSCs were of special interest as the energetic lineup determines the efficiciencies of the solid-state DSSCs.

Another goal of this work was to determine the behavior and influence of sodium which is part of the TiO_2 precursor on the solid-state DSSC. As TiO_2 films prepared in different laboratories often lead to varying efficiencies of the cells using the same TiO_2 precursor material and the same recipe, systematic ex-situ heat treatments using a hot plate and a heat gun were performed on different ex-situ prepared nc-TiO_2 films. Nanocrystalline and blocking layer TiO_2 films which were obtained from the project partners BASF and Bosch and used as the substrate for most of the experiments in this work were characterized by different methods.

Moreover, the influence of different anchor groups and additives on the energetic properties and allignments of ruthenium-free perylene dyes to the TiO_2 electrode and the hole conductor Spiro-MeOTAD were investigated by SXPS. Those dyes are a good alternative to the standard dyes as they usually do not contain expensive ruthenium. Also their production is most often easier and more cost-effective and their absorption and electrochemical properties are easier tunable than those of the standard dyes.

7 Titanium dioxide (TiO_2)

In this chapter, the titanium dioxide substrates, dense TiO_2 blocking layers (BL-TiO_2) and nanocrystalline mesoporous TiO_2 films (nc-TiO_2), which were used in this work are characterized. The substrates were supplied by the project partners BASF and Bosch as well as from EPFL. Hereby, thin films of the TiO_2 blocking layer were deposited by spray pyrolysis at 450 °C onto FTO conducting glass samples and nanocrystalline TiO_2 films were prepared on the compact TiO_2 blocking layer by screen printing, followed by sintering at nominally 450 °C.
In the first part of the chapter, the topography, especially the roughness and denseness, of the TiO_2 films are probed by AFM, the morphology and thickness of the films are determined by REM pictures and the anatase crystal phase of the TiO_2 is verified by XRD and Raman spectroscopy. In addition, the electronic properties of the films are investigated by SXPS. In the second part, changes of the chemical surface composition of nanocrystalline TiO_2 films induced by systematic temperature variations are studied by SXPS and XPS. The influence of small amounts of Na at the surface on the efficiency of solid-state dye-sensitized solar cells with two different dyes is shown.

7.1 Investigation of TiO_2 substrates

In order to inhibit an ohmic contact between Spiro-MeOTAD and the FTO electrode leading to charge carrier recombination at the interface [37], a TiO_2 blocking layer (BL-TiO_2) is used between the FTO film and the naocrystalline, mesoporous TiO_2 film (nc-TiO_2) [31, 38]. Therefore, the blocking layers have to be dense without any pinholes but thin enough to ensure electron conduction to the electrode. On the other hand nc-TiO_2 films need a high surface area to enhance dye adsorption and thus the efficiency of the solid-state DSSC [31]. Additionally, the crystal phase and the thickness of the TiO_2 films play an important role and, hence, have to be controlled precisely. With an anatase instead of a rutile photoelectrode a larger maximum photovoltage can be achieved because the flat band potential of anatase is reported to be 0.2 eV more negative than that of rutile [56, 67]. Furthermore, the anatase crystal phase of TiO_2 has a higher diffusion coefficient of conduction band electrons than rutile and is thus favored [66]. The thickness of the TiO_2 films requires a compromise: the films have to be thick enough for a higher overall surface area (nc-TiO_2) and less pinholes (BL-TiO_2) but at the same time thin enough to avoid long charge carrier diffusion and, thus, higher charge carrier recombination [28, 31, 40].

7.1.1 AFM

AFM measurements and the height profile of an FTO film, a TiO_2 dense blocking layer and a nanocrystalline, mesoporous TiO_2 are shown in Figure 7.1. The topography was surveyed over an area of 25 μm^2 and the height profile over a length of 5 μ. The measurements show that the TiO_2 particles of the blocking layer mimic the structure of the FTO underlayer, which is also observed in a similar roughness of the two layers. Therefore, it can be assumed that the TiO_2 is covering the FTO evenly without pinholes. As the blocking layer and also the nc-TiO_2 show a similar but a little larger grain structur than the FTO, the possible existance of pinholes in this layer cannot be completely neglected, as the distinction between FTO and TiO_2 is difficult.

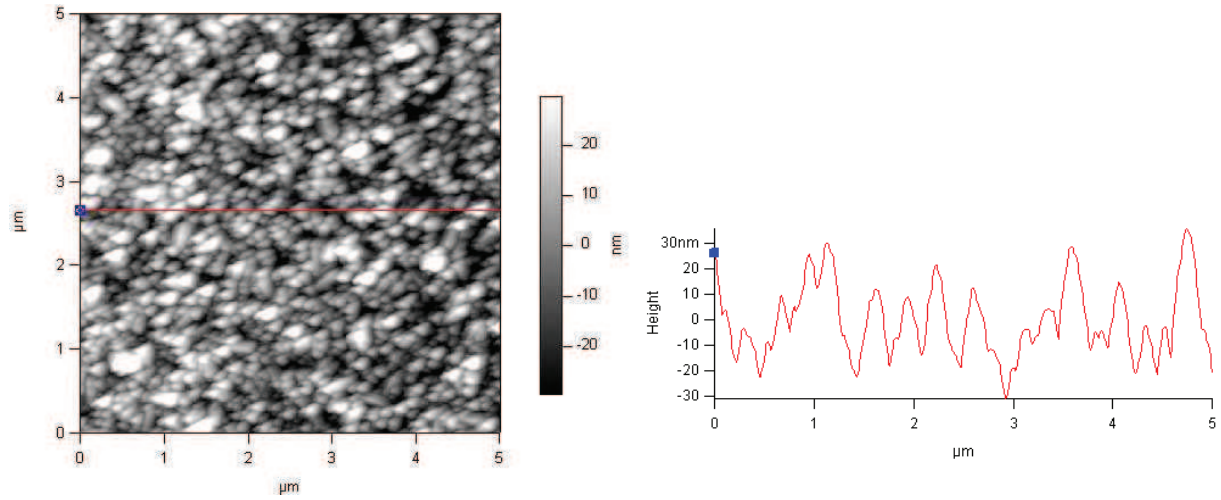

(a) FTO underlayer

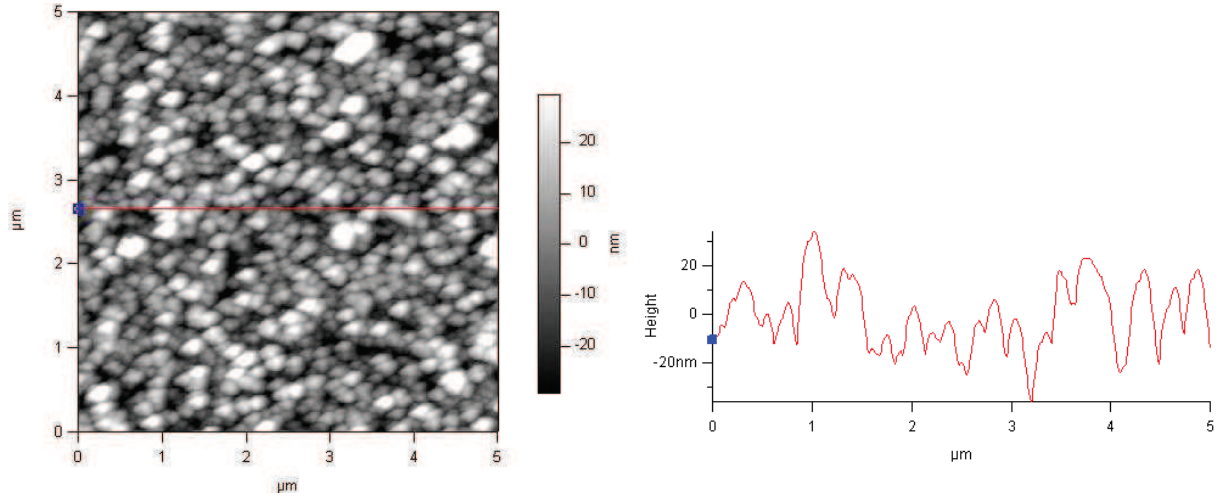

(b) TiO_2 blocking layer

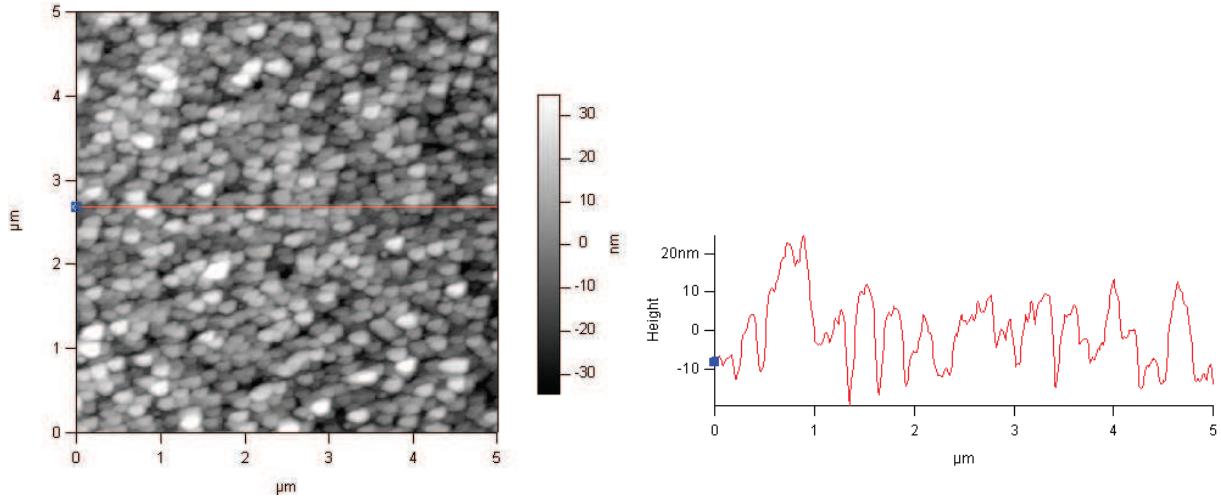

(c) nc-TiO_2 layer

Figure 7.1.: AFM-picture of FTO underlayer (a), TiO_2 blocking layer (b) and nc-TiO_2 layer (c). The red line indicates the course of the height profile over the sample.

7.1.2 REM

REM pictures were taken on a TiO_2 blocking layer and a blocking layer / nc-TiO_2 layer sequence, both on FTO. The film thicknesses of the samples were as follows and shown in Figure 7.2: a) TiO_2 blocking layer (100 nm) deposited on FTO (590 nm) and b) FTO layer (520 nm) / TiO_2 blocking layer (200 nm) / nc-TiO_2 layer (1.65 μm) sequence. Inhomogeneous film thicknesses within the samples and distortions of the picture due to fractured surfaces which were not parallel to the sample holder lead to complications on the precise determination of the film thicknesses.

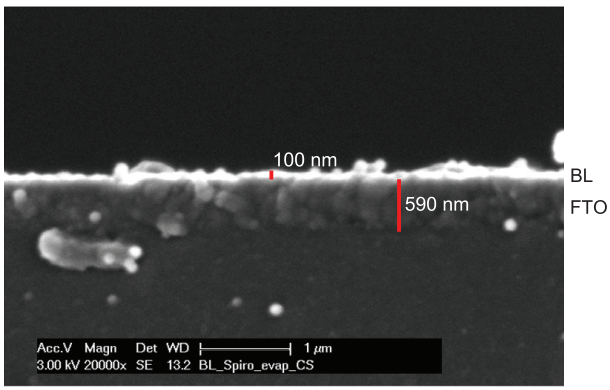

(a) TiO_2 blocking layer (BL-TiO_2)

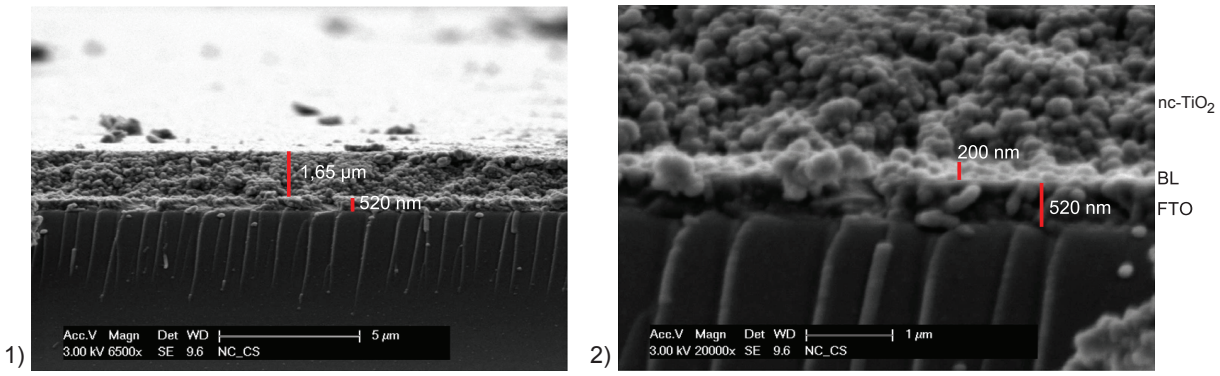

(b) nanocrystalline TiO_2 (nc-TiO_2): overview (1) and enlarged image detail (2)

Figure 7.2.: REM-pictures of: a) TiO_2 blocking layer (100 nm) deposited on FTO (590 nm) and b) FTO layer (520 nm) / TiO_2 blocking layer (200 nm) / nc-TiO_2 layer (1.65 μm) sequence.

No pinholes are visible in the REM pictures within the cross section of the samples, which confirms the conclusions of the AFM measurements. The thicknesses of the blocking layers (100 nm for the blocking layer substrate and 200 nm for the blocking layer / nc-TiO_2 layer sequence) match well with thicknesses proposed in literature [33, 43]. Karthikeyan et al. state that a continuous, compact and pinhole-free TiO_2 blocking layer, which is necessary for inhibiting charge recombination at the FTO/Spiro-MeOTAD interface, is provided by a blocking layer thickness in the range of 120-200 nm. The thickness found for the nc-TiO_2 layer (1.65 μm) is a little smaller than the value commonly given in literature (2 μm [28, 43]). As discussed in chapter 2.3, there are two factors that limit the thickness of the nc-TiO_2 layer of the solid-state DSSCs to a maximum thickness of 2 μm: electron-hole recombination and the incomplete pore filling of the mesoporous nc-TiO_2 films with Spiro-MeOTAD [41].

7.1.3 XRD and Raman spectroscopy

X-ray diffraction and Raman spectroscopy were performed on a TiO_2 blocking layer and a nc-TiO_2 layer substrates to validate the anatase crystal phase. As the TiO_2 substrate acts as the electron conducting material in the DSSC and the anatase crystal phase of TiO_2 is higher conductive than the rutile phase, the phase purity is of high importance.

In the X-ray diffraction pattern of the nc-TiO_2 sample, reflections of the anatase crystal phase and the SnO_2 substrate can be identified (Figure 7.3), whereas in the pattern of the BL-TiO_2 sample no TiO_2 refletions but only SnO_2 substrate reflections are found. Hence, the anatase crystal phase of the nc-TiO_2 can be validated, whereas the thickness of the TiO_2 blocking layer is too thin to be probed by XRD. A detailed table of all reference reflections and their indices, 2θ values and relative intensities is given in the appendix (see Section 12).
According to Grätzel et al., who investigated screen-printed nc-TiO_2 with HRTEM, the (101) surface orientation of the nanoparticles is mostly exposed followed by the (100) and the (001) surface orientations [6]. In the XRD pattern of the investigated nc-TiO_2, only the (101) reflection is detected. As the reflection at ca. 38° is a superposition of the (004) reflex of anatase and the (200) reflex of SnO_2, the (101) surface orientation of TiO_2 is also the most prominent in the 2θ range from 24 to 90°.

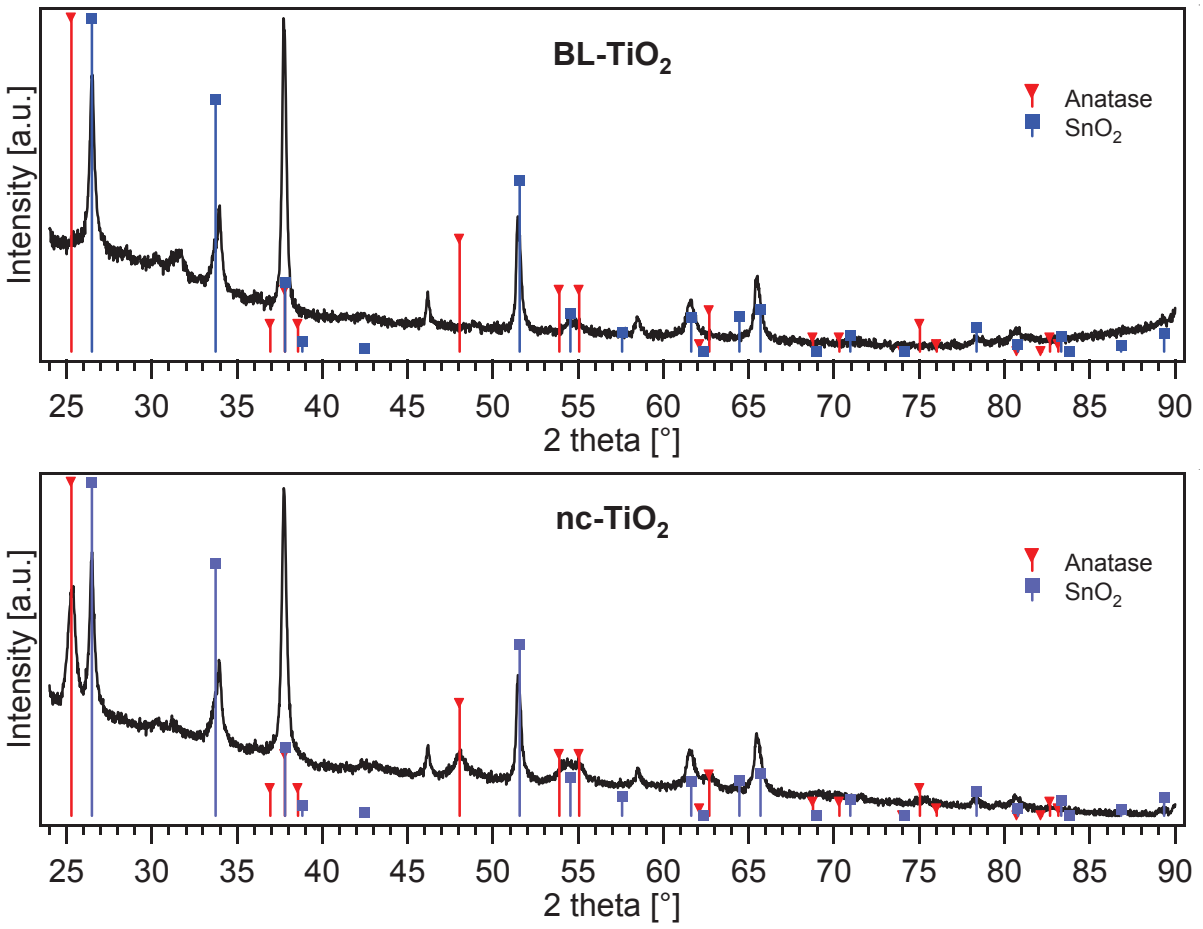

Figure 7.3.: XRD spectra of BL-TiO_2 (top) and nc-TiO_2 (bottom) samples: The layer thickness of the BL-TiO_2 is to thin to be detected by XRD. The nc-TiO_2 measurement shows both SnO_2 substrate reflections and anatase.

Raman spectra on both nc-TiO_2 and TiO_2 blocking layer (Figure 7.4) show only Raman modes which belong to the anatase phase. Literature values of the Raman active modes of anatase are 144, 197, 399, 513, 519 and 639 cm^{-1} [62, 170]. The experimentally found values and the literature values are compared in Table 7.1. The literature spectra of the anatase phase and the spectra of the TiO_2 substrates used in this work match excellently.

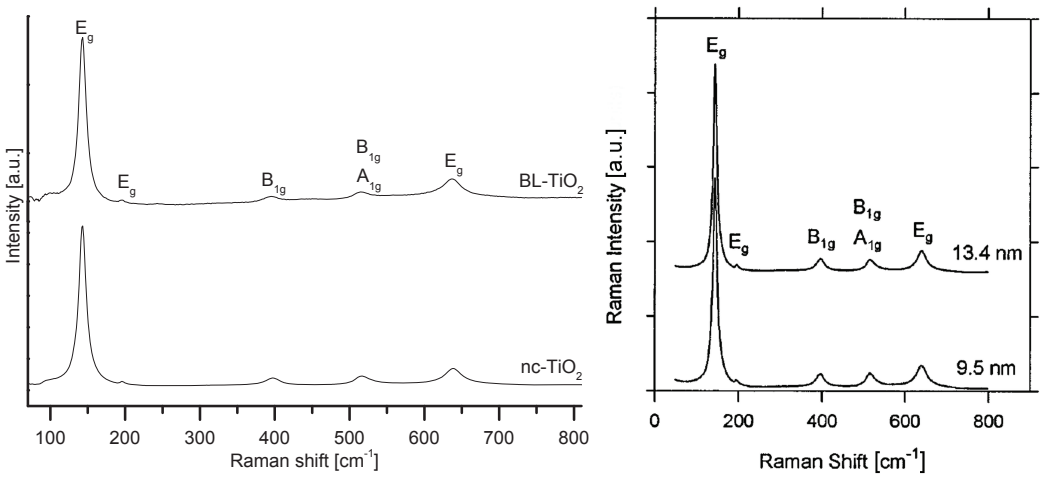

Figure 7.4.: Raman spectra of nc-TiO_2 and BL-TiO_2 samples (left) and literature spectra (right) [62]. Raman active anatase modes are indicated in the spectra.

Table 7.1.: Comparisson of Raman shifts and literature data [171] of nc-TiO_2 and BL-TiO_2

	$\mathbf{E}_g$	$\mathbf{E}_g$	$\mathbf{B}_{1g}$	$\mathbf{A}_{1g}$	$\mathbf{B}_{1g}$	$\mathbf{E}_g$
Raman shift$_{exp}$	144 cm^{-1}	197 cm^{-1}	399 cm^{-1}	513 cm^{-1}	519 cm^{-1}	639 cm^{-1}
Raman shift$_{lit}$	144 cm^{-1}	197 cm^{-1}	399 cm^{-1}	513 cm^{-1}	519 cm^{-1}	639 cm^{-1}

7.1.4 SXPS

All measurements presented in this work were performed on ex-situ prepared substrates. SXPS measurements on in-situ prepared TiO_2 by CVD compared to ex-situ sintered films proved that the chemical and electronic structure can be well compared even when measuring with the highest surface sensitivity [81]. It was found that the TiO_2 gap-state distribution is varied, specifically dependent on the adsorbed electrolyte solvent. Furthermore, the acetonitrile solvent separates the N3 dye molecules from each other and induces a beneficial alignment of the molecular dye charge-transfer vector normal to the TiO_2 surface [82].
Survey spectra of the TiO_2 blocking layers and nc-TiO_2 films (Figure 7.5) show identical binding energy positions of all core level emission lines. The carbon contamination originates from the precursor used to prepare the TiO_2 substrates. Because both samples were stored in ambient air and should have similar amounts of organic adsorbants on it, the higher relative C1s emission of the BL-TiO_2 sample compared to the nc-TiO_2 sample indicates more residues of the TiO_2 precursor. The most intense core level emissions are labeled in Figure 7.5 and listed in Table 7.2.

Table 7.2.: Comparison of measured binding energies and literature data [11] of TiO_2

	O1s	**Ti2p**$_{3/2}$	**C1s**	**Ti3p**	**O2s**
$\mathbf{E}_{Bin,exp}$	530.8 eV	459.3 eV	285.3 eV	37.9 eV	22.8 eV
$\mathbf{E}_{Bin,lit}$	530.8 eV	459.3 eV			

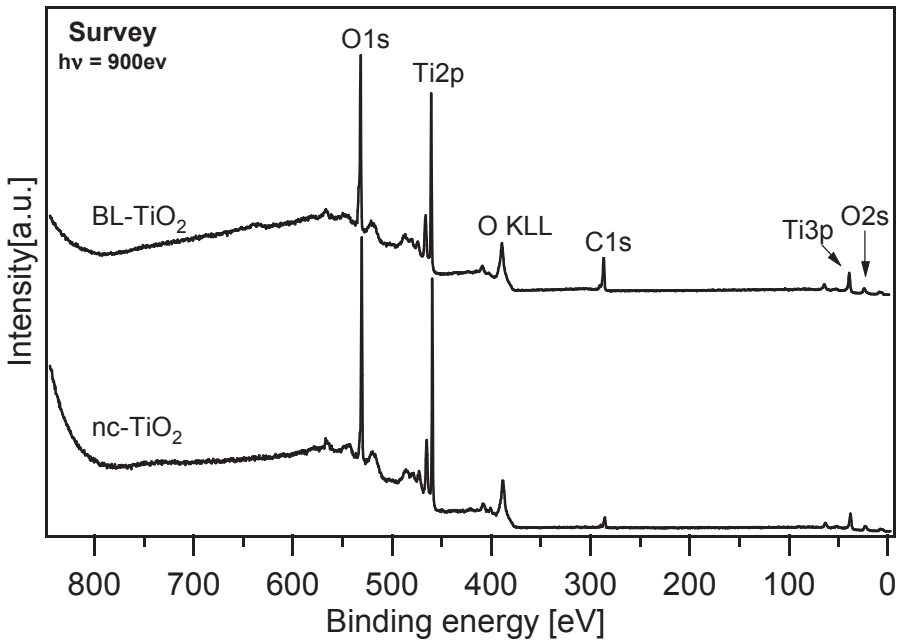

Figure 7.5.: Survey spectra of a dense TiO_2 blocking layer (BL-TiO_2) and a nanocrystalline TiO_2 (nc-TiO_2) sample measured at 900 eV photon energy. The most intense core level emissions are labeled.

O1s and Ti2p

The O1s and Ti2p core level spectra both measured at 600 eV photon energy are shown in Figure 7.6. Ti2p core level measurements of both films show no shift with respect to each other and the same amount of reduced Ti^{3+} states which appear as a shoulder of the duplett on the lower binding energy side. The species in the O1s core level measurements ranging from approximately 531.3 to 535.1 eV can be assigned to residual precursor which was not completely burnt off in the sintering process. Another possibility is adsorbed water. Jaegermann and Mayer showed that a second species of GaAs can be found ca. 2 eV at higher binding energies in the gallium and arsenide spectra after water adsorption [146].

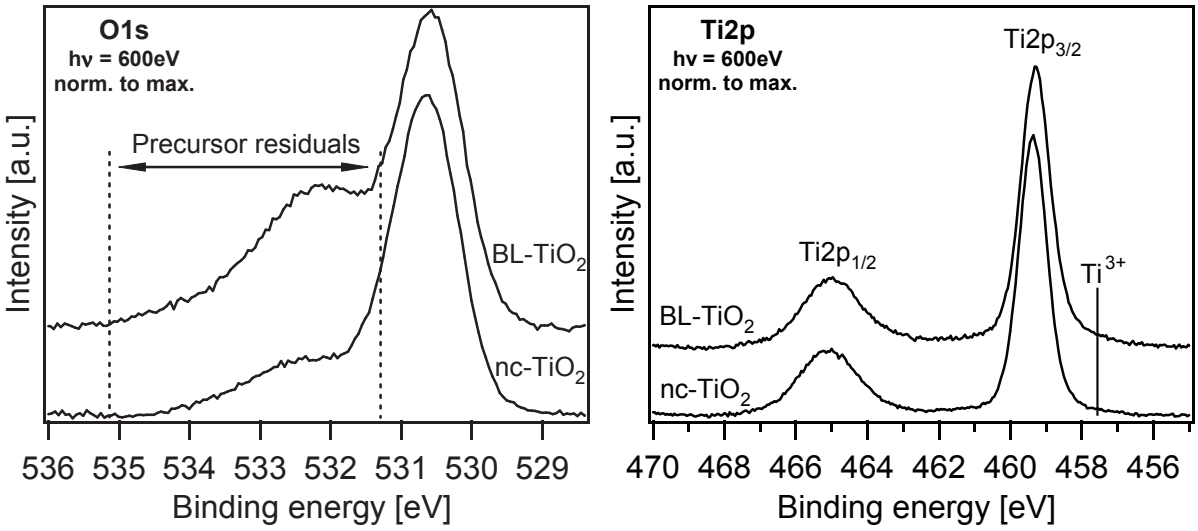

Figure 7.6.: O1s and Ti2p core level spectra of dense TiO_2 blocking layer (BL-TiO_2) and nanocrystalline TiO_2 (nc-TiO_2) measured at 600 eV photon energy. In the O1s detail spectra, emissions (from 531.2 to 535.2 eV) originating from the residual precursor material are visible. In the Ti2p spectra a shoulder which is attributed to reduced Ti^{3+} is found on the lower binding energy side of the main emissions.

Valence band

The valence band structure, measured at 90 eV photon energy, coincides well with results on anatase presented in literature [72], which reconfirms the conclusions made after the XRD and Raman measurements concerning the anatase crystal phase. The most prominent structure is found in the binding energy range from 10 to 3.6 eV and can be mainly attributed to the O2p emission (Figure 7.7) as shown in Section 3.2.

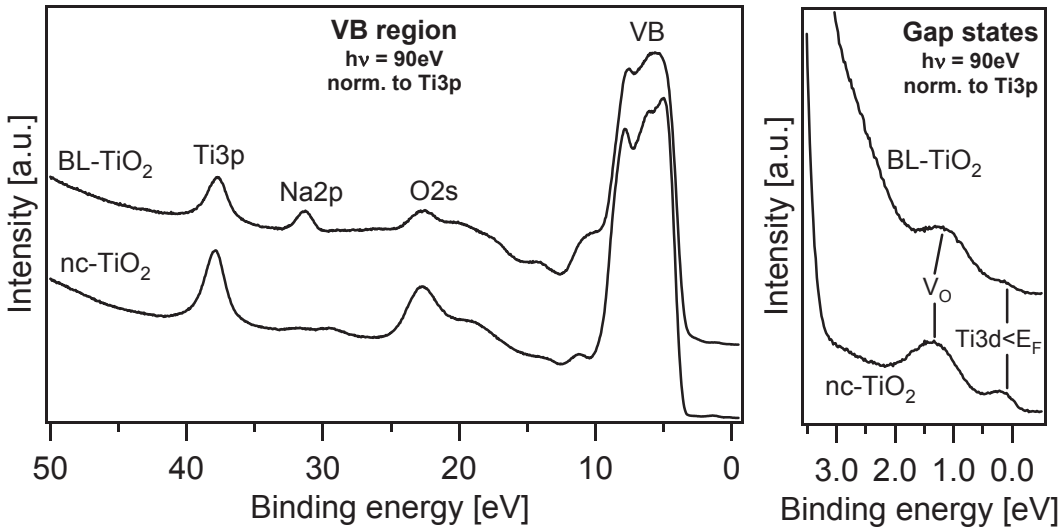

Figure 7.7.: Valence band and gap-states spectra of dense TiO_2 blocking layer (BL-TiO_2) and nanocrystalline TiO_2 (nc-TiO_2) measured at 90 eV photon energy. Sodium contamination (Na2p) in the valence band region originates from the precursor (see 7.2). Oxygen vacancies (V_0) and states just below the Fermi level (Ti3d<E_F) are indicated on the right.

Shallow core levels of TiO_2 are located at 22.8 eV (O2s) and 37.9 eV (Ti3p). The gap-state region shows two kinds of gap-states, one just below the Fermi level (Ti3d<E_F) and the second at 1.1 eV for the BL-TiO_2 and at 1.3 eV for the nc-TiO_2 gap-states. In literature the ones (labeled "V_O") at around 1 eV binding energy are attributed to oxygen vacancies [64]. In the work of Schwanitz on TiO_2, which was deposited in the same way as in this work, and TiO_2 prepared by CVD, the author determined the energetic position of the V_O gap-state to be 1.3 eV and 1.2 eV [11]. This values are in excellent agreement with the ones obtained in this work. The sodium impurity with its Na2p emission located at ca. 31.4 eV originates from the precursor material used to prepare the TiO_2 substrates. The behavior of sodium upon heat treatment and its influence on the efficiency of the solar cell was investigated and is described later on in this work (see Section 7.2).

Determination of the valence band maximum: The valence band spectra shown in Figure 7.8 taken at different photon energies (90, 360, 465, 600, 900 and 950 eV) show the difficulty of the determination of the valence band maximum of TiO_2 due to the interference of TiO_2 gap-states in that region and the underestimation of minor electron states contribution building up the valence band. All spectra were recorded on the same sample at the U49-PGM-2 beamline at BESSY.

The gap-states resulting from oxygen vacancies at the surface are well detectable at photon energies that match resonance excitations of Ti3d states. The Ti3p-3d resonance is strongly excited in the photon energy range from 40 to 90 eV and the Ti2p-3d resonance in the range from 450 to 480 eV [11]. In order to avoid a possible error by the overlap of the TiO_2 gap-states with electron states forming the valence band (mostly 02p), excitation energies are chosen outside these resonance ranges. The valence band maximum recorded at 90 eV photon energy could not be clearly determined as the overlapping of the gap-states is too high in the spectrum.

In addition, minor emissions of the valence band which are indicated with a second line in the spectra shown in Figure 7.8 become more prominent with increasing photon energies and thus are tendentially underestimated for small photon energies. The reason for this is probably either different cross sections of the Opσ and the Opπ bonds due to the polarization of the incident synchrotron light or O2p tail states due to non-interaction with Ti3d states. Alternatively, Ti3p states which also contribute to the valence band in a minor way (see Figure 3.4) could be the origin of those minor emissions as the cross section decreases slower than the cross section of O2p for increasing photon energies (Figure 7.8). In order to clarify this, measurements of single crystals, which were not available during this work, are necessary. The value of the valence band maximum (3.0 eV) given in this work is in good agreement with the literature value for rutile and anatase [72]. Furthermore, the fitting procedure is similar to the procedures proposed by Kampen and Kumarasinghe [172, 173].

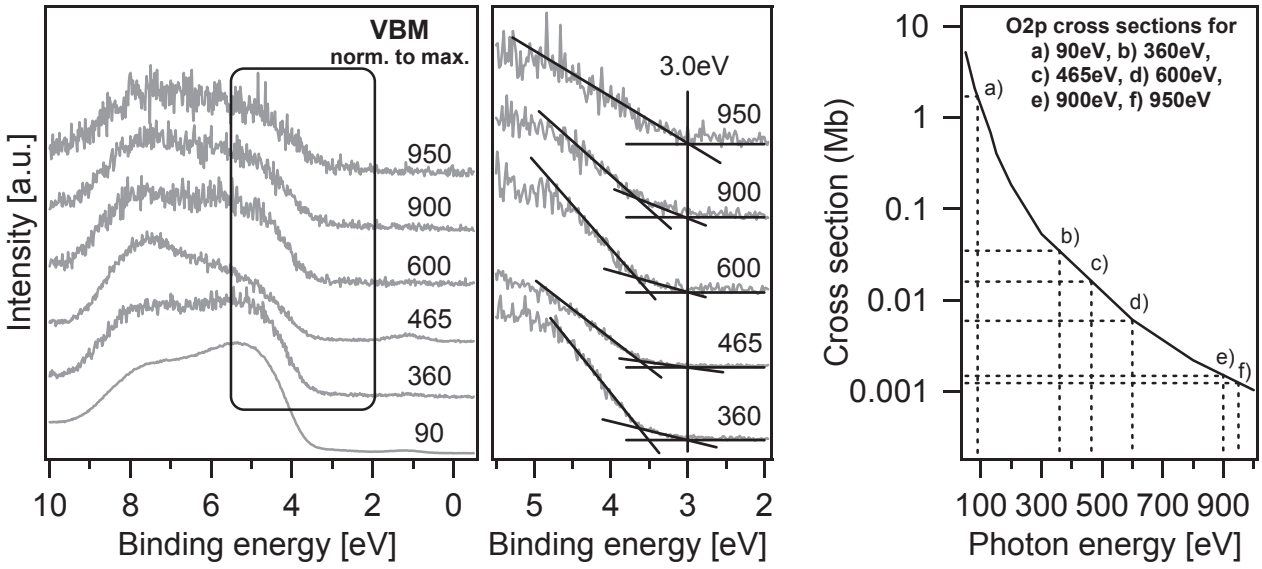

Figure 7.8.: The determination of the valence band maximum of a TiO_2 blocking layer measured at 90, 360, 465, 600, 900 and 950 eV photon energies: The position of the valence band maximum is determined by fitting the spectra with straight lines, which is shown enlarged in the middle. The edge and the tail of the valence band as well as the zero line are each indicated with a line. It can be seen from the figure on the right that with increasing photon energy the cross section of the mainly O2p dominated valence band decreases (data were obtained from [157]) and, thus, the tail of the VB becomes more visible. In addition, the intensity of the TiO_2 gap-states depend on the excitation energy. Resonant excitation energies (90 and 465 eV) increase the intensity of the gap-states drastically, which complicates the determination.

7.2 The behavior and influence of sodium in TiO_2

So far, large efforts have been invested in synthesizing novel dyes and hole conductors to improve the efficiency of solid-state dye-sensitized solar cells [174, 175]. However, despite the same TiO_2 precursor material and apparently the same preparation procedure, films prepared in different laboratories often lead to varying efficiencies.

TiO_2 nanocrystalline films which are used as the photoanode of DSSCs and solid-state DSSCs are usually exposed to temperatures in the range of 450-550 °C during sintering. After sintering, the samples are stained whith a dye. In this step, the films can be put into the dye solution directly after sintering, which means that they are still warm from the sintering process. The other alternative is to use samples stored at room temperature and heat them directly before dye staining [176, 177]. The effect of an ex-situ heat treatment on the chemical composition of nc-TiO_2 films was investigated using photoelectron and Raman spectroscopy to clarify whether these different treatments lead to variations in composition and maybe in solar cell efficiencies.

In this section, changes in the chemical surface composition induced by an ex-situ temperature treatment on ex-situ sintered nc-TiO_2 films for the application in solid-state DSSCs are investigated and discussed. For this, a hot plate to imitate the sintering process and a heat gun in similarity to heating before staining were used. Stepwise heated samples were analyzed at room temperature using synchrotron induced photoelectron spectroscopy at BESSY II in Berlin, X-ray photoelectron spectroscopy at the DAISY-SOL in Darmstadt and Raman spectroscopy.

7.2.1 Experimental

Ex-situ sintered nc-TiO_2 samples were prepared by BOSCH and École Polytechnique Fédérale de Lausanne (EPFL) using anatase TiO_2 powder from different commercial sources. Thin films of the TiO_2 blocking layer were deposited by spray pyrolysis at 450 °C onto FTO conducting glass samples. In a second step nanocrystalline TiO_2 films were prepared on the compact TiO_2 blocking layer by spreading the paste made from different batches of TiO_2 powders using screen printing, followed by sintering at nominally 450 °C. The same procedure was applied for nc-TiO_2 films deposited onto Si(111) wafer substrates which were covered with native oxide. The as-received samples were heated ex-situ in air by a hot plate or using a heat gun and transferred rapidly into the UHV chamber via the load lock.
In both heating experiments the temperature was varied stepwise in the range of 300 to 600 °C and kept constant for 30 min at each step. SXPS experiments were performed at the TGM7 and U49/PGM2 beamlines of the BESSY storage ring in Berlin using the experimental station SoLIAS. The XPS study was carried out in the Darmstadt Integrated System for Solar Research (DAISY-SOL) [178] by using an ESCALAB 250 spectrometer equipped with a monochromated Al Kα X-ray source (hν = 1486.6 eV). Binding energies were calibrated with sputter-cleaned Ag samples by setting the Ag3d binding energy to 386.27 eV. The overall energy resolution for the Al Kα excited photoelectron spectra was better than 400 meV and the base pressure of the system was below 10^{-9} mbar.

For the efficiency measurements, solid-state DSSCs were prepared and measured by Bosch. The measurements were carried out on DSSCs with TiO_2 electrodes without and with heat treatment for 15 min at 150 °C in an oven just before dye staining. The solid-state DSSCs were built up of commercial FTO on glass (Hartford TEC 15), a 50 nmTiO_2 blocking layer deposited by spray pyrolysis of diisopropoxytitanium bis(acetylacetonate), a 1.9 μm nanoporous TiO_2 film that was screen-printed and sintered for 30 min at 450 °C, two different dyes, the organic hole conductor Spiro-MeOTAD, and a Ag back contact. I-V curves were recorded in a solar simulator of AM 1.5 (1 sun) and a 0.1 gray filter (0.1 sun).

Heat treatment with a hot plate

In order to simulate the sintering process of the nc-TiO_2 films, a series of heat treatments using a hot plate were carried out on nc-TiO_2 films deposited on FTO substrates. SXPS survey spectra (Figure 7.9) were recorded at 900 eV at the U49-PGM-2 beamline showing the $Ti2p_{3/2}$ emission at 459.5 eV, the O1s emission at 530.8 eV and the C1s contamination with its main emission at 285.8 eV. Detail spectra of all core-level emissions are shown in Figure 7.10. All TiO_2 substrate emissions show no energetic shift during the heat treatment.

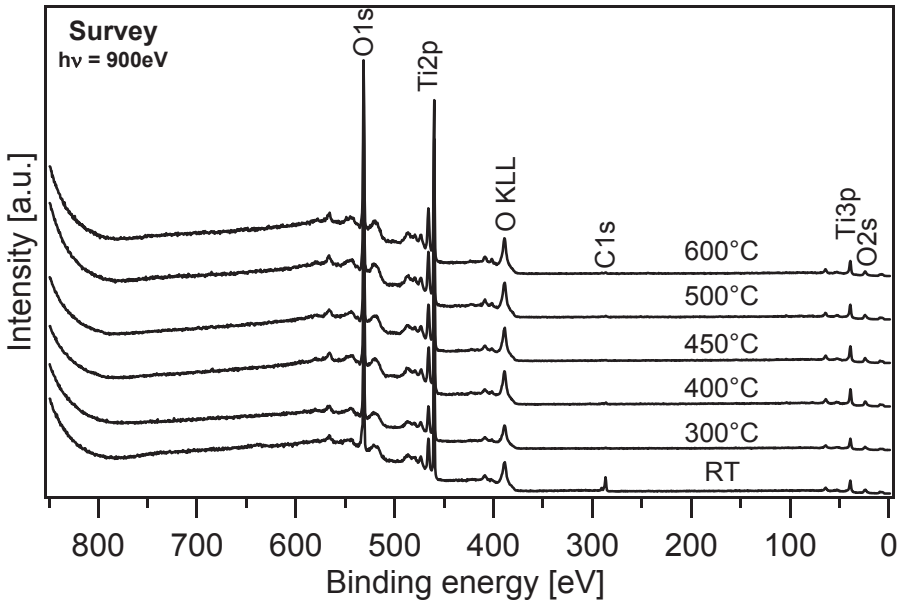

Figure 7.9.: Survey SXPS spectra of the nc-TiO_2 film in the course of hot plate heat treatment recorded at 900 eV: O1s, Ti2p, O KLL, Ti3p and O2s TiO_2 emission and C1s contamination.

The intensity of the C1s main emission at 285.8 eV, which is mainly attributed to adsorbates on the surface, decreases after heating, indicating desorption of the adsorbates, whereas the second emission at 289.7 eV which is attributed to the precursor decreases only a little. Conclusively, the heat treatment before dye staining has only a little effect on the decomposition and desorption of the precursor residuals. In relation with this observation, the curve shape of the O1s signal changes after heat treatment, which also indicates the desorption of adsorbates and to some extend the decomposition and desorption of precursor residuals.

In contrast to that, the shape of the Ti2p emissions does not change, which strengthens the assumption that the TiO_2 stays unchanged but the precursor and adsorbants desorb. As the heat treatment was performed in ambient air, the measurments of the secondary edges did not provide reliable results and are therefore not shown.

SXPS measurements of the valence band region, including the O2p dominated valence band between 3 and 9.9 eV, the O2s emission located at 22.8 eV binding energy, and the Ti3p core level at 37.9 eV were taken with 90 eV photon energy. The spectra recorded during the heat treatment are displayed in Figure 7.11. The measurement was started with a nonheated sample after which the temperature was increased stepwise to 600 °C. The spectra of the nontreated sample coincide with spectra shown in Figure 7.7 in Subsection 7.1.4 taken on ex-situ prepared samples. After normalization of the spectra to the intensity of the Ti3p substrate emission, a small emission at about 31.6 eV becomes visible in the spectrum of the nontreated sample (Figure 7.11). This emission is assigned to the Na2p orbital of Na^+ cations, as the

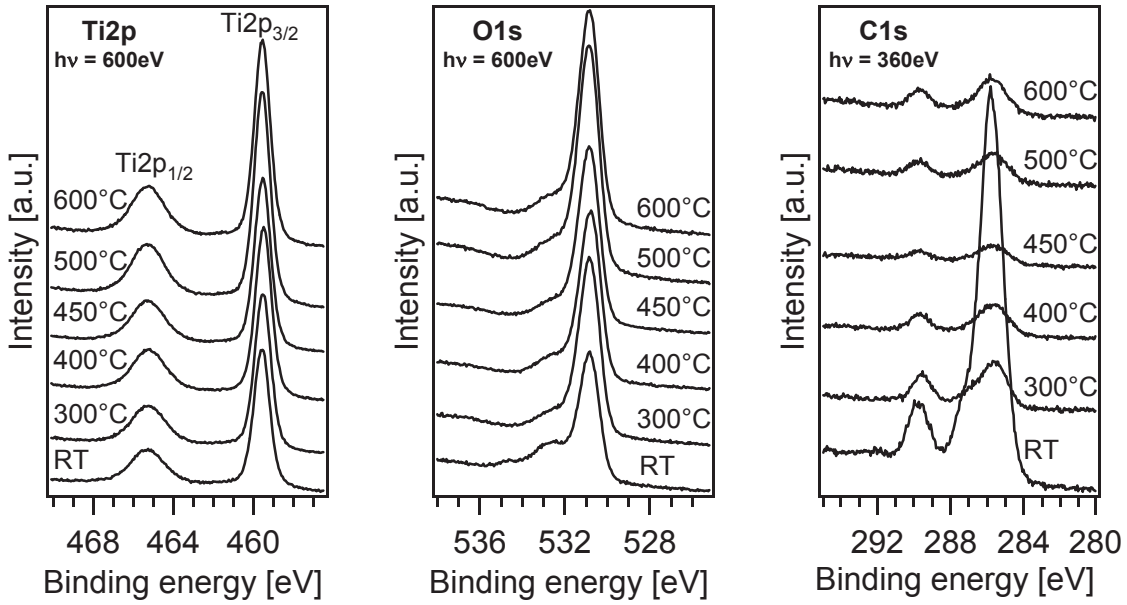

Figure 7.10.: Additional information for Subsection 7.2.2: Survey SXPS spectra of the nc-TiO_2 film in the course of hot plate heat treatment recorded at 900 eV: O1s, Ti2p, O KLL, Ti3p and O2s TiO_2 emission and C1s contamination.

binding energy position matches with Na^+ ions on WSe_2 [179], whereas the literature value of metallic Na is 30.6 eV [179, 180]. An increase of this emission is observed in the spectrum measured after heating at 500 °C. The Na2p to Ti3p intensity ratio is displayed in Figure 7.12 as a function of the heating temperature.

The photoemission intensity of an overlayer and the substrate for a homogeneous overlayer on a substrate is given by

$$I_0 = I_0^\infty \left[1 - \exp\left(\frac{-d}{\lambda_a^0 \cdot cos\Theta} \right) \right] \tag{7.1}$$

$$I_S = I_S^\infty \cdot \exp\left(\frac{-d}{\lambda_a^S \cdot cos\Theta} \right) \tag{7.2}$$

where I_0^∞ and I_S^∞ are intensities (i.e. peak areas) for the overlayer of infinite thickness and the clean substrate, d is the thickness of the overlayer, λ_a^0 and λ_a^S are the mean free path for the photoelectrons, which are generated in the overlayer and the substrate, traversing the overlayer, and Θ is the angle between the analyzer and the sample surface normal. The following approximation was made for Na2p and Ti3p

$$\lambda_a^0 = \lambda_a^S = \lambda \tag{7.3}$$

$$d = \ln\left(\frac{I_0 I_S^\infty}{I_S I_0^\infty} + 1 \right) \cdot \lambda \cos\Theta = \ln\left(\frac{I_0 I_S^\infty / \sigma_0 \sigma_S}{I_S I_0^\infty / \sigma_0 \sigma_S} + 1 \right) \cdot \lambda \cos\Theta = \ln\left(\frac{I_0 / \sigma_0}{I_S / \sigma_S} + 1 \right) \cdot \lambda \,. \tag{7.4}$$

The $cos\Theta = 1$ is given by the experimental setup and $(I_S^\infty/\sigma_S)/(I_0^\infty/\sigma_0) = 1$ by definition, where σ_0 and σ_S are cross sections for the respective overlayer and substrate orbitals. The approximate values of λ, σ_{Na2p} and σ_{Ti3p} at 90 eV photon energy are 5 Å, 5.5 Mb, and 1.25 Mb, respectively [157].

Hence, calculated from Equation 7.4 with a Na2p to Ti3p cross section ratio of 4.4, the integrated emission can be converted to a formal Na layer thickness of 0.05 Å at room temperature and to 0.20 Å at 600 °C. The results are plotted in Figure 7.11. An activation temperature of the Na diffusion in TiO_2 of approximately 420 °C can be determined from the point of intersection of the two fitting lines.

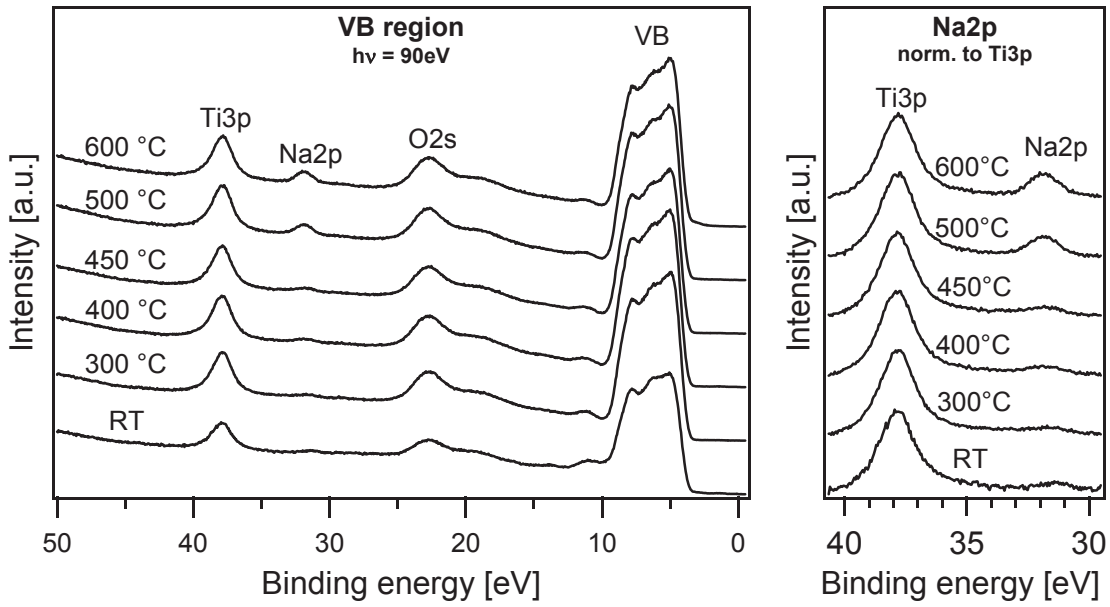

Figure 7.11.: SXPS spectra of the nc-TiO_2 film in the course of a hot plate heat treatment recorded at 90 eV: valence band region (left) and Na2p emission (right) normalized to the Ti3p intensity.

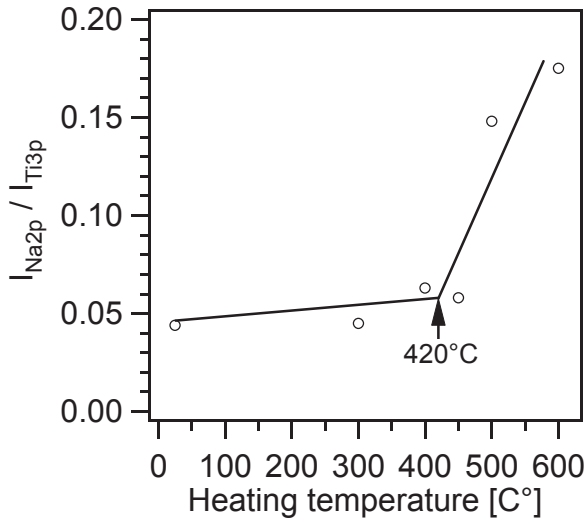

Figure 7.12: Plot of the Na2p to Ti3p intensity ratio: an activation temperature of the Na diffusion in TiO_2 of approximately 420 °C can be determined from the point of intersection of the two fitting lines.

Heat treatment with a heat gun

In a second experiment, similar prepared samples as before were heated stepwise using a heat gun to simulate the heat treatment before dye staining. As the SXPS spectra were recorded at the beamline TGM7, no core level emissions with binding energies higher than ca. 100 eV could be measured. Spectra of the valence band region recorded at 90 eV photon energy are shown in Figure 7.13. Like in the previous experiment, the Na2p emission is already observed at room temperature beside the Ti3p and O2s shallow core levels. After the heat treatment, the intensity of the Na2p core level increases. This can be clearly observed in the spectra which are normalized to the intensity of the Ti3p substrate emission.

The formal Na layer thickness calculated using Equation 7.4 increases from 0.12 at RT to 0.77 Å at 600 °C. At 450 °C, additional changes of the curve shape are observed in both the O2s core level and the valence band.

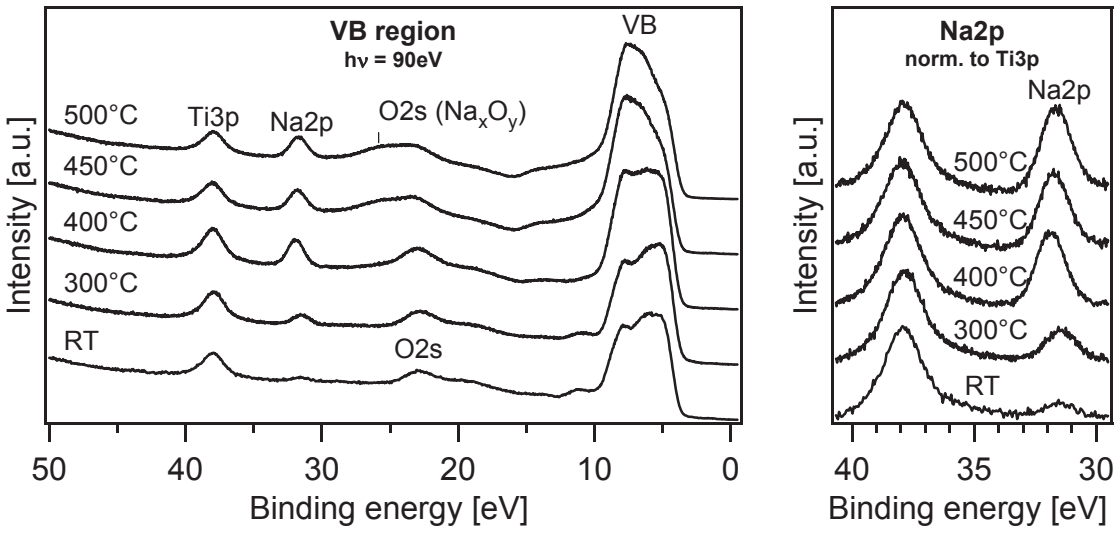

Figure 7.13.: SXPS spectra of the nc-TiO_2 film in the course of heat gun heat treatment recorded at 90 eV: valence band region (left) and Na2p emission normalized to the Ti3p intensity (right).

In order to exclude a phase transition of the TiO_2 from anatase to rutile as a reason for the changes in the valence band spectra Raman measurements were performed to analyze the crystal phase (Figure 7.14). No differences between the spectra of the untreated and the 500 °C heated sample can be observed. Comparing the spectra to a literature spectrum of the anatase phase [62], the anatase crystal phase can be verified. In literature structural changes from anatase to rutile can be found in nanocrystalline TiO_2 beginning at T=650 °C [171], in single crystals anatase TiO_2 at T=900 °C [181] and in polycrystalline anatase TiO_2 powders at T=750 °C [63, 182].

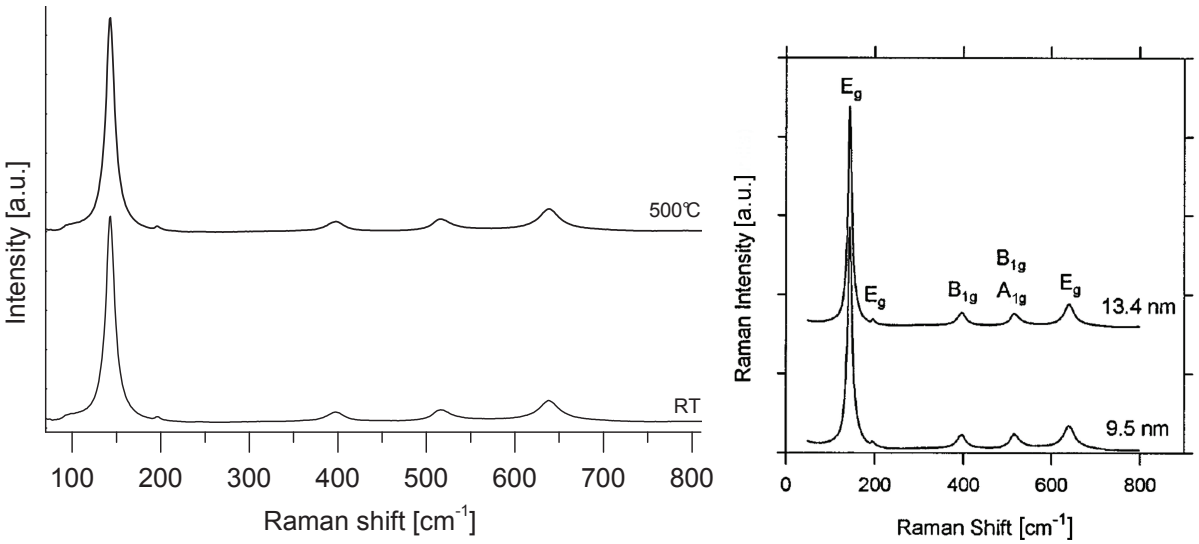

Figure 7.14.: Raman spectra of an untreated nc-TiO_2 layer and a sample heated at 500 °C (left) and literature spectra (right) [62] for comparison.

In parallel to the valence band change beginning at 450 °C, a higher binding energy component arises in the O2s core level, indicating the formation of an oxide. A similar valence band structure was also

reported by Wu et al. in their study on Na deposition on V_2O_5 films and identified as Na_xO_y [183, 184]. Therefore, the changes in the O2*s* core level and the valence band at high temperature are ascribed to the formation of Na_xO_y. As the formation of the sodium oxide is not observed by heating with the hot plate, it is assumed that additional activation of oxygen is necessary to induce the reaction with the Na^+ ion. This activation may be induced by the hot kanthal wire heater spiral of the heat gun, which appears yellow-reddish during the treatment, indicating a temperature well above 1000 °C. During the treatment the sample is heated by a flow of hot air, which is heated by passing the heater spiral. Hereby, oxygen-containing species may, in part, be modified during the treatment: for example, they can be ionized by the capture of thermionic emitted electrons or catalytically decomposed similar in the technological process of hot wire activated chemical vapor deposition (HWCVD) [185]. In contrast, in the hot plate treatment, the sample is heated by a heater spiral through a glass ceramic plate with the plate temperature set to 500-600 °C. Therefore, the suggested modification of the oxygen species can be neglected for the hot plate treatment.

The origin of sodium

In order to prove that the emission at 31.6 eV originates from sodium, a nc-TiO_2 sample with a high Na content was measured with XPS before and after heat treatment at 600 °C using a hot plate (Figure 7.15). In addition to the emission at 31.6 eV, the intensity of an emission at 1072.5 eV, which can be unmistakably assigned to the Na1s core level, increases with temperature. This observation is in accordance to the increase in the emission at 31.6 eV, which is therefore concluded to originate from Na2p as suggested.

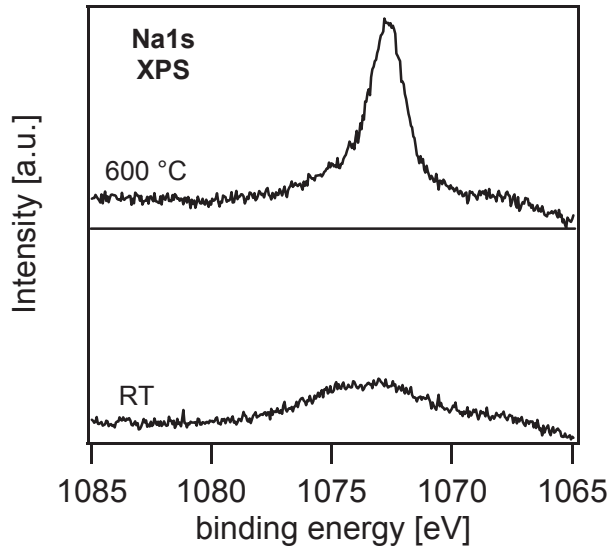

Figure 7.15.: XPS spectra of the Na1s core level for a sample with a high Na content at RT and heated to 600 °C using a hot plate (same sample for which SXPS results are shown in Figure 7.18).

As the mobility of Na ions in both glass [186–188] and TiO_2 [189–191] is well known, the soda lime glass substrate as well as Na contaminations in the TiO_2 precursor itself are possible sources for the temperature-enriched Na at the surface. In order to identify the origin of the sodium, a series of heat treatments using both a hot plate and a heat gun were performed on samples from a nc-TiO_2 film prepared on a Si(111) wafer substrate. The SXPS spectra of the valence band region normalized to the beam current are shown in Figure 7.16. Again, the Na2p emission increases after heating with the hot plate as well as with the heat gun. Similarly to the experiments with FTO covered glass substrates, no obvious changes, except the appearance of the Na2p emission, are induced with the hot plate, but additional changes in the O2*s* shallow core level and the valence band appear during the treatment with

the heat gun. The change in the Na2p core level can be seen more clearly in the normalized spectra in Figure 7.16. For the samples that were heated at 400 and 600 °C with the hot plate, charging effects occurred during the measurements. Therefore, the spectra were adjusted in binding energy for a better comparison. Thus, the small change in the energetic distance between the Ti3p and Na2p emissions might be an artifact rather than a chemical shift. Because the influence of the Na-containing glass substrate can be excluded, the SXPS results shown in Figure 7.16 indicate that the sodium observed at the surface of TiO_2 is related to the sodium contained in the TiO_2 powder which is used for sintering.

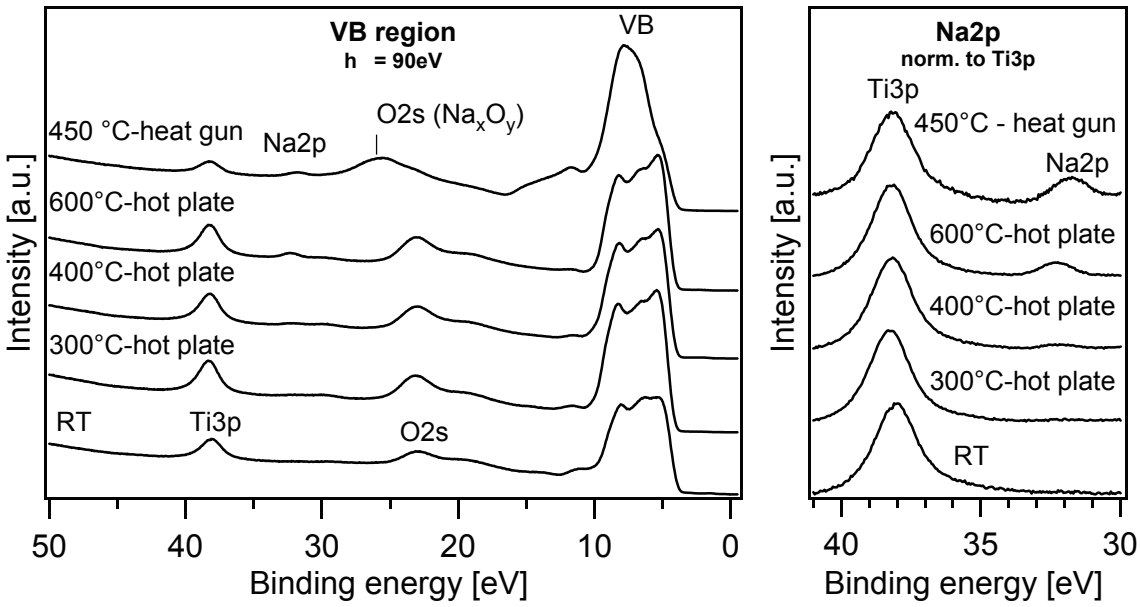

Figure 7.16.: SXPS spectra on samples of a nc-TiO_2 film prepared on Si(111); the samples were heated with a hot plate and a heat gun under different temperatures: the valence band region is normalized to the beam current and the Na2p core level is normalized to the intensity of Ti3p. The spectra were recorded with a photon energy of 90 eV.

Investigation of TiO_2-powders with different Na contents

To investigate the correlation between bulk and surface sodium contents, several nc-TiO_2 films prepared from TiO_2 powders with known upper limits of Na contents were investigated. The sodium content of the TiO_2 powders was determined by inductively coupled plasma optical emission spectroscopy (ICP-OES), a method to determine the bulk elemental composition. In general, structure-directing agents, for example sodium dodecyl sulfate, are used in the sol-gel synthesis of TiO_2 nanoparticles [192]. The variation of the Na content can be caused by variations in the respective synthesis and purification parameters. To some extent, a correlation of the Na2p intensity to the sodium content in the TiO_2 powder can be deduced from the SXPS spectra of the Na2p core level normalized to the intensity of the Ti3p core level (Figure 7.17). With increasing sodium content the intensity ratio of Na2p to Ti3p is increasing. This correlation becomes more obvious in the plot of the Na2p to Ti3p intensity ratio as a function of the upper limit of the Na content of the TiO_2 powders, which were used for sintering of the films.

In order to investigate the effect of the Na content of the TiO_2 powders on the intensity increase of the Na2p core level with temperature, two samples prepared from TiO_2 powders with high and low sodium contents on FTO substrates were heated using a hot plate. Figure 7.18 plots the Na2p to Ti3p intensity ratio versus the heating temperature. With increasing heating temperature, the intensity increase of the Na2p emission of the sample prepared from a TiO_2 powder with a high sodium content is much higher than the intensity increase of the sample prepared from a powder with a low sodium content.

This supports the assumption that the temperature-increased surface Na content is due to the Na content in the TiO_2 powder.

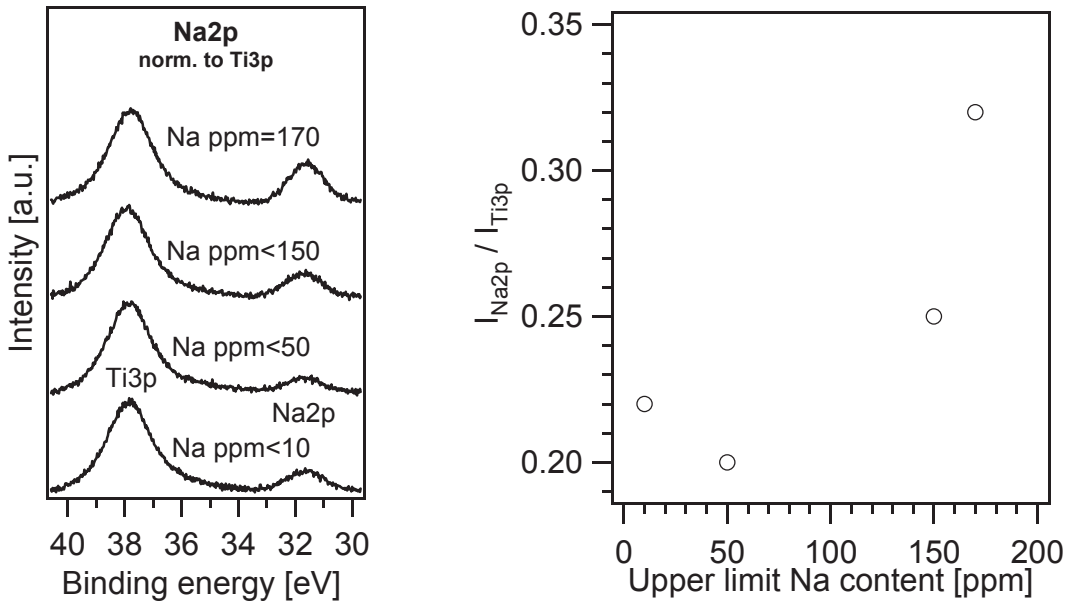

Figure 7.17.: SXPS spectra of Ti3p and Na2p shallow core levels for nc-TiO_2 films sintered using powders with different Na contents as indicated (left). The spectra are taken at 90 eV photon energy and normalized to the intensity of Ti3p. Plot of the intensity ratio of Na2p to Ti3p versus the upper limit of the Na content (right).

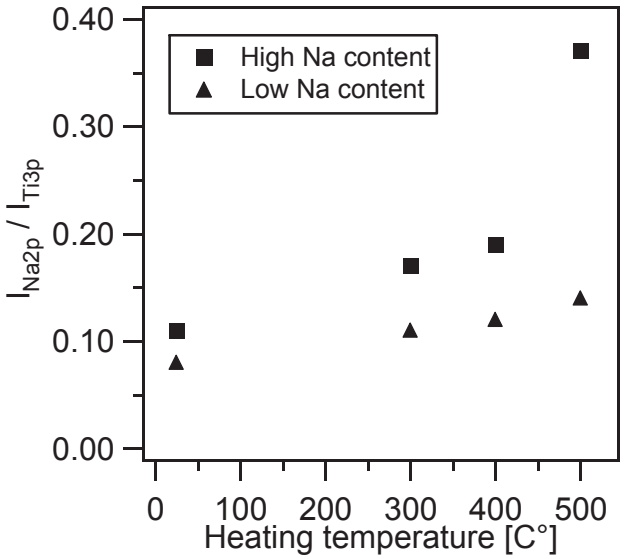

Figure 7.18: The intensity ratio of Na2p to Ti3p core levels as a function of heating temperature for nc-TiO_2 films prepared from TiO_2 powder with high and low Na contents.

A model of the Na distribution

At this point, a model of the Na distribution is deduced fromt the different results of the hot plate and the heat gun experiments. When the TiO_2 films were annealed using the hot plate, the Na2p emission increased while other features of the TiO_2 spectra did not change. In particular, the valence band which is very sensitive to structural and chemical changes was not altered. In contrast, when the films were heated by the heat gun, changes in the valence band region were observed. In the model, during the hot plate treatment, the Na^+ ions are assumed to migrate from the bulk of the respective TiO_2

crystallite toward its surface but do not transmit the surface. Thus, a stabilized subsurface configuration for Na^+ ions is proposed in analogy to the stabilized subsurface Ti interstitial, as calculated by Wendt et al. [193]. Before the heat treatment, the Na^+ ions are randomly distributed in the bulk of the TiO_2 crystallites. The heat treatment with the hot plate starts the migration of Na^+ ions from the bulk of the TiO_2 nanoparticles to subsurface sites, where they are stabilized. Using a heat gun at high temperatures, Na^+ ions can transmit the TiO_2 surface and react with activated oxygen species from the heat gun. A sketch of the Na distribution for the respective treatments is given in Figure 7.19.

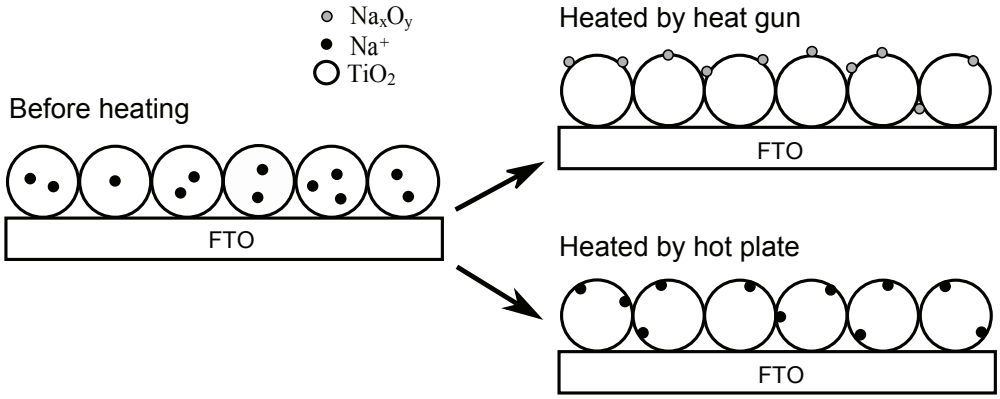

Figure 7.19.: Sketch of the Na distribution for the indicated heat treatments.

Efficiency measurements

For the application in dye-sensitized solar cells the TiO_2 surface has to be very large. Because of their direct influence on different crucial processes influencing the efficiency, such as anchoring of the dye, electron transfer from the LUMO of the dye to the conduction band of the TiO_2 and recombination of electrons in TiO_2 with holes in the HOMO of the dye [194], chemical and electronic surface variations have to be controlled precisely. Using the example of sodium, the surface and subsurface Na contents are expected to influence the performance of the solar cell strongly. In addition to this, TiO_2 surface gap-states are widely thought to play an important role in the electron transport and recombination processes (see Section 3.2). Therefore, the surface gap-state distribution was probed with resonant photoemission spectroscopy. The principles of resonant photoemission spectroscopy are described in Subsection 5.1.2. Measurements with both heating plate and heat gun (see Figures .1 and .2 in the Appendix) show similar, temperature independent attenuation of the gap-states intensity but no change of the spectral features upon heat treatment. No clear correlation between the intensity of the gap-states and the surface Na content can be found.

Figure 7.20 shows efficiency measurements on two different types of solid-state DSSCs with an area of 20 mm^2. The measurements were performed by the project partner Bosch. One was built with the standard metal-free indoline dye ID30 (A) [34] and the other with a modified dye from BASF (B). Both types of solar cells were tested with different TiO_2 substrates containing different amounts of sodium at 1/10 and 1 sun illumination under a solar simulator before and after annealing at 150 °C for 15 min in air. Up to around 150 ppm Na content, an efficiency increase with the annealing of the TiO_2 electrodes is observed at both intensities and for both dyes, which is probably caused by an increased dye adsorption due to OH^- desorption from the TiO_2 surface. At 170 ppm Na content, the efficiency ID30 decreases at 1/10 sun, whereas at 1 sun, no change is observed. With the BASF dye a decrease after the heat treatment is measured at both intensities, being stronger at the higher intensity. According to the SXPS measurements (see Figures 7.11,7.12 and 7.18), only minor changes of the surface Na content are expected at 150 C. Sorting the efficiency measurements according to the Na bulk content (Figure 7.20) indicates that the efficiency could be influenced by the surface Na content which varies depending on

the bulk content. An optimum Na concentration range can be given for the ID30 (50 to 150 ppm) dye. However, more efficiency measurements using TiO_2 with varied Na content and varied heat treatments are needed to differentiate the role of surface Na in solid-state DSSCs.

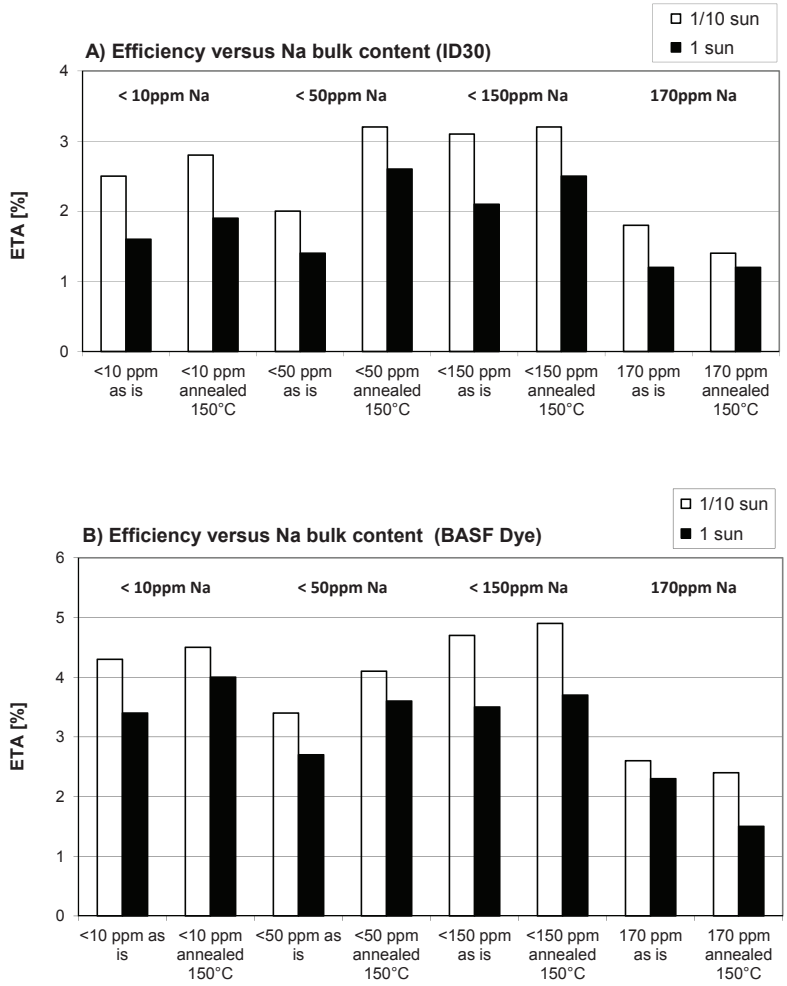

Figure 7.20.: The efficiency measurements of solid-state DSSCs sorted according to the Na bulk content of the TiO_2 electrode for two intensities before and after heat treatment at 150 °C before dye staining for the (A) indoline dye ID30 and (B) BASF dye. The cells were built and the measurements were performed by the project partner Bosch.

7.3 Conclusions

Investigation of the TiO_2 substrates

Titanium dioxide substrates, dense TiO_2 blocking layers (BL-TiO_2) and nanocrystalline, mesoporous TiO_2 films (nc-TiO_2) were characterized employing different analyzing methods. Electron microscopy and atomic force microscopy pictures show pinhole-free TiO_2 films, which is important to avoid short circuits in the device. The TiO_2 layers are found to imitate the grain structure of the FTO underlying substrate. Film thicknesses of the TiO_2 blocking layer (100 nm for the blocking layer sample and 200 nm for the nc-TiO_2 sample) as well as the for the nc-TiO_2 sample (1.65 μm) are in good agreement to literature values. Another important aspect of the TiO_2 substrate, the anatase crystal phase, was verified by XRD, Raman and photoemission spectroscopy. In addition, the electronic properties of the films were investigated by SXPS.
Both types of substrates (BL-TiO_2 and nc-TiO_2) show valence band, gap-states distribution and core level spectra in good agreement to each other and experiments conducted by Schwanitz et al. [82]. Valence band measurements taken at different photon energies show the difficulty of the determination of the valence band maximum due to the underestimation of the tail of the valence band. The origin of these states is probably either different cross sections of the Opσ and the Opπ bonds due to the polarization of the incident synchrotron light or O2p tail states due to non-interaction with Ti3d states (illustrated in Figure 7.21 on the right side). In addition for some energies interfering gap-states, which are located right at the surface, complicate the determination. Surface sensitive measurements recorded with photon energies, which match resonant excitation energies, show increased gap-states intensities. The results of the bulk measurement, recorded with a photon energy of 950 eV, and the surface sensitive measurement, recorded with a photon energy of 90 eV, are illustrated in Figure 7.21.

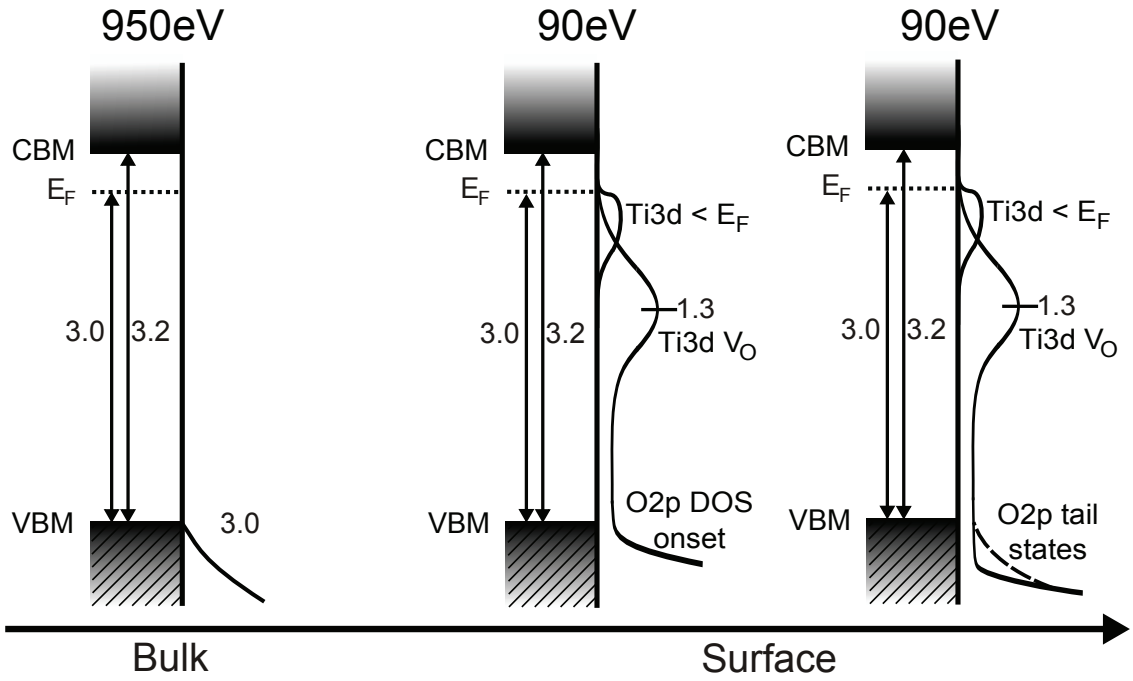

Figure 7.21.: The energy diagrams of TiO_2 measured at different photon energies. Oxygen vacancies (V_0) are observed in the surface sensitive measurement recorded at 90 eV photon energy (middle and right), whereas the valence band maximum is easier to determine in the bulk measurment recorded at 950 eV photon energy (left). The two graphics for the surface sensitive measurement illustrate the two different inerpretations in this work of the origin of the tail of the valence band.

Behavior and influence of sodium in TiO_2

TiO_2 films prepared in different laboratories often lead to varying efficiencies of the cells using the same TiO_2 precursor material and apparently the same recipe. Therefore, in the second part, changes of the chemical surface composition of nanocrystalline TiO_2 films induced by systematic temperature variations were studied by SXPS, XPS and Raman.

Systematic ex-situ heat treatments using a hot plate and a heat gun were performed on different ex-situ prepared nc-TiO_2 films. In both cases, the intensity of the Na2p core level increased after heat treatment. The binding energy of the Na2p species indicates the presence of Na^+ ions. Comparing both heat treatments, the increase of the Na2p emission for the heat gun experiment is more obvious than the increase for the hot plate experiment. Additional changes in both the O2s shallow core level and the valence band are observed above 450 °C in the case of the heat gun experiment and are assigned to the formation of Na_xO_y on top of the surface of the TiO_2 crystallites. Because the temperature-driven increase of the surface Na content was also observed in measurements on TiO_2 on a Si substrate, the TiO_2 powder itself as the source of the surface Na content was identified. The higher the Na content of the TiO_2 powder, the more obviously the Na2p peak increases with temperature. In conclusion, variations in surface Na content, distribution, and chemical composition due to variations in temperature treatment are the possible causes of different efficiencies of solid-state DSSCs prepared from the same materials at different laboratories. Efficiency measurements performed by Bosch on solid-state DSSCs using TiO_2 with different bulk Na contents and heat treatment at 150 °C lead to the conclusion that surface Na can influence the cell performance.

8 Spiro-MeOTAD

Organic hole-conducting molecules are currently under investigation to replace the liquid I_3^-/I^- redox couple in dye-sensitized solar cells to overcome practical issues with liquid electrolytes, like solvent evaporation due to sealing problems. One of the most promising molecular hole conductors that can be infiltrated into the nc-TiO_2 electrode is Spiro-MeOTAD, which was introduced in Section 3.3 and is commonly used in solid-state dye-sensitized solar cells.
In this chapter, different deposition methods, physical vapor deposition (PVD) and drop-casting, are compared and different dopants of Spiro-MeOTAD are investigated. Moreover, Li-TFSI salt which is already used as a dopant to increase the conductivity of Spiro-MeOTAD and whose influence on Spiro-MeOTAD and the whole cell is still under discussion and WO_3 as a model doping system are presented and their doping mechanisms discussed.

8.1 Comparison of preparation methods

The two different deposition methods, physical vapor deposition (PVD) and drop-casting, were employed and are compared in means of electronic equality. With PVD thin layers can be deposited stepwise, which is why it is a highly suitable method for interface experiments and hence for the characterization of DSSCs. Drop-casting is close to infiltration and spin-coating which are widely used in industry to deposit cost-effectively thin films of organic materials. Films of Spiro-MeOTAD were deposited with both methods and investigated by synchrotron-induced photoemission spectroscopy (SXPS).

8.1.1 Physical Vapor Deposition (PVD)

An important question which has to be answered in order to compare physical vapor deposition (PVD) with drop-casting is the thermal stability of the Spiro-MeOTAD molecule during evaporation. For example, chemical reactions, bond breaking and carbonization of the molecule can occur during heat treatment and, therefore, during evaporation, as well.
The thermogravimetric analysis (TGA) of Spiro-MeOTAD performed by BASF shows one point of inflection of the TG curve at a temperature of ca. 427 °C and a second at a temperature of ca. 456 °C (Figure 8.1). The differential thermal analysis (DTA) also obtained from BASF shows an endothermic inflection point at approximately 247 °C that coincides well with the melting point of 246 °C, which is given in literature [50, 88]. The exothermic inflection point at ca. 457 °C is located at the same temperature as the second reversal point of the TG measurement. Because the decomposition of a material is an exothermic reaction paired with a loss of mass, the exothermic feature at 456 °C is interpreted as the decomposition temperature of the material. In literature, the proposed decomposition temperature of Spiro-MeOTAD is 440 °C [50, 88], which is in good agreement to the obtained value. The temperatures (280-300 °C) used to evaporate Spiro-MeOTAD are well below the decomposition temperature. Therefore, the decomposition of the material can be neglected. Further proof of the volatility and temperature stability of Spiro-MeOTAD and similar spiro molecules like Spiro-TAD and Spiro-m-TTB can be found in literature [93]. In particular, Rana et al. studied the hole mobility, dielectric and transport behavior of thermally evaporated Spiro-MeOTAD thin films [102, 195].

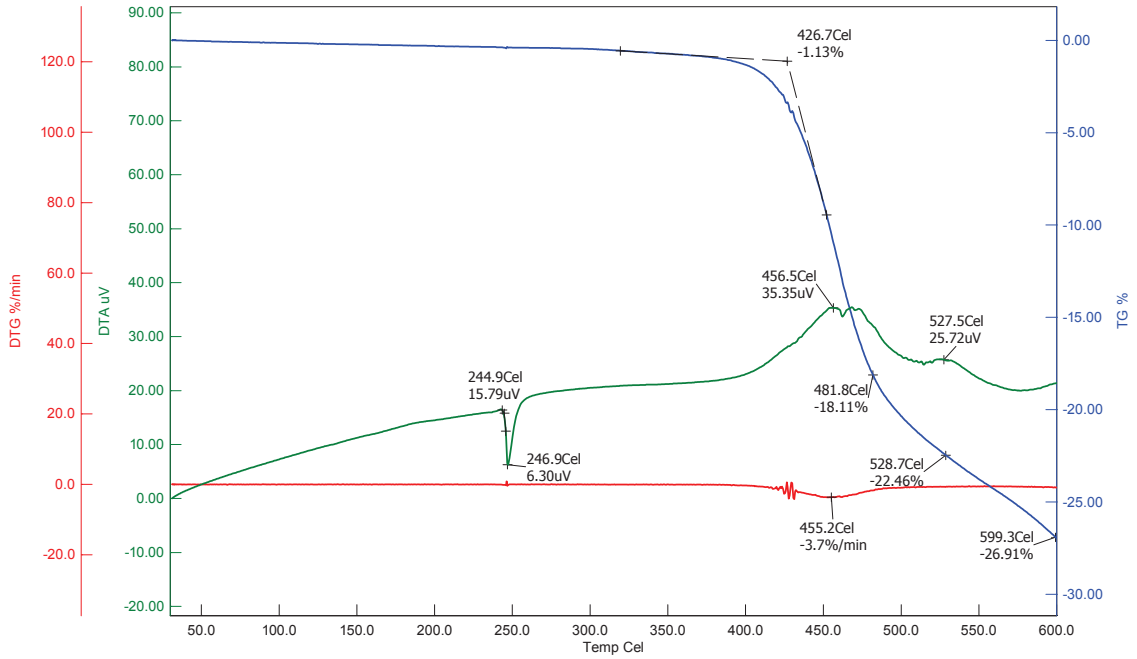

Figure 8.1.: Thermogravimetric analysis (blue), differential thermal analysis (green) and differential thermogravimetric analysis (red) measurements of Spiro-MeOTAD performed by the project partner BASF.

TiO_2/Spiro-MeOTAD interface experiment

In order to investigate the TiO_2/Spiro-MeOTAD interface as well as the Spiro-MeOTAD bulk properties, an interface experiment was performed at the U49/2-PGM-2 beamline at BESSY II. Spiro-MeOTAD was evaporated stepwise with a rate of approximately 2.3 Å/s onto a TiO_2 blocking layer. The experiment was performed at room temperature, whereas the source temperature was 298 °C. Valence band measurements were performed at 90 eV, O1s and Ti2p core level at 600 eV, N1s at 450 eV and C1s core level at 360 eV photon energy.

Valence band: The valence band of the TiO_2 substrate (Figure 8.2) shows the Ti3p and Na2s emission lines at 37.8 eV and 31.4 eV, respectively. The origin and the influence of sodium was discussed in Section 7.2. The emissions in the valance band region as well as the O1s (530.4 eV) and Ti2p (459.3 eV) emissions, which belong to the TiO_2 substrate, are damped with growing Spiro-MeOTAD overlayer thickness. In contrast, emissions related to Spiro-MeOTAD evolve with increasing overlayer thickness. The bulk values of Spiro-MeOTAD are obtained from the last deposition step (layer thickness of 137 Å) where all substrate signals are completely damped.

Core levels: The peak maxima of the C1s (285.4 eV), N1s (400.5 eV) and O1s (534.2 eV) core levels are determined by a Gaussian fit (Table 8.1). Both core level emissions of the TiO_2 substrate ($Ti2p_{1/2}$ and $Ti2p_{3/2}$) and the HOMO of Spiro-MeOTAD do not shift with growing overlayer thickness. This is confirmed by the core levels of Spiro-MeOTAD (C1s, N1s and O1s) shown in Figure 8.3 which also show no shift of their energetic binding energy position.

Ti2p / gap-states: Figure 8.4 shows the Ti2p core level emission, the normalized Ti2p spectra and the gap-state region of the first two Spiro-MeOTAD deposition steps (8 Å and 18 Å) on the TiO_2 substrate. The energetic positions of the $Ti2p_{1/2}$ (465.3 eV) and the $Ti2p_{3/2}$ (459.3 eV) substrate emissions do not change after the deposition of Spiro-MeOTAD. In the Ti2p spectra that are normalized to the maximum and the binding energy, a second Ti species can be observed. In the BL-TiO_2 sample, a reduced Ti^{3+} species is present at a lower binding energy. After evaporation of Spiro-MeOTAD, the species is damped

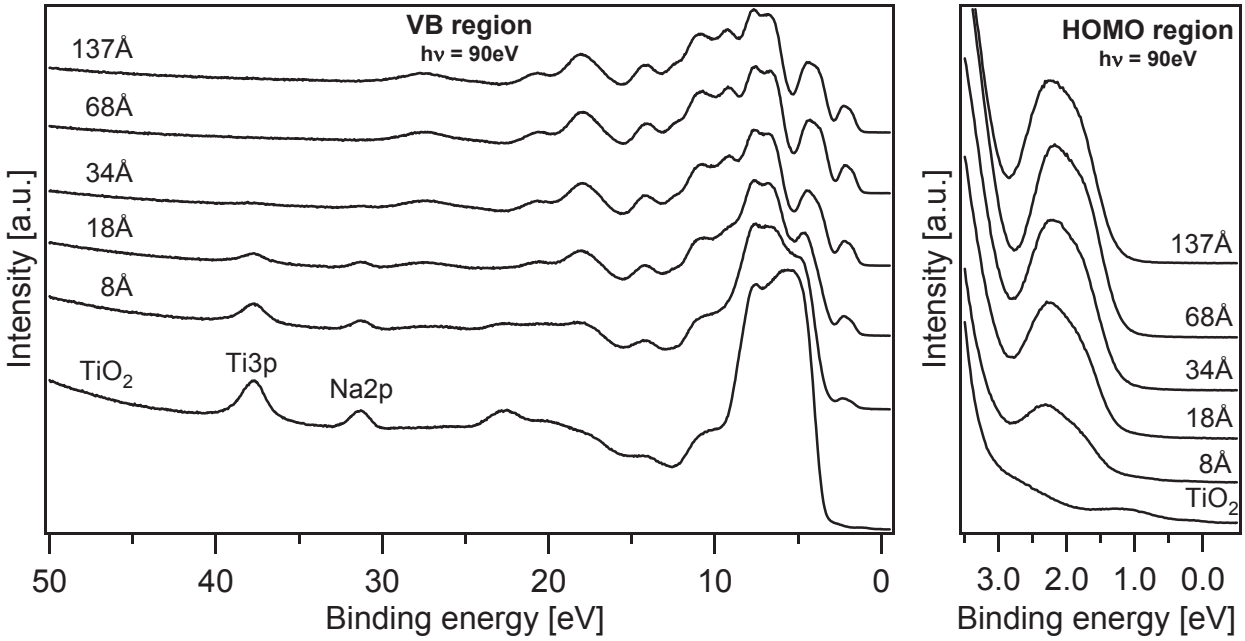

Figure 8.2.: The valence band and the detailed HOMO / gap-states region of TiO_2 and the stepwise evaporated Spiro-MeOTAD (formal thickness of the Spiro-MeOTAD layers is indicated). The TiO_2 features are damped while Spiro-MeOTAD features grow in intensity. The energy positions of the two HOMO state maxima do not change. The spectra were recorded with a photon energy of 90 eV.

but not quenched. This indicates that Spiro-MeOTAD does not react with TiO_2.
The gap-state region recorded at a photon energy of 465 eV show two kinds of TiO_2 gap-states, one just below the Fermi level and one at approximately 1.3 eV, as was shown in Subsection 7.1.4. Here, the gap-states vanish with growing Spiro-MeOTAD layer thickness but are not quenched. The photon energy to measure the gap-state region was chosen to match the Ti2p-Ti3d resonance, which enhances the intensity of the gap-states as explained in Subsection 7.1.4 as well.

Lineup: No band bending and thus charge transfer can be derived at the interface of both materials. The results are summarized in the band diagram of the TiO_2/Spiro-MeOTAD interface in Figure 8.5. The work functions of TiO_2 (4.3 eV) and Spiro-MeOTAD (4.1 eV) were taken from the TiO_2/ID224 (see Section 9.2) and WO_3/Spiro-MeOTAD (see Subsection 8.2.1) interface experiments, respectively. The difference of the work functions of 0.2 eV is assigned to an interface dipole. As was shown in Subsection 7.1.4, the valance band maximum cannot be determined correctly in spectra recorded at 90 eV, therefore the value (3.0 eV) was taken from the measurement performed at a photon energy of 950 eV.

Table 8.1.: The core level binding energy positions of Spiro-MeOTAD, which was deposited on TiO_2 via PVD: The given positions are the maxima of the respective emissions, which were fitted by a Gaussian curve.

	HOMO	**C1s**	**N1s**	**O1s**	**Work function**
Photon energy	**90 eV**	**360 eV**	**450 eV**	**600 eV**	**90 eV**
Emission maximum	1.9 eV	285.4 eV	400.5 eV	534.2 eV	4.1 eV

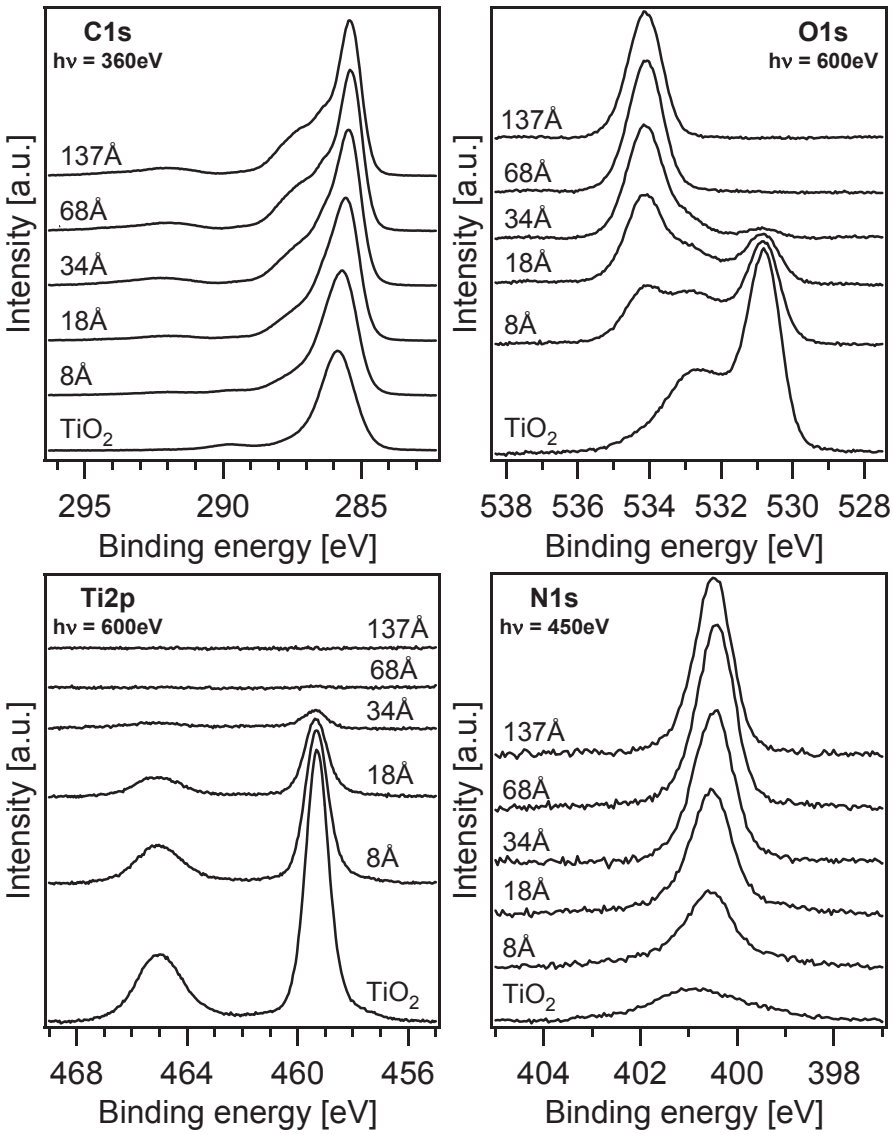

Figure 8.3.: The C1s, O1s, Ti2p and N1s core level spectra of the stepwise evaporated Spiro-MeOTAD on TiO_2 (bottom). No shift in neither of the core levels belonging to Spiro-MeOTAD (C1s, N1s and O1s) nor in the core level belonging to TiO_2 (Ti2p) can be observed. The C1s and N1s emissions of TiO_2 and Spiro-MeOTAD overlap, which complicates the evaluation, whereas O1s contributions of both materials are clearly discriminable. C1s spectra were recorded with a photon energy of 360 eV, N1s with 450 eV and O1s as well as Ti2p with 600 eV.

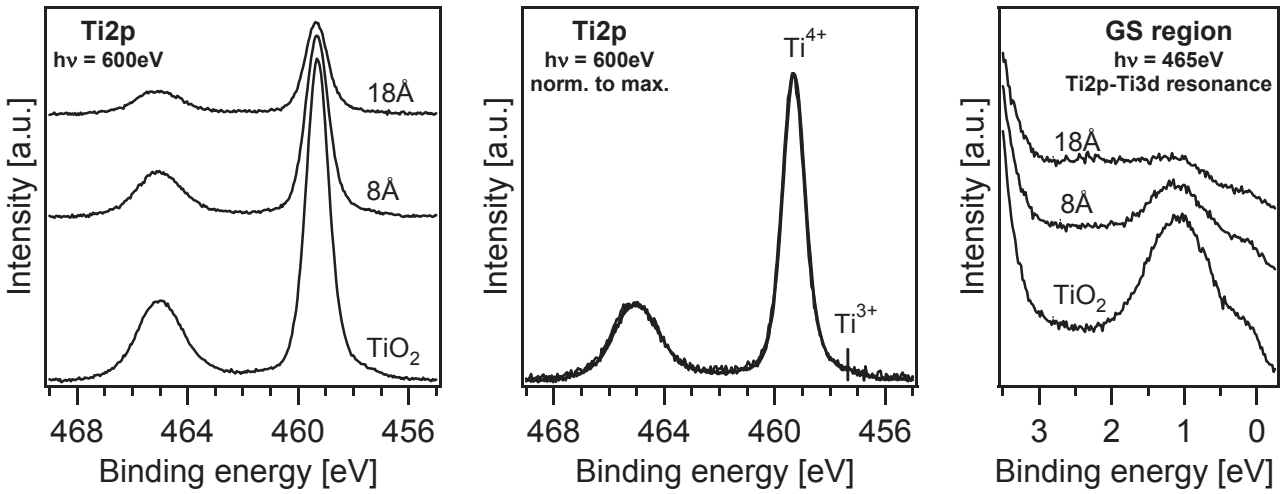

Figure 8.4.: The Ti2p core level spectra, the normalized Ti2p spectra and the gap-state region measured in Ti2p-Ti3d resonance of the first two Spiro-MeOTAD deposition steps (8 Å and 18 Å) on TiO_2 (bottom). No shift in the Ti2p spectra and no damping of the reduced Ti^{3+} species in the normalized spectra can be observed after the two deposition steps. The gap-states in the resonance measurements are damped but not quenched with growing Spiro-MeOTAD thickness. The detailed Ti2p and gap-states region spectra were recorded with a photon energy of 600 and 465 eV, respectively.

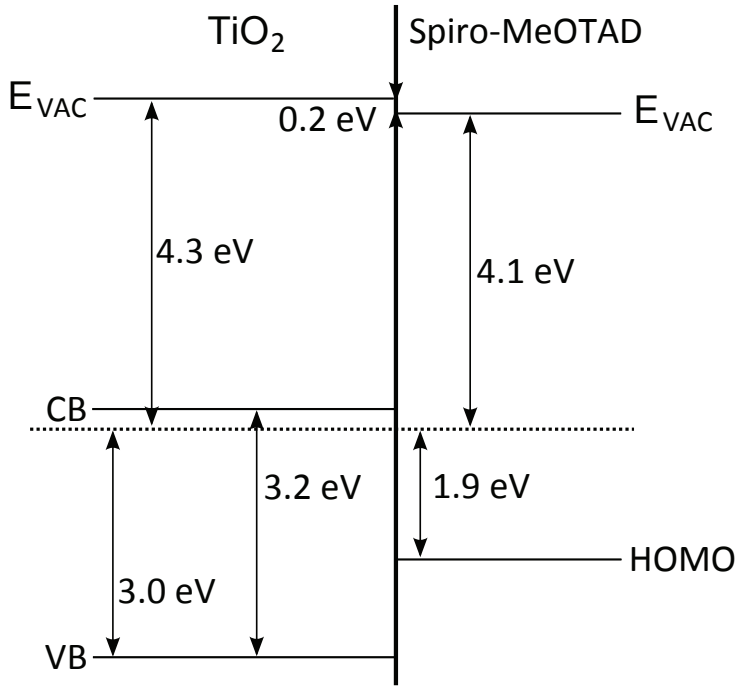

Figure 8.5.: The band diagram of the TiO_2/Spiro-MeOTAD interface of Spiro-MeoTAD deposited onto a TiO_2 blocking layer. The work functions of TiO_2 (4.3 eV) and Spiro-MeOTAD (4.1 eV) were taken from the TiO_2/ID224 (see Section 9.2) and WO_3/Spiro-MeOTAD (see Subsection 8.2.1) interface experiments, respectively. The difference of the measured work functions of 0.2 eV is assigned to an interface dipole. The HOMO binding energy values refer to the photoemission maximum position.

8.1.2 Drop-casting

In contrast to PVD, drop-casting is a method which does not implicate thermal stress by heating but employs solvents that can interact with the organic molecules. It was shown by Schwanitz et al. that by coadsorption of acetonitrile the HOMO and the N1s core level of the Ru-dye N3 are shifted and shift reversibly back after desorption [81]. Polar solvents like acetonitrile, chlorobenzene (C_6H_5Cl) and cyclohexanone ($C_6H_{10}O$) - the last two are used to dissolve Spiro-MeOTAD in this work - can build up a solvation shell around the molecule, which induces a dipole or influences an existing dipole at the surface. Therefore, drop-casting experiments should clarify the influence of the solvents on Spiro-MeOTAD and the energetic lineup of drop-casted Spiro-MeOTAD to TiO_2.

The drawback of this deposition method is the difficult control of the amount of deposited material and thus the film thickness. This complicates the XPS and especially SXPS measurements of those layers because the probability of charging increases with increasing film thickness. In addition, film thicknesses are not uniform all over the deposited layer, which originates from non-uniform Spiro-MeOTAD deposition during solvent evaporation. The patterns are similar to patterns obtained from the so called coffee-ring effect, which describes the typical ring-like pattern left from droplets of dissolved material after solvent evaporation. This effect causes a non-uniform thickness distribution within the deposited layer [196]. However, this enables one to measure "thin" and "thick" Spiro-MeOTAD layers on the same sample. In this way, the charging of the sample due to too thick layers can be controlled. The typically obtained pattern after drop-casting of a dye is shown in Figure 8.6. The intensely colored outer ring is due to the mask which was used to fix the sample. Some of the solution sticks to the edge of the mask and dries there, which causes an increased deposition of material at the edges of the mask.

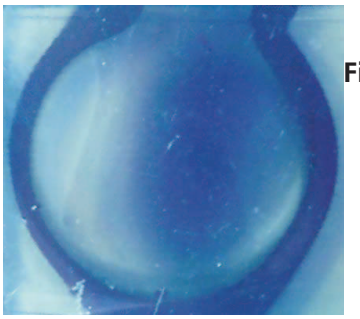

Figure 8.6: The figure shows a typical pattern of a dried dropplet of a drop-casted dye, which should exemplify the typical ring-like pattern obtained after drop-casting. Different regions of different intense coloring show different thicknesses.

Experimental

Drop-casting experiments were carried out in the SoLIAS system (see Section 4.1) at the U49/2-PGM-2 beamline. Dissolved Spiro-MeOTAD was drop-casted onto a TiO_2 blocking layer in a glass cell which was permantly rinsed with pure argon. Before transferring the samples into the buffer-chamber, residual solvent was blown off with argon. Anhydrous chlorobenzene (99.8%) and cyclohexanone (99.5%) purchased from Sigma-Aldrich were used to dissolve Spiro-MeOTAD. In the following, the measurements of both experiments are shown and discussed.

Chlorobenzene

A 0.2 g/ml solution of Spiro-MeOTAD dissolved in chlorobenzene was drop-casted onto a blocking layer. Prior to drop-casting, the solution was sonicated for 10 min in order to dissolve possible agglomerates within the solution. The measurements presented in this Subsection were performed in single-bunch mode of BESSY II, which resulted in lower absolute intensities and worse signal to noise ratios of the measurements compared to measurements in multi-bunch mode which is the normally used mode.

The valence band was measured at 90 eV, the O1s and Ti2p core levels at 600 eV, the C1s core level at 360 eV and the N1s core level at 450 eV photon energy. Compared to the blocking layer measurements presented in Section 7.1.4, the TiO_2 substrate spectra (Figure 8.8) show identical binding energy positions of the core levels and the same curve shape of those levels and of the valance band. One difference is the absence of sodium in the valence band region.

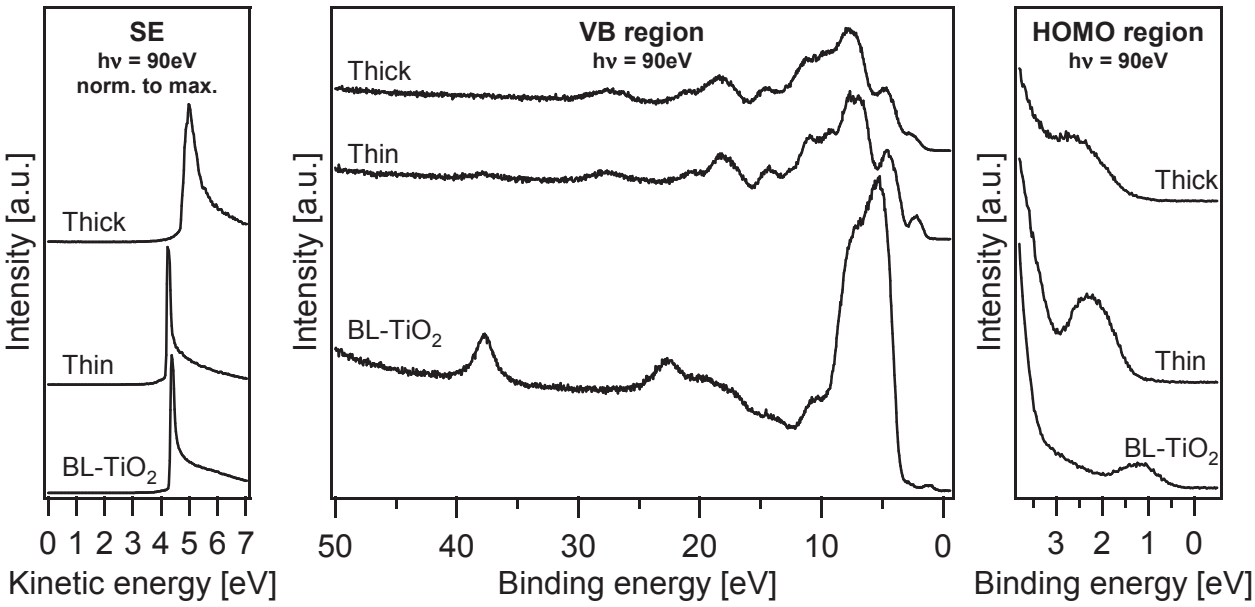

Figure 8.7.: The secondary edge, valence band and the detailed HOMO / gap-states region of the TiO_2 blocking layer and the drop-casted Spiro-MeOTAD, which was dissolved in chlorobenzene: Measurements were performed in the inner part (labeled as "thin") and the outer part (labeled as "thick") of the dried droplet. The thickness in the inner part is smaller than in the outer part due to non-uniform Spiro-MeOTAD deposition during solvent evaporation. In the spectra of the inner part, the TiO_2 features are not completely damped. Due to charging the binding energy positions of the two HOMO state maxima of the Spiro-MeOTAD at the outer part are broadened and shifted to higher binding energies and the work function is increased. The valence band and HOMO / gap-states region spectra as well as the secondary edge were recorded with a photon energy of 90 eV.

The spectra taken in the inner part of the dried Spiro-MeOTAD droplet (labeled as "thin") show TiO_2 features in the O1s spectrum and not fully damped Ti2p emissions originating either from a not fully closed or thin Spiro-MeOTAD layer (Figure 8.8). Spectra taken at the outer part of the droplet (labeled as "thick") show no TiO_2 substrate features but a broadening of the emissions and an unequal shift in binding energies of all core levels with varying photon energies. Also the HOMO orbitals are energetically shifted to higher binding energies and broadened (Figure 8.7). The unequal shifts and the broadening of those peaks is most probably due to charging of the film at that point on the sample and not due to band bending. As the conductivity is low for organic semiconductors (see Section 3.1), the thickness of the films is very critical to avoid charging. The binding energy positions of all three measurements are listed in Table 8.2. The non-unifromal film thickness within the layer as described in the beginning of this paragraph originates from non-uniformal Spiro-MeOTAD deposition during solvent evaporation.

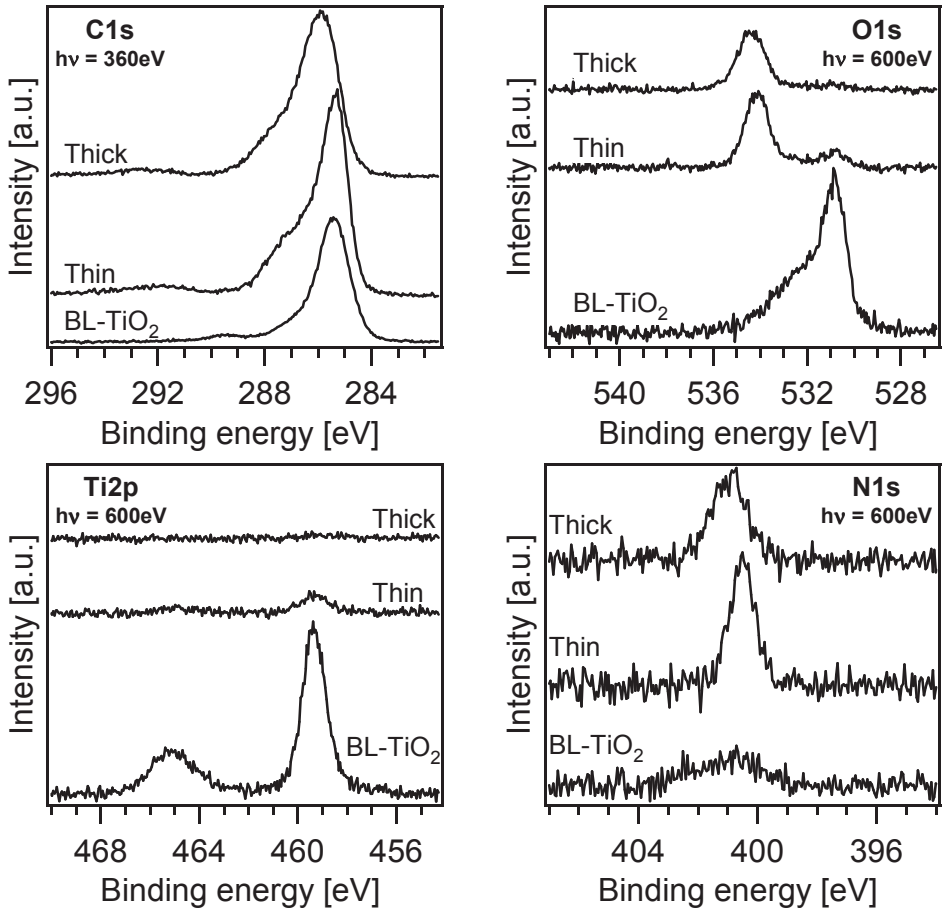

Figure 8.8.: The C1s, O1s, Ti2p and N1s core level spectra of TiO_2 and drop-casted Spiro-MeOTAD which was dissolved in chlorobenzene: Measurements were performed in the inner part (labeled as "thin") and the outer part (labeled as "thick") of the dried droplet. The thickness in the inner part is smaller than in the outer part due to non-uniform Spiro-MeOTAD deposition during solvent evaporation. The Ti2p and O1s spectra of the "thin" measurement show not completely damped TiO_2 features. Due to charging of the Spiro-MeOTAD at the outer part, the core levels are shifted to higher energies and broadened. C1s spectra were recorded with a photon energy of 360 eV, N1s with 450 eV and O1s as well as Ti2p with 600 eV.

Table 8.2.: The core level binding energy positions of the drop-casted Spiro-MeOTAD, which was dissolved in chlorobenzene: The given positions are the maxima of the respective emissions, which were fitted by a Gaussian curve. Due to charging, the positions from the measurement labeled as "thick" are not correct but shifted unequally to higher energies.

	HOMO	C1s	N1s	O1s	Work function
Photon energy	90 eV	360 eV	450 eV	600 eV	90 eV
thin	1.9 eV	285.4 eV	400.5 eV	534.2 eV	4.0 eV
thick	2.1 eV	285.8 eV	400.8 eV	534.4 eV	4.1 eV

Cyclohexanone

In a second drop-casting experiment, the solvent of Spiro-MeOTAD was changed to cyclohexanone. A 0.2 g/ml solution of Spiro-MeOTAD was used for drop-casting. The solution was sonicated for 10 min to dissolve agglomerates within the solution.
As in the previous experiment, the valence band was measured at 90 eV, the O1s and Ti2p core level at 600 eV, the C1s core level at 360 eV and the N1s core level at 450 eV photon energy. Again, measurements were performed at two regions of the sample. All spectra of the measurement recorded at the inner part of the Spiro-MeOTAD droplet (labeled as "thin") show TiO_2 features, whereas the spectra recorded at the outer part of the droplet and labeled as "thick" does not show those features (Figure 8.10). As discussed earlier, drop-casting leads to non-uniform thicknesses due to non-uniform deposition during solvent evaporation, which is accompanied by a thickness gradient within the deposited layer. All binding energy positions of the three measurements are listed in Table 8.3.
Unlike for the previous experiment with drop-casted Spiro-MeOTAD dissolved in chlorobenzene, the HOMO region spectra do not differ in binding energy or in the curve shape (Figure 8.9). Also the work function (4.0 eV) is the same in both cases. The shapes of the work functions were influenced by an measurement artifact of the SoLIAS, which occured probably due to inhomogeneities of the applied bias distribution. Therefore, the work functions were determined as indicated by the lines drawn in the respective spectra. Because no difference in binding energies, curve shapes and work functions were observed, charging of the sample can be excluded. The TiO_2 substrate shows a Na2p emission at approximately 31.3 eV. Sodium and its origin and influence on the dye-sensitized solar cell were discussed in Section 7.2.

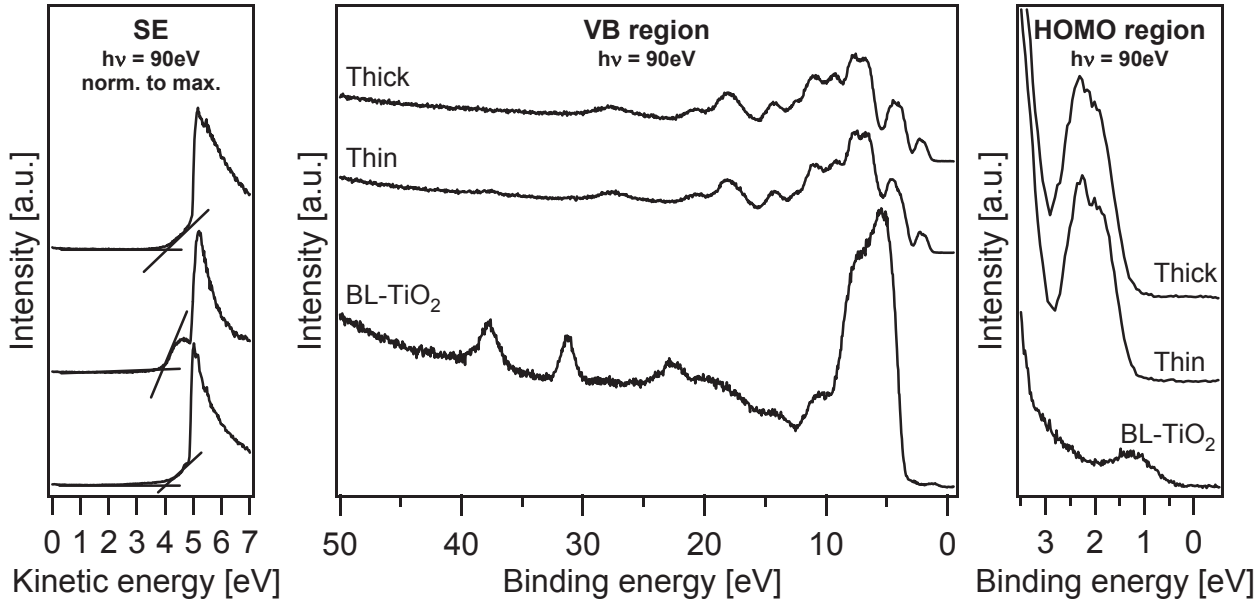

Figure 8.9.: The secondary edge, valence band and the detailed HOMO / gap-states region measurements of the TiO_2 blocking layer and the drop-casted Spiro-MeOTAD dissolved in cyclohexanone: Measurements were performed in the inner part (labeled as "thin") and the outer part (labeled as "thick") of the dried droplet. The thickness in the inner part is smaller than in the outer part due to non-uniform Spiro-MeOTAD deposition during solvent evaporation. In the measurements in the inner part the TiO_2 features are not completely damped. No difference in the binding energy positions of the two HOMO state maxima and the work function of both Spiro-MeOTAD measurements the two measurements can be observed. The work functions were influenced by an measurement artifact and, therefore, were determined as indicated by the lines drawn in the respective spectra. The valance band and HOMO / gap-states region spectra as well as the secondary edge were recorded with a photon energy of 90 eV.

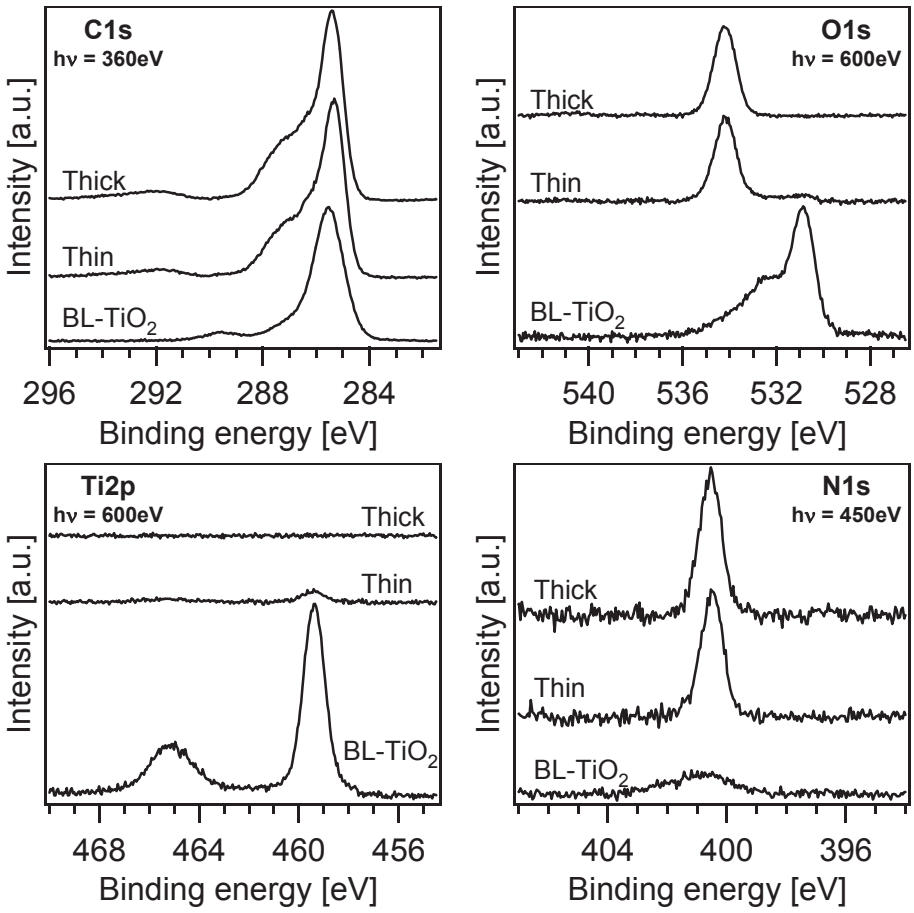

Figure 8.10.: The C1s, O1s, Ti2p and N1s core level spectra of the TiO_2 blocking layer and the drop-casted Spiro-MeOTAD dissolved in cyclohexanone: Measurements were performed in the inner part (labeled as "thin") and the outer part (labeled as "thick") of the dried droplet. The layer thickness in the inner part is smaller than in the outer part due to non-uniform Spiro-MeOTAD deposition during solvent evaporation. The Ti2p and O1s TiO_2 substrate emissions are not completely damped in the "thin" measurement. All emissions from both Spiro-MeOTAD measurements show the same binding energy position. C1s spectra were recorded with a photon energy of 360 eV, N1s with 450 eV and O1s as well as Ti2p with 600 eV.

Table 8.3.: The core level binding energy positions of drop-casted Spiro-MeOTAD, which was dissolved in cyclohexanone: The given positions are the maxima of the respective emissions which were fitted by a Gaussian curve.

	HOMO	C1s	N1s	O1s	Work function
Photon energy	**90 eV**	**360 eV**	**450 eV**	**600 eV**	**90 eV**
thin	1.9 eV	285.4 eV	400.5 eV	534.2 eV	4.0 eV
thick	1.9 eV	285.4 eV	400.5 eV	534.2 eV	4.0 eV

8.1.3 Discussion and comparison of deposition methods: PVD vs. drop-casting

Drop-casting experiments of Spiro-MeOTAD dissolved in chlorobenzene and cyclohexanone produce equivalent results with respect to the binding energy as well as to the shape of the core levels and the valence band. In the first drop-casting experiment with Spiro-MeOTAD dissolved in chlorobenzene, no reliable spectra measured at the "thick" spot which did not show any TiO_2 substrate signals could be obtained. Therefore, in the following comparison between drop-casted and PVD-deposited Spiro-MeOTAD, only the spectra of Spiro-MeOTAD dissolved in cyclohexanone are used as a representative for the drop-casted samples.

Valence band

Figure 8.11 shows the valence band of the drop-casting experiment with cyclohexanone as the solvent (labeled "drop-casting") and the PVD experiments (labeled "PVD"). The curve shape as well as the binding energy positions of the HOMO orbitals and the valence band features are almost identical. The difference in binding energies of both measurements is ca. 0.1 eV (Table 8.4). The work function of the drop-casted Spiro-MeOTAD is decreased by 0.1 eV in comparison with the evaporated Spiro-MeOTAD. Especially in the valence band, differences become obvious as it is extremely sensitive to contaminations and different chemical environments. For example, Jaegermann et al. showed the change of the valence band structure of the WSe_2 and GaAs semiconductors due to, among others, water absorption [146, 197]. It can thus be concluded that the energetic lineup of Spiro-MeOTAD is not altered by using either of the solvents and possible residual solvent in the films. The films are assumed to be mostly solvent free because no outgasing in the UHV chamber was observed. Neverthelss, residual solvent could be trapped in voids within the films.

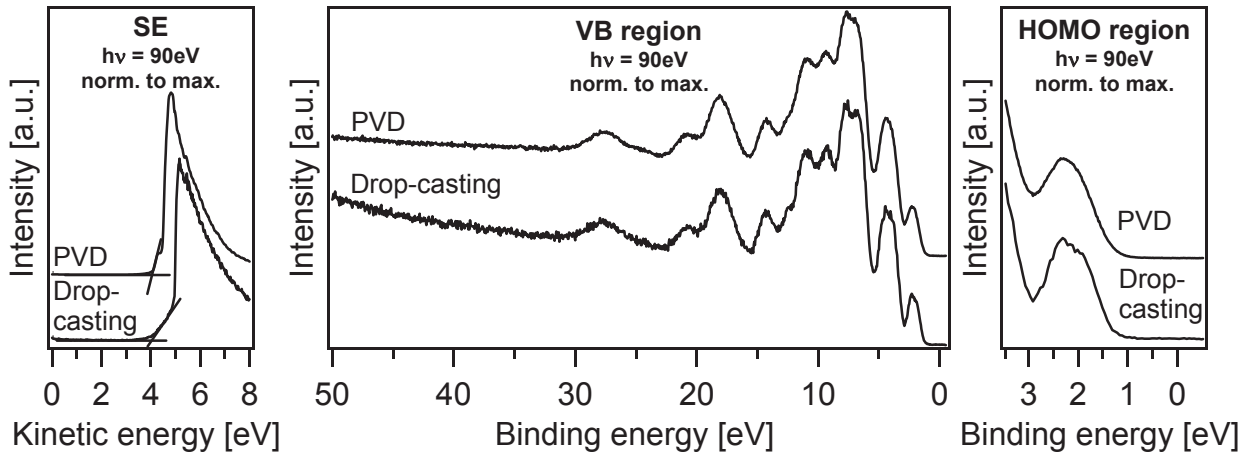

Figure 8.11.: The comparison of the secondary edges, valence band region and HOMO region of Spiro-MeOTAD deposited via PVD and drop-casting: Both valence band regions show approximately the same curve shape and the same binding energy positions of the orbitals. The spectra are normalized to the respective maxima.

According to the theoretical calculated density of states of the HOMO orbitals of Spiro-6P and Spiro-PBD, which are structural comparable to Spiro-MeOTAD, performed by Johansson et al. [54], the valence peak with the lowest binding energy consists of a HOMO and HOMO-1, separated by ca. 0.4 eV. The fitted binding energies of the emission maxima of the molecular orbitals of the respective valence peak of undoped drop-casted Spiro-MeOTAD are approximately 1.9 and 2.3 eV (labeled as "I" and "II" in Figure 8.12) which is accordance to the calculations of Johansson. The detailed binding energy positions for both deposition methods are listed in Table 8.4 and discussed later on.

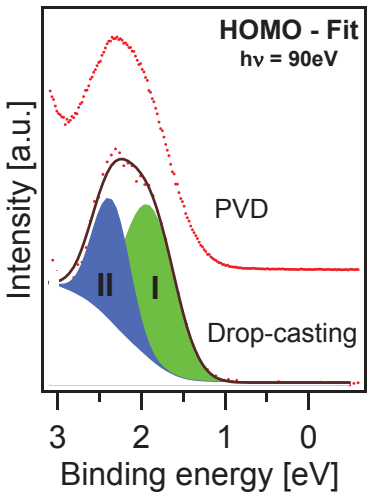

Figure 8.12: The HOMO emission of evaporated and drop-casted Spiro-MeOTAD taken at 90 eV photon energy: The HOMO of drop-casted Spiro-MeOTAD, as an example, is decomposed into HOMO (I) at 1.93 and HOMO-1 (II) at 2.37 eV.

Core levels

A shift of ca. 0.1 eV, which was observed in the HOMO orbitals, is also observed in the C1s, N1s and O1s core level emissions. A detailed comparison of binding energy positions is given in Table 8.4. As the respective curve shapes of the core levels are the same, the two deposition methods are considered to be equivalent and chemical reactions of the solvent with Spiro-MeOTAD can be excluded.

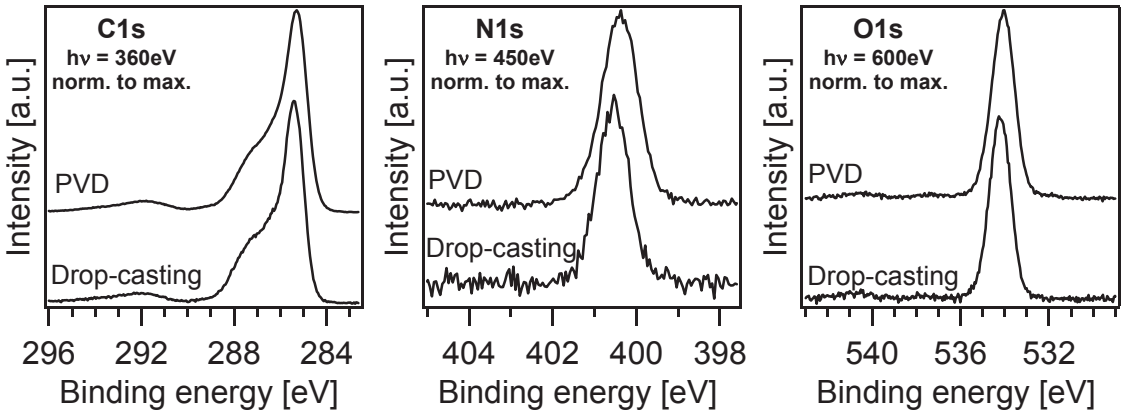

Figure 8.13.: The comparison of the C1s, N1s and O1s core levels of Spiro-MeOTAD deposited via PVD and drop-casting: All core levels of the drop-casted Spiro-MeOTAD show the same shift of ca. 0.1 eV to higher binding energies. Spectra are normalized to the respective maxima.

Because the shape of the curves of evaporated and drop-casted Spiro-MeOTAD is identical, the fitting procedure is assumed to be similar. As an example, the C1s fit of the drop-casted Spiro-MeOTAD is shown in Figure 8.14. The fit was conducted with a Gauss-Lorentz mixed Voigt profile after Shirley-background subtraction [198] according to the relative intensities of the bonds present in the Spiro-MeOTAD molecule. The spectrum can be decomposed into five peaks, which are assigned to emissions of five of the six different kind of carbon bonds existing in the Spiro-MeOTAD molecule and which are coloured and labeled in Figure 8.14. According to electronnegativity considerations, the emissions are assigned to the C-H bond at 285.37 eV (labeled as I and drawn in blue in the figure), the C-C bond at 286.01 eV (II-black), the C-N bond at 286.50 eV (III-red), the aromatic C-O bond at 287.14 eV (IV-green) and the C-O bond at 287.78 eV (V-grey). The aromatic C-C bond to the spiro-linked carbon atom in the middle of the Spiro-MeOTAD molecule was neglected in the fit as the relative intensity of the respective peak was too low to contribute evidently. The spectrum also contains satellites located at higher binding energies ranging from ca. 291 to 294 eV. Those emissions were also not fitted in the presented spectrum

but can also interfere with the main C1s emissions, what can explain the non perfect curve fitting in the binding energy range from 285 to 289 eV. This was shown for PA-PTCDI by Decker et al., who showed a satellite contribution within the C1s main emissions [199]. Nevertheless, the fitted curve and the measurement are in good agreement and supports the assumption that no chemical reaction has taken place during the deposition either by PVD or drop-casting.
The other elements, which build up the Spiro-MeOTAD molecule, oxygen and nitrogen, are all bonded in the same way in Spiro-MeOTAD and thus lead to only one characteristic emission as can be seen in Figure 8.13.

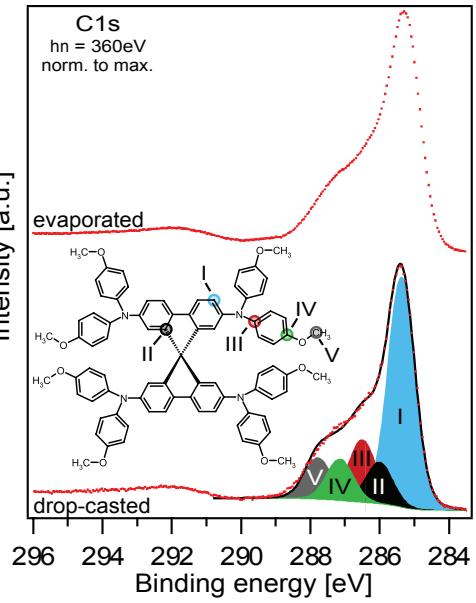

Figure 8.14: The C1s emission of evaporated and drop-casted Spiro-MeOTAD taken at 360 eV photon energy: The C1s spectrum of drop-casted Spiro-MeOTAD, as an example, can be decomposed into five peaks, which are assigned to emissions originating from different bonds as indicated in the figure: (I-blue) C-H at 285.37 eV, (II-black) C-C at 286.01 eV, (III-red) C-N at 286.50 eV, (IV-green) aromatic C-O at 287.14 eV and (V-grey) C-O at 287.78 eV. The relative intensities are chosen according to the stoichiometry of Spiro-MeOTAD.

Table 8.4.: The detailed comparison of the core level binding energy positions of drop-casted and evaporated Spiro-MeOTAD: The positions are the maxima of the respective emissions, which were fitted by a Gaussian curve. For better comparison the values are listed up to the second decimal place.

	HOMO	HOMO-1	C1s	N1s	O1s	Work function
Photon energy	**90 eV**	**90 eV**	**360 eV**	**450 eV**	**600 eV**	**90 eV**
PVD	1.87 eV	2.31 eV	285.32 eV	400.44 eV	534.11 eV	4.07 eV
Drop-casting	1.93 eV	2.37 eV	285.39 eV	400.54 eV	534.21 eV	3.99 eV
Difference	0.06 eV	0.06 eV	0.07 eV	0.10 eV	0.10 eV	0.08 eV

Lineup

The results are summarized in the energetic lineups shown in Figure 8.15. The difference of ca. 0.1 eV in the binding energies of the core levels of Spiro-MeOTAD deposited by PVD and drop-casting onto TiO_2 blocking layers is compensated by the difference in work function of ca. 0.1 eV. Hereby, the ionization potential of the evaporated Spiro-MeOTAD (5.94 eV) is in good agreement with the one of the drop-casted Spiro-MeOTAD (5.92 eV). Thus, the origin of the shift is very probably due to a different interface dipole forming during the deposition onto TiO_2. This behavior can be explained by a different ordering in the films. Rana et al. state that the ordering in evaporated films is higher than in solution processed films [102]. The authors compared parameters of the Gaussian disorder model obtained from current-voltage characterization of evaporated Spiro-MeOTAD films with the same parameters of solution-casted films determined by Poplavskyy et al. [100].

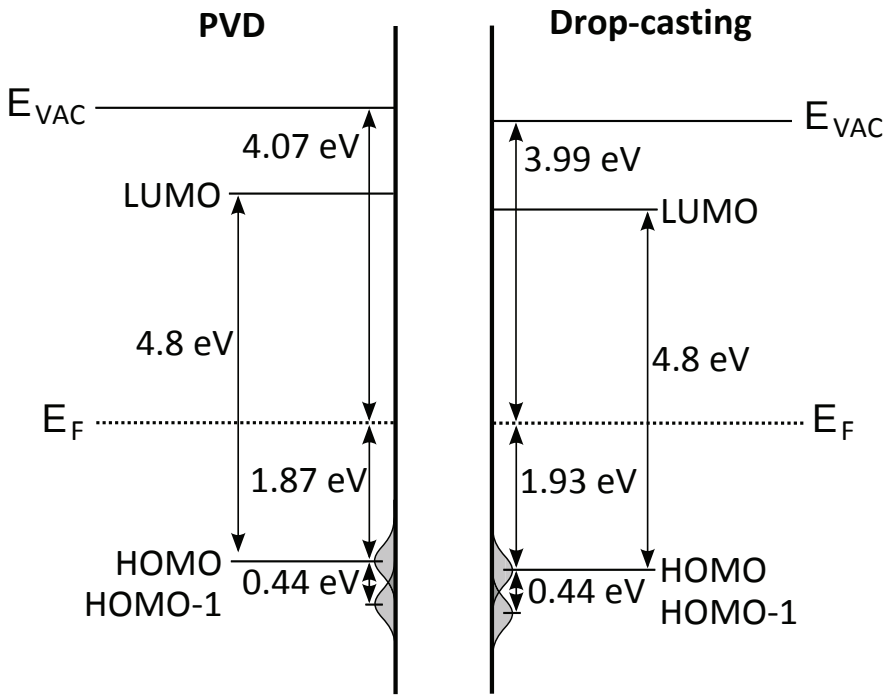

Figure 8.15.: The comparison of the surface energy diagram of evaporated (left) and drop-casted (right) Spiro-MeOTAD: the energy diagram of drop-casted Spiro-MeOTAD is in good agreement with the one of evaporated Spiro-MeOTAD. All values, except the bandgap which is determined from the absorption maximum, are deduced from the measurements.

Furthermore, Bröker and coworkers showed a direct correlation between the work function and the reorientation during layer growth of the electron acceptor HATCN on top of a Ag(111) surface [200]. Parallel to the reorientation of the molecules, the work function changes up to 1.0 eV dependent on the grade of reorientation during layer growth (Figure 8.16).

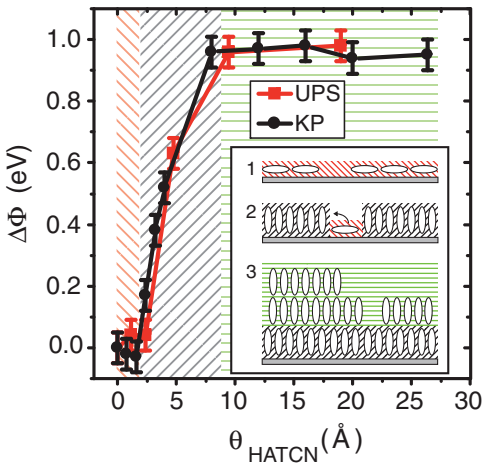

Figure 8.16: The relative work function change $\Delta\Phi$ of HATCN molecules adsorbed on Ag(111) relative to the work function of Ag(111). The change was measured with UPS (red dots) and Kelvin probe (black squares) and is plotted as a function of HATCN thickness θ. The inset shows the proposed density-dependent orientation of HATCN on Ag(111), whereas the color coding represents the three different regimes observed during the growth. The graphic is taken from [200].

In the case of Spiro-MeOTAD, the ordering of the film could also influence the surface dipole in the same way leading to the observed shift. However, the Spiro-MeOTAD molecule is more symmetrical than the HATCN molecule and the layers are considered to be amorphous, which leaves less space for reorientation and would explain the lower work function change. In order to proof this, further studies to investigate the growth of Spiro-MeOTAD using either deposition techniques are necessary.

The LUMO position was determined by the measured HOMO position and a calculated band gap E_{PES}, which would be measured by photoelectron spectroscopy and inverse photoelectron spectroscopy. E_{PES} was calculated by transforming an optical band gap E_g, which was obtained from the energetically lowest absorption of 3.2 eV [88], using the following equation introduced by Mankel [201]:

$$E_{PES} = 1.17 \cdot E_g + 0.97\,\text{eV} \tag{8.1}$$

Another explanation of the difference in binding energies as well as in the work functions could be the charging of the drop-casted films due to too thick layers as observed for the "thick" measurement of the drop-casted film employing chlorobenzene as the solvent (Figures 8.8 and 8.7). Charging causes a broadening of the peaks and a shift in the binding energy to higher binding energies. A shift of the core level emissions of the drop-casted Spiro-MeOTAD to higher binding energies compared to the evaporated Spiro-MeOTAD can be observed, indeed, but no broadening of the emissions. In addition the work function is decreased, whereas it should increase in case of charging. Also the amount of the shift of the drop-casted Spiro-MeOTAD films is the same for both experiments. Therefore, charging of the drop-casted films can be most probably excluded.

8.2 Doping

In solid-state DSSC, Li-salts and other additives are added as dopants to the dissolved Spiro-MeOTAD to enhance its intrinsically poor conductivity and thus the efficiency of the DSSC [49]. Another approach of the p-type doping of organic semiconductors is the codeposition of transition metal oxides, such as WO_3 and MoO_3. This was already shown for different semiconducting molecules, like CBP, pentacene and CuPc [129–132]. Under discussion as a possible doping mechanism is an energetically favored electron transfer from the HOMO of the organic molecule to the unoccupied states of the oxide, namely the conduction band. In this work, Spiro-MeOTAD is doped with Li-TFSI ($CF_3SO_2NLiSO_2CF_3$) and WO_3 to investigate the doping limit and mechanism as well as the function of WO_3 in contact with Spiro-MeOTAD as a hole injection layer.

8.2.1 WO_3 dopant

Experimental

Thin film samples were prepared by stepwise evaporation of powder materials from homemade effusion cells in an ultrahigh vacuum-chamber with a base pressure of 10^{-9} mbar. Deposition rates of Spiro-MeOTAD and WO_3 were approximately 0.3 Å/s for the interface experiments and were varied during coadsorption experiments according to the desired doping concentration. All film thicknesses as well as the deposition rates were determined by the damping of the respective substrate emission lines. Drop-casted films of Spiro-MeOTAD were prepared from cyclohexanone (>99%) solution in a glass cell directly attached to the UHV system (see Figure 4.2), which was rinsed with pure argon (5.0) and allowed the transfer of the samples to vacuum without contact to ambient air. Dense TiO_2 blocking layers on top of a FTO film obtained from BASF were used as substrates. Spiro-MeOTAD (>99%) was purchased from Lumtec and WO_3 powder (99.9%) from Sigma Aldrich.

Synchrotron-induced photoelectron spectroscopy (SXPS) of interfaces and codeposited as well as drop-casted films were performed in the SoLIAS (see Section 4.1) at the beamlines U49/2-PGM2 and TGM7. All spectra were recorded with a SPECS Phoibos 150 hemispherical analyzer under a base pressure of 10^{-10} mbar. In the photon energy range from 90 to 600 eV at the U49/2-PGM2 and from 47 to 120 eV at the TGM7, the obtained resolution, determined by the FWHM of the Fermi-edge at room temperature, was in the range of 180-240 meV depending on the excitation energy. The binding energy scale was calibrated against the Fermi-edge of a silver standard. Work functions were derived from the secondary electron edge position, which was measured with an applied bias voltage of 6 eV. Binding energy positions were derived from a fit of the photoemission lines using the Gauss-Lorentz mixed Voigt profile after the Shirley-background subtraction. [198].

Results and discussion

Pristine WO_3

Dense films of WO_3 (25 nm) were deposited on Spiro-MeOTAD and on TiO_2 substrates. The valence band and the low-lying O2s and W4f core levels measured with 90 eV photon energy are displayed in Figure 8.17. The WO_3 film on the TiO_2 substrate shows a stronger gap-state emission with a maximum at 0.8 eV binding energy and a stronger W4f component shifted by 1.2 eV to lower binding energy with respect to the main emission assigned to W^{6+} of stoichiometric WO_3. Similar gap-state and core level emissions were measured previously on WO_3(001) surfaces and were related to oxygen defects causing occupation of the W5d orbital of neighbor W atoms that appear as reduced W^{5+} component in the W4f

emission[124–126]. The WO_3 valence band maxima of 3.24 eV on Spiro-MeOTAD and 3.33 eV on TiO_2 were determined as the onset of the valence band edge. The work function of WO_3 is 6.1 eV on TiO_2 and 6.8 eV on Spiro-MeOTAD as derived from the secondary emission edge. The decreased value on TiO_2 may be correlated to induced oxygen defects and increased density of W^{5+} species.

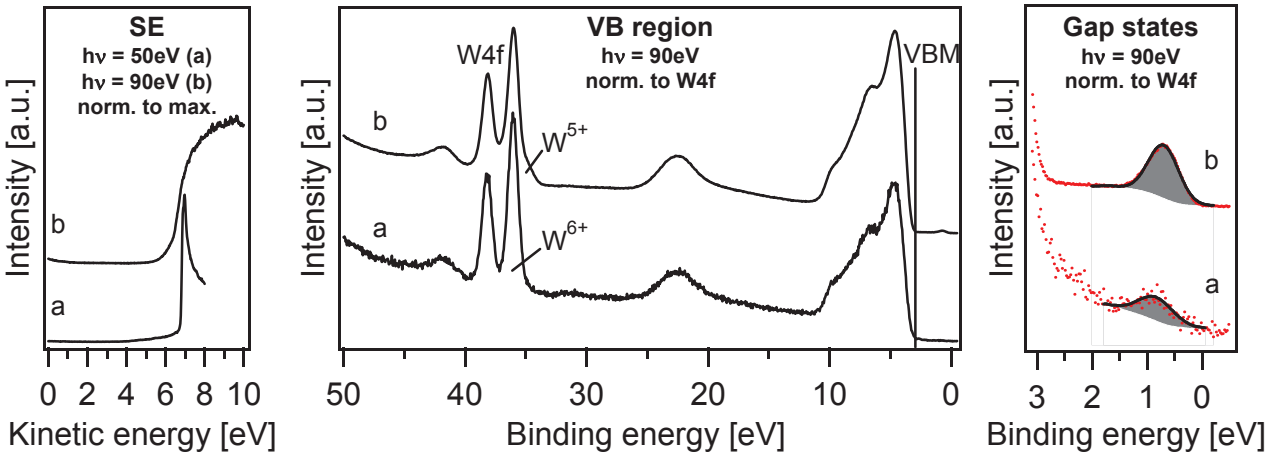

Figure 8.17.: The secondary edge (left), valence band (middle) and gap-states (right) spectra of the in-situ evaporated WO_3 onto Spiro-MeOTAD (a) and on TiO_2 (b). On TiO_2, increased W^{5+} and gap-state emissions are evident. The derived work function values are 6.8 (a) and 6.1 eV (b). Valence band, gap-state spectra, and secondary edge (b) were recorded with 90 eV photon energy, secondary edge (a) with 50 eV.

The electronic structure of pristine Spiro-MeOTAD and (marginally reduced) WO_3 films are compared in the vacuum level alignment, the so-called Anderson lineup in Figure 8.18. The comparison shows the situation before contact, neglecting a possible interface dipole (see later), and visualizes the possible charge transfer from WO_3 to Spiro-MeOTAD. The band gap of WO_3 prepared in a vacuum PVD process depends on the substrate temperature at which the deposition was performed [118]. At room temperature, the gap is 3.26 eV, which is related to amorphous WO_3 [118, 202] that may contain crystalline precipitates [117]. Due to the high WO_3 electron affinity of 6.7 eV and work function of 6.8 eV compared to the low Spiro-MeOTAD ionization energy of 6.0 eV and work function of 4.1 eV, electron transfer from Spiro-MeOTAD to WO_3 can be expected at the WO_3/Spiro-MeOTAD bilayer interface and in codeposited films.

TiO_2/WO_3 interface: To analyze the TiO_2/WO_3 interface formation, WO_3 was stepwise deposited onto TiO_2 blocking layers which are used in the solid-state DSSC to inhibit contact between the FTO electrode and Spiro-MeOTAD. The measurements of both nanocrystalline TiO_2 and TiO_2 blocking layers showed electronic equivalency, concerning valence band spectra, gap-state distribution and work function, shown in Subsection 7.1.4 and by Schwanitz et al. [82]. In Figure 8.19, the changes in the W4f emission (top) and Ti2p emission (bottom) are displayed. The TiO_2 substrate shows a Ti2p component shifted to a lower binding energy assigned to reduced Ti^{3+} and a gap-state emission assigned to occupied Ti3d states (shown in Figure .3 in the Appendix) due to oxygen defects [163]. With WO_3 deposition, the $Ti2p^{3+}$ emission disappears while the reduced W^{5+} component is strongest right at the interface and decreases with increasing WO_3 thickness. Thus, it can be concluded that the oxygen-defective titanium becomes oxidized at the TiO_2/WO_3 interface while tungsten oxide, which is assumed to evaporate as W_3O_9 clusters [110], is reduced.

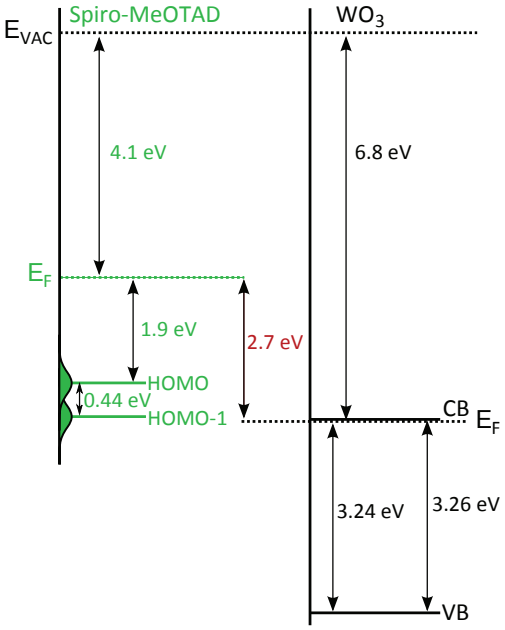

Figure 8.18: Comparison of the band diagrams of pristine Spiro-MeOTAD and pristine WO_3 on Spiro-MeOTAD (b in Figure 8.17) in the vacuum level lineup before contact. The HOMO binding energy values refer to the photoemission maximum position.

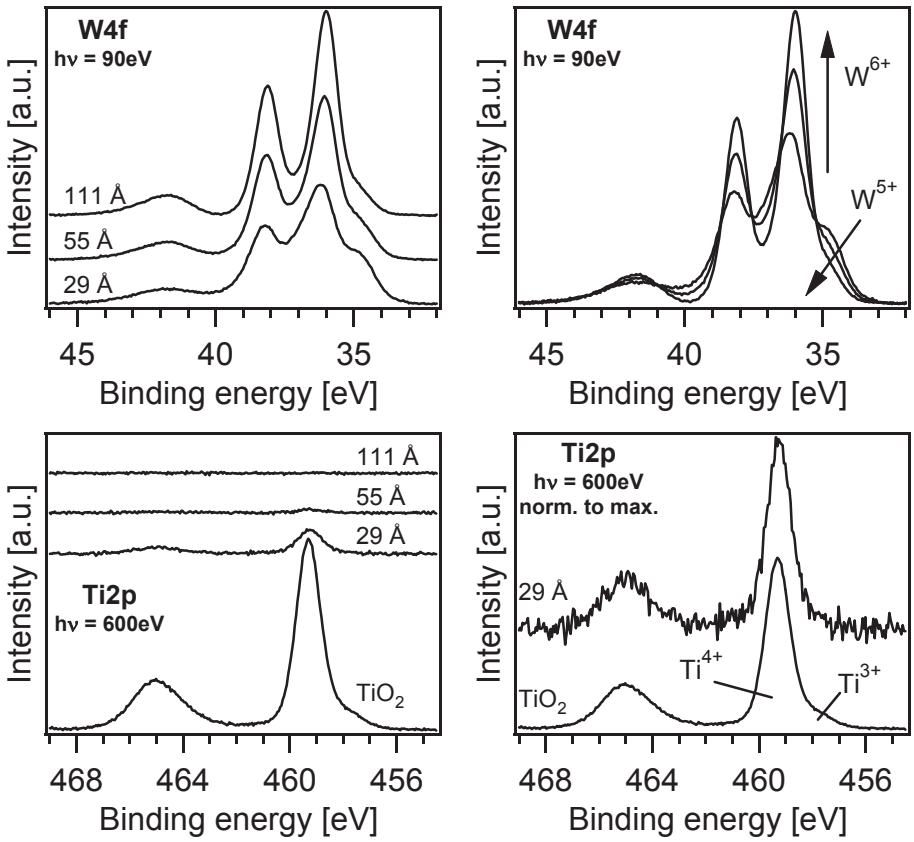

Figure 8.19.: The W4f spectra of the WO_3 deposition onto TiO_2 (top) and the Ti2p spectra of the TiO_2 substrate and the WO_3 deposition steps, taken at 90 and 600 eV photon energy, respectively. The W4f spectra are shown as measured; the Ti2p spectra as measured on the bottom left and the TiO_2 substrate spectrum and the first WO_3 deposition step normalized to the intensity maximum on the bottom right. The W4f emission shoulder at a lower binding energy is assigned to W^{5+} and the low energy shoulder in Ti2p to Ti^{3+} due to oxygen defects. The W^{5+} emission is strong in the first step while Ti^{3+} disappears, indicating an O^{2-} ion transfer from WO_3 to defective TiO_2.

W4f: Figure 8.20 shows a comparison of the Shirley background-subtracted W4f detail spectra of pristine WO_3 deposited on TiO_2 (indexed as b in Figure 8.17) recorded at 90, 210 and 600 eV photon energy. By varying the photon energy two things become obvious: one is the vanishing $W5p_{3/2}$ emission with increasing photon energy due to strongly varying cross sections [203] (1 for 90, 0.2 for 210 and 0.07 Mb for 600 eV[157]), the other is the different $W4f_{5/2}$ to $W4f_{7/2}$ branching ratios of the W4f emissions. The branching ratio can deviate from the statistical (0.75) due to e.g. discrepancies in the photoexcitation cross section and the availability of final states for different photon energies [203].

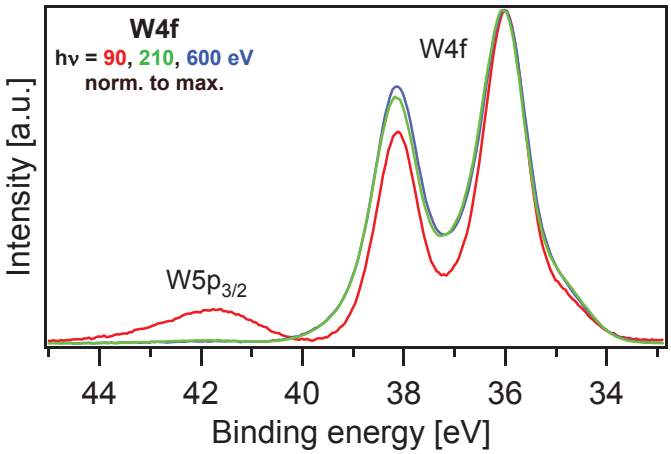

Figure 8.20: W4f core level spectra recorded at different photon energies: 90 (red), 210 (green) and 600 eV, showing the decreasing doublet intensity fraction $W4f_{5/2}$ / $W4f_{7/2}$ (0.65, 0.72 and 0.75) and the decreasing $W5p_{3/2}$ intensity with decreasing photon energy.

Spiro-MeOTAD:WO_3 Composites

To investigate the doping of Spiro-MeOTAD with WO_3 dense films (25 nm) of Spiro-MeOTAD:WO_3 composites with varying WO_3 contents (0.0%, 0.9%, 7%, 34%, 76% and 100%) were prepared. As the measurements on the composites were performed at the beamline TGM7 with maximum photon energy of 120 eV, the C1s core level could not be measured.

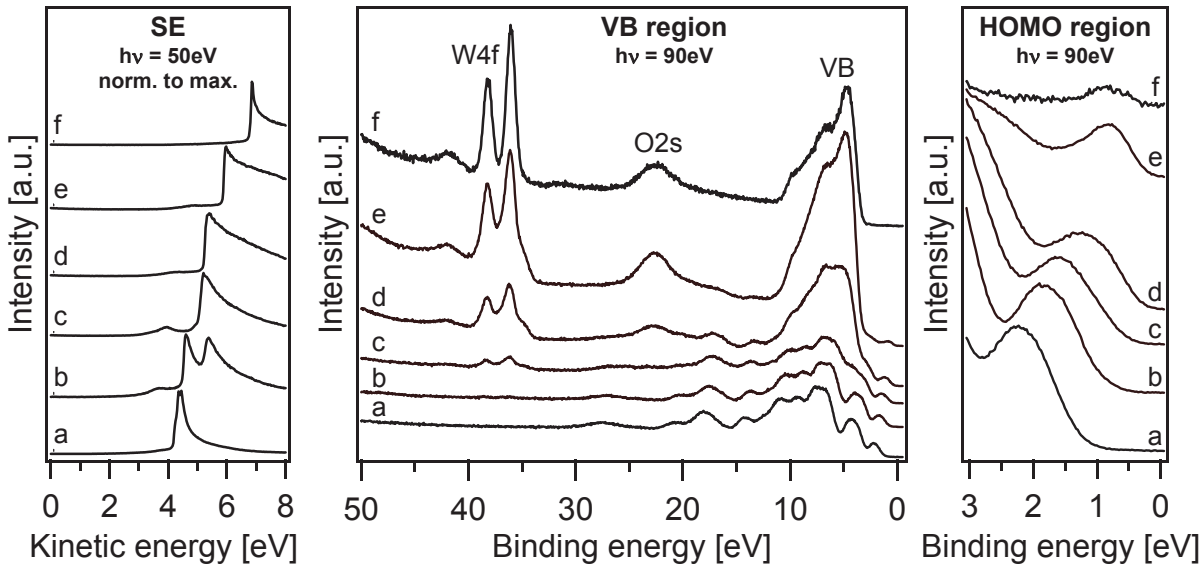

Figure 8.21.: From the left to the right, the secondary electron emission edge, valence band spectra and detailed HOMO / gap-state region of the Spiro-MeOTAD:WO_3 composites: (a) pristine Spiro-MeOTAD, (b) 0.9%, (c) 7%, (d) 34%, and (e) 76% WO_3-content, (f) pristine WO_3. The Spiro-MeOTAD emissions shift to lower binding energy, as evidenced by the HOMO spectra. All spectra were recorded at 90 eV photon energy and the secondary emission edges at 50 eV.

The WO_3 content of the composites was estimated by the intensity fraction of WO_3 gap-states to Spiro-MeOTAD HOMO emission. A gradual change from Spiro-MeOTAD to WO_3 spectral characteristics can be observed in Figures 8.21, 8.23 and 8.24. With increasing WO_3 content, the intensity of the W4f core level lines (at $\sim$ 36 eV) is increasing. The HOMO of Spiro-MeOTAD shifts up to 0.98 eV to lower binding energies with increasing dopant content (Figure 8.21), proving the p-doping. The gap-states of WO_3 (indexed as "III") and the two HOMO orbitals of Spiro-MeOTAD (indexed as "I" and "II") both contribute to the features of the composites in the HOMO and gap-state region (Figure 8.23) measured at 90 eV photon energy. As relative positions and intensities of emissions from the two materials also change with the content of WO_3, the shape of the valence band and of the HOMO and gap-state region changes. For the fitting procedure, the binding energy distance of the WO_3 gap-states and the W4f emission line of 35.3 eV, the energy distance of the Spiro-MeOTAD HOMO orbitals of 0.44 eV, and their intensity ratio of 0.83 were kept constant.

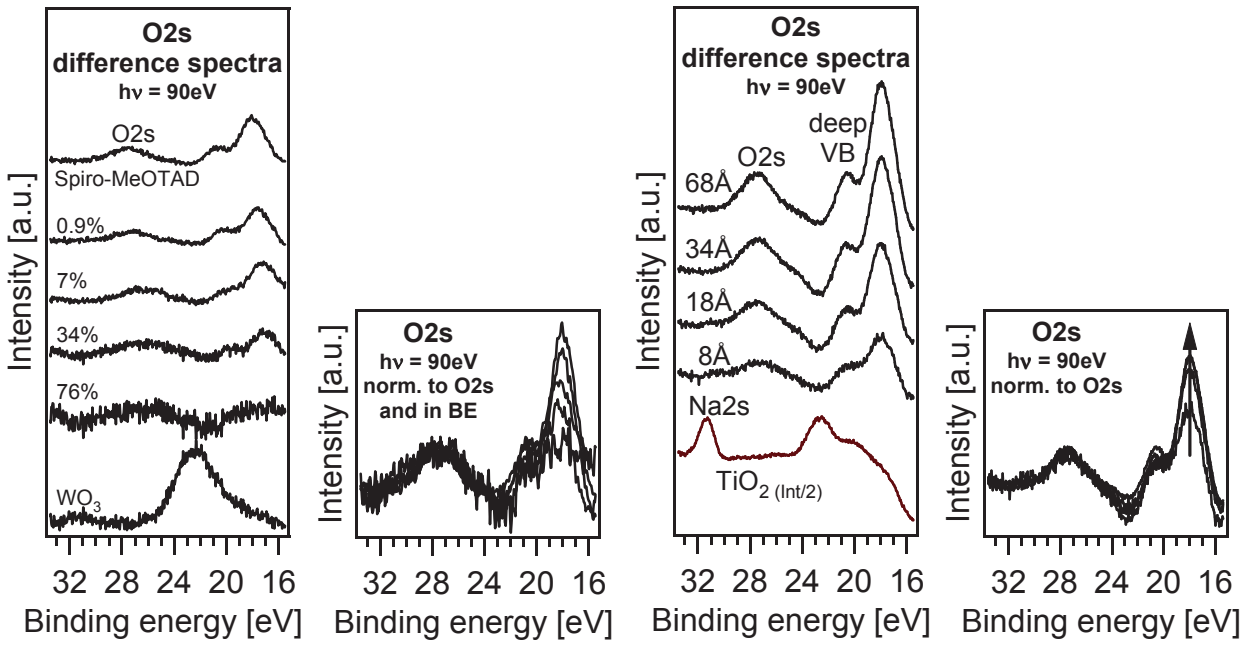

Figure 8.22.: (a) O2s difference spectra (left) and spectra normalized to maximum and in binding energy (right): no change of the spectral O2s features are visible, therefore no chemical reaction is assumed. Spectra were obtained by subtracting the pristine WO_3 valence band spectrum from the respective composite spectrum. (b) The O2s difference spectra (left) and spectra normalized to maximum and in binding energy (right) of the TiO_2/Spiro-MeOTAD interface experiment taken from Subsection 8.1.1 for comparison: the normalized O2s spectra show the same evolution of the deep valence band structure with increasing Spiro-MeOTAD thickness as the composites spectra with increasing Spiro-MeOTAD content. Therefore, a chemical reaction can be excluded. The spectra were obtained in the same way as for the Spiro-MeOTAD:WO_3 composites.

The O2s difference spectra (Figure 8.22) show no significant change in the curve shapes of the composites. The normalized O2s spectra of the TiO_2/Sp interface experiment (taken from Subsection 8.1.1) show the same evolution of the deep valence band structure with increasing Spiro-MeOTAD thickness as the normalized O2s spectra of the composites spectra with increasing Spiro-MeOTAD content. Therefore, a chemical reaction can be excluded. The shown spectra were obtained as follows: After the background subtraction of all valence band spectra shown in Figure 8.21, the WO_3 substrate spectrum was subtracted from the respective composite spectrum. Hereby, the intensity of the WO_3 signal was multiplied with

a factor in order to eliminate the W4f signal in the difference spectra. The WO_3 and Spiro-MeOTAD spectra are also shown in the left figure for comparison.

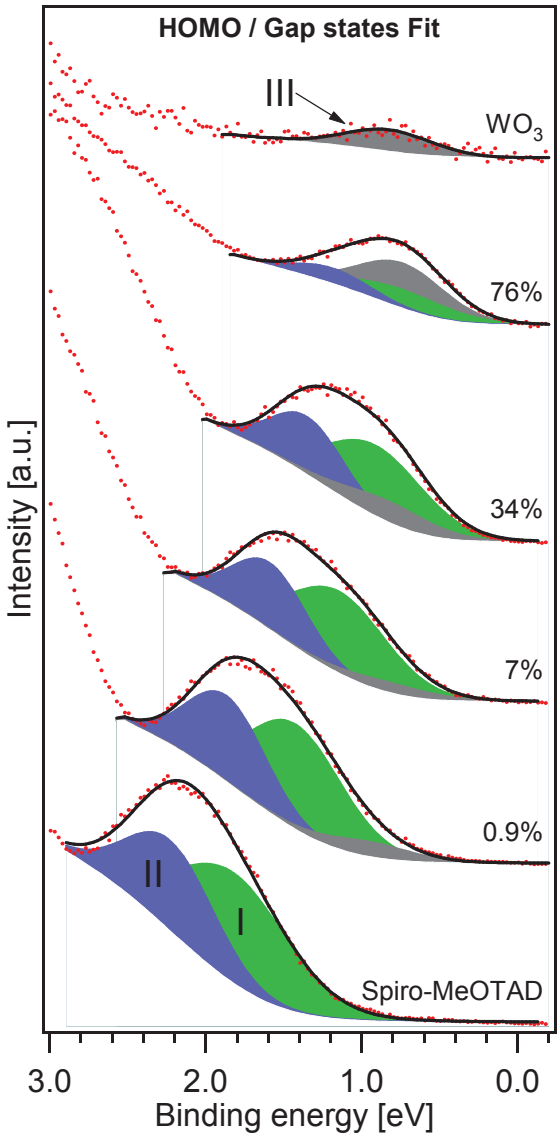

Figure 8.23.: The decomposition of the HOMO and gap-state emissions of Spiro-MeOTAD:WO_3 composites of the indicated composition into HOMO (I-green), HOMO-1 (II-blue), and WO_3 gap-states (gray). The binding energy of WO_3 gap-states was chosen assuming a fixed distance with respect to the W4f binding energy given in Figure 8.24. The intensity ratio and energy distance of HOMO and HOMO-1 were kept constant.

Figure 8.24 shows the Shirley background-subtracted W4f detail spectra of the composites and pristine WO_3. Fits were performed with a $W4f_{5/2}/W4f_{7/2}$ doublet splitting of 2.15 eV [204] and a fitted doublet intensity fraction $W4f_{5/2}/W4f_{7/2}$ of 0.65. The branching ratio can deviate from the statistical one (0.75) because of discrepancies in the photoexcitation cross section and the availability of final states for different photon energies, for example [203]. All W4f spectra show a component located approximately at 1.3 eV lower binding energies with respect to the W^{6+} emission, which is attributed to a reduced species in the formal W^{5+} oxidation state. In addition to the W4f emission, an emission from the W5p orbital appears at approximately ca. 42 eV. This emission was was fitted with two components: the 6+ and 5+ oxidation species, where the latter is shifted by ca. 1.3 eV, similarly to the W4f emission. The change of the $W4f^{5+}$ to $W4f^{6+}$ fraction and the Spiro-MeOTAD binding energy shift with increasing WO_3 content is

plotted in Figure 8.25. The ratio between the $W4f^{5+}$ and $W4f^{6+}$ components of WO_3 is constant (0.26) up to approximately 34% WO_3 content and decreases for higher contents. The HOMO shift increases strongly up to around 34% WO_3 content and saturates at 0.98 eV.

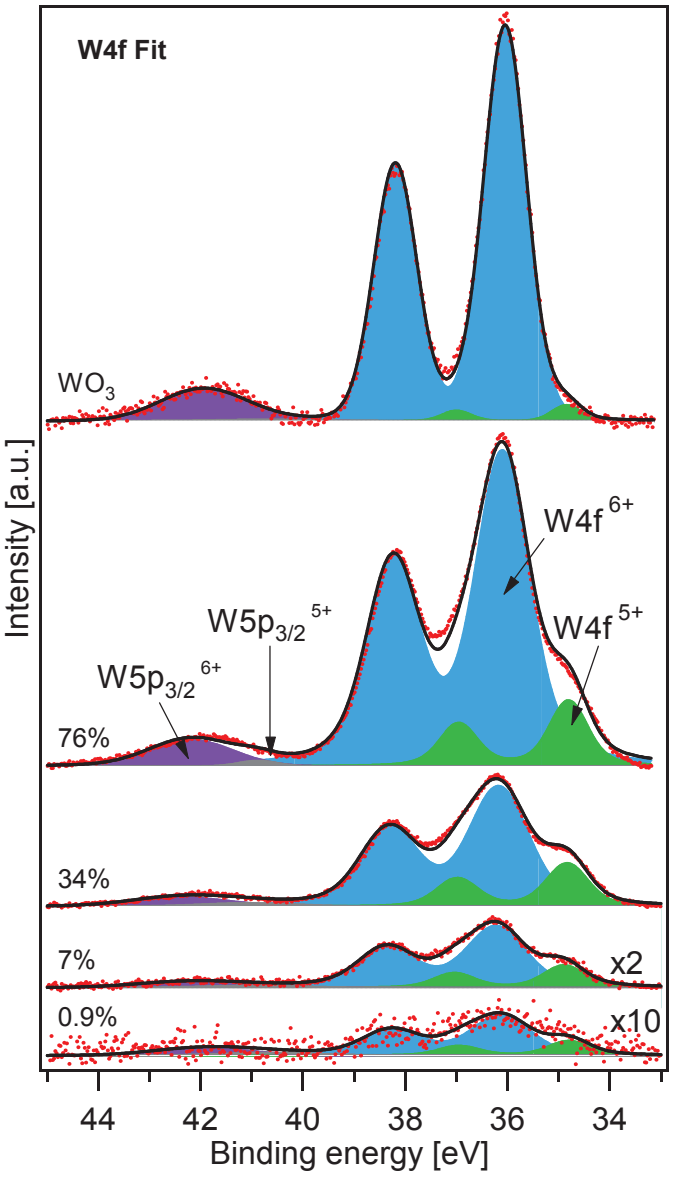

Figure 8.24: The W4f emission of Spiro:WO_3 composites with indicated WO_3 content and of pristine WO_3. Decomposition into $W4f^{6+}$ (blue), $W4f^{5+}$ (green), $W5p_{3/2}^{6+}$ (lilac), and $W5p_{3/2}^{5+}$ (gray) is indicated. The absolute intensity of the low binding energy component W^{5+} increases with the increasing WO_3 content. The W^{5+} intensity is very low for WO_3 on Spiro-MeOTAD (compare to Figure 8.17).

WO_3/Spiro-MeOTAD Interface

To investigate systematically the reduced W4f species in the codeposited films and its possible correlation to charge transfer indicated by the binding energy shift of the Spiro-MeOTAD emissions in the codeposited films, interface experiments were performed. Spiro-MeoTAD was in-situ-evaporated stepwise onto a dense and thick layer of WO_3 (25 nm) on a TiO_2 film. With increasing Spiro-MeOTAD thickness, the valence band spectra (Figure 8.26) show a shift of the HOMO of Spiro-MeOTAD of up to 1.12 eV to higher binding energies. The W4f, HOMO and gap-state emission features were fitted in the same way as described for the composites. The work function decreases from 6.2 eV to the value of pure Spiro-MeOTAD of 4.1 eV. The W4f emission is damped but not energetically shifted. The W4f emission of the pure WO_3 shows a small binding energy shoulder due to the oxidation of oxygen vacancies of the TiO_2 surface as described above. The relative intensity of the $W4f^{5+}$ position increases with increasing Spiro-MeOTAD thickness as evidenced in the Shirley background-subtracted detailed spectra normalized to $W4f^{6+}$ (Figure 8.27). Figure 8.28 plots the relative increase of the reduced W4f species along with

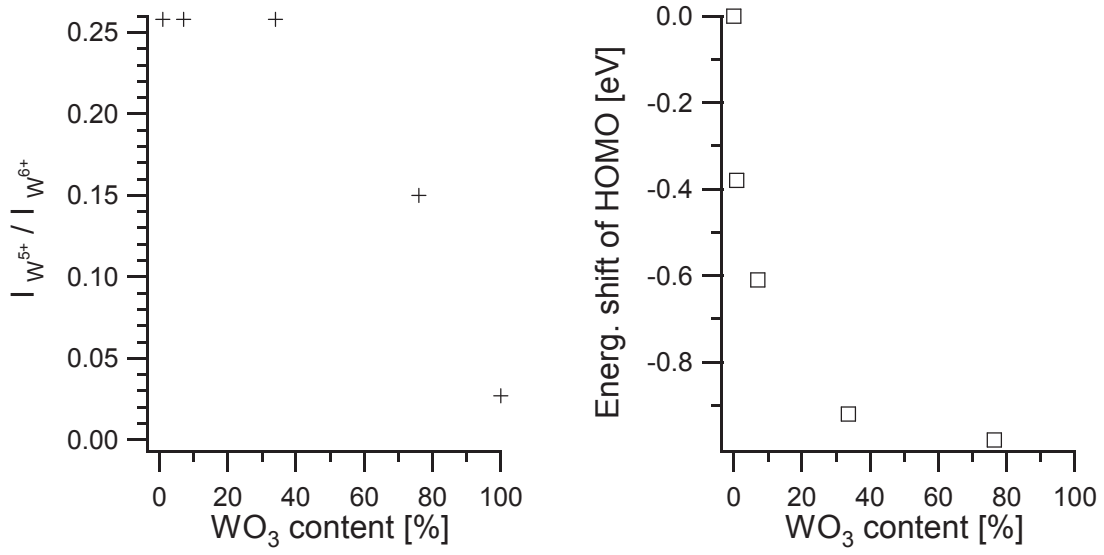

Figure 8.25.: The W^{5+}/W^{6+} emission intensity ratio and the shift of the Spiro-MeOTAD HOMO binding energy in Spiro-MeOTAD:WO_3 composites. While the absolute intensity of W^{5+} increases with WO_3 content, the relative intensity is constant in the first three steps and decreases after this. The HOMO energy shift due to p-doping is strong in the first three steps and levels then off.

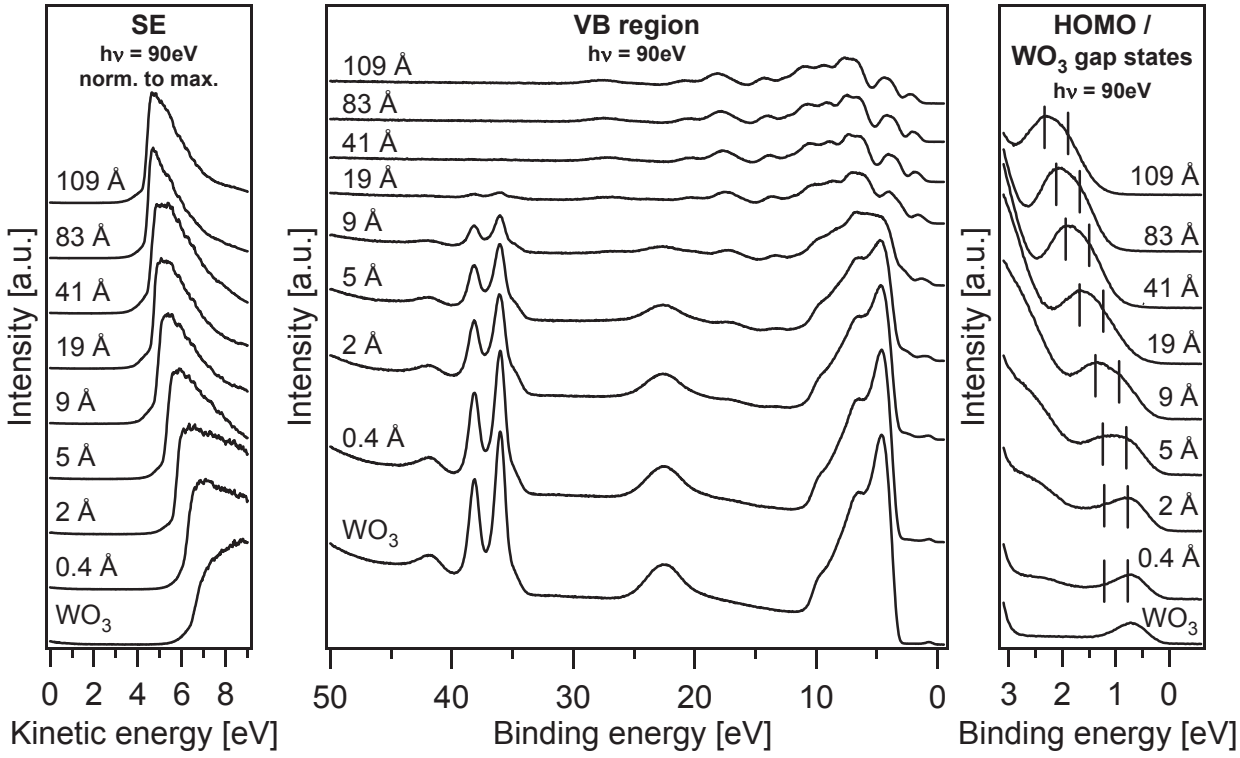

Figure 8.26.: The secondary electron emission edge, valence band and W4f core level spectra as well as the detailed HOMO/gap-state region of WO_3 (bottom-black) and the stepwise evaporated Spiro-MeOTAD (green) of indicated thickness. The work function decreases until it reaches the value of pure Spiro-MeOTAD at 4.1 eV. The WO_3 features are damped while Spiro-MeOTAD features grow in intensity. The energy positions of the two HOMO-state maxima are marked. An upward band bending toward the interface is evident, indicating electron transfer to WO_3. The spectra were recorded with a photon energy of 90 eV.

the binding energy shift of the HOMO with increasing Spiro-MeOTAD thickness. At the interface to the WO_3 substrate, a band bending of 1.12 eV is induced in Spiro-MeOTAD. The fact that no band bending is observed in the WO_3 film can be explained by Fermi level pinning to W5d gap-states. As the work function changes by ca. 2.1 eV, a dipole formation of 1.0 eV at the interface is indicated.

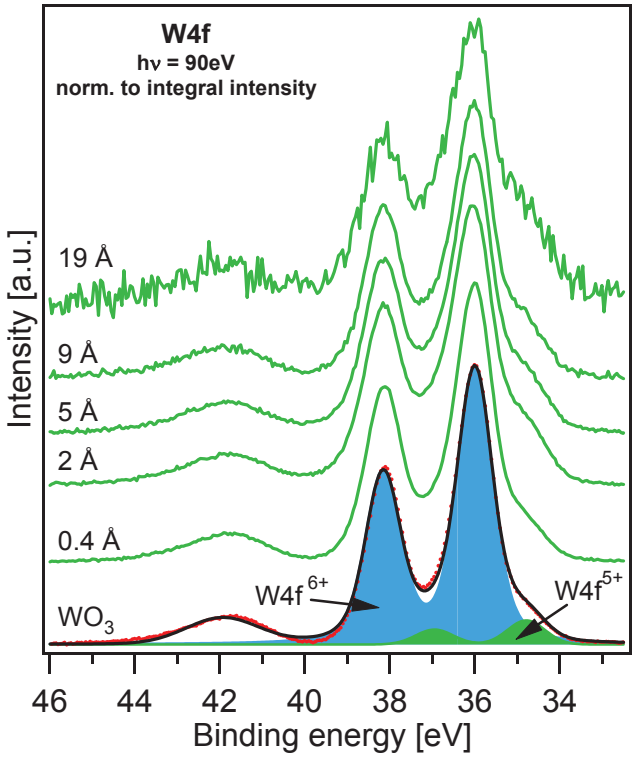

Figure 8.27.: The integral intensity-normalized W4f detailed spectra in the course of the Spiro-MeOTAD deposition (green) onto a WO_3 layer (bottom-black) on TiO_2. Because of the oxidation by defective TiO_2, $W4f^{5+}$ is present in the pristine WO_3 film (compare to Figure 8.17). The relative intensity of the low energy shoulder increases with growing Spiro-MeOTAD thickness. The spectra were recorded with 90 eV photon energy.

In parallel to the HOMO the C1s core level line displayed in Figure 8.31 shifts by 1.12 eV with a final binding energy position of the maximum at 285.25 eV. The shape of the core level line varies with increasing Spiro-MeOTAD thickness as evidenced in the background-subtracted C1s emissions displayed in Figure 8.31. For direct comparison of the line shape, the spectra were normalized in intensity and in binding energy. In the range from 284.5 to 286.5 eV a decrease of intensity with growing Spiro-MeOTAD thickness is observed. As indicated in Figure 8.14, this binding energy coincides with oxidized carbon species in the Spiro-MeOTAD molecule. Therefore, the increased relative intensity in the first Spiro-MeOTAD deposition steps could be interpreted as a chemical oxidation of Spiro-MeOTAD reacting with tungsten oxide. However, in general, at reactive organic or inorganic semiconductor heterojunctions band bending is not observed because of Fermi level pinning induced by interface states created by the reaction. This is explicitly shown by Prietsch et al. [205] for reactive p- and n-GaAs surfaces, which show a common Fermi-level position at the Na/GaAs interface and by Mayer et al. for Br_2 on n-InSe, which show band bending for nonreacted Br_2 on n-InSe and no band bending after a reaction was activated by synchrotron radiation [179]. Therefore, a chemical reaction is excluded and, tentatively, the increased relative C1s emission in the broad oxidized binding energy region at the interface is correlated to an intramolecularly localized hole charge resulting from electron transfer to WO_3 to form the strong interface dipole of 1.0 eV. The negative charge of the interface dipole together with the negative charge from the Spiro-MeOTAD space charge adds up to the W4f intensity assigned to reduced W^{5+}.

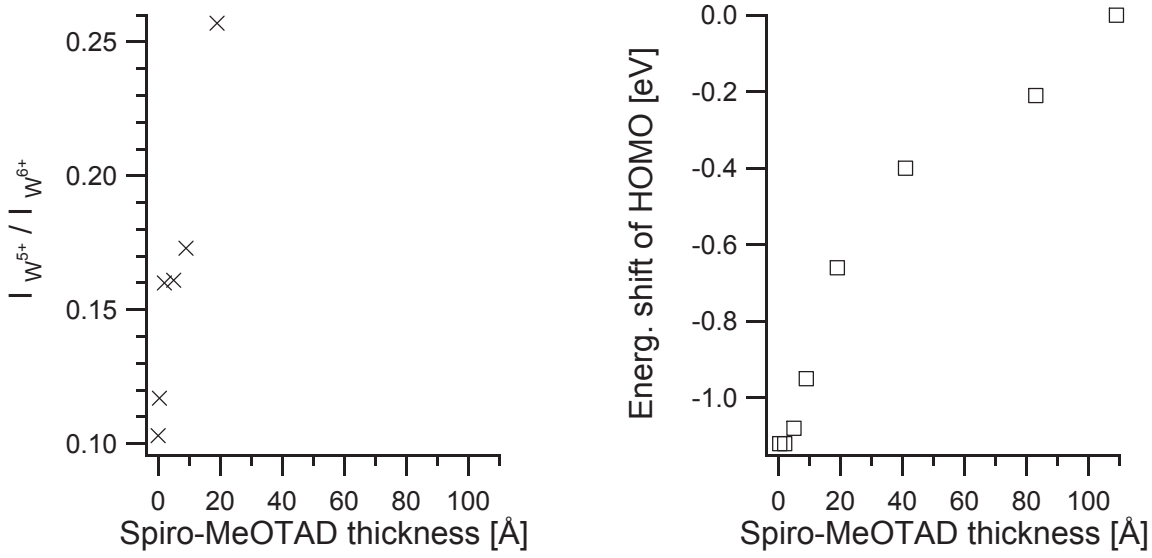

Figure 8.28.: The W^{5+}/W^{6+} intensity ratio in the W4f spectra and the shift of the Spiro-MeOTAD HOMO binding energy at the WO_3/Spiro-MeOTAD interfaces. The relative intensity of the low energy shoulder labeled as $W4f^{5+}$ in Figure 8.27 increases with increasing space charge. The HOMO energy shift corresponds to the electron transfer from Spiro-MeOTAD to WO_3.

The O2s difference spectra, which are attributed mainly to Spiro-MeOTAD, show no change of the emission (Figure 8.29). The difference spectra were obtained as described before (see Paragraph 8.2.1). The O2s spectra look very similar to the ones obtained for the composites (see Figure 8.22). In parallel, a chemical reaction at the interface can be excluded. The electronic potentials of the WO_3/Spiro-MeOTAD contact are summarized in the interface band diagram sketched in Figure 8.30.

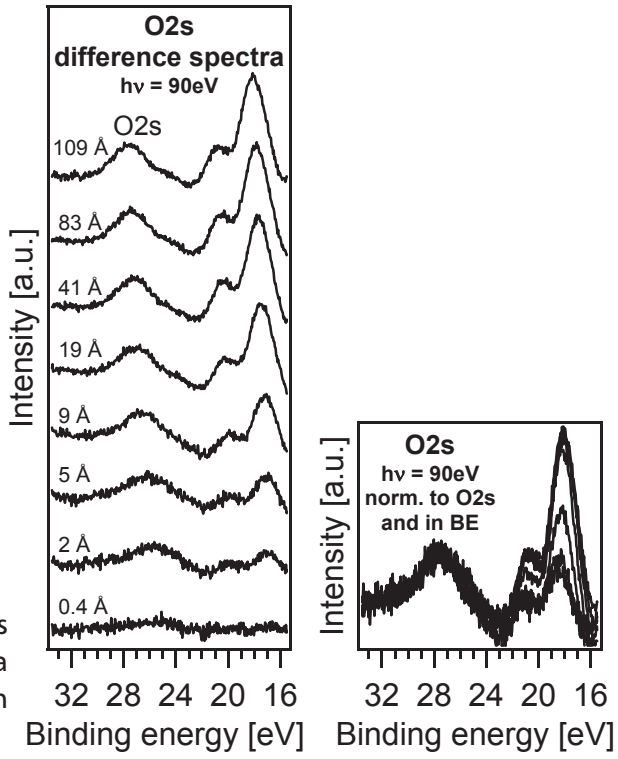

Figure 8.29: The comparison of the O2s emission spectra: Difference spectra show no evidence of a chemical reaction at the interface.

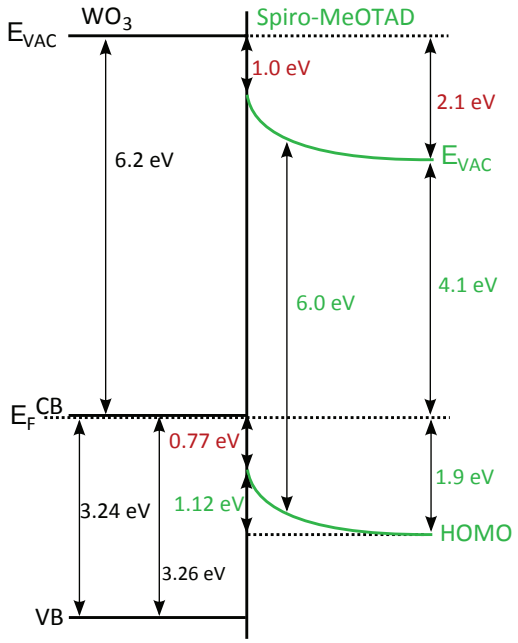

Figure 8.30: The band diagram of the WO_3/Spiro-MeOTAD interface as formed for PVD of Spiro-MeOTAD onto a WO_3 film on TiO_2. The difference between the measured work function change of 2.1 eV and the measured band bending of 1.12 eV in Spiro-MeOTAD is assigned to an interface dipole of 1.0 eV. The HOMO binding energy values refer to the photoemission maximum position.

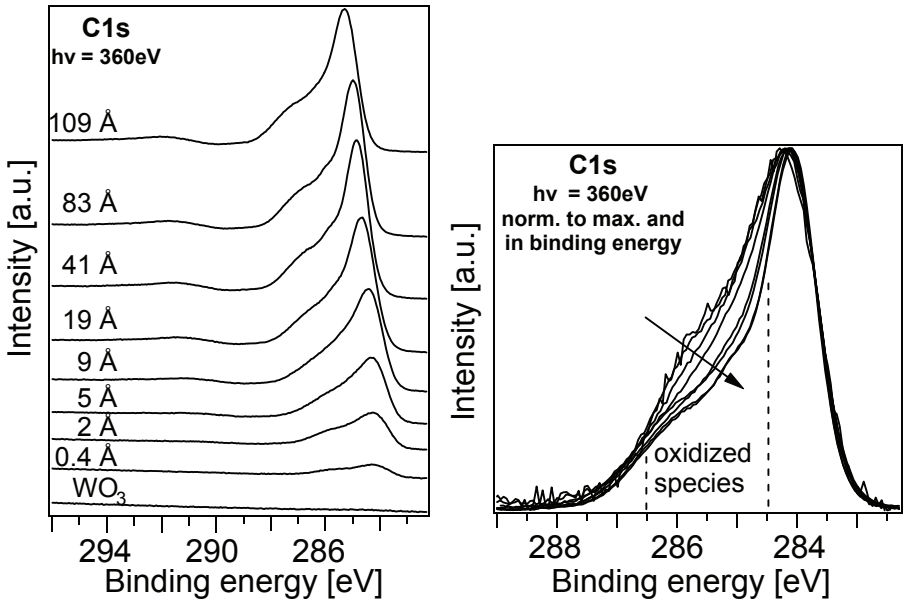

Figure 8.31.: The C1s core level spectra of the stepwise evaporated Spiro-MeOTAD on WO_3 (left) and the normalized spectra (right): The C1s emission shifts (in parallel to the HOMO, see Figure 8.26) to higher binding energy positions, indicating a band bending at the WO_3/Spiro-MeOTAD interface. Toward the interface, the emission in the range of the oxidized C species (compare to Figure 8.14) is increased and decreases with growing Spiro-MeOTAD thickness. The spectra were recorded with a photon energy of 360 eV.

C1s - doping model: In the model the first layer of molecules is assumed to form the interface dipole, which is supported by the difference spectra shown in Figure 8.32. The first evaporation step is interpreted to consist only of charged molecules, which form the interface dipole. Therefore, this spectrum, drawn in red in the figures, was subtracted from the other spectra of the interface experiment with decreasing relative intensity while keeping the binding energy constant. The resulting difference spectra, drawn in blue and illustrated in a normalized form in Figure 8.33 on the left, show the same shape but energetically shifted emissions. Therefore, those spectra are assumed to show the actual band bending due to charge transfer.
As the two branches of Spiro-MeOTAD are energetically decoupled, which was explained in Section 3.3, it can be assumed that only the branch which is in direct contact to the WO_3 forms the interface dipole. This assumption can be confirmed by the difference spectrum. Hereby, the spectrum of Spiro-MeOTAD with the highest thickness is subtracted from the spectrum of the first evaporation step (labeled as 0.4 Å). The resulting curve, drawn in green in Figure 8.33 on the right, can be interpreted as a modification of the blue curve (spectrum 109 Å). The C-C bonds located at lower binding energies are shifted to higher binding energies within the curve due to positive charge caused by the formation of the interface dipole.

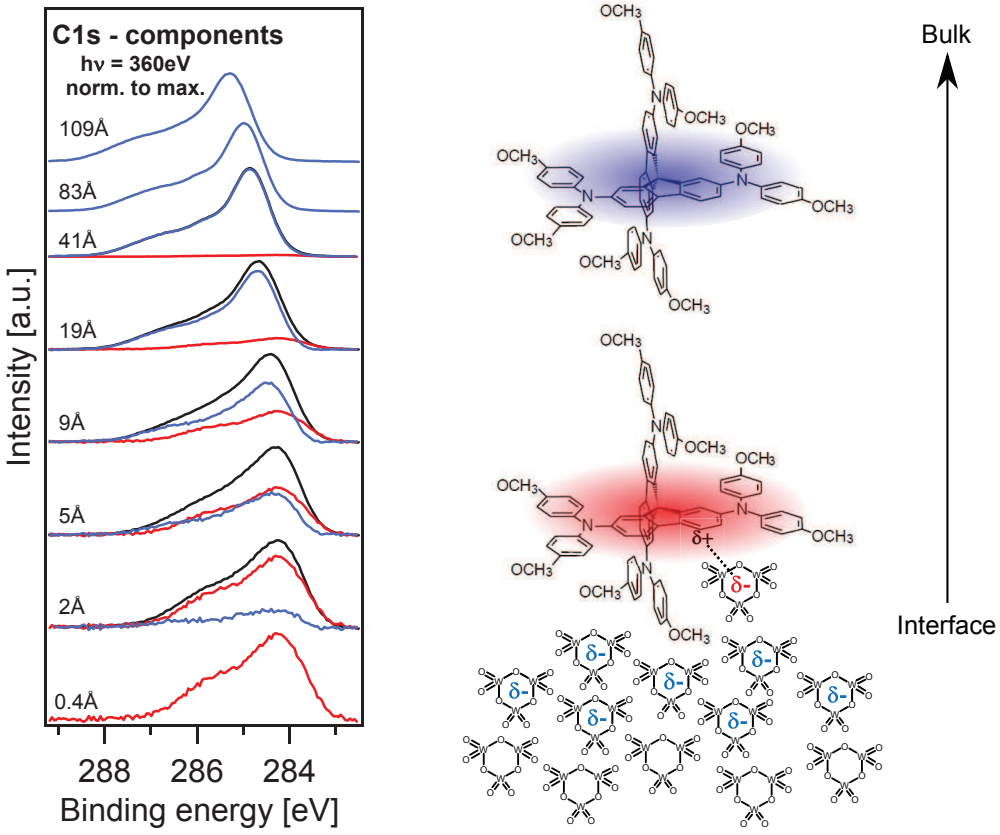

Figure 8.32.: The normalized C1s spectra and the difference spectra with its components: measured spectra (black), difference spectra (blue) and subtracted spectrum (red), which is the first Spiro-MeOTAD deposition step (0.4 Å) and is assumed to represent the molecules forming the interface dipole. In the graph, WO_3 is assumed to be built up of W_3O_9 clusters at the interface.

Spiro-MeOTAD/WO_3 Interface

For the application of WO_3 as a hole injection layer, the Spiro-MeOTAD/WO_3 interface band diagram is also measured by a stepwise WO_3 deposition onto a Spiro-MeOTAD film. As these experiments were performed at the beamline TGM7 with a maximal photon energy of 120 eV, the C1s core level could not

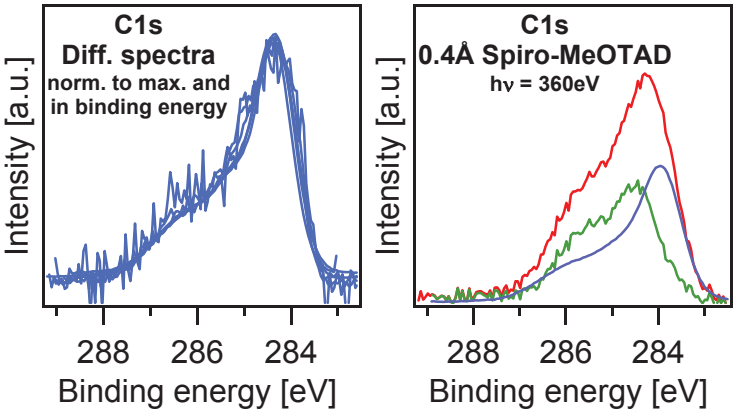

Figure 8.33: The normalized and in binding energy shifted difference spectra from Figure 8.32 (left) and the components of the subtracted spectrum (labeled as 0.4 Å Spiro-MeOTAD, right). The curve shape of the difference spectra is the same for all deposition steps. The difference spectra represent the molecules of the Spiro-MeOTAD layer that do not contribute to the dipole. The subtracted spectrum consists of two parts which can be assigned to the two branches of Spiro-MeOTAD.

be measured. Following the HOMO position of Spiro-MeOTAD in the first WO_3 deposition steps and the W4f position later on, a band bending of up to 1.17 eV was measured (Figures 8.34,8.35 and 8.36).

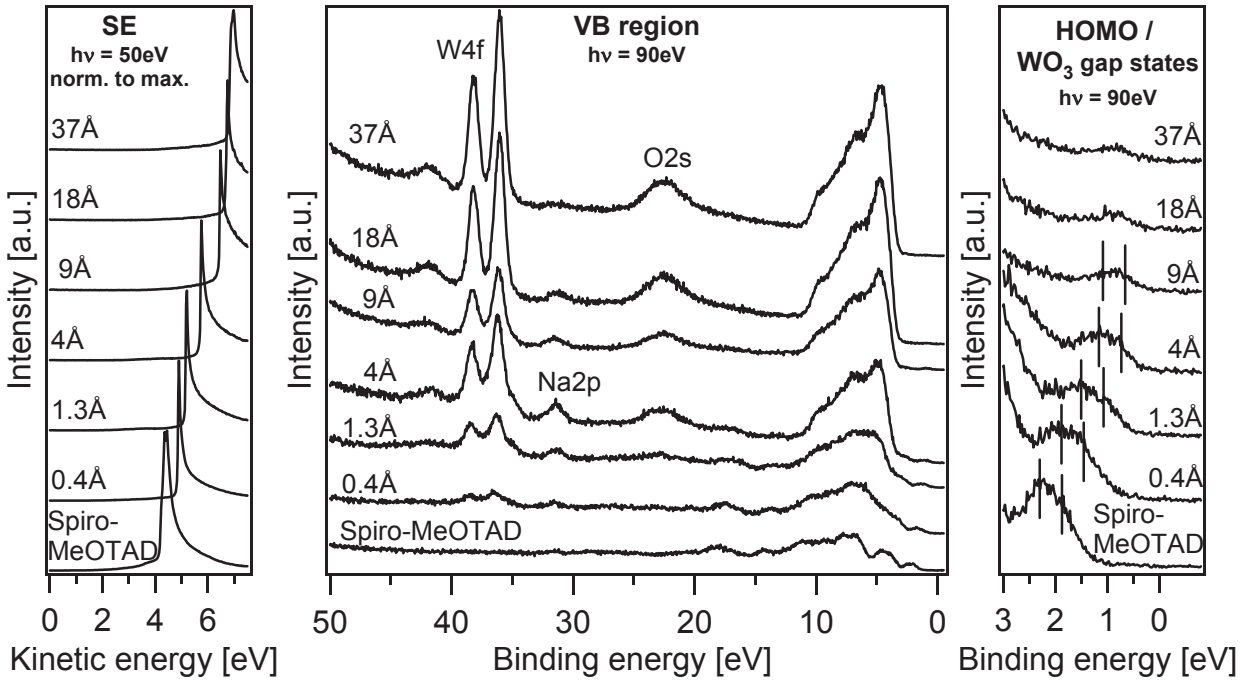

Figure 8.34.: The secondary electron emission edge, valence band and W4f core level spectra as well as the detailed HOMO/gap-state region of Spiro-MeOTAD (bottom) and the stepwise evaporated WO_3 of indicated thickness. The work function changes from 4.1 eV of Spiro-MeOTAD to 6.8 eV of WO_3. With growing WO_3 thickness, the Spiro-MeOTAD features are damped and the WO_3 features grow in intensity. The marked HOMO and HOMO-1 emission maxima of Spiro-MeOTAD shift to lower binding energy indicating induced band bending up toward the interface. In the two topmost spectra, the Spiro-MeOTAD HOMO emission is completely damped and the emission corresponds to W^{5+}. Valence band spectra were taken with a photon energy of 90 eV and secondary edge measurements with a photon energy of 50 eV.

As in the reversed experiment described above Fermi level pinning in WO_3 is assumed and the shifts are assigned to a band bending in Spiro-MeOTAD. The total W4f shift, after extrapolation to 0 Å (shown in Figure 8.35), is equal to that of the Spiro-MeOTAD HOMO. Hereby, the W4f core level follows the shift of the Spiro-MeOTAD substrate. At the interface, also a reduced $W4f^{5+}$ component is observed

that disappears with WO_3 thickness, which becomes evident in the Shirley background-subtracted W4f spectra (Figure 8.35). In the first deposition step, the W^{5+}/W^{6+} ratio is 0.29. An additional emission line appearing at 31.5 eV is attributed to sodium which is part of the precursor used to prepare the TiO_2 substrate material. In Section 7.2 and in literature the diffusion of Na to the TiO_2 surface by thermal activation was shown [112, 206]. Therefore, Na is assumed to originate from the TiO_2 substrate and diffuses through Spiro-MeOTAD activated by the heat of the WO_3 source (1100 °C).
The electronic structure of the Spiro-MeOTAD/WO_3 interface is summarized in Figure 8.37. The work function changes from 4.1 of the Spiro-MeOTAD surface to 6.8 eV after WO_3 deposition. A 1.17 eV portion of the work function difference (2.7 eV) is supplied by the band bending in the space charge region in Spiro-MeOTAD. The remaining 1.5 eV is assigned to an interface dipole.

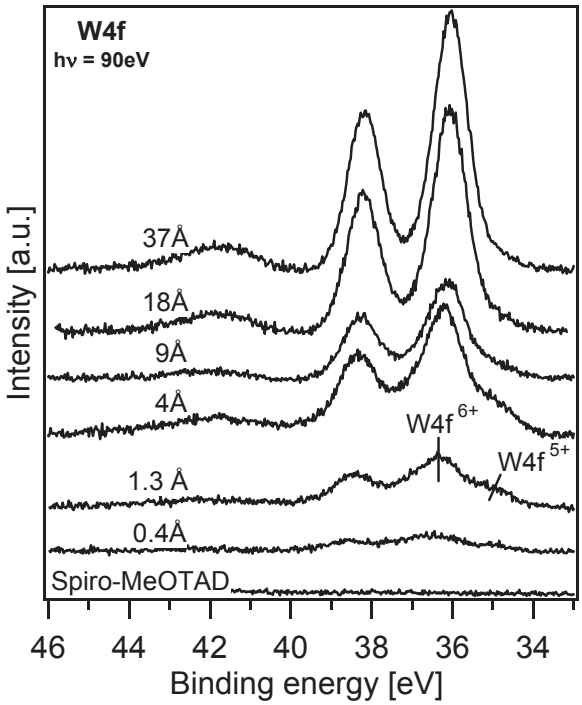

Figure 8.35: The W4f detailed measurements of Spiro-MeOTAD/WO_3 interfaces with the indicated formal WO_3 thickness. The decrease in the relative intensity of the low energy component is evident. The W4f emissions follow the shift of the Spiro-MeOTAD substrate. The spectra were recorded with a photon energy of 90 eV.

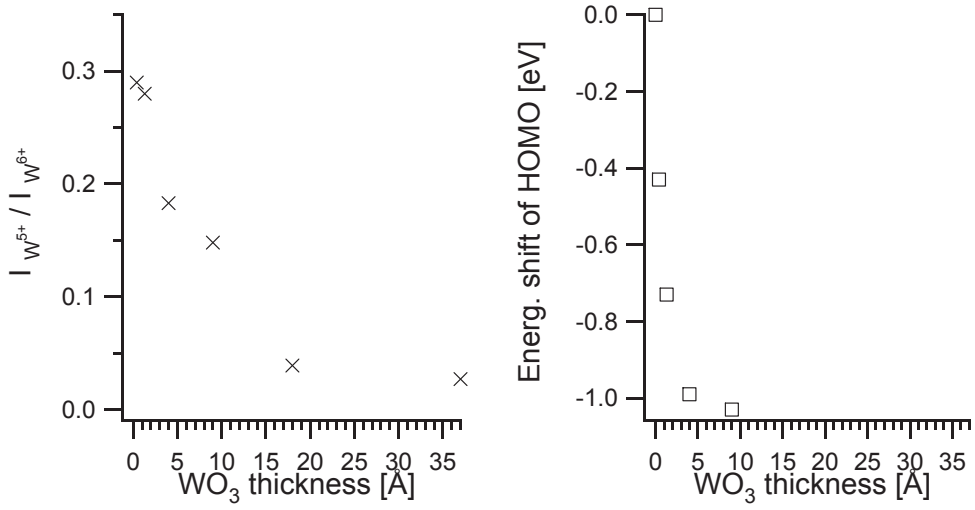

Figure 8.36.: The W^{5+}/W^{6+} intensity ratio in W4f spectra and shift of Spiro-MeOTAD HOMO binding energy at Spiro-MeOTAD/WO_3 interfaces with increasing formal WO_3 thickness. The relative intensity of the low energy shoulder labeled $W4f^{5+}$ increases along with increasing space charge in Spiro-MeOTAD. The HOMO energy shift corresponds to an electron transfer from Spiro-MeOTAD to WO_3.

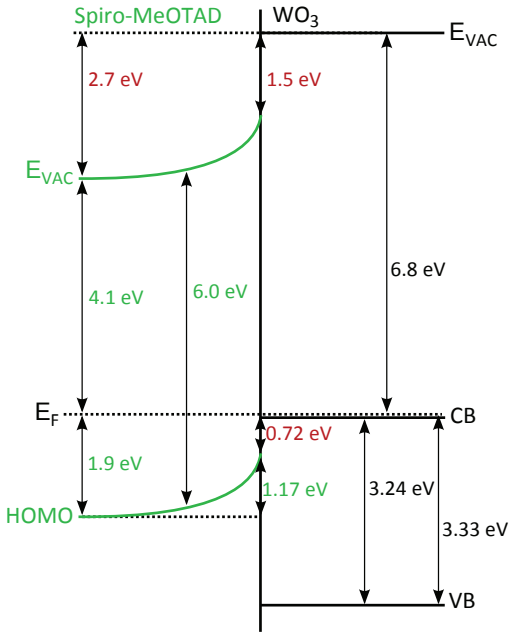

Figure 8.37: The band diagram of the Spiro-MeOTAD/WO_3 interface as formed for PVD of WO_3 onto a film of Spiro-MeOTAD. The difference of the measured work function change of 2.7 eV and the measured band bending of 1.17 eV in Spiro-MeOTAD is assigned to an interface dipole of 1.5 eV. The line up of the Spiro-MeOTAD HOMO maximum with the WO_3 conduction band is 0.72 eV, very similar to the 0.77 eV measured in the reverse deposition sequence (8.30).

Discussion

In the vacuum level alignment of the pristine materials, the Spiro-MeOTAD HOMO maximum is found ca. 0.8 eV above the conduction band minimum of almost defect-free WO_3 and ca. 0.1 eV above the conduction band minimum of oxygen-defective WO_3 that was reduced by oxygen-defective TiO_2. At the experimental WO_3/Spiro-MeOTAD and Spiro-MeOTAD/WO_3 contacts, the HOMO is found 0.77 and 0.72 eV below the WO_3 conduction band, respectively, and band bending due to positive space charge in Spiro-MeOTAD of 1.12 and 1.17 eV is induced. Thus, the line up and band bending of the two deposition sequences seem to be independent of the initial and final work function of WO_3 of 6.2 and 6.8 eV, respectively. The shift of the Spiro-MeOTAD HOMO below the WO_3 conduction band is caused by the formation of interface dipoles of 1.0 and 1.5 eV which compensates the different WO_3 work functions. The doping limit in the Spiro-MeOTAD:WO_3 composites is similar to the band bending values measured at the interfaces. Therefore in precipitation of WO_3, a similar band lineup and charge transfer are assumed at internal interfaces as measured in the bilayer experiments in accordance with the internal interface charge transfer model (see Subsection 3.4.2).

In the composites and at the interfaces an increased emission of a low binding energy W4f component in WO_3 labeled with the formal oxidation state W^{5+} is found. The maximum W^{5+} to W^{6+} ratios obtained for the Spiro-MeOTAD/WO_3 (0.29) and the WO_3/Spiro-MeOTAD (0.26) interface experiments are in good agreement with the ratios (0.26) obtained for the composites with a WO_3 content of 34% and below. Thus, the $W4f^{5+}$ component is assumed to correlate to the electrons transferred fom Spiro-MeOTAD to WO_3 corresponding to the space charge in Spiro-MeOTAD and the dipole at the Spiro-MeOTAD/WO_3 interfaces. In the WO_3/Spiro-MeOTAD case performed at the undulator beamline U49-PGM-2, the C1s orbital could also be measured. An increased emission in the binding energy range corresponding to oxidized carbon species was measured. No such additional C1s emission has been observed for Spiro-MeOTAD deposited onto TiO_2 (see Figure 8.3), where the interface dipole is small (0.24 eV). As previously discussed in this subsection, no band bending at reactive semiconductor heterojunctions can be observed because of the formation of defect states in the semiconductor energy gap. In addition, the difference spectra (Figure 8.38) of the O2s emissions, located at ca. 27.9 eV binding energy, show the same line shape and very similar curve shapes of the O2s spectra as well as very similar evolution of the deep valence band states. Thus, no hint of a chemical reaction, neither for the composites nor for the WO_3/Spiro-MeOTAD interface can be found. The difference spectra were obtained by subtracting the

pristine WO_3 and TiO_2 spectra from the respective spectra. Therefore, a chemical oxidation reaction with transfer of O-bonds from WO_3 to carbon in the Spiro-MeOTAD molecule can be excluded. The additional C1s emission at the interface is correlated to the positive charge of the interface dipole. This charge is assumed to be localized on parts of the Spiro-MeOTAD molecules that are closest to WO_3, giving rise to an increased relative emission in the oxidized C1s binding energy region.

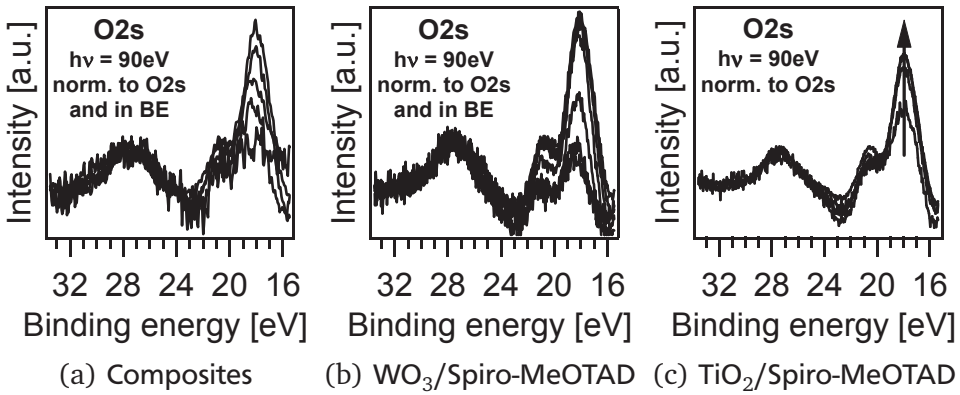

(a) Composites (b) WO_3/Spiro-MeOTAD (c) TiO_2/Spiro-MeOTAD

Figure 8.38.: The normalized and in binding energy shifted O2s spectra of the Spiro-MeOTAD:WO_3, the WO_3/Spiro-MeOTAD interface and the TiO_2/Spiro-MeOTAD interface for comparison (taken from Subsection 8.1.1): all spectra show no change of the shape and very similar curve shapes of the O2s emissions as well as very similar evolution of the deep valence band states.

In a simplified model, WO_3 is supposed to consist of W_3O_9 clusters, the smallest species that can be considered as a molecular model for bulk WO_3 from an electronic structure and chemical point of view. The transferred integer electron charge is shared between three W atoms that form the HOMO of negatively charged $W_30_9^-$ clusters [127], leading to a partial charge, which corresponds to the W species in the formal oxidation state 5+ induced by the charge transfer. Assuming the charged clusters to be homogenously distributed among neutral clusters, the number of transferred integer charges per square centimeter (Q) of each deposition step in the Spiro-MeOTAD/WO_3 bilayer experiments is given as

$$Q = 1/3 \cdot \frac{\varphi \cdot d}{V_{mol}}. \tag{8.2}$$

where d is the formal WO_3 thickness, φ the respective $W4f^{5+}$ to $W4f^{6+}$ ratio, and V_{mol} the molar volume of WO_3. The factor 1/3 stems from the above given argument that W_3O_9 clusters may have one integer electron charge. The areal charge density is highest ($6.63/3{\cdot}10^{13}$ 1/cm^2) for a formal WO_3 thickness of 9 Å, which roughly corresponds to the W_3O_9 cluster size (Figure 8.39) [127].

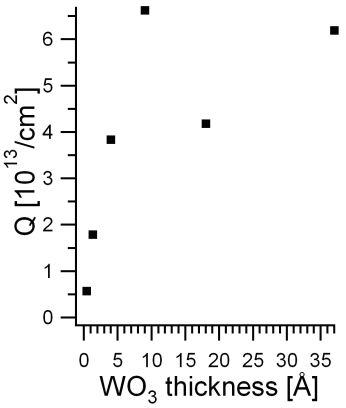

Figure 8.39: Calculated areal density of charges in WO_3 at the Spiro-MeOTAD/WO_3 interface with increasing formal WO_3 thickness.

Composites

Assuming that the energy gap of WO_3 and the energetic distance between the WO_3 gap-states and the W4f core level emission are constant, energetic alignments of WO_3 to Spiro-MeOTAD for each composite can be deduced from the measurements (Figure 8.40). In order to obtain the position of the WO_3 valence band maximum and gap-state position in each composite, the respective shift of the W4f emission is added to the pristine WO_3 valence band maximum and gap-state position. The Spiro-MeOTAD HOMO positions are taken from the fits shown in Figure 8.23.

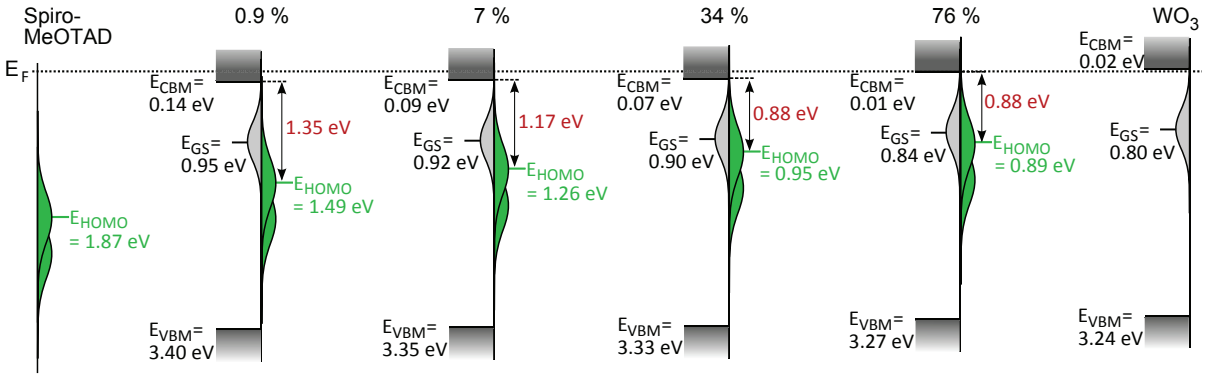

Figure 8.40.: The energetic Spiro-MeOTAD HOMO and WO_3 gap-state positions of pristine Spiro-MeOTAD, the Spiro-MeOTAD:WO_3 composites (the composites are labeled according to the WO_3 content) and pristine WO_3 deduced from the SXPS measurements.

Starting from the pristine Spiro-MeOTAD, the HOMO of Spiro-MeOTAD moves with increasing WO_3 content towards the gap-state position of the WO_3 dopant until both are overlapping and thus hinders further doping of Spiro-MeOTAD. This is the case for the composite with 76% WO_3 content. At the same time, the gap-state position and the valence band maximum move slightly towards the Fermi level (0.15 eV).

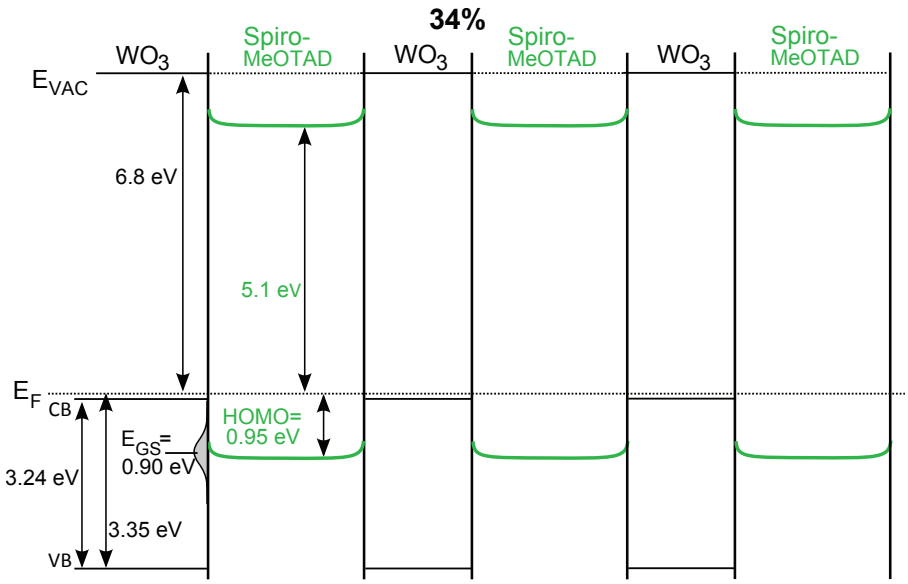

Figure 8.41.: The simplified band diagram of the Spiro-MeOTAD:WO_3 composite with a WO_3 content of 34%: the diagram is drawn as an alternating sequence of WO_3/Spiro-MeOTAD and Spiro-MeOTAD/WO_3 interfaces to show the WO_3 precipitates within the organic matrix. The values are taken from the respective composite measurement.

According to the proposed doping model (see Subsection 3.4.2), the organic matrix is filled with WO_3 precipitates, which are approximately 5 nm in size [135]. Therefore, the simplified band diagram of the Spiro-MeOTAD:WO_3 composites can be drawn as an alternating sequence of WO_3/Spiro-MeOTAD and Spiro-MeOTAD/WO_3 interfaces, as it is done for the composite with 34% WO_3 content in Figure 8.41. Hereby, as verified in the interface experiments, flat band potentials are observed in the WO_3 phase.

8.2.2 Li-TFSI dopant

Experimental

The drop-casted films of Spiro-MeOTAD:Li-TFSI composites were prepared from different blends of Spiro-MeOTAD dissolved in chloromethane (anhydrous, 99.8%) and Li-TFSI dissolved in cyclohexanone (>99%). The blends consisted of 950 μl of 0.17 M (0.21 g/ml) Spiro-MeOTAD and 50 μl of 0.6 and 1.2 M (0.18 and 0.36 g/ml) Li-TFSI solutions, which are referred to as "0.6 M" and "1.2 M" in the following, respectively. Drop-casting was performed in the glass cell of the SoLIAS (see Section 4.1) which is directly attached to the UHV-system and rinsed with pure argon (5.0). This allows the transfering of the samples to vacuum without contact to ambient air. Dense TiO_2 blocking layers on top of FTO films obtained from BASF were used as substrates. Spiro-MeOTAD (>99%) was purchased from Lumtec and the Li-TFSI powder (≥ 99.0%) from Sigma Aldrich.

Results

Pristine Li-TFSI and Spiro-MeOTAD:Li-TFSI composites with different contents of Li-TFSI were investigated at the U49/2-PGM-2 beamline to study the doping dependence on the relative amount of Li-TFSI dopants.

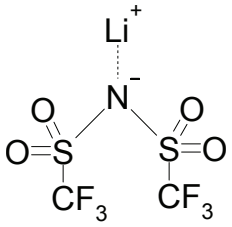

Figure 8.42: The structural formula of the lithium bis(trifluoromethylsulfonyl) amine lithium salt (Li-TFSI).

Survey

Each of the survey spectra of the Spiro-MeOTAD:Li-TFSI composites and the Li-TFSI drop-casted film, measured at 900 eV photon energy, (Figure 8.43) shows F1s, O1s, N1s, C1s and S2p emissions as expected from the structural formula (Figure 8.42). From the absence of the Ti2p substrate emission lines, dense layers of the composites are concluded. Lithium is not detected because the amount of lithium and the cross section of the Li1s emission at a photon energy of 900 eV ($0.8{\cdot}10^{-3}$ Mb[157]) are too low.

Core levels

The detailed spectra of the individual core levels are shown in Figure 8.44. The F1s emission measured at 900 eV photon energy, S2p at 210 eV and Li1s at 106 eV can directly be attributed to the Li-TFSI salt, whereas the C1s emission measured at 360 eV photon energy, O1s emission measured at 360 eV photon energy and N1s measured at 450 eV consist of emissions originating from both materials. In the case of the C1s emission, the features of both materials are precisely distinguishable. The feature at approximately 284.3 eV ($C1s_{Spiro}$) is assigned to Spiro-MeOTAD similar to the C1s emission shown in Subsection 8.1.3, whereas the feature at approximately 292.9 eV ($C1s_{Li-TFSI}$) belongs to the counterion of the dopant, which is only detected for films containing Li-TFSI and pristine Li-TFSI. Compared to

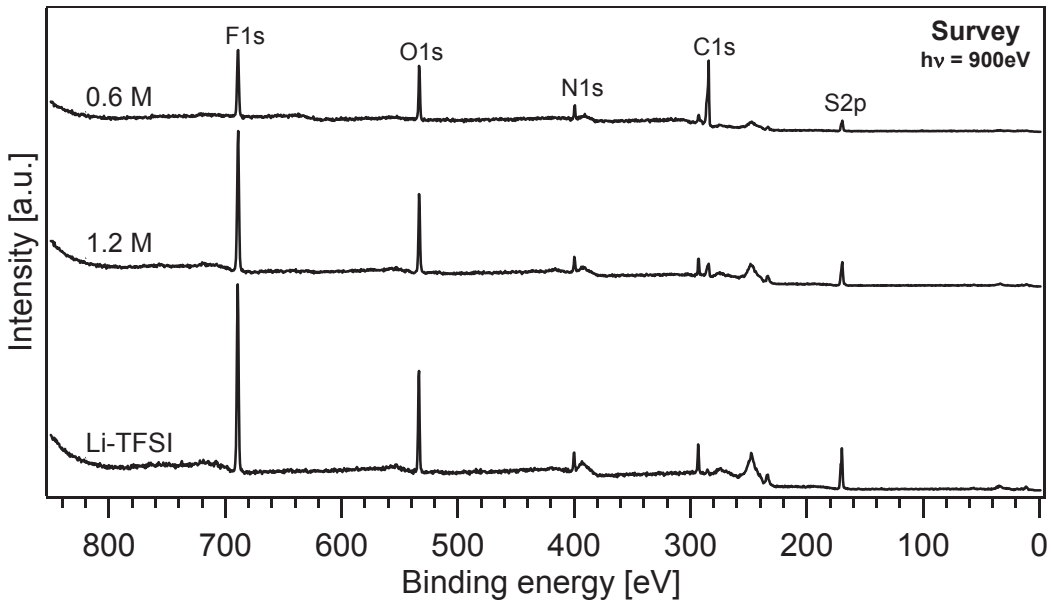

Figure 8.43.: The survey measurements of (from the buttom up) Li-TFSI, Spiro-MeOTAD:Li-TFSI (prepared with a 1.2 M Li-TFSI solution) and Spiro-MeOTAD:Li-TFSI (prepared with a 0.6 M Li-TFSI solution): O1s, N1s and C1s emissions consist of both Spiro-MeOTAD and Li-TFSI emissions, whereas the F1s and S2p emissions can be attributed solely to Li-TFSI. Spectra were recorded with a photon energy of 900 eV.

the position of pristine Spiro-MeOTAD, the $C1s_{Spiro}$ binding energy positions of the 0.6M and the 1.2M composite shift 1.06 and 1.00 eV to higher binding energies, respectively. Compared to the position of pristine Li-TFSI the $C1s_{Li-TFSI}$ binding energy positions of the 0.6M and the 1.2M composite shift 0.40 and 0.31 eV to lower binding energies, respectively. Also the S2p and F1s emissions of the counterion shift in the same way to lower binding energies. The shifts of the S2p emission are 0.43 eV for the 0.6M composite and 0.27 eV for the 1.2M composite and the shifts of the F1s emission are 0.76 eV for the 0.6M composite and 0.72 eV for the 1.2M composite, respectively. The shifts of the Li1s emission of the 0.6M and the 1.2M composite are 0.59 and 0.45 eV, respectively. In the O1s and N1s spectra, the features of both materials are overlapping and, therefore, are neglected here for further evaluation. Detailed binding energy values of the C1s, Li1s and S2p core levels are listed in Table 8.5.

Table 8.5.: The detailed comparison of the core level binding energy positions of Spiro-MeOTAD, Spiro-MeOTAD:Li-TFSI prepared with a 0.6 M Li-TFSI solution, Spiro-MeOTAD:Li-TFSI prepared with a 1.2 M Li-TFSI solution and Li-TFSI: The positions are the maxima of the respective emissions which were fitted by a Gaussian curve. For better comparison the values are listed up to the second decimal place.

	$C1s_{Spiro}$ 360 eV	$C1s_{Li-TFSI}$ 360 eV	Li1s 106 eV	S2p 210 eV	F1s 900 eV
Spiro-MeOTAD	285.32 eV				
0.6M	284.26 eV	292.87 eV	56.19 eV	169.30 eV	688.97 eV
1.2M	284.32 eV	292.96 eV	56.33 eV	169.46 eV	688.93 eV
Li-TFSI		293.27 eV	56.78 eV	169.73 eV	689.21 eV

Li1s, S2p and F1s emissions

In Figure 8.45, the Li1s, S2p and F1s spectra of Li-TFSI and the two composites which can be attributed solely to Li-TFSI are normalized to their maximum intensity and additionally in binding energy for direct comparison. In contrast to the Li1s emission of Li-TFSI which shows only one emission, the normalized

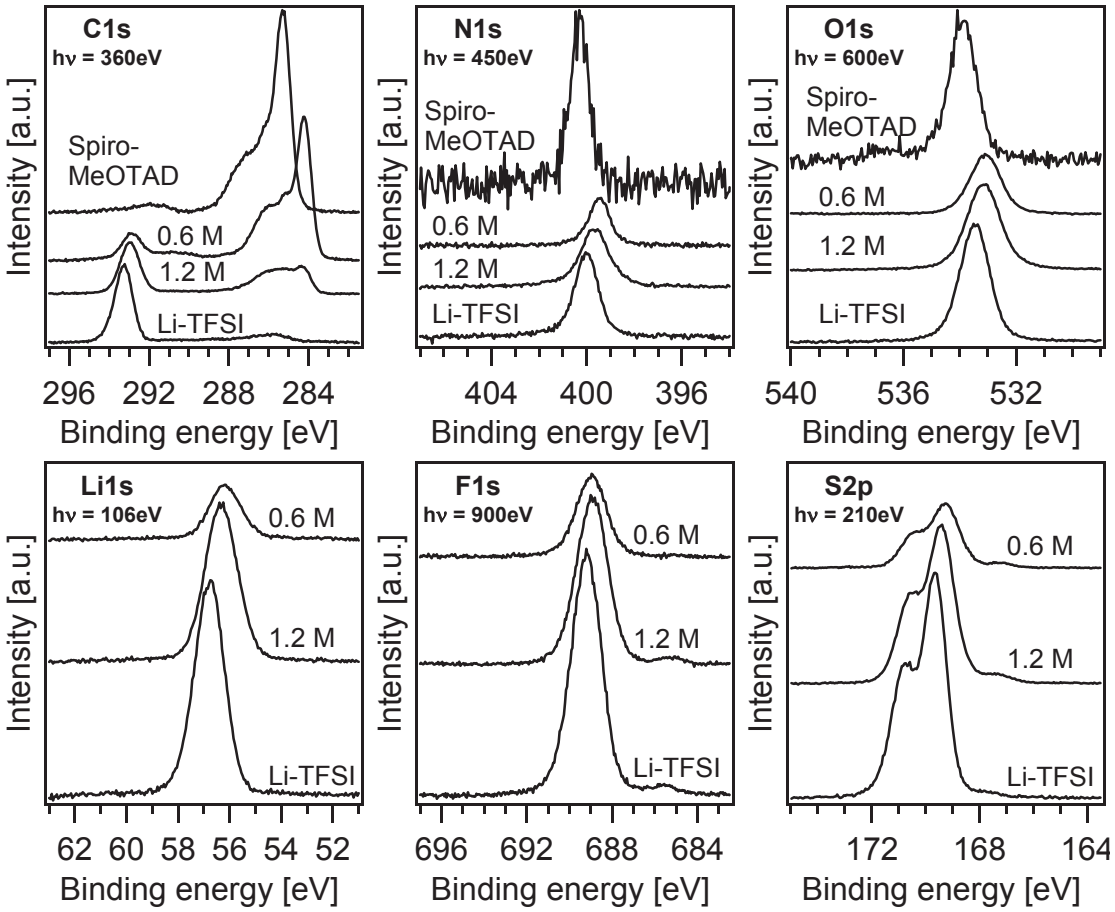

Figure 8.44.: The C1s, N1s, O1s, Li1s, F1s and S2p core level spectra of (from the bottom up) Li-TFSI, Spiro-MeOTAD:Li-TFSI prepared with a 1.2 M Li-TFSI solution, Spiro-MeOTAD:Li-TFSI prepared with a 0.6 M Li-TFSI solution and pristine Spiro-MeOTAD: Li1s, F1s and S2p belong solely to the Li:TFSI salt, whereas the C1s, N1s and O1s emissions consist of both Li:TFSI and Spiro-MeOTAD. C1s spectra were recorded at a photon energy of 360 eV, N1s at 450 eV, O1s and F1s at 900 eV, Li1s at 106 eV and S2p at 210 eV.

Li1s spectra of the composites show a small shoulder at lower binding energies. Hereby, the main emission at ca. 57 eV is assigned to oxidized Li-TFSI$^+$ as a product of the charge transfer between Spiro-MeOTAD and Li-TFSI and the second emission at ca. 56 eV to neutral Li-TFSI. The energetic position of the neutral Li-TFSI fits well with Li bound in LiF which is similar to Li-TFSI [152]. In the fitting procedure, the distance between the main emission and the shoulder was kept constant at 0.65 eV and the intensity ratio, as well as the binding energy position of the main oxidized Li-TFSI$^+$ emission were varied.
Both, the normalized S2p and F1s emissions, show a small shoulder at lower binding energies. Again, the main emission is attributed to the oxidized part of Li-TFSI which forms due to the electron transfer from Spiro-MeOTAD to Li-TFSI and the shoulder to neutral Li-TFSI.

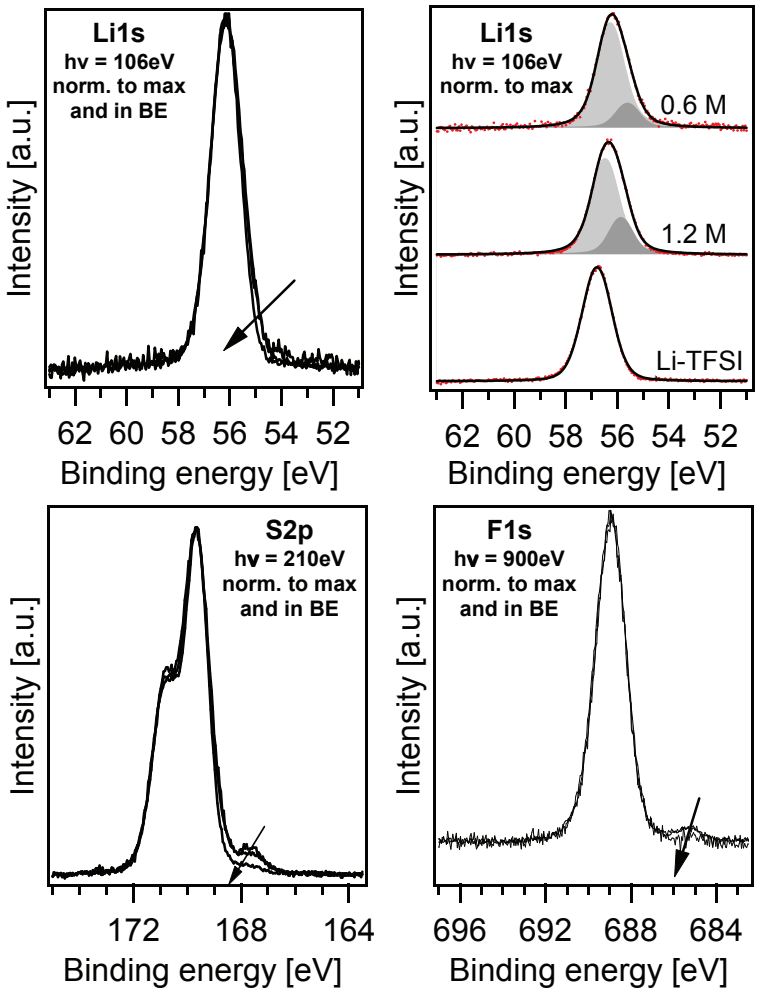

Figure 8.45.: The normalized Li1s core level spectra of Li-TFSI and the two composites (top). The spectra of the composites can be decomposed into two peaks wich are assigned to the emission of oxidized Li-TFSI$^+$ (main emission) and neutral Li-TFSI (shoulder), whereas the Li-TFSI emission consists solely of the neutral Li-TFSI species. Similarly, the normalized S2p (bottom left) and the normalized F1s core level spectra (bottom right) show a small shoulder at lower energies which is also attributed to neutral Li-TFSI.

Valence band

In Subsection 8.1.3 the HOMO of pristine Spiro-MeOTAD was fitted with two peaks (labeled as "I" and "II" in Figure 8.12) for both deposition processes. The HOMO of the Spiro-MeOTAD:Li-TFSI composites were fitted in the same way but with a third component. The peaks can be attributed to the HOMO or-

bitals and an orbital induced by Li-doping ($HOMO_{Li}$) which could arise due to the filling of the LUMO of Li-TFSI states by the electron transfer from Spiro-MeOTAD to Li-TFSI. The evolution of a third feature for Li-doped spiro-linked *p*-quarterphenyl was shown by Crispin et al., who correlated photoelectron spectroscopy and DFT-calculated total densities of valence states [207]. Similar to the fitting of the HOMO of the pristine material, the HOMO orbitals of Spiro-MeOTAD were fitted with a fixed ratio of 0.83 and an energetic splitting of 0.44 eV between the HOMO and HOMO-1. The energetic difference between the HOMO and the $HOMO_{Li}$ was also kept constant at 0.31 eV. The maximum positions of those orbitals increase by 0.05 eV with decreasing Li-TFSI content, whereas the work function decreases from 5.10 eV to 5.02 eV, as shown in Table 8.6.

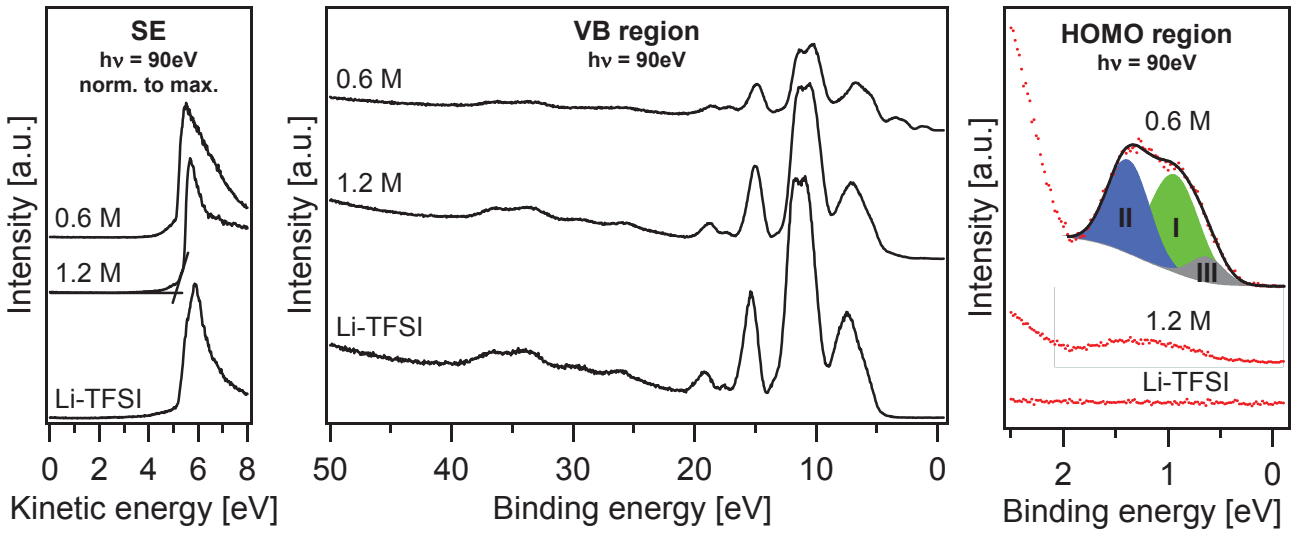

Figure 8.46.: The secondary electron emission edge, valence band and detailed HOMO region of (from the buttom up) Li-TFSI, Spiro-MeOTAD:Li-TFSI prepared with a 1.2 M Li-TFSI solution and Spiro-MeOTAD:Li-TFSI prepared with a 0.6 M Li-TFSI solution: The HOMO emission of the Spiro-MeOTAD:Li-TFSI (0.6M) is decomposed into HOMO (I) at 0.94 and HOMO-1 (II) at 1.38 eV and a third orbital $HOMO_{Li}$ at 0.63 eV. Spectra were recorded with a photon energy of 90 eV.

Table 8.6.: HOMO, HOMO-1 and $HOMO_{Li}$ binding energy positions and work functions of Li-TFSI, Spiro-MeOTAD:Li-TFSI prepared with a 1.2 M Li-TFSI solution, Spiro-MeOTAD:Li-TFSI prepared with a 0.6 M Li-TFSI solution and drop-casted Spiro-MeOTAD: the position of the intensity maxima are given.

	HOMO	HOMO-1	$HOMO_{Li}$	Work function
Spiro-MeOTAD	1.93 eV	2.37 eV		3.99 eV
0.6M	0.94 eV	1.38 eV	0.63 eV	5.10 eV
1.2M	0.99 eV	1.43 eV	0.68 eV	5.02 eV
Li-TFSI				5.14 eV

The experiments clearly show a Fermi level shift which is deduced from the shift of the maximum binding energies of the emissions of both composites. Thus, Li-TFSI acts, similarly to WO_3 (see Subsection 8.2.1), as a p-dopant for Spiro-MeOTAD and causes due to its dipole moment a vacuum level offset at the Spiro-MeOTAD/Li-TFSI interface. The Li1s but also the S2p and F1s emissions of the Li-TFSI counterion show two emissions. These were assigned to neutral (shoulder) and oxidized (main emission) Li-TFSI according to their binding energies (Figure 8.45). However, Snaith et al., who investigated Spiro-MeOTAD doped with Li-TFSI, found no evidence of a Spiro-MeOTAD cation which would be observable after p-doping [49].
The fits show that the relative amount of the oxidized Li-TFSI$^+$ species is smaller for the composite with higher Li-TFSI content (1.2 M). This can be explained by the higher relative amount of Li-TFSI and, hence, relatively less amount of reduced Li-TFSI compared to the other composite. The drop-casting experiments with Li-TFSI on BL-TiO_2 showed no influence of Li-TFSI on the TiO_2 substrate. In Figure 8.47, the Ti2p emission of the BL-TiO_2 substrate before and after drop-casting of Li-TFSI is shown. Neither the position nor the shape related to the Ti^{4+} to Ti^{3+} ratios changed. This is somewhat contradictory to the literature. There, lithium is reported to influence the potential and move the conduction band edge after being adsorbed to the TiO_2 surface [208].

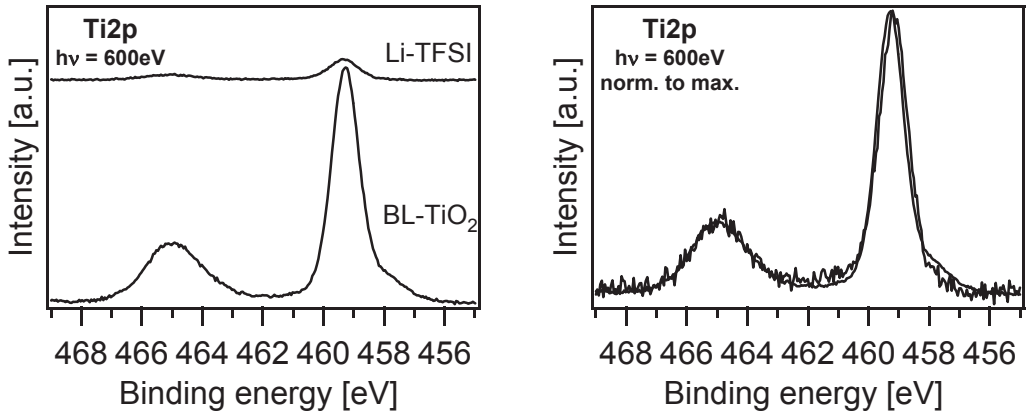

Figure 8.47.: The Ti2p and the normalized spectra of the BL-TiO_2 substrate before and after drop-casting of Li-TFSI: no change neither in the position nor in the shape related to the Ti^{4+} to Ti^{3+} ratio can be observed.

On one hand, the observed energetic shift of the emissions of both composites is approximately 1 eV compared to the values of drop-casted Spiro-MeOTAD (see Table 8.4), which was deduced from the binding energy positions of the HOMO and the $C1s_{Spiro}$ emissions. On the other hand, the work function increases by ca. 1.0 eV compared to the work function of drop-casted Spiro-MeOTAD. Thus, the distance between HOMO and the vacuum level, the ionization potential, is constant. The results are summarized in the energetic lineups shown in Figure 8.48. The difference in the shift of the different composites (ca. 0.05 eV) is rather a local variation of the composite or an uncertainty in the fitting procedure than a physical effect, otherwise the higher shift of the composite with a smaller relative amount of dopant is hardly explainable in the proposed p-doping model. Both the uncertainty of the photoelectron spectroscopy measurements and the background subtraction, which is performed before fitting, can contribute to the variation.
The origin of the shift can be a charge transfer and/or an interface dipole. In order to clarify this, Li-TFSI/Spiro-MeOTAD interface experiments, similar to the shown WO_3/Spiro-MeOTAD experiments, were conducted in this work, but failed. After the installation of a refocusing mirror in the U49/2-PGM-2 beamline, Li-TFSI was destroyed by the radiation during the measurements. As both composites

with different relative amounts of dopant lead to the same HOMO binding energy position, both are assumed to be saturated and have thus already reached the maximum Fermi level shift. In addition, the Fermi level shift of ca. 1.0 eV is in very good agreement to the observed value (ca. 1.0 eV) of the Spiro-MeOTAD:WO_3 composites. More composites have to be prepared and measured to investigate the correlation of the relative amount of the dopant and the Fermi level shift. However, the Li1s and S2p emissions of the Li-TFSI dopant show the same shift of approximately 0.6 eV for the 0.6M composite and 0.45 eV for the 1.2M composite, whereas the shift of the $C1s_{Li-TFSI}$ emission is different (0.4 eV and 0.3 eV, respectively) but lies within the uncertainty of the measuring method.
In general at reactive semiconductor hetero junctions, no band bending can be observed, due to the formation of defect states in the semiconductor energy gap, as explained in the previous Subsection 8.2.1. Therefore, a chemical reaction of the Li-TFSI dopant with Spiro-MeOTAD can be excluded. In addition the curve shape of the N1s and O1s Spiro-MeOTAD core levels do not change compared with drop-casted Spiro-MeOTAD.

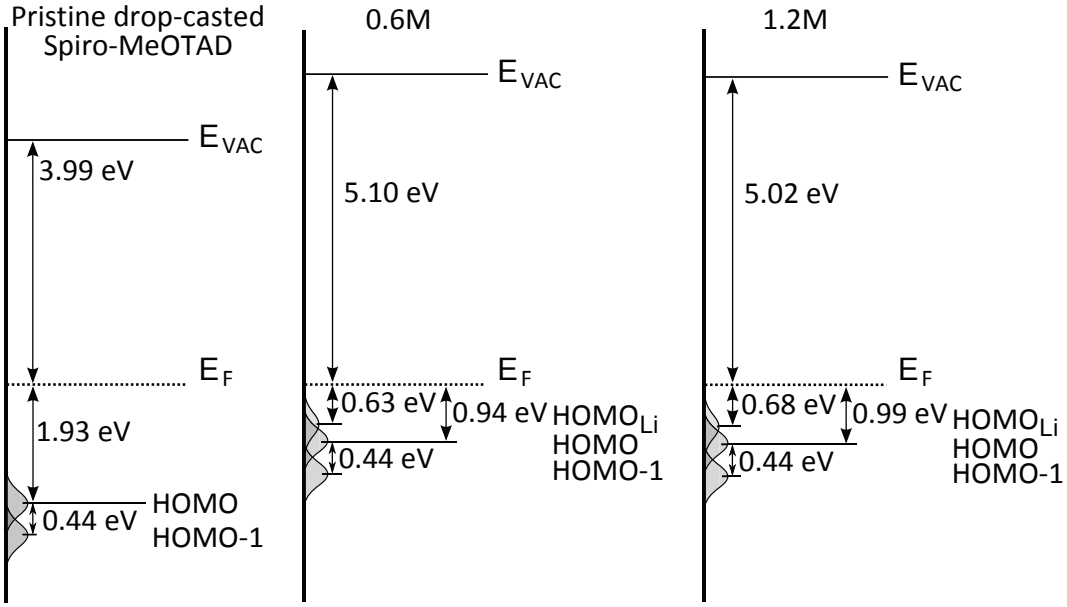

Figure 8.48.: The comparison of the energetic lineups (from left to right) of drop-casted Spiro-MeOTAD, Spiro-MeOTAD:Li-TFSI (prepared with a 0.6 M Li-TFSI solution) and Spiro-MeOTAD:Li-TFSI (prepared with a 0.6 M Li-TFSI solution). All investigated layers were deposited on TiO_2 blocking layers. Pristine Li-TFSI has no emissions up to 5 eV and was, therefore, not included here (see Figure 8.46).

C1s emission

In order to investigate the mechanism leading to the Fermi level shift in more detail, C1s difference spectra were created by subtracting the Li-TFSI spectrum from the respective Spiro-MeOTAD:Li-TFSI composite spectrum. Figure 8.49 shows on the left the difference spectra together with the Spiro-MeOTAD reference spectrum and on the right the same spectra normalized in intensity and in binding energy.
As observed for the Spiro-MeOTAD/WO_3 interface (see Figure 8.31), an additional species ranging from 284.5 to 287.5 eV is increasing in intensity with increasing relative amount of Li-TFSI. Due to the higher binding energy position of the additional species compared to the C-C bond (compare to Figure 8.14), the species is attributed to an "oxidized" spezies. In this case, as a reaction with TiO_2 can be excluded as shown in the TiO_2/Spiro-MeOTAD interface experiment, this species is assigned to a charge transfer forming an interface dipole between Spiro-MeOTAD and Li-TFSI. The fact that the difference between the work functions and the absolute positions of the C1s emissions of the composites and Spiro-MeOTAD is

approximately 1 eV supports a charge transfer and excludes an interface dipole between Spiro-MeOTAD and Li-TFSI within the composite. The emissions of the composite difference spectra appearing at about ca. 292 eV are related to errors in background subtraction and the calculation of the difference of the respective spectra than real emissions.

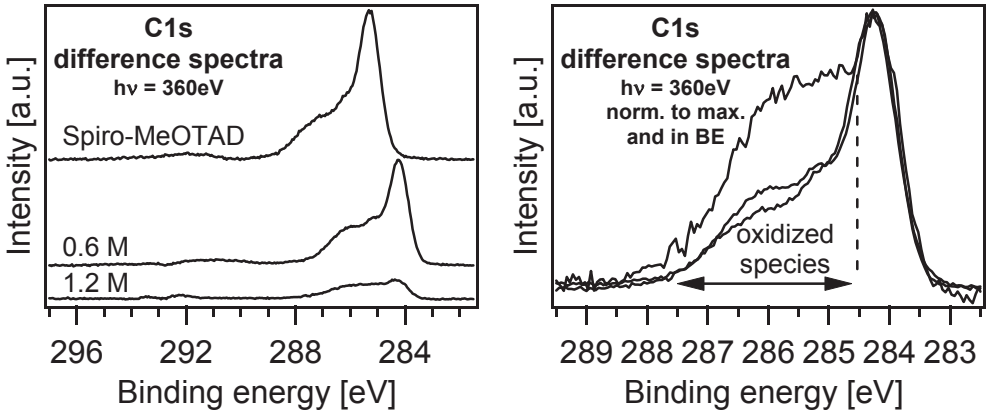

Figure 8.49.: The C1s difference spectra (left) and spectra normalized in intensity and binding energy (right): difference spectra were obtained by subtracting the Li-TFSI spectrum from the respective Spiro-MeOTAD:Li-TFSI composite spectra; the Spiro-MeOTAD bulk spectrum is included to show the "oxidized" species and its decrease with decreasing Li-TFSI content.

8.3 Summary

In this chapter the organic hole conductor Spiro-MeOTAD was investigated. The deposition methods drop-casting, a method close to spin-coating, which is widely used in industry to deposit thin layers of organic semiconductors, and physical vapor deposition, a method, which is suitable for interface experiments, were compared. In the second part Spiro-MeOTAD was doped with different dopants (WO_3 and Li-TFSI) to investigate the doping mechanisms and the doping limit. The Spiro-MeOTAD:dopant composites were deposited either by coevaporation (WO_3) or by drop-casting (Li-TFSI).

Deposition methods

Synchrotron induced photoemission measurements of in inert atmosphere drop-casted and in-situ-evaporated Spiro-MeOTAD layers showed almost identical results. The energetic lineup differed by only 0.1 eV, which was explained by the work function difference due to a different ordering of the molecules within the films. Especially, the valence band spectra of Spiro-MeOTAD, which are very sensitive to different environments and chemical reactions, showed no change of the curve shape. Also the C1s, N1s and O1s core levels were, except the binding energy positions, identical. This proves that evaporated Spiro-MeOTAD can be used as an in-situ model for drop-casted Spiro-MeOTAD and thus for the industry standard. In that way, by the stepwise evaporation of Spiro-MeOTAD, one can investigate the interfaces of Spiro-MeOTAD to another material, for example.
Furthermore, the drop-casting experiments with two different solvents, cyclohexanone and chlorobenzene, also showed identical results excluding an influence of the solvent on the energetic lineup. Because of the coffee ring effect, measurements of thick and thin Spiro-MeOTAD layers could be performed on the same sample which enabled one to investigate the substrate and Spiro-MeOTAD in contact to each other and the bulk of Spiro-MeOTAD on the same sample. Similar to Spiro-MeOTAD evporated onto TiO_2, those measurements showed no shift of the core level binding energy positions and, thus, no charge transfer and band bending.

Doping

The p-doping of Spiro-MeOTAD by coevaporation with the transition metal oxide WO_3 was demonstrated. The doping mechanism and the formation of a positively charged space charge region in Spiro-MeOTAD at the WO_3/Spiro-MeOTAD and Spiro-MeOTAD/WO_3 interfaces was shown. The maximum Fermi level shift of 0.98 eV in the Spiro-MeOTAD:WO_3 composites matched well with the Fermi level shift of 1.12 and 1.17 eV at the WO_3/Spiro-MeOTAD and Spiro-MeoTAD/WO_3 interfaces. Compared to the maximum Fermi level shift of 0.69 eV achieved for CuPC:WO_3 composites [135], the maximum Fermi level shift is a little higher but in the same order of magnitude. At the interface to Spiro-MeOTAD a reduced W4f component, which was assigned to W^{5+}, and an increased emission of the C1s orbital in the binding energy range corresponding to oxidized carbon species were observed. The W^{5+} emission was correlated to the charge transferred from the space charge region of Spiro-MeOTAD to WO_3 and the transferred charge, which forms the interface dipole.
In the interface experiments, a dipole formation of 1.0 eV was shown for Spiro-MeOTAD deposited onto WO_3 and of 1.5 eV for WO_3 deposited onto Spiro-MeOTAD. The different dipole values compensate for the different WO_3 work functions so that a similar lineup of the Spiro-MeOTAD HOMO and the WO_3 conduction band of 0.72 and 0.77 eV was found. The work function of WO_3 is 6.8 eV for a thick layer showing only a little emission of a $W4f^{5+}$ component and 6.2 eV for WO_3 deposited on TiO_2 where a strong W^{5+} emission was found. Again, those findings are comparable to the dipoles found for the CuPc/WO_3 (2.0 eV) and WO_3/CuPc (1.4 eV) interfaces. For those interfaces, the interface dipole is dependant on the deposition sequence. Hence, the same dependancy cannot be fully excluded for the Spiro-MeOTAD/WO_3 system.
In a simple model, an area electron density of around $6.63 \cdot 10^{13}$ 1/cm^2 was calculated to reside in the W^{5+} species as the negative pole of a dipole potential drop. The additional C1s emission at the interface

was correlated to the positive charge of the interface dipole. This charge is assumed to be localized on the branch of the Spiro-MeOTAD molecules closest to WO_3 as deduced from the difference spectra.

In a second doping experiment Spiro-MeOTAD/Li-TFSI composites were drop-casted onto TiO_2 substrates. The measurements clearly indicate a Fermi level shift and, thus, p-doping of Spiro-MeOTAD and/or an vacuum level offset due to the dipole moment of Li-TFSI. The measured maximum Fermi level shift of 0.99 eV is in very good agreement to the one observed for the coevaporation with WO_3 experiment (0.98 eV). Furthermore, the C1s spectra also show an oxidized species in the same binding energy region as the spectra of the Spiro-MeOTAD:WO_3 composites. Therefore, the doping mechanism may be similar. For further clarification a Li-TFSI/Spiro-MeOTAD interface experiment has to be performed. This experiment was done in this work, but failed as the Li-TFSI was destroyed dúring the measurements due to the installation of a refocusing mirror in the U49/2-PGM-2 beamline. However, the difference between both doping experiments is a third HOMO orbital ($HOMO_{Li}$), which is assumed to be induced by the Li-TFSI dopant or originates from filled up Li-TFSI LUMO states. Because the shapes of the N1s and O1s Spiro-MeOTAD core levels do not change, a chemical reaction can be excluded.

9 Dyes

So far, ruthenium complexes are the material of choice for the dye-sensitized solar cells as they yield power efficiencies of 10-11% [209, 210]. However, because of the cost, the availability and the environmental non-compatibility of 4d metals, research is focusing more and more on metal-free organic dyes [211–214]. Therefore, three perylene dyes, ID94, ID224 and ID504, obtained from the project partner BASF were investigated.
In general, the dye plays an important role in the function of the dye-sensitized solar cell. Incoming light is absorbed by the dye which is adsorbed on TiO_2 and creates electron-hole pairs. Subsequently, those pairs have to be separated and transported to the respective electrode. For this purpose, the dyes have to be engineered to match certain requirements: most importantly, the HOMO and LUMO positions have to match the HOMO of Spiro-MeOTAD and the conduction band of TiO_2, respectively. Furthermore, different anchoring groups and the interaction of the dye with the gap-states of TiO_2 as well as additives are assumed to influence strongly the performance of the DSSC. By changing the anchoring group, one hopes to improve the separation of the dye molecules and to minimize the interaction and, thus, charge quenching.
Therefore, SXPS measurements were performed to show the influence of the additive ID662 on the energetical lineup of the dye ID504 and the influence of the different anchoring groups of the dyes ID94 and ID224. In this work, the investigated molecules were drop-casted onto unheated TiO_2 substrates and the band lineup to TiO_2 as well as to Spiro-MeOTAD are investigated.

9.1 Influence of additive

According to the project partner BASF, the additive ID662 which is deposited on the TiO_2 substrate before the dye ID504 improves the efficiency of the solid-state DSSC. So far, the origin of this enhancement is unknown. Therefore, drop-casting experiments with and without the additive were performed in order to investigate the interfaces and the energetic lineup of the dye ID504 to TiO_2 and Spiro-MeOTAD.

9.1.1 Investigation of drop-casted ID504 and its additive ID662

The perylene dye ID504 (Figure 9.1) and its additve ID662 were investigated in the SoLIAS system (see Section 4.1) at the U49/2-PGM-2 beamline. Both materials were drop-casted either individually or as an additive-dye sequence one after another to investigate the materials and the influence of the additive on the dye and the TiO_2/dye/Spiro-MeOTAD lineup.

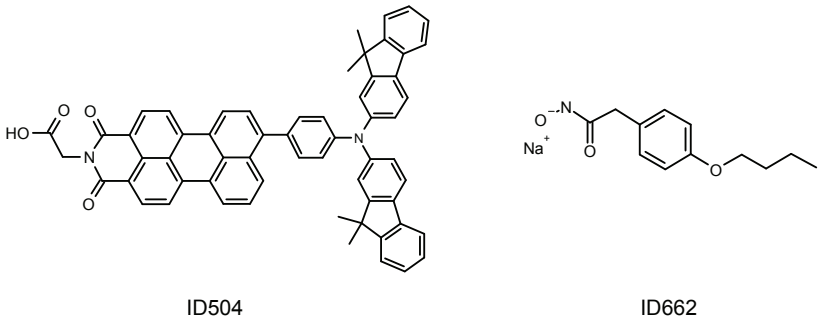

ID504 ID662

Figure 9.1.: The structural formula of the perylene dye ID504 and its additive ID662.

For this purpose, a 4.28 g/ml solution of ID504 dissolved in anhydrous dichloromethane (99.8%) was drop-casted onto a nanocrystalline TiO_2 layer in a glass cell, which was permantly rinsed with pure argon. The same was done in a second experiment for a 1.23 g/ml solution of the additive ID662 dissolved in anhydrous ethanol (99.5%). In order to investigate the influence of the additive ID662 on the dye ID504, the additive was drop-casted previous to the dye, according to a recipe obtained from BASF. Before transferring the samples into the buffer chamber residual solvent was blown off with argon.

Valence band

Figure 9.2 plots the valence band spectra of ID504, ID662 and the sequence ID662+ID504 recorded at a photon energy of 90 eV. The Ti3p emission of the nc-TiO_2 substrate is present in all the spectra, which indicates that the dye layers are thin or not closed. The valence band spectra are a superposition of the respective dye spectrum and the TiO_2 substrate spectrum labeled as "nc-TiO_2". The Ti3p substrate emission is detected at 37.9 eV for the nc-TiO_2 substrate and the spectrum of ID504, whereas the emission is shifted by 0.2 eV to lower binding energies for the ID662 and the ID662+ID504 sequence spectra. The emission at ca. 31.3 eV can be assigned to sodium which is part of the additive ID662.

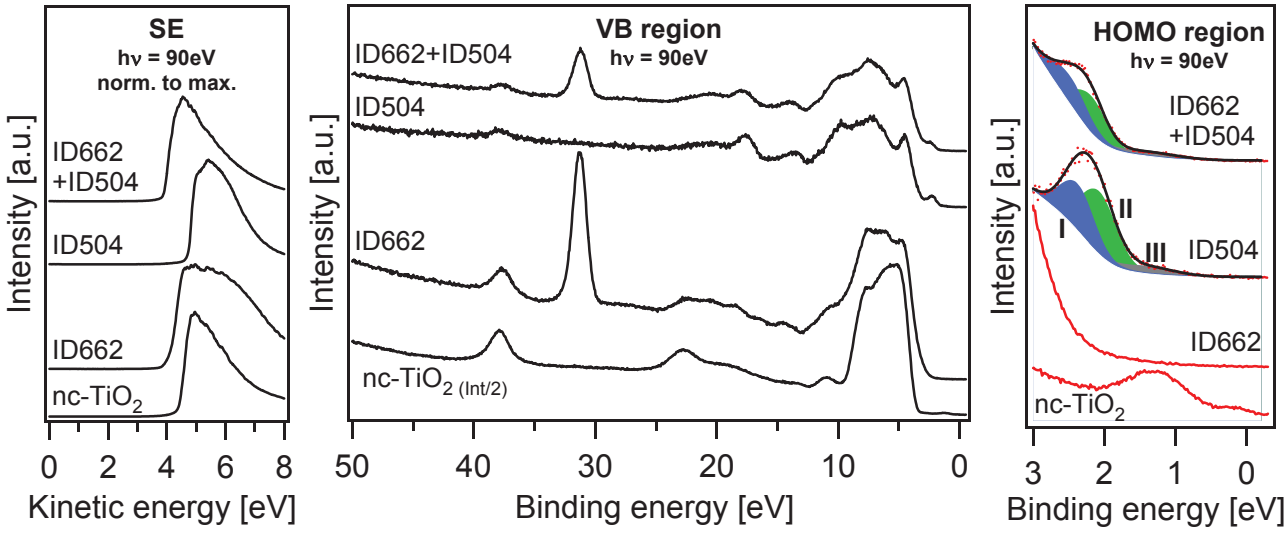

Figure 9.2.: The secondary edge, valence band and the detailed HOMO region recorded at a photon energy of 90 eV of the nanocrystalline TiO_2 substrate, the drop-casted ID662, ID504 and the successively drop-casted ID662+ID504 sequence: the work functions of nc-TiO_2 (4.3 eV), ID504 (4.7 eV), ID662 and ID662+ID504 (both 3.9 eV) were recorded at a photon energy of 90 eV. After the drop-casting of ID504, ID662 and the ID662+ID504 sequence, the TiO_2 features are not completely damped. The HOMO emission of ID504 is decomposed into a HOMO (I) at 2.1 eV, a HOMO-1 (II) at 2.4 eV and the V_0 gap-state (III) of TiO_2 at ca. 1.3 eV, whereas the HOMO (2.2 eV) and HOMO-1 (2.5 eV) of the ID662+ID504 sequence is 0.1 eV higher. The emission located at 31.3 eV is assigned to Na2p, which is part of the additive.

The HOMO emission of ID504 can be decomposed into a HOMO (2.1 eV) and a HOMO-1 (2.4 eV) molecular orbital. Because of the thin or not closed dye layer, a TiO_2 gap state contribution is found at ca. 1.3 eV, which is attributed to V_O gap-states as shown in Subsection 7.1.4. The fit was performed with an HOMO-1/HOMO intensity ratio of 0.73 and an energetic difference of HOMO-1 to HOMO of 0.30 eV. For the ID662+ID504 sequence the same fitting parameters were used. The HOMO and HOMO-1 position at 2.2 eV and 2.5 eV differ ca. 0.1 eV from the pristine ID504. The decomposition of the HOMO of similar organic dyes into two HOMO orbitals can be found also in literature. One example is the

publication of Westermark et al., who studied the adsorption of ruthenium and osmium complexes on nanostructured TiO_2 and ZnO by synchrotron induced photoelectron spectroscopy [215].
The secondary edges were recorded at a photon energy of 90 eV. The work functions of the nc-TiO_2 and the dye ID504 are 4.3 and 4.7 eV, respectively. In contrast to that, the work functions of the additive and the additive-dye sequence ID662+ID504 are 3.9 eV in both cases. Because the value of the work function does not change the work function spectrum of the additive-dye sequence is assumed to represent only the work function spectrum of the additive whereas the spectrum of the dye is superimposed.

Core levels

The detailed core level spectra of the nc-TiO_2 substrate, the additive ID662, the dye ID504 and the sequence ID662+ID504 are shown in Figure 9.3. The C1s, N1s and O1s spectra were measured with photon energies of 360, 450 and 600 eV, respectively. The shown C1s difference spectrum was obtained by subtracting the spectrum of the additive ID662 from the spectrum of the ID662+ID504 sequence. Hereby, the energetic position of the ID662 spectrum was kept constant and the intensity ratio was varied.

Figure 9.3 shows the detailed spectra of C1s, N1s and O1s orbitals of the materials. As was observed for the valence band spectra, all spectra are superpositions of the nc-TiO_2 substrate and either the pristine materials, ID662 or ID504, or the combination of ID662 and ID504. For the comparison of the C1s spectra of the pristine dye ID504 and the ID662+ID504 sequence, a difference spectrum was performed as described above. The spectrum of the pristine ID504 differs from the difference spectrum of the ID662+ID504 sequence by ca. 0.1 eV. The difference spectrum labeled as "ID504" in Figure 9.3 shows the contribution of ID504 to the C1s sequence spectrum of the additive-dye sequence. This confirms the findings of the HOMO fit in the previous paragraph. The additive is assumed not to undergo a shift upon the adsorption of the dye. Therefore, the difference spectrum was performed by keeping the energetic position of the additive spectrum constant.
The N1s detailed spectrum of the additive ID662 shows two components that are distinguishable. The component located at a higher binding energy (399.2 eV) is assigned to the additive. The emission at ca. 400.6 eV is assigned to the not completely damped TiO_2 substrate emission, which is shifted similarly to the Ti3p substrate emission by 0.2 eV to lower binding energies compared to the emission of the untreated nc-TiO_2 (400.8 eV). The emission of the N1s spectrum of ID504 at 400.4 eV is shifted by approximately 0.1 eV to lower binding energies compared to the N1s emission assigned to the dye ID504 of the ID662+ID504 sequence at 400.5 eV. This is in good agreement with the found HOMO and C1s shifts of the dye ID504. In the N1s ID662+ID504 sequence spectrum, the emission at 399.2 eV, which is assigned to the additive ID662, does not shift. Again, the position of the additive emission does not change after the drop-casting of the dye which reconfirms the assumption made for the difference spectrum that the contribution of the additive is not shifting. The same is true for the O1s emission. It consists of multiple components: one at lower binding energies originates from TiO_2, whereas the components at higher binding energies are contributed to the dye and the additive. Drop-casting the additive ID662 and the additive-dye sequence ID662+ID504 lead to a shift of the TiO_2 emission maximum from 530.7 to 530.9 eV. In contrast to this, the drop-casting of only the dye ID504 does not shift the TiO_2 emission. Moreover, no shift of the additive is observed upon dye adsorption in the sequence ID662+ID504.

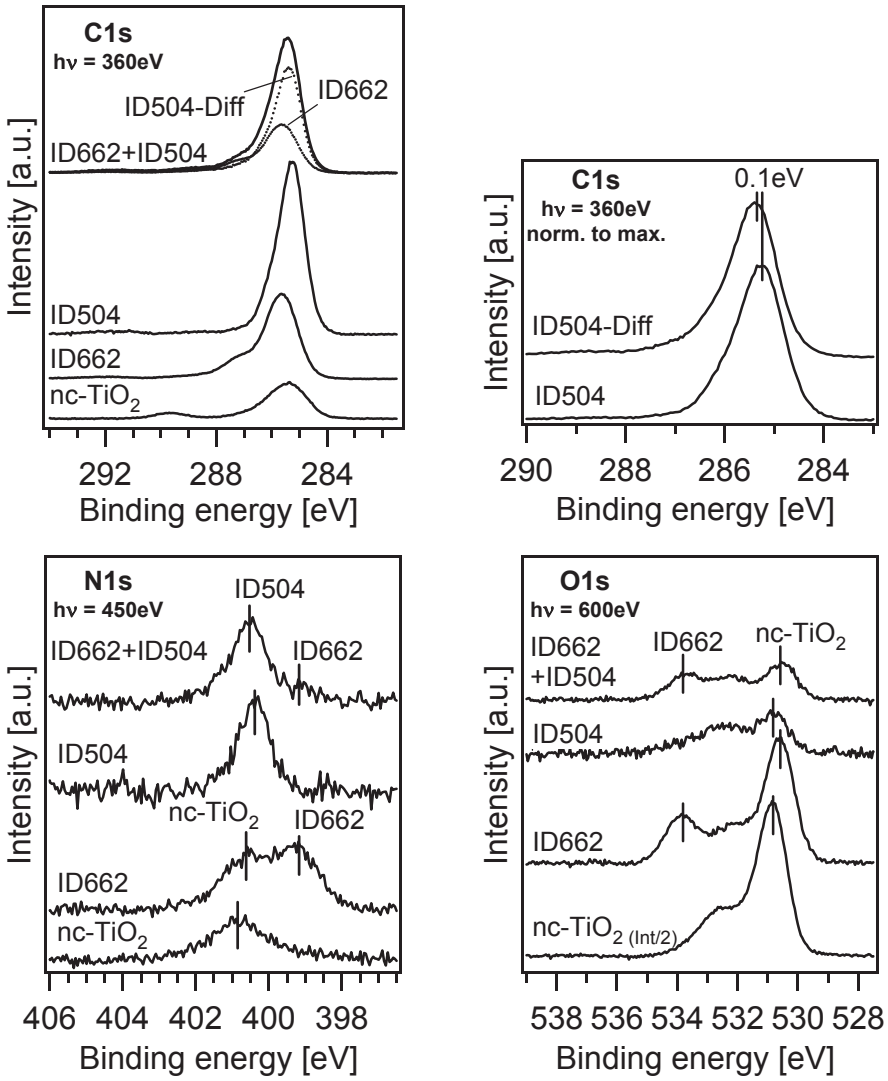

Figure 9.3.: The C1s (top left), the comparison of the ID504 C1s and the ID662+ID504/ID662 difference spectra labeled "ID504-Diff" (top right), N1s (bottom left) and O1s (bottom right) core level spectra of (from the bottom up) the nc-TiO_2 substrate, the drop-casted ID662, ID504 and the successively drop-casted ID662+ID504 sequence. According to the ID504 C1s spectrum and the C1s difference spectrum (ID504-Diff) of ID662+ID504, which was obtained by subtracting the C1s spectrum of ID662 from the C1s spectrum of ID662+ID504, a difference of 0.1 eV between the pristine ID504 and the ID504 in the ID662+ID504 sequence is observed. Upon ID662 adsorption the energetic binding energy positions attributed to TiO_2 shift by ca. 0.2 eV to lower binding energies. The energetic positions of ID504, ID662 and the nc-TiO_2 sample are marked in the detailed N1s spectra. C1s spectra were recorded at a photon energy of 360 eV, N1s at 450 eV and O1s at 600 eV.

Ti2p / gap-states

Figure 9.4 shows the Ti2p interface core level emission, the normalized Ti2p spectra and the gap-state region of each of the TiO_2/organic experiments. The energetic positions of the $Ti2p_{1/2}$ (465.3 eV) and the $Ti2p_{3/2}$ (459.3 eV) substrate emissions do not change after the drop-casting of ID504 but they do shift by ca. 0.2 eV to lower binding energies after the drop-casting of ID662 and the ID662+ID504 sequence. In the Ti2p spectra that are normalized to the maximum and the binding energy, a second Ti species can be observed. In the nc-TiO_2 sample, a reduced Ti^{3+} species is present at a lower binding energy. After drop-casting the dye ID504, the species is damped but not completely vanished, but after drop-casting the additive ID662 and the successively drop-casted ID662+ID504 sequence the Ti^{3+} species is completely quenched. Probably, the negative charged oxygen of the additive which is a sodium salt takes over the place of the missing oxygen in the TiO_2 and "heals" the oxygen vacancy in this way. Because the reduced Ti^{3+} species are a consequence of the oxygen vacancies (see Section 3.2), the emission vanishes, too.

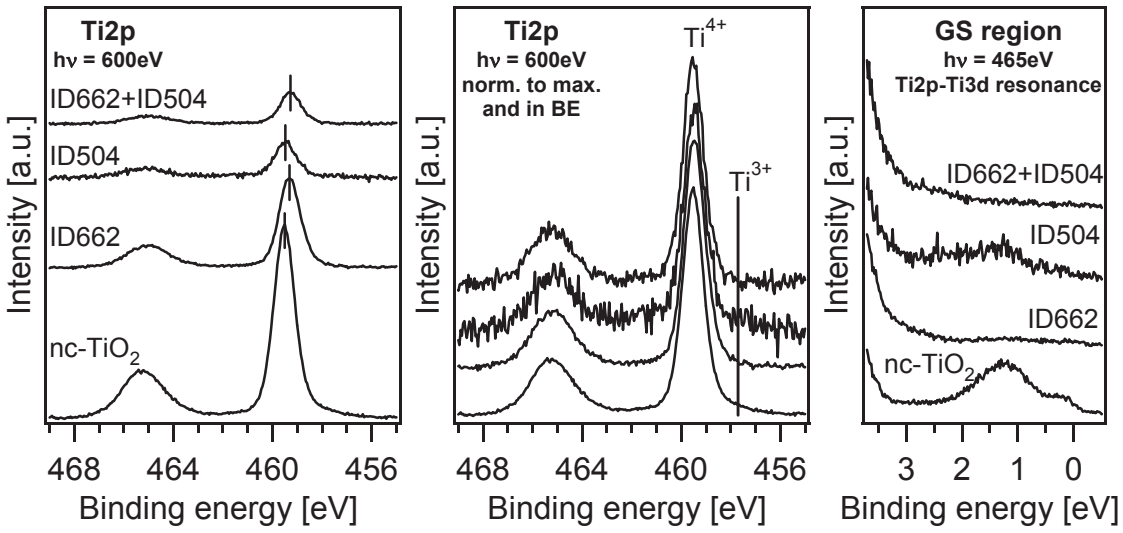

Figure 9.4.: The Ti2p core level spectra, the normalized Ti2p spectra and the normalized gap-state region measured in Ti2p-Ti3d resonance of (from the bottom up in all graphs) the nc-TiO_2 substrate, the drop-casted ID662 additive, the drop-casted ID504 dye and the successively drop-casted ID662+ID504 sequence. A shift in the Ti2p spectra as well as a damping of the reduced Ti^{3+} species in the normalized spectra and a damping of the gap-states in the resonance measurements can be observed for ID662 and ID662+ID504. Upon ID504 adsorption the reduced Ti^{3+} species and the gap-states are damped but can still be observed. The detailed Ti2p and gap-states region spectra were recorded with a photon energy of 600 and 465 eV, respectively.

The gap-state region recorded at a photon energy of 465 eV shows two kinds of TiO_2 gap-states, one just below the Fermi level and one at approximately 1.3 eV, as was shown in Subsection 7.1.4. The photon energy to measure the gap-state region was chosen to match the Ti2p-Ti3d resonance, which enhances the intensity of the gap-states as explained in Subsection 7.1.4 as well. Similar to the reduced Ti^{3+} species a correlation is observed for the TiO_2 gap-states and the additive. Here, the gap-states vanish upon ID662 adsorption, both as a pristine layer and in the ID662+ID504 sequence, and are not completely damped upon ID504 adsorption. Therefore, the additive ID662 seems to heal the TiO_2 gap-states, similarly to 4TBP which also causes a general overall shift by 0.2 eV to lower binding energy due to the healing of oxygen vacancies at the surface [85].

Lineup

The results of the experiments are summarized in the energetic lineup of the nc-TiO_2/ID504 and nc-TiO_2/ID662 interfaces and the nc-TiO_2/ID662+ID504 sequence in Figure 9.5 and in Table 9.1. The nc-TiO_2/ID504 interface show no shift in either of the layers. From the work function difference, an interface dipole of 0.4 eV is concluded. Because of the interference of the TiO_2 gap-states and the underestimation of minor valence band emissions, the determination of the valence band maximum of TiO_2 is very difficult at lower photon energies. Therefore, the value was taken from Subsection 7.1.4. The intensity maxima of the HOMO and HOMO-1 of ID504 are 2.1 and 2.4 eV, respectively. The optical band gap of 2.0 eV which is the difference of the the HOMO and LUMO onsets was obtained from the project partner BASF. According to Equation 8.1 in Subsection 8.1.3, the optical band gap can be transformed into a band gap of 3.3 eV which would be measured by PES and inverse photoelectron spectroscopy. Thus, the theoretical energetic binding energy position of the LUMO maximum is 1.2 eV above the Fermi level, which is above the conduction band minimum of TiO_2. This is important for the function of the DSSC as the photo-excited electrons in the dye do not have to overcome a barrier in this way.
At the other interface, nc-TiO_2/ID662+ID504, the influence of the additive on the lineup becomes visible. The intensity maxima of the HOMO (2.2 eV), HOMO-1 (2.5 eV) and LUMO (1.1 eV above the Fermi level) of ID504 are 0.1 eV higher than the maxima of the pristine ID504. As is also observed for the nc-TiO_2/ID662 interface, the substrate emissions are shifted by 0.2 eV to lower binding energies. Therefore, the conduction band minumum and the valence band maximum are assumed to shift by the same amount and the work function of nc-TiO_2 is assumed to increase by that amount. Therefore, a work function difference of 0.6 eV between TiO_2 and the additive ID662 results. Assuming that the additive is only influencing the TiO_2 and thus does not change the ionization potential of the dye, the work function difference between TiO_2 and ID504 is approximately 0.1 eV. Due to the shift of the TiO_2 emissions to lower binding energies the open circuit voltage of the solid-state DSSC should increase. This can be one reason why the incorporation of the additive ID662 in solid-state DSSCs increases the efficiency of these cells as stated by the project partner BASF. As was mentioned in Section 2.1, the obtainable voltage under illumination depends on the energetic difference between the quasi-Fermi level of the electrons in TiO_2 and the HOMO of the hole transport material. Therefore, a rise in the open-circuit voltage can be expected.

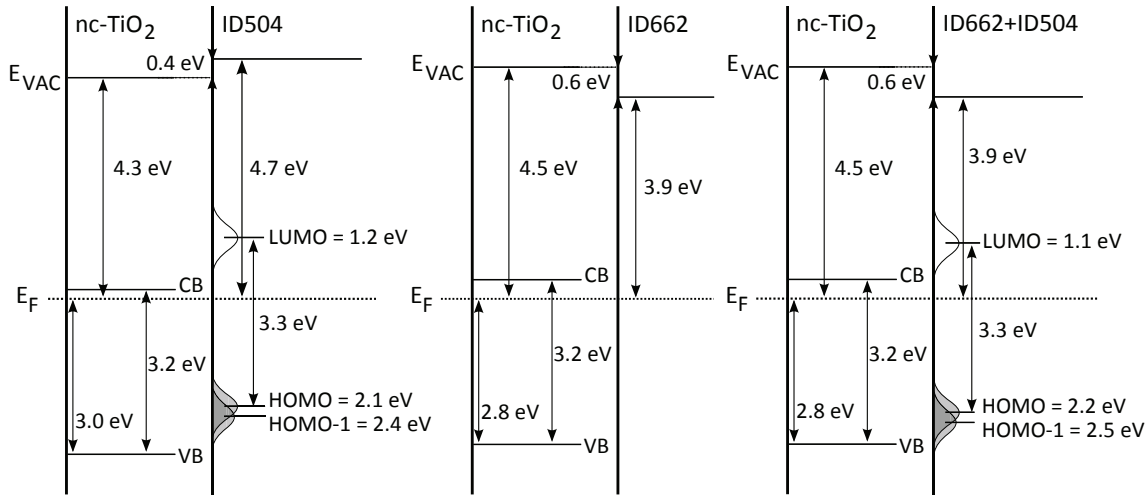

Figure 9.5.: The band diagrams of the TiO_2/ID504, TiO_2/ID662 interfaces and the successively drop-casted TiO_2/ID662+ID504 sequence after correction for the substrate shift. The work function difference is in the case of nc-TiO_2/ID504 0.4 eV and in the case of the nc-TiO_2/ID662 and nc-TiO_2/ID662+ID504 sequence -0.6 eV. Upon drop-casting of the additive ID662 the nc-TiO_2 substrate emissions shift to lower binding energies by ca. 0.2 eV and the ID504 emissions to higher binding energies by ca. 0.1 eV. The difference between the HOMO and HOMO-1 positions are ca. 0.3 eV.

Table 9.1.: The binding energy positions of the HOMO, the $C1s_{ID504}$ emission which is assigned to the ID504 dye, the $O1s_{ID662}$ emission which is assigned to the ID662 additive and the $Ti2p_{3/2}$ emission and the work functions of the nc-TiO_2 substrate, the drop-casted ID662 and ID504 and the successively drop-casted ID662+ID504 sequence: The given core level positions are the maxima of the emissions as measured without any corrections of the substrate shift.

Positions as measured	nc-TiO_2	ID662	ID504	ID662+ID504
HOMO			2.1 eV	2.2 eV
$C1s_{ID504}$			285.3 eV	285.4 eV
$O1s_{ID662}$		399.2 eV		399.2 eV
$Ti2p_{3/2}$	459.5 eV	459.3 eV	459.5 eV	459.3 eV
Work function	4.3 eV	3.9 eV	4.7 eV	3.9 eV

9.1.2 Investigation of the TiO_2/ID662+ID504/Spiro-MeOTAD sequence

The nc-TiO_2/ID662+ID504/Spiro-MeOTAD sequence, meaning the substrate/dye/hole conductor sequence as it is used in a dye-sensitized solar cell, was investigated in the SoLIAS system (see Section 4.1) at the U49/2-PGM-2 beamline. According to the recipe obtained from BASF, a 1.23 g/ml solution of the additive ID662 dissolved in anhydrous ethanole (99.5%) was drop-casted onto a nanocrystalline TiO_2 layer in a glass cell, which was permantly rinsed with pure argon, following a 4.28 g/ml solution of ID504 dissolved in anhydrous dichloromethane (99.8%). Before transferring the samples into the buffer-chamber residual solvent was blown off with argon. Subsequently, Spiro-MeOTAD was deposited stepwise with a rate of approximately 0.1 Å/s. The spectra of a thick and dense layer of Spiro-MeOTAD of 137 Å thickness are taken from the TiO_2/Spiro-MeOTAD interface experiment shown in Subsection 8.1.1.

Valence band

The valence spectra and the secondary edges were recorded at a photon energy of 90 eV. The Ti3p emission of the nc-TiO_2 substrate is detected at 37.7 eV in the the valence band spectrum of the ID662+ID504 sequence (Figure 9.6) and thus is shifted by 0.2 eV to higher binding energies compared to the nc-TiO_2 substrate. From the Ti3p emission a thin or not closed layer of the ID662+ID504 sequence is concluded. Therefore, the valence band spectrum labeled as "ID662+ID504" is a superposition of the ID662+ID504 sequence spectrum and the TiO_2 substrate spectrum labeled as "nc-TiO_2". As shown in the previous subsection, the HOMO emission of ID504 can be decomposed into a HOMO (2.2 eV) and a HOMO-1 (2.5 eV) molecular orbital, which are shifted by ca. 0.1 eV to higher binding energies. Also the V_O gap-state of the TiO_2 substrate is found at ca. 1.3 eV.

With increasing Spiro-MeOTAD overlayer thickness the features of the nc-TiO_2 sample and the drop-casted ID662+ID504 sequence are damped and the features of Spiro-MeOTAD increase. Therefore, the Ti3p substrate emission and the Na2p emission at ca. 31.3 eV, which is part of the additive ID662, vanish. As the HOMO emissions and the valence band structures of the ID662+ID504 sequence and Spiro-MeOTAD coincide, the evaluation of the spectra with Spiro-MeOTAD thicknesses of 9, 18 and 33 Å are difficult. Nevertheless, the HOMO emission of Spiro-MeOTAD seems not to shift, which has to be assured by the core level emissions.
The work functions of the nc-TiO_2, the ID662+ID504 sequence and Spiro-MeOTAD are 4.3, 3.9 and 4.1 eV which confirms the previous measurements. At the first interface, nc-TiO_2/ID662+ID504, a work function difference of ca. 0.4 eV is found, and at the second interface, ID662+ID504/Spiro-MeOTAD, a difference of ca. 0.2 eV.

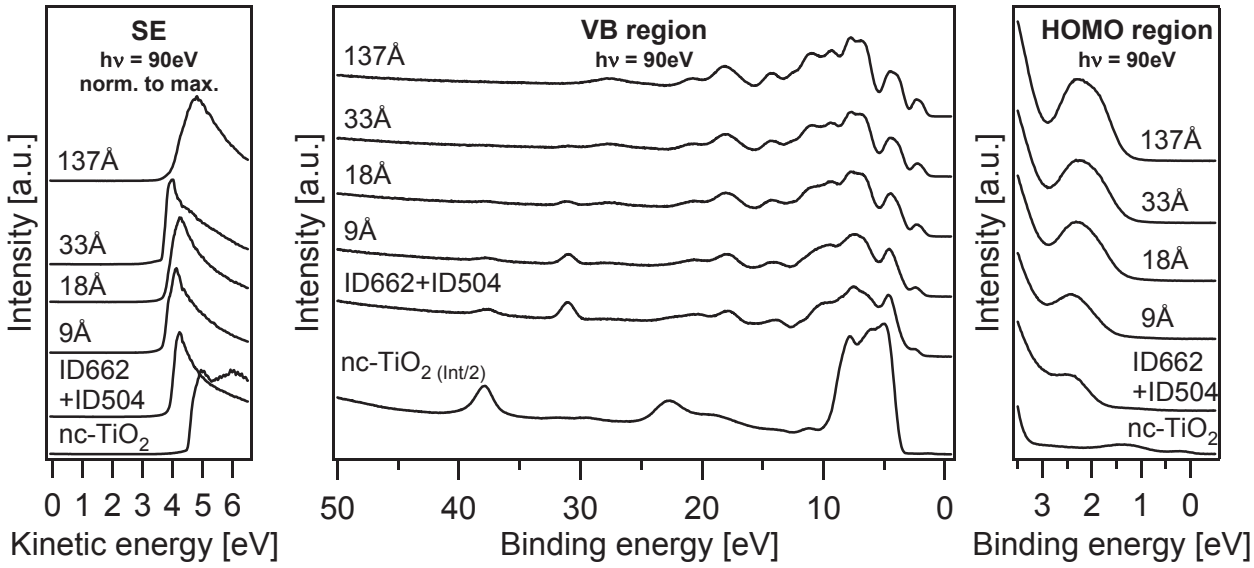

Figure 9.6.: The valence band and the detailed HOMO region recorded with a photon energy of 90 eV of the nanocrystalline TiO_2 substrate, the drop-casted ID662+ID504 sequence and the stepwise evaporated Spiro-MeOTAD (formal thickness of the Spiro-MeOTAD layer is indicated). The secondary edges of nc-TiO_2 (4.3 eV), the ID662+ID504 sequence (3.9 eV) and Spiro-MeOTAD (4.1 eV) were recorded at a photon energy of 90 eV. After the drop-casting of the ID662+ID504 sequence, the TiO_2 features are not completely damped. The HOMO emission of ID504 is decomposed into HOMO at 2.2 eV and HOMO-1 at 2.5 eV. With increasing Spiro-MeOTAD thickness the features of this molecule evolve.

Core levels

The detailed core level spectra of the nc-TiO_2 substrate, the sequence ID662+ID504 and the stepwise evaporated Spiro-MeOTAD are shown in Figure 9.3. The C1s, N1s and O1s spectra were measured with a photon energy of 360, 450 and 600 eV, respectively. As described in the previous subsection, after the drop-casting of the ID662+ID504 sequence, the nc-TiO_2 substrate O1s emission at 530.7 eV shifts by around 0.2 eV to lower binding energies. During the stepwise deposition of Spiro-MeOTAD neither the TiO_2 substrate emission nor the emissions at ca. 534.1 eV which is attributed to Spiro-MeOTAD (see the O1s emission of evaporated Spiro-MeOTAD in Figure 8.3) and at ca. 532.1 eV which is attributed to the sequence shift. In the C1s and N1s spectra, the features of the sequence and Spiro-MeOTAD are not precisely distinguishable and, therefore, are neglected here for evaluation.

Ti2p / gap-states

Figure 9.8 shows the Ti2p emission of each step of the TiO_2/ID662+ID504/Spiro-MeOTAD experiment. The energetic positions of the $Ti2p_{1/2}$ (465.3 eV) and $Ti2p_{3/2}$ (459.5 eV) shift after the drop-casting of the sequence by ca. 0.2 eV to lower binding energies but does not change during the evaporation of Spiro-MeOTAD. Before the drop-casting of the sequence, in the normalized to the maximum Ti2p spectra, the nc-TiO_2 spectrum shows a reduced Ti^{3+} species, which can be observed as a low binding energy shoulder and is completely quenched after the drop-casting of the ID662+ID504 sequence.

As shown in the previous subsection, the gap-states region recorded at a photon energy of 465 eV show two kinds of TiO_2 gap-states, one just below the Fermi level and one at approximately 1.3 eV. The photon energy to measure the gap-states region was chosen to match the Ti2p-Ti3d resonance and enhance the intensity of the gap-states. After drop-casting of the sequence the gap-states are completely damped, which is in accordance to the quenching of the Ti^{3+} species (compare to Figure 3.6). The region shows besides the gap-states the HOMO emission of Spiro-MeOTAD, which increase in intensity with growing Spiro-MeOTAD thickness.

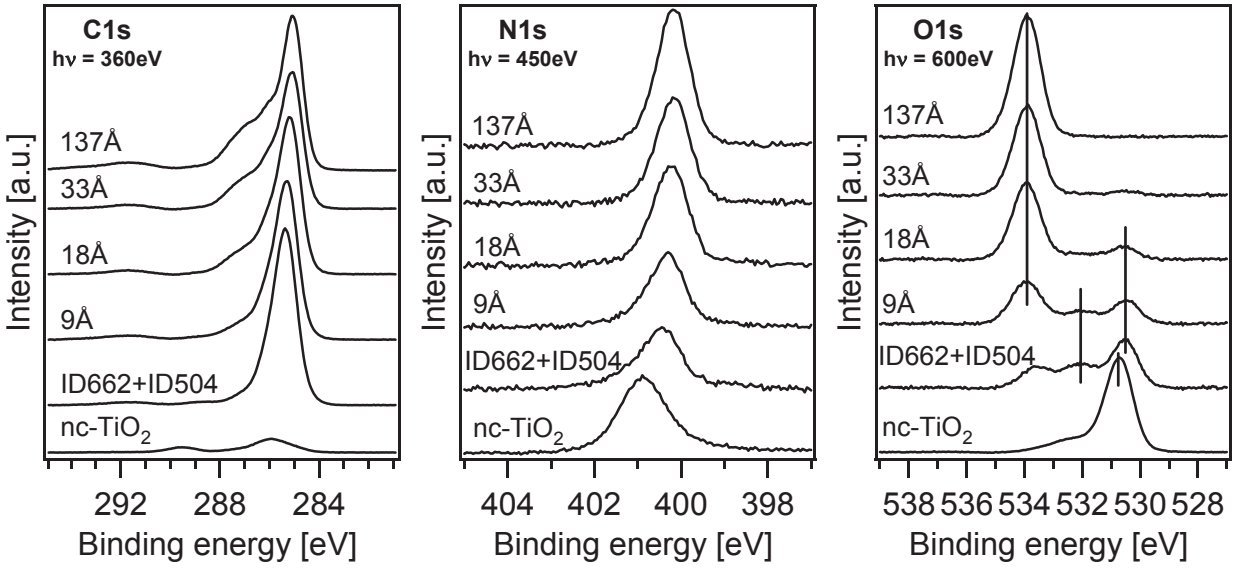

Figure 9.7.: The C1s (left), N1s (middle), O1s (right) detailed core level spectra of (from the bottom up in the respective graph) the nc-TiO_2 substrate, the drop-casted ID662+ID504 sequence and the stepwise evaporated Spiro-MeOTAD: the O1s emissions at 534.1 eV, which can be attributed to Spiro-MeOTAD (see the O1s emission of evaporated Spiro-MeOTAD in Figure 8.3) and at 532.1 eV which can be attributed to the sequence show no shift. The O1s substrate emission at 530.9 eV shifts by ca. 0.2 eV to lower binding energies after the drop-casting of the sequence and does not shift during Spiro-MeOTAD deposition. The positions of the emissions are indicated with a line in the figure. C1s spectra were recorded at a photon energy of 360 eV, N1s at 450 eV and O1s at 600 eV.

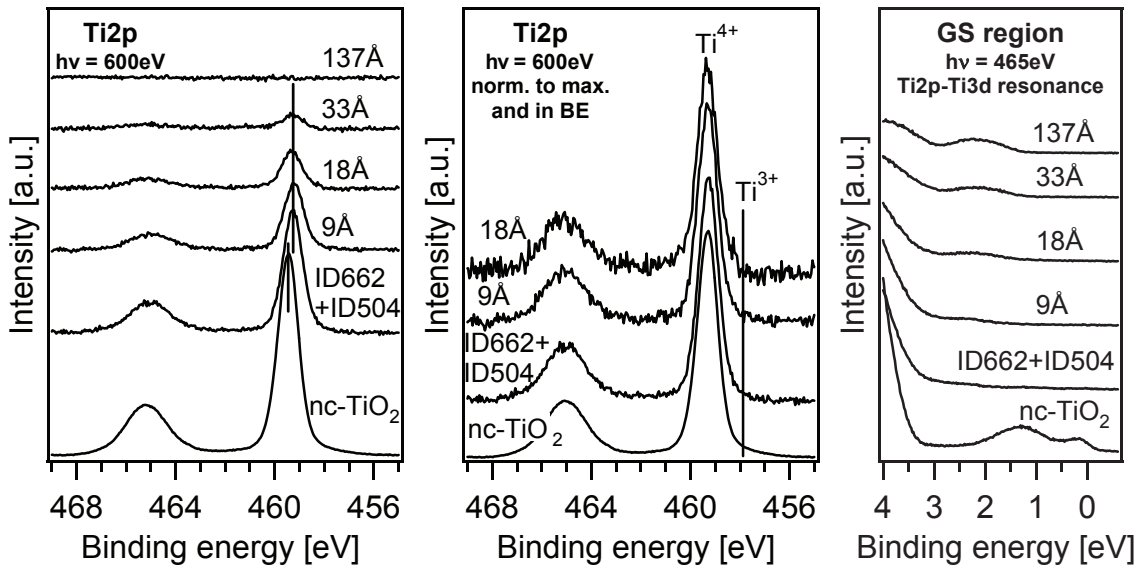

Figure 9.8.: The Ti2p core level spectra, the normalized Ti2p spectra and the normalized gap-states region measured in resonance (Ti2p-Ti3d resonance) of (from the bottom up in the respective graph) the nc-TiO_2 substrate, the ID662+ID504 sequence and the stepwise evaporated Spiro-MeOTAD: after the drop-casting of the ID662+ID504 sequence, a shift of ca. 0.2 eV can be observed in the Ti2p spectra. The reduced Ti^{3+} species in the normalized spectra are also completely damped after this step. In parallel, the resonance measurements show a complete damping of the TiO_2 gap states after the drop-casting of the sequence. With growing Spiro-MeOTAD overlayer thickness the Ti2p position does not change. The detailed Ti2p and gap-states region spectra were recorded with a photon energy of 600 and 465 eV, respectively.

Lineup

The results of the nc-TiO_2/ID662+ID504/Spiro-MeOTAD sequence are summarized in the energetic lineup in Figure 9.9. The nc-TiO_2/ID662+ID504 interface shows a shift of 0.2 eV of the nc-TiO_2 substrate emissions. From the work function difference, an interface dipole of 0.6 eV is concluded. Due to the calculated band gap of ID504 (3.3 eV see previous Subsection) obtained from BASF, the binding energy position of the LUMO is 1.1 eV above the Fermi level and thus 0.7 eV above the conduction band minimum of the nc-TiO_2 substrate. At this point it has to be mentioned that the LUMO itself has a certain extension energy wise, which is unknown because the energy gap and the LUMO position was not measured by inverse photoemission spectroscopy. As the optical gap is the difference of the HOMO and LUMO onsets and the HOMO onset has an extension of ca. 1 eV in every direction, the LUMO onset whould end up ca. 0.1 eV below the conduction band minimum. In this case, every photo-excited electron has no barrier to overcome to transfer to the conduction band of TiO_2, which promotes this process. As the determination of the valence band of TiO_2 is very difficult, see Subsection 7.1.4, the value was taken from that Subsection but corrected for the Ti2p shift. Also the work function of TiO_2 was corrected by that amount resulting in the given value of 4.5 eV.

At the second interface, ID662+ID504/Spiro-MeOTAD, because of the work function difference an interface dipole of 0.2 eV is assumed. The binding energy position of the HOMO of ID504 is 0.3 eV below the one of Spiro-MeOTAD, but matches with the complete HOMO emission (HOMO and HOMO-1) of Spiro-MeOTAD. At this interface the energetic offset of both materials is important for the reduction of the dye after the photoexcited electron is transferred to the TiO_2 electrode. The fact that the HOMO orbitals of Spiro-MeOTAD is energetic higher than the HOMO of ID504 and both HOMO orbitals are overlapping promotes the electron transfer from the HTM to the dye. Because the LUMO of Spiro-MeOTAD (2.9 eV above the Fermi level, see Subsection 8.1.3) has a relatively large offset of 1.8 eV to the LUMO of the dye, a charge transfer of the photo-excited electron which would be a loss mechanism should be negligible.

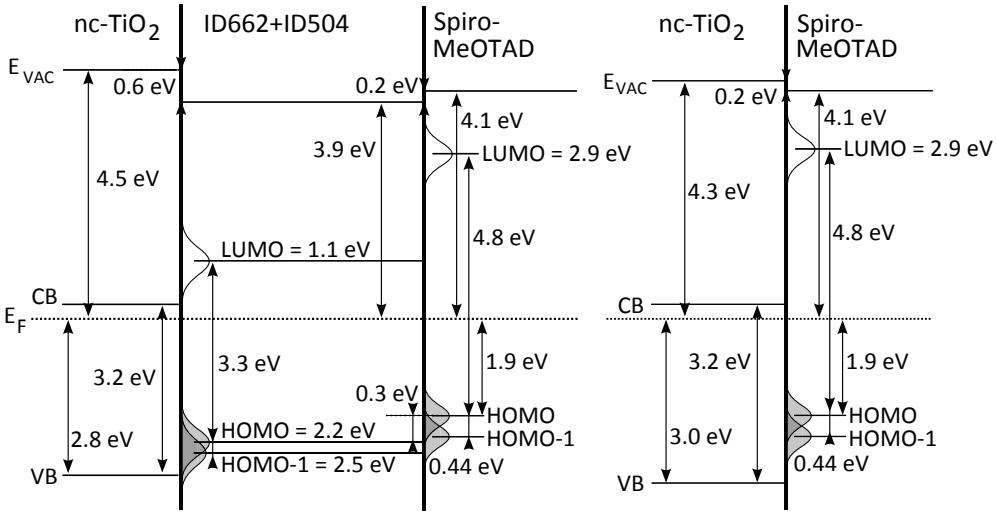

Figure 9.9.: The band diagrams of the TiO_2/ID662+ID504/Spiro-MeOTAD as formed for drop-casting of the ID662+ID504 sequence and subsequently PVD of Spiro-MeOTAD and the TiO_2/Spiro-MeOTAD sequence (see Subsection 8.1.1) for comparison. The LUMO maximum position of ID504 is determined by the calculated energy gap of the dye (3.3 eV). The offset of the conduction band minimum of TiO_2 and the LUMO of ID504 is 0.7 eV.At the interface to Spiro-MeOTAD no band bending is observed and an interface dipole of 0.2 eV is concluded from the work function difference. The lineup of the Spiro-MeOTAD HOMO maximum to the HOMO maximum of ID504 is 0.3 eV.

9.2 Influence of the anchoring group

The project partner BASF reported different efficiencies for dye-sensitized solar cells and solid-state dye-sensitized solar cells which were built with two almost identical perylene dyes, ID94 and ID224. The difference between these dyes is the anchoring group. The dye ID94 docks via two Ti-O bonds to the TiO_2 substrate, whereas the dye ID224 docks via one Ti-O bond (Figure 9.10). Solid-state DSSCs built with Spiro-MeOTAD as the solid-state hole conductor and the dye ID224 showed better efficiencies than cells built with the dye ID94. For DSSCs, the results were vice versa. Therefore, drop-casting experiments with the dyes ID94 and ID224 were performed in order to investigate the interfaces and the energetic lineup of the dyes to TiO_2. Furthermore, the interface between the hole conductor Spiro-MeOTAD and the dye ID224, which showed better efficiencies in the solid-state DSSC than the dye ID94, was analyzed.

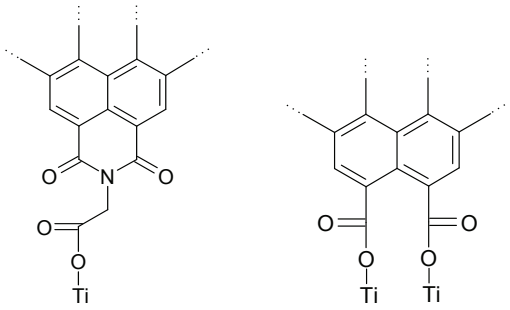

Figure 9.10: The binding of the perylene dyes ID224 (left) and ID94 (right) to TiO_2.

9.2.1 Comparison of the dyes ID224 and ID94

The perylene dyes ID224 and ID94 (Figure 9.11) were investigated in the SoLIAS system (see Section 4.1) at the U49/2-PGM-2 beamline. The dyes were dissolved in anhydrous chlorobenzene (99.8%). Afterwards, the solutions with a concentration of 0.12 g/ml were drop-casted onto nanocrystalline TiO_2 layers in the glass cell attached to the SoLIAS (see Section 4.1), which was permantly rinsed with pure argon. Before transferring the samples into the buffer-chamber, residual solvent was blown off with argon.

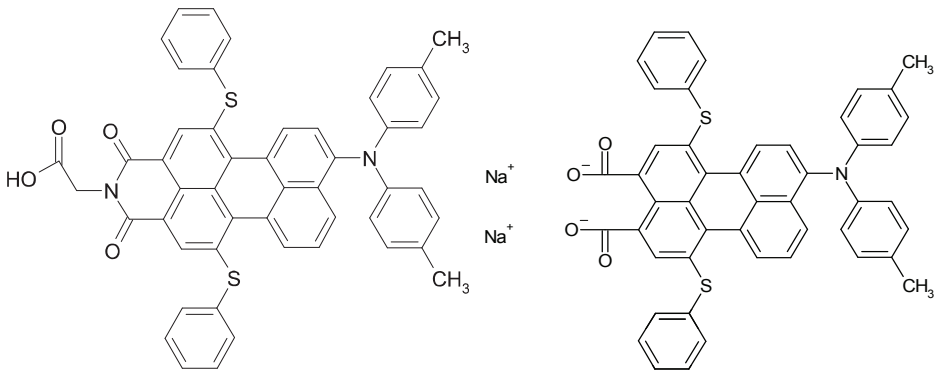

Figure 9.11.: The structural formula of the perylene dyes ID224 (left) and ID94 (right).

Valence band

The valence band spectra of the nc-TiO_2 substrate and the drop-casted dyes ID224 and ID94 were recorded at a photon energy of 90 eV and are shown normalized to the maximum in Figure 9.12. The shapes of the dye spectra are in very good agreement. This is in accordance to the expectations, as the HOMO of the dyes should not be influenced by a different anchoring group which is located on the opposite end of the molecule.

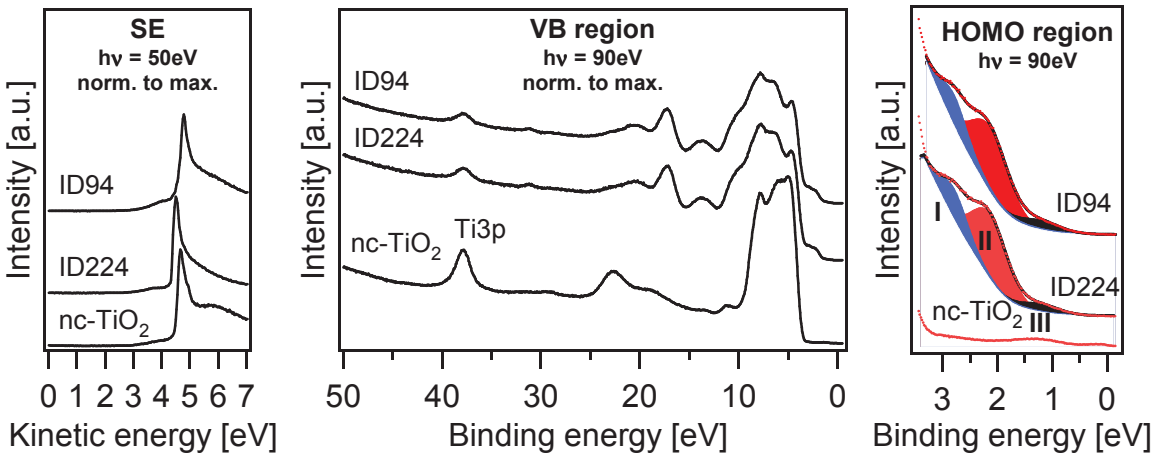

Figure 9.12.: The normalized valence band and the normalized detailed HOMO region of the nanocrystalline TiO_2 substrate and the drop-casted ID224 and ID94 were recorded at a photon energy of 90 eV. The secondary edges of nc-TiO_2 (4.3 eV), ID224 (4.3 eV) and ID94 (4.3 eV) recorded at a photon energy of 50 eV at the TGM7 beamline are taken from other experiments. After the drop-casting of ID224 and ID94, the TiO_2 features are similarly damped. The HOMO emissions of ID224 and ID94 is decomposed into the HOMO (I) at 2.1 eV, the HOMO-1 (II) at 2.7 eV and the V_0 gap state (III) of TiO_2 at ca. 1.3 eV.

Similarly to the additive-dye sequence ID662+ID504 (see Subsection 9.1.1), the Ti3p emission of the nc-TiO_2 substrate (at ca. 37.9 eV) is also observable in the valence band measurements of the dyes. Therefore, thin or not closed layers of ID224 and ID94 are concluded. Furthermore, the emission is damped equally for both dyes, which is why an effect of the anchoring group on the coverage and the layer thickness can be excluded.
The HOMO emissions of ID224 and ID94 can be decomposed equally into a HOMO (2.1 eV) and a HOMO-1 (2.7 eV) molecular orbital. Because of that, a difference in the energetic lineup can be excluded. Due to the thin or not closed dye layers, a TiO_2 gap state contribution is found at ca. 1.3 eV. These gap-states are attributed to oxygen vacancies (V_O) as was shown in Subsection 7.1.4. The fits were performed with an HOMO-1/HOMO intensity ratio of 0.46 and an energetic difference between the HOMO-1 and the HOMO and between the HOMO and the V_O of 0.65 and 0.93 eV, respectively. The decomposition of the HOMO of organic dyes into two HOMO orbitals was performed in accordance to the literature [215]. The secondary edges are taken from other experiments at the beamline TGM7. The work functions of the nc-TiO_2 and the dyes ID224 and ID94 are 4.3 eV. Therefore, no interface dipole can be deduced from these values.

Core levels

The detailed C1s, N1s, O1s and S2p core level spectra, which were measured at a photon energy of 360, 450, 600 and 210 eV, respectively, are shown in Figure 9.13. The C1s, N1s and S2p emissions found at 285.7, 400.7 and 164.1 eV, respectively, are caused mainly by the organic dyes and are composed of the emissions of the different bonds of the respective kind of atom in the molecule. The shapes and the positions of these emissions are the same for both dyes. This reconfirms the conclusion drawn from the HOMO measurements that the lineup is the same in both cases.

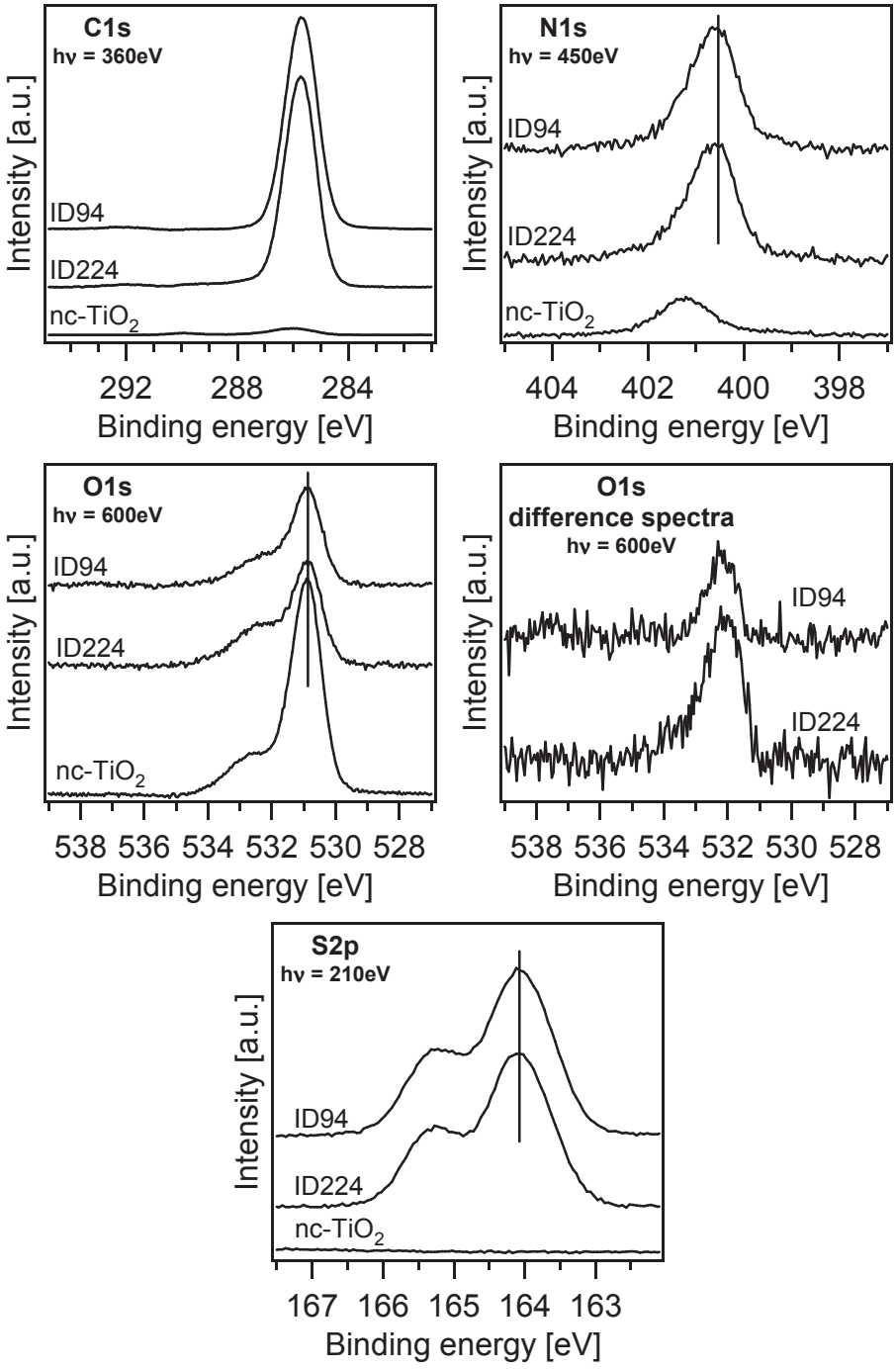

Figure 9.13.: The C1s (top left), N1s (top right), O1s (middle left), O1s difference (middle right) and S2p (bottom) core level spectra of nc-TiO_2, drop-casted ID224 and ID94: the C1s (285.7 eV), N1s (400.7 eV), S2p ($S2p_{3/2}$ at 164.1 eV) and the O1s main emission (534.1 eV), which can be attributed to TiO_2, show no shifts (positions are indicated with a line), which shows that no charge transfer occurs for both dyes. The O1s diffence spectra show the dye emissions of the dyes ID94 and ID224 which can be attributed mainly to double-bonded oxygen. C1s spectra were recorded at a photon energy of 360 eV, N1s at 450 eV, O1s at 600 eV and S2p at 210 eV.

The anchoring of the dyes to the TiO_2 substrate occurs via O-Ti bonds. Therefore, the oxygen emissions can provide information about the anchoring mechanism. The O1s emission is a combination of emissions originating from the TiO_2 substrate and the dyes. The maximum of the O1s emissions at 530.7 eV which is attributed to the TiO_2 substrate does not shift after drop-casting of both dyes. The O1s difference spectra, which show the O1s dye emissions, were obtained by subtracting the TiO_2 substrate emission from the respective dye emission. The emission maxima of both dyes are located at 532.3 eV. Therefore, no charges are transferred at the interface. As the oxygen emissions of both dyes originate mainly from similarly double-bonded and single-bonded oxygen (see Figure 9.11) the curve shape is similar but not exactly the same.

Ti2p / gap-states

Figure 9.14 shows the Ti2p emissions of the nc-TiO_2 substrate, ID224 and ID94. After drop-casting ID224 and ID94, the energetic positions of the $Ti2p_{1/2}$ (465.1 eV) and $Ti2p_{3/2}$ (459.3 eV) emissions do not change. Similar to the additive/dye sequence ID662+ID504 (see Subsection 9.1.1), the normalized Ti2p spectra show a small reduced Ti^{3+} species. It can be seen as a low binding energy shoulder in the spectra and is also verified by the appearance of gap-states which are mentioned later in this paragraph. After the deposition steps, this species is damped but not quenched completely. Therefore, an interaction of the dye with the gap-states of TiO_2 can be excluded.

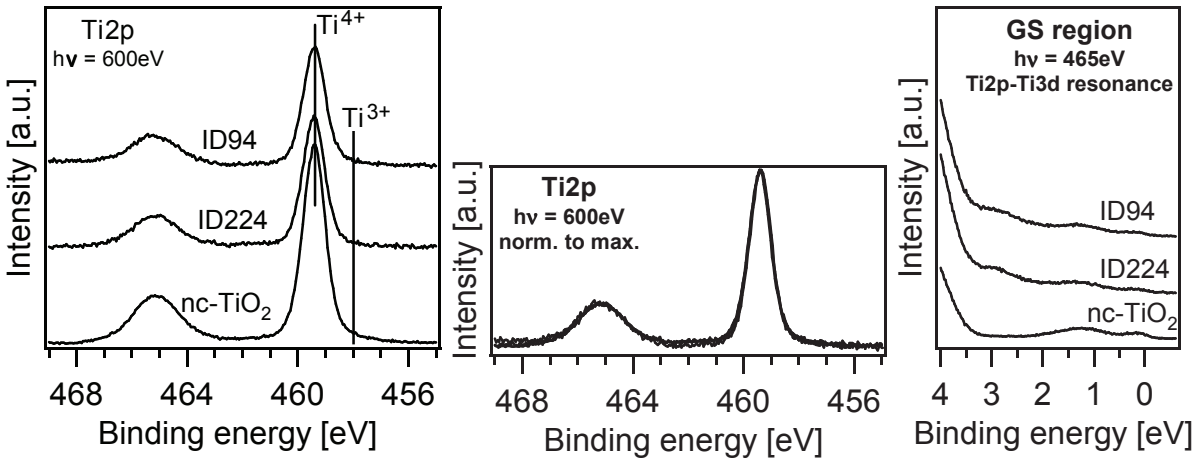

Figure 9.14.: The Ti2p core level spectra, the normalized Ti2p spectra and the gap-states region measured in resonance (Ti2p-Ti3d resonance) of (from the bottom up) nc-TiO_2, drop-casted ID224 and ID94: no shift can be observed in the Ti2p spectra and also a reduced Ti^{3+} species in the Ti2p spectra. The measurements in resonance does not show a complete damping of the TiO_2 gap states. The detailed Ti2p and gap-states region spectra were recorded with a photon energy of 600 and 465 eV, respectively.

The gap-states region was recorded at a photon energy of 465 eV. The photon energy was chosen to match the Ti2p-Ti3d resonance and enhance the intensity of the gap-states as explained in Subsection 7.1.4. The spectra show two kinds of TiO_2 gap-states: one just below the Fermi level and one at approximately 1.3 eV, as was shown in Subsection 7.1.4. Upon drop-casting the gap-states are not completely damped. The region shows besides the gap-states the HOMO emission of ID224 and ID94, respectively. Therefore, it is concluded that neither of the dyes preferentially docks at the oxygen vacancies and thus forming O-Ti bonds at these sites, as one could expect.

Lineup

The energetic lineups of both dyes to nc-TiO_2 are shown in Figure 9.15. The results are equal and, therefore, the lineups are the same. The nc-TiO_2/dye interfaces do not show a band bending in neither of the layers. Also no interface dipole is concluded, as the work functions (4.3 eV) are the same for TiO_2, ID224 and ID94.

The calculated optical band gap of ID224 and ID94 (2.1 eV for both) obtained from the project partner BASF is the difference of the HOMO and LUMO onset. The band gap was calculated according to Equation 8.1, which transforms the optical band gap into the band gap which would be measured by photoelectron spectroscopy and inverse photoelectron spectroscopy. Due to the band gap of 3.4 eV, the theoretical binding energy positions of the LUMO is 1.3 eV above the the Fermi level and thus 1.1 eV above the conduction band minimum of TiO_2. Again the value of the conduction band maximum was taken from Subsection 7.1.4 as the determination of the valence band maximum of TiO_2 is very difficult due to the underestimation of minor valence band emissions and the interference of TiO_2 gap-states.

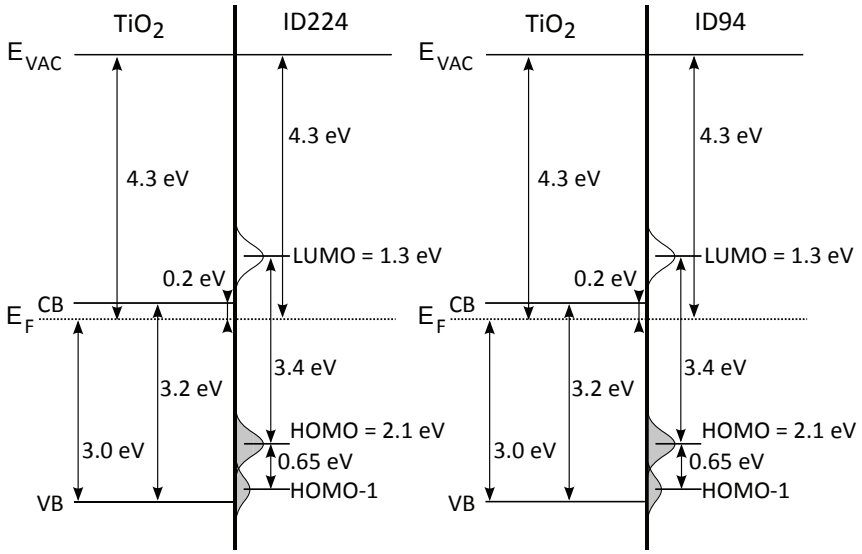

Figure 9.15.: The band diagrams of the TiO_2/ID224 and the TiO_2/ID94 interfaces as formed after drop-casting of ID224 and ID94. The LUMO maximum positions of ID224 and ID94 are determined by the calculated energy gap of the dyes (3.4 eV) and result 1.3 eV above the Fermi level. The offsets of the conduction band minimum of TiO_2 and the LUMO of ID224 and ID94 are 1.1 eV, whereas the work functions of all materials are the same, which indicates no interface dipole.

9.2.2 Dye/Spiro-MeOTAD interface

In a second experiment, the nc-TiO_2/ID224/Spiro-MeOTAD sequence, meaning the substrate/dye/hole conductor sequence as it is used in a dye-sensitized solar cell, was investigated in the SoLIAS system (see Section 4.1) at the U49/2-PGM-2 beamline. According to the project partner BASF, solid-state DSSCs built with this dye reach better efficiencies than cells built with the dye ID94. Therefore, the dye ID224 was chosen to perform this experiment. Hereby, the shown TiO_2/dye interface measurements are the same as in the previous subsection and are, therefore, not discussed in detail here.

The dye was drop-casted as described in the previous subsection. Before transferring the samples into the buffer-chamber residual solvent was blown off with argon. Subsequently, Spiro-MeOTAD was deposited stepwise with a rate of 0.1 Å/s. SXPS measurements were performed in between each deposition step.

Valence band

As discussed in the previous subsection, the valence band spectrum labeled as "ID224" is a superposition of the ID224 spectrum and the TiO_2 substrate spectrum labeled as "nc-TiO_2 " due to either a thin or not closed dye layer. Moreover, the HOMO emission of ID224 can be decomposed into a HOMO (2.1 eV) and a HOMO-1 (2.7 eV) molecular orbital. Because of the thin or not closed dye layer, a TiO_2 gap state contribution is found at ca. 1.3 eV which is attributed to V_O gap-states as shown in Subsection 7.1.4.
The features of the nc-TiO_2 sample and the drop-casted ID224 are damped with increasing Spiro-MeOTAD overlayer thickness. The Ti3p emission does not shift, which indicates that no band bending takes place in the nc-TiO_2 substrate. The features of Spiro-MeOTAD grow in intensity with increasing overlayer thickness. The spectrum of the thick and dense layer of Spiro-MeOTAD reached at 137 Å originates from the TiO_2/Spiro-MeOTAD interface experiment of the same measuring period (Subsection 8.1.1). As the HOMO emissions and the valence band structures of ID224 and Spiro-MeOTAD overlap, the spectra with Spiro-MeOTAD thicknesses of 1.2 and 2 Å are difficult to evaluate.
The secondary edges are taken from other experiments at the beamline TGM7. The work functions of the nc-TiO_2 and the dye ID224 are both 4.3 eV. In contrast to that, at the second interface, ID224/Spiro-MeOTAD, a work function difference of ca. 0.2 eV is found. This difference is concluded to form an interface dipole of the same magnitude.

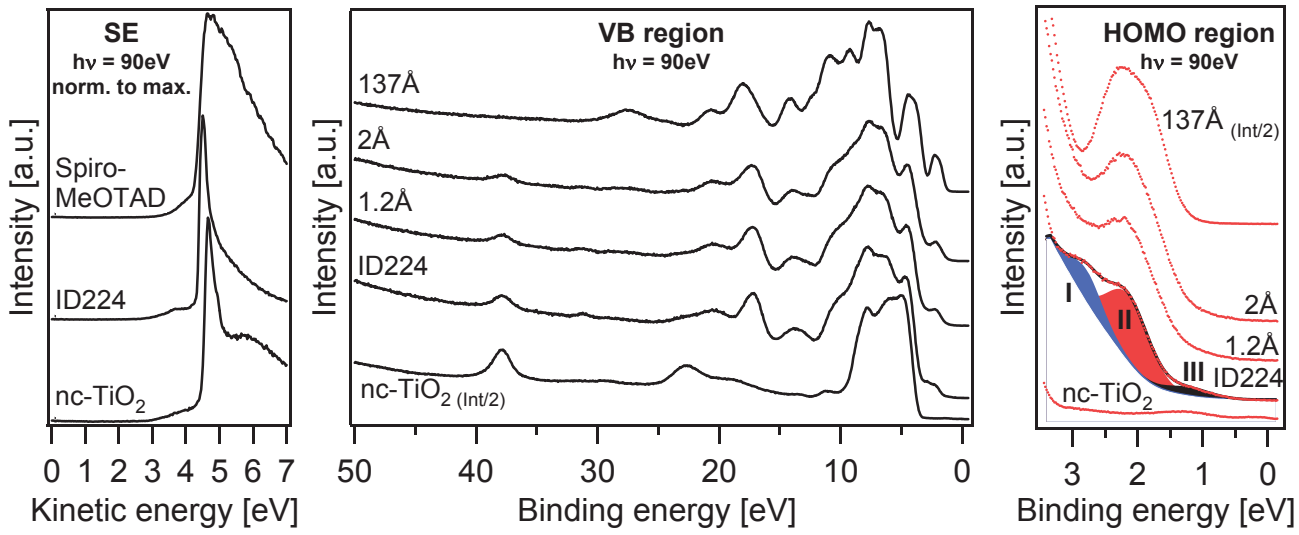

Figure 9.16.: The valence band and the detailed HOMO region of the nanocrystalline TiO_2 substrate, the drop-casted ID224 and the stepwise evaporated Spiro-MeOTAD (formal thickness of the Spiro-MeOTAD layer is indicated), recorded with a photon energy of 90 eV. The secondary edges of nc-TiO_2 (4.3 eV), ID224 (4.3 eV) and Spiro-MeOTAD (4.1 eV) recorded at a photon energy of 50 eV at the TGM7 beamline are taken from other experiments. After the drop-casting of ID224, the TiO_2 features are not completely damped. The HOMO emission of ID224 is decomposed into HOMO (I) at 2.1 eV, HOMO-1 (II) at 2.7 eV and the V_0 gap state (III) of TiO_2 at ca. 1.3 eV. With increasing Spiro-MeOTAD thickness the features of this molecule evolve.

Core levels

The detailed C1s, N1s, O1s and S2p core level spectra, which were measured with a photon energy of 360, 450, 600 and 210 eV, respectively, are shown in Figure 9.17. Again, the spectra of the "thick" Spiro-MeOTAD layer with a thickness of 137 Å are borrowed from the TiO_2/Spiro-MeOTAD interface experiment of the same measuring period (compare to Subsection 8.1.1).
After drop-casting of ID224 no shift in the O1s emission maximum at 530.7 eV is observed. This maximum is attributed to TiO_2. Strong C1s, N1s and S2p emissions at 285.7, 400.7 and 164.1 eV, respectively,

arise upon drop-casting. Those emissions are caused only by the organic dye and are composed of the emissions of the different bonds of the respective kind of atom in the molecule. In contrast, the O1s emission is a combination of emissions originating from both nc-TiO_2 and the dye.

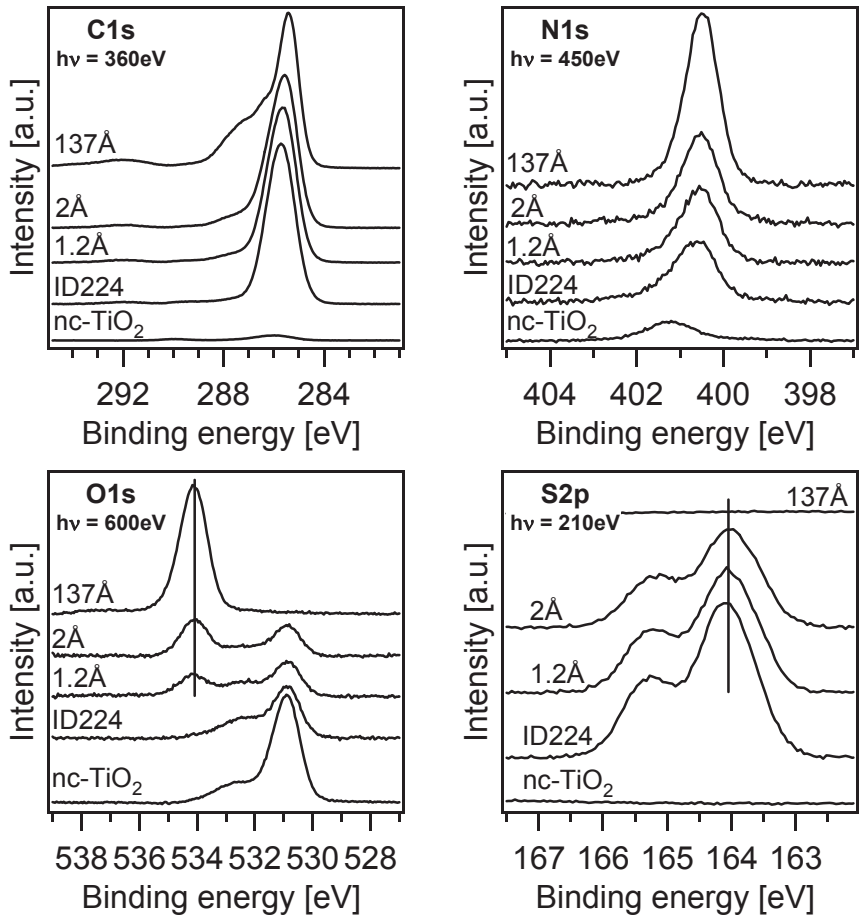

Figure 9.17.: The C1s (top left), N1s (top right), O1s (bottom left) and S2p (bottom right) core level spectra of (from the bottom up) nc-TiO_2, drop-casted ID224 and stepwise evaporated Spiro-MeOTAD. According to the S2p emission ($S2p_{3/2}$ at 164.1 eV), which can be solely attributed to the dye, no shift is observed (indicated with a line); the O1s emission at 534.1 eV, which can be attributed to Spiro-MeOTAD (compare to the O1s emission of evaporated Spiro-MeOTAD in Figure 8.3), show no shift either (the position of the emission of Spiro-MeOTAD is indicated with a line). C1s spectra were recorded at a photon energy of 360 eV, N1s at 450 eV, O1s at 600 eV and S2p at 210 eV.

The S2p core level, which is only present in the dye and, therefore, indicates solely the energetic shift of the dye, shows no shift in the dye during Spiro-MeOTAD deposition. The emission with the highest binding energy in the O1s detailed spectrum at 534.1 eV which is attributed to Spiro-MeOTAD (see the O1s emission of the TiO_2/Spiro-MeOTAD interface experiment in Figure 8.3) shows no shift either. The other core levels, C1s and N1s, consist of overlapping emissions of both molecules and, therefore, are neglected here for evaluation.

Ti2p / gap-states

Figure 9.18 shows the Ti2p emission of each step of the TiO_2/ID224/Spiro-MeOTAD experiment. The energetic positions of the $Ti2p_{1/2}$ (465.1 eV) and $Ti2p_{3/2}$ (459.3 eV) do not change either after the drop-casting of ID224 or during the evaporation of Spiro-MeOTAD. As seen in the previous subsection, the normalized Ti2p spectra show a small amount of reduced Ti^{3+} species, which can be seen as a low bind-

ing energy shoulder in the spectra. As mentioned in previous subsections, the reduced titanium species is accompanied by the appearance of TiO_2 gap-states and vice versa. The reduced species is damped but not quenched after the deposition of the dye and the first two deposition steps of Spiro-MeOTAD. Besides the gap-states, the region shows the HOMO emission of ID224. Therefore, an interaction of either the HOMO of the dye or the HOMO of Spiro-MeOTAD with the TiO_2 gap-states can be excluded.

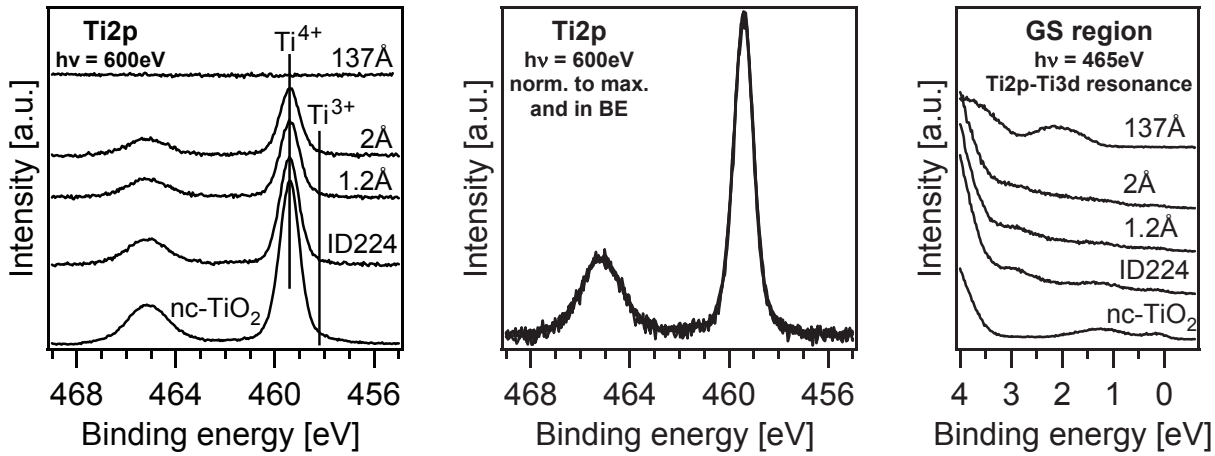

Figure 9.18.: The Ti2p core level spectra, the normalized Ti2p spectra and the gap-states region measured in Ti2p-Ti3d resonance of (from the bottom up) nc-TiO_2, drop-casted ID224 and stepwise evaporated Spiro-MeOTAD. No shift can be observed in the Ti2p spectra but a small amount of reduced Ti^{3+} species in the normalized spectra. The resonance measurements show no complete damping of the TiO_2 gap-states for the dye and the first two Spiro-MeOTAD deposition steps. The detailed Ti2p and gap-states region spectra were recorded with a photon energy of 600 and 465 eV, respectively.

Lineup

The results of the experiment are summarized in the energetic lineup of the nc-TiO_2/ID224/Spiro-MeOTAD sequence in Figure 9.19. The nc-TiO_2/ID224 interface, which was shown and discussed in the previous subsection, does not show a shift in either of the layers and no interface dipole. The binding energy position of the LUMO is 1.3 eV above the Fermi level and thus 1.1 eV above the conduction band minimum of TiO_2. The energetic offset is very similar to the obtained offset for the dye ID504 (1.0 eV see Subsection 9.1.1). The offset is important for the function of the DSSC as an offset in the other direction would cause a barrier for charge transfer. The LUMO position of the dye has a systematic error as it was not measured by inverse photoemission spectroscopy and has a certain energetic extension which is unknown. If one consider the extension of the HOMO (ca. 1.1 eV in both directions) and the optical gap (2.0 eV) which is the energetic difference between HOMO and LUMO onset, the LUMO onset of the dye ends up at 1.0 eV above the Fermi level. Hence, the onset is 0.8 eV above the conduction band minimum of TiO_2, which means that all photo-excited electrons in the dye do not have to overcome a barrier, and the extension of the LUMO (1.0 eV) is the same as the extension of the HOMO.

At the second interface, ID224/Spiro-MeOTAD, an interface dipole of 0.2 eV is assumed because of the work function difference. The binding energy position of the HOMO of ID224 is 0.2 eV below the one of Spiro-MeOTAD and thus comparable to the offset of the dye ID504 (0.3 eV see Subsection 9.1.1), but matches with the superposition of HOMO and HOMO-1 of Spiro-MeOTAD. In both cases, the electron injection should be very efficient as the electrons do not have to overcome this energetic offset but the transfer is driven by this overpotential. Nevertheless, this overpotential is a built-in loss potential, which is why the energetic HOMO position of the dye ID224 fits better to the HOMO of Spiro-MeOTAD. The loss mechanism of the photo-excited electron via a charge transfer to the LUMO of Spiro-MeOTAD

(2.9 eV above the Fermi level, see Subsection 8.1.3) should be negligible as the offset of 1.6 eV is too high for efficient charge transfer.

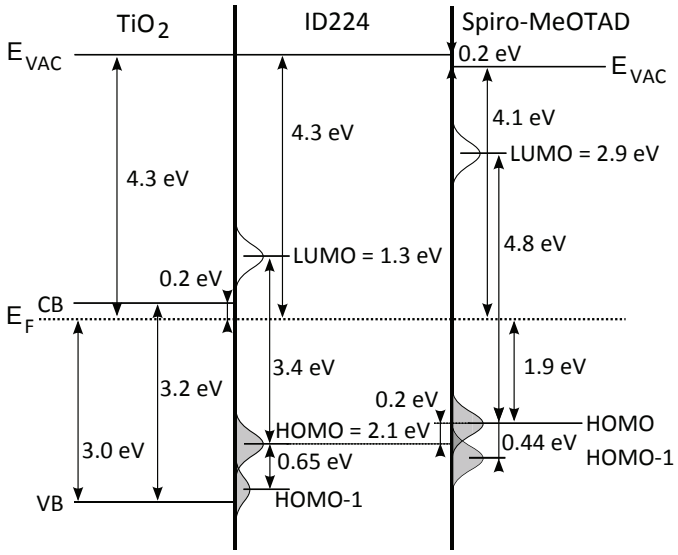

Figure 9.19.: The band diagram of the TiO_2/ID224/Spiro-MeOTAD sequence as formed by drop-casting of ID224 and subsequently PVD of Spiro-MeOTAD. The LUMO maximum position of ID224 (1.3 eV) is determined by the calculated energy gap of the dye (3.4 eV). The offset of the conduction band minimum of TiO_2 and the LUMO of ID224 is 1.1 eV, whereas the work functions of both materials are the same, which indicates no interface dipole. At the interface to Spiro-MeOTAD no band bending is observed and an interface dipole of 0.2 eV is concluded from the work function difference. The lineup of the Spiro-MeOTAD HOMO maximum to the HOMO maximum of ID224 is 0.2 eV.

9.3 Summary and discussion

In this chapter the influence of the additive ID662 on the nc-TiO_2/ID504 interface and the influence of the anchoring groups of the dyes ID224 and ID94 were investigated. Additives and the anchoring groups are believed to play an important role for the energetic lineup and, thus, for the function of the DSSC. Moreover, the project partner BASF reported that DSSCs with the the dye ID504 and additive ID662 work better than cells without the additive. Therefore, three different dyes obtained from BASF, namely ID504, ID224 and ID94, were investigated by SXPS. In order to investigate the energetic lineups of the dyes to the TiO_2 substrate as well as to the organic hole conductor Spiro-MeOTAD, the dyes were drop-casted onto nc-TiO_2 substrates and, subsequently, Spiro-MeOTAD was evaporated stepwise on top of it.

SXPS measurements

The HOMO emissons of all dyes can be decomposed into HOMO and HOMO-1 emissions. Also in literature, the HOMO emissions of organic dyes, for example of ruthenium and osmium complexes adsorbed on nanostructured TiO_2 and ZnO, are decomposed into two HOMO orbitals [215]. The HOMO position is the same (2.1 eV) for all dyes, but the energetic splitting between HOMO and HOMO-1 is different (0.3 eV for ID504 and 0.65 eV for ID224 and ID94). This indicates that the different anchoring group does not affect the energetic lineup of the dyes ID224 and ID94. Upon the adsorption of the additive ID662, the energetic positions of both the HOMO and HOMO-1 of ID504 increase by ca. 0.1 eV.

At the substrate/dye interface, TiO_2 gap-states are of special interest as they are believed to play an important role for the function and the efficiency of the dye-sensitized solar cell (see Chapter 2). The one at approximately 1.3 eV is attributed to oxygen vacancies and the other just below the Fermi level is assumed to originate from conduction band states which are caused by under-coordinated surface Ti atoms (see Section 3.2). The TiO_2 gap-states are accompanied by the appearance of reduced titanium Ti^{3+} species in the spectra and vice versa, which is why one can assume the reduced species to be present despite its low intensity in the measurements.
After the drop-casting of the pristine materials, ID224, ID94 and ID504, the gap-states are damped by the overlayer but are still observable. Therefore, the dyes seem not to form O-Ti bonds at the oxygen vacancy sites of TiO_2 as one could expect. However, using the additive ID662 in the ID662+ID504 sequence, the gap-states vanish completely. The same is true for the reduced Ti^{3+} species, which is allocated as a low binding energy shoulder in the Ti2p emission. One explanation for this is that the negatively charged oxygen of the additive, which is a sodium salt, interacts with the oxygen vacancies and the under-coordinated Ti atoms forming the conduction band states of the TiO_2, maybe by a charge transfer, and, thus "heals" those gap-states, similarly to 4TBP. 4TBP causes a general overall shift by 0.2 eV to lower binding energy in TiO_2 due to the healing of oxygen vacancies at the surface and thus increases the open-circuit voltage of the DSSC [85]. Therefore, the benefitial effect of the additive ID662 is assumed to be the same.

Energetic lineup

The influence of the addive ID662 on the interface of the dye ID504 to the nc-TiO_2 substrate becomes most obvious in the energetic lineup of the nc-TiO_2 to the dye without and with the additve (9.5). On one hand, the additive is changing the binding energy positions of the TiO_2 substrate emissions by ca. 0.2 eV shifting the valence band maximum and the conduction band minimum up in the energetic lineup and thus increasing the possible open circuit voltage. On the other hand, the energetic position of the HOMO of the dye ID504 is increased by ca. 0.1 eV. This realignes also the offset between LUMO and conduction band, which changes from 1.0 to 0.7 eV, and the interface dipole, which also changes from

0.4 to 0.6 eV. Nevertheless, an efficient electron transfer from the LUMO of the dye to the conduction band minimum of TiO_2 is guaranteed.

The lineup of the other dyes, ID224 and ID94, are the same and similar to the lineup of the pristine ID504 to the TiO_2 substrate. In contrast to the additive, the organic molecules do not modify the TiO_2 substrate. The HOMO positions are the same (2.1 eV) as that of ID504, but the energetic splitting between HOMO and HOMO-1 is different (0.3 eV for ID504 and 0.65 eV for ID224). The LUMOs of the dyes have a similar offset to the conduction band minimum (1.1 eV as the dye ID504. Again, the electron transfer from the LUMO of the dye to the conduction band minimum of TiO_2 is promoted.
Therefore, the difference of the efficiencies between solid-state DSSCs and DSSCs built with the dyes ID224 and ID94 cannot be explained by the energetic lineup. Another reason can be different interactions of the dyes due to different separations of the individual molecules, which was shown by Schwanitz [11]. He stated that a separation of N3 dye molecules by adsorbed acetonitrile leads to a reduced luminescence and, thus, to an improved charge carrier injection. Therefore, the more flexible single O-Ti bond of the dye ID224 could lead to a better separation than the two O-Ti bonds of the dye ID94. In order to learn more about the intermolecular dye interaction, a marker atom could be built into the molecules opposite to the anchoring group. The sulfur atoms of the two dyes are no candidates as the attached benzene groups prevent them to interact with other molecules.

Evaporating Spiro-MeOTAD on top of ID224 and the ID662+ID504 sequence does not induce band bending in either of the dye/Spiro-MeOTAD interfaces. Again both lineups are similar. The HOMO offset of both materials are with 0.2 and 0.3 eV for ID224 and ID662+ID504, respectively, equivalent, which is energetically favorable for the hole transfer and, thus, the dye regeneration. Also the absolute values of the interface dipoles, deduced from the work function differences, are the same (0.2 eV) but in different directions. One possible loss mechanism of the DSSC is the charge transfer of a photo-excited electron via the LUMO of the dyes to the LUMO of Spiro-MeOTAD. It was shown that this is negligible as the offset of 1.8 eV for the ID662+ID504/Spiro-MeOTAD interface and 1.6 eV for the ID94/Spiro-MeOTAD and ID224/Spiro-MeOTAD interfaces are too high for efficient charge transfer.

10 Gold

In the DSSC the back contact consists of Pt clusters on a glass substrate. The redox potential of the I_3^-/I^- electrolyte fits to the ionization potential of platinum (work function of 6.35 eV). In contrast to that, the back contact material of the solid-state DSSC has to match energetically to Spiro-MeOTAD. This means that the work function of the metal has to be aligned to the HOMO of Spiro-MeOTAD [104]. The material of choice in literature is gold which has a work function of 5.1 eV [216]. Another way to match the energy levels is the altering of the Spiro-MeOTAD HOMO position by doping to match with the back contact. In this work, doping was realized with Li-TFSI. This chapter presents the investigations of the interfaces Au/Spiro-MeOTAD and Au/Spiro-MeOTAD:Li-TFSI in order to evaluate the influence of doping on the energetic matching on the back contact. The reverse interface experiments Spiro-MeOTAD/Au and Spiro-MeOTAD:Li-TFSI/Au were also performed in this work, but failed as no contamination free gold layer could be deposited onto the organic layers. The origin of these contaminations were probably residual organic material, which were reevaporating from the UHV-chamber walls of the SoLIAS during the deposition process due to the high evaporation temperature of gold (ca. 1100 °C). Moreover, the heating of the gold source caused the interdifussion of Spiro-MeOTAD and gold.

10.1 Gold / evaporated Spiro-MeOTAD interface

In order to investigate the Au/Spiro-MeOTAD interface, an interface experiment was performed at the U49/2-PGM-2 beamline. Spiro-MeOTAD was evaporated stepwise with a rate of about 0.3 Å/s onto an in-situ sputter-cleaned gold foil. The experiment was carried out at room temperature with a source temperature of 284 °C.

Core levels

The interface experiment was performed with a clean gold foil. No carbon, oxygen and nitrogen contaminations are visible in the gold detail spectra labeled as "Au" in Figure 10.1. In the subsequent evaporation steps, the evolving emissions can be attributed solely to Spiro-MeOTAD. The band bending towards the Fermi level of Spiro-MeOTAD (1.25 eV) was determined by the shift of the C1s emission maximum from 283.84 to 285.09 eV. All core level spectra show approximately the same relative shift and evolution of band bending. The evolution of the work function which is plotted in Figure 10.1 decreases in the same way as the energetic position of the core levels increase. After the first deposition steps, the work function decreases in parallel to the core level shifts. Therefore, the initially stronger change in the work function is assigned to the formation of an interface dipol. The shift of the N1s core level is from 399.05 to 400.30 eV and the one of the O1s from 532.30 to 533.51 eV. Hereby, as for all core level spectra, a curve-fitting was performed with a Gaussian curve to obtain the binding energy position of Spiro-MeOTAD. The binding energy position for 0 Å was extrapolated via a fit of the obtained values. Additionally, no change in the curve shapes and no additional features are visible, which is why a chemical reaction at the interface is not probable.
In contrast to the Spiro-MeOTAD adsorbant, the Au4f core level emissions of the gold substrate undergo no shift in the energy position (Figure 10.2), which is in good agreement to the literature value for etched gold [217] at approximately 83.9 eV. In general, metals show no band bending due to their high charge carrier densities, which causes a rapid potential equalization right at the interface. As seen for the Spiro-MeOTAD core levels, the shape of the Au4f emission does not change with growing Spiro-MeOTAD thickness, which is also a proof that Spiro-MeOTAD does not chemically react with the gold substrate. In addition, the completely damped Au4f signal at 248 Å thickness proofs a dense Spiro-MeOTAD layer.

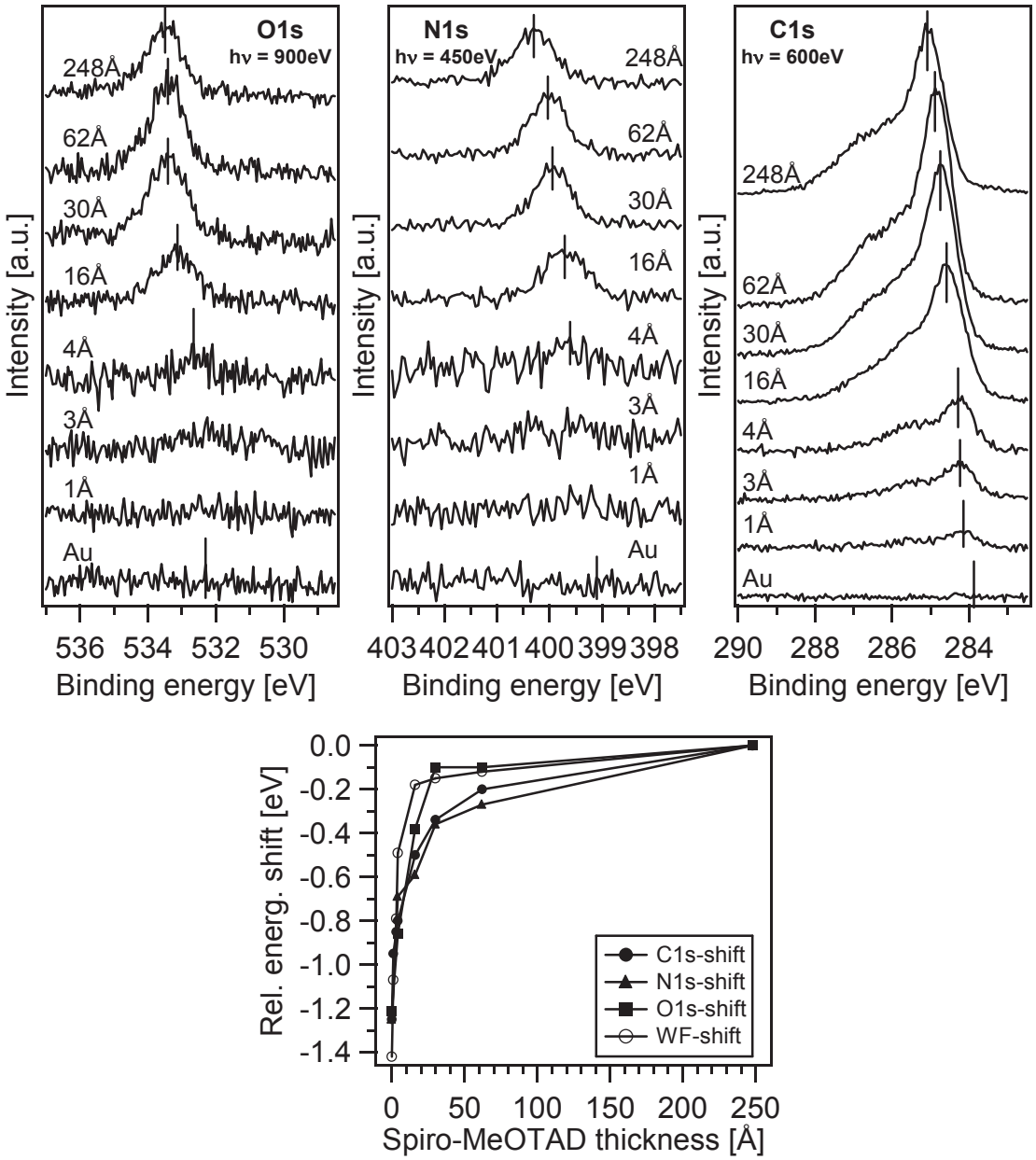

Figure 10.1.: O1s (left), N1s (middle) and C1s (right) core level measurements of the Au/Spiro-MeOTAD interface experiment: the energetic positions of 0 Å are extrapolated; the energetic positions of the intensity maxima are marked in the figures. The shifts of all three core level emissions and the course of the work function are plotted in the figures at the bottom. The initial stronger change in the work function (0.15 eV) is assigned to the formation of an interface dipole. O1s were measured with a a photon energy of 900 eV, C1s spectra with a photon energy of 600 eV and N1s spectra with a photon energy of 450 eV.

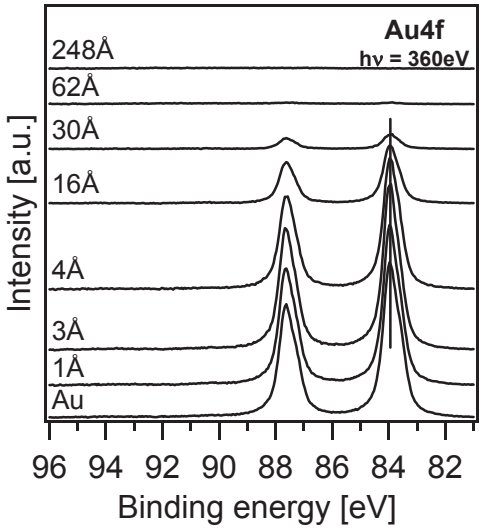

Figure 10.2: The Au4f substrate emission measurements of the Au/Spiro-MeOTAD interface experiment: the signal is completely damped in the last evaporation step proofing a dense Spiro-MeOTAD layer. All spectra were recorded with photon energy of 360 eV.

Valence band

Valence band measurements were recorded at 90 eV, O1s core level at 900 eV, C1s and Ti2p core levels at 600 eV, N1s core level at 450 eV and Au core level at 360 eV photon energy. The evalutation of the O1s and C1s spectra is complicated by the overlapping $N_{67}O_{45}O_{45}$ gold Auger line, which coincides with the energetic position of the O1s and C1s emission recorded at the previously used photon energies of 600 and 360 eV, respectively. Because the characteristic kinetic energy of the measured photoelectrons of an Auger line does not change with varying photon energies, the positions of the Auger lines change with varying photon energies in a plot intensity versus binding energy. Therefore, O1s spectra were measured at 900 eV photon energy and C1s spectra 600 eV to avoid this problem.

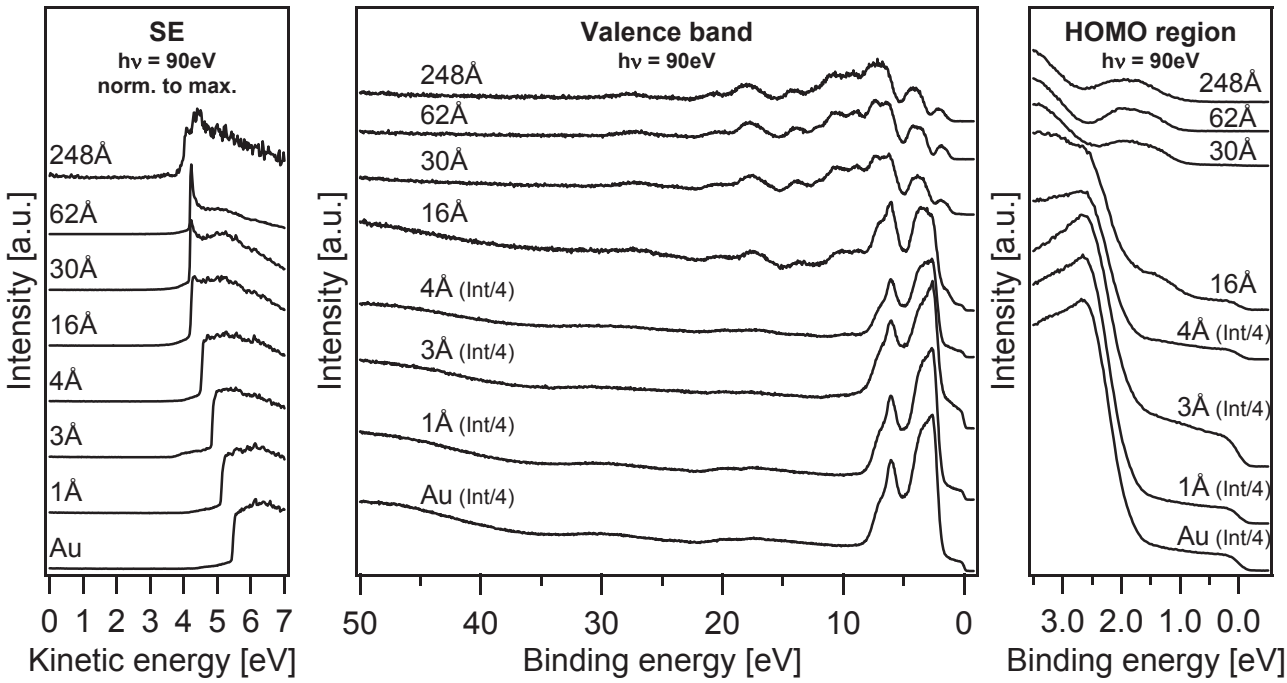

Figure 10.3.: Secondary edge (left), valence band (middle) and HOMO region (right) measurements of the Au/Spiro-MeOTAD interface experiment. All spectra were recorded with a photon energy of 90 eV.

Illustrated in Figure 10.3, the work function of the sputter-cleaned gold is determined to be 5.4 eV and thus 0.3 eV higher than reported in literature (5.1 eV [216]). With increasing Spiro-MeOTAD thickness

the work function decreases to 4.0 eV (at 248 Å thickness), which is a little lower than found for the TiO_2/Spiro-MeOTAD interface (4.1 eV). The Fermi edge and the HOMO of Spiro-MeOTAD overlaps in the region close to 0 eV binding energy. Therefore, the band bending cannot be determined precisely in those spectra, but is taken from the core level shifts instead.

Lineup

The energetic lineup derived from the measurements shown above is summarized in Figure 10.4. The band bending in Spiro-MeOTAD (1.25 eV) is visualized in the figure under the assumption that ionization potential of 5.9 eV stays unaltered. Hereby, the HOMO of Spiro-MeOTAD shifts from the bulk value of 1.9 eV to 1.25 eV right at the interface. The Fermi level/HOMO offset of 0.65 eV is in good agreement with the HOMO extension in one direction (ca. 1 eV). Therefore, the HOMO tail is assumed to overlap with the Fermi level and represents the maximum obtainable band bending in Spiro-MeOTAD. The difference in work function and band bending of 0.15 eV is attributed to an interface dipole.

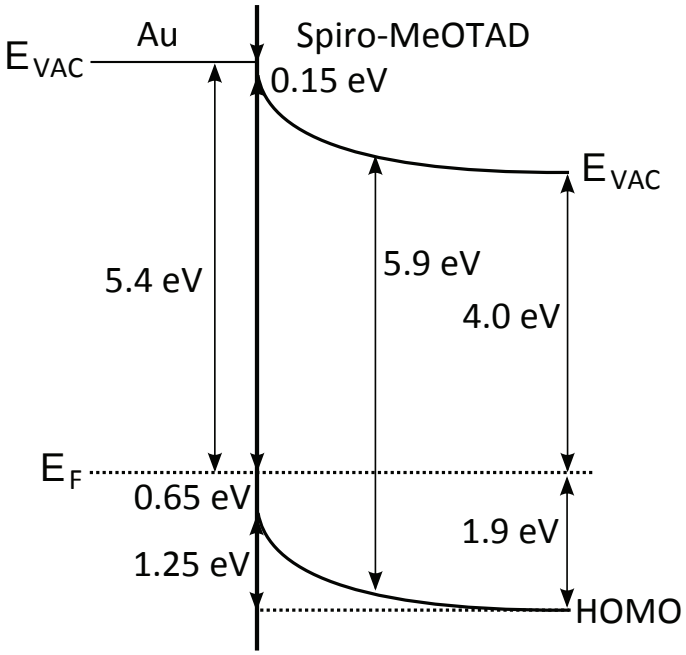

Figure 10.4: The energetic lineup of the Au/Spiro-MeOTAD interface. Energetic positions are deduced from the measurements shown in this section.

C1s-spectra

An additional species in the range of 285.2 to 286.5 eV becomes obvious in the normalized and in binding energy shifted C1s spectra (Figure 10.5). This species located at the interface decreases with increasing Spiro-MeOTAD thickness, which is similar to the oxidized species which evolved during doping of Spiro-MeOTAD with WO_3 and formed due to a dipole at the Spiro-MeOTAD/WO_3 interface (see 8.2.1).

In order to get a more detailed impression of what happens at the interface, difference spectra of the C1s spectra which were normalized to the maximum were created (Figure 10.6). These spectra were obtained by subtracting the bulk spectrum labeled as "248 Å" from the respective spectra. Hereby, the intensity but not the position of the bulk spectrum was varied. All difference spectra show the same curve shape which is comparable to that of the uncharged bulk spectrum. Because no change in the curve shapes and no additional features are visible in the core levels, a chemical reaction can be excluded. The difference as seen in the C1s spectra is rather attributed to an additional oxidized species which forms the dipole at the interface and decreases with increasing Spiro-MeOTAD thickness than to a chemical reaction. Hereby, this species is assumed to originate from the charge transfer to gold.

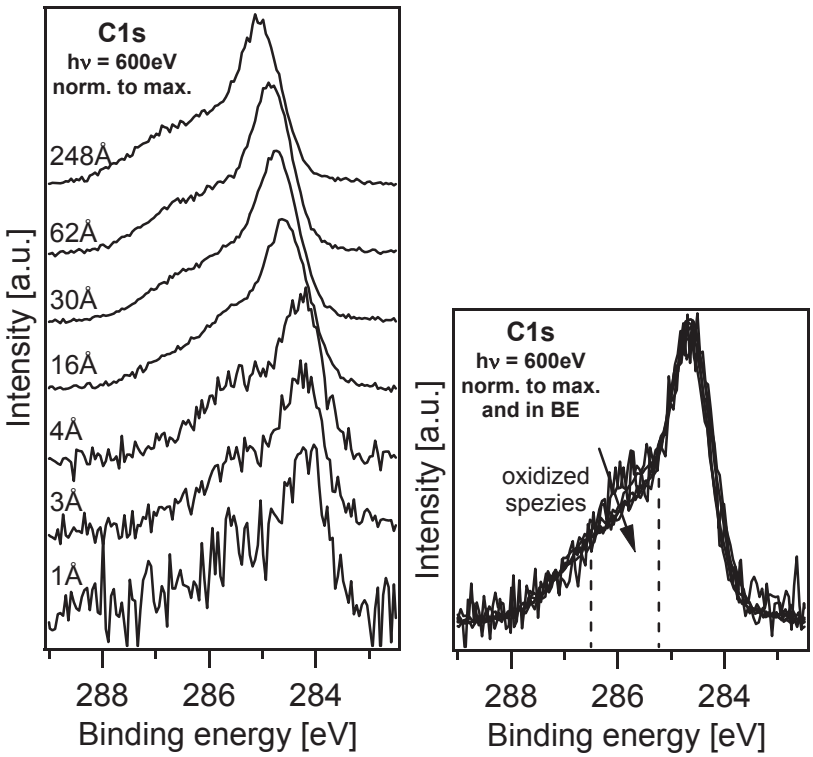

Figure 10.5.: The background subtracted C1s spectra (left) and the same spectra normalized in intensity and binding energy (right): towards the interface, the emission in the range of oxidized C species is increased and decreases with growing Spiro-MeOTAD thickness. The spectra were taken with a photon energy of 600 eV.

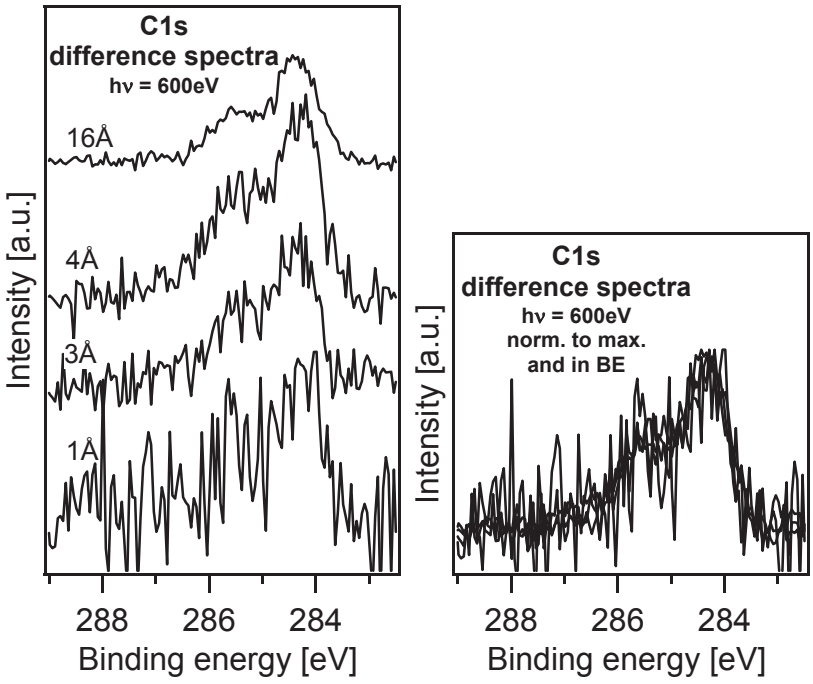

Figure 10.6.: The C1s difference spectra of the normalized C1s spectra shown in Figure 10.5 (left) and the difference spectra normalized in intensity and shifted in binding energy (right). The difference spectra were obtained by subtraction of spectrum "248 Å" from the other spectra.

10.2 Gold / drop-casted Spiro-MeOTAD:TFSI composite

For the solid-state DSSC, the situation at the Au/hole conductor interface is different to the previous interface experiment. The Li-TFSI doping shifts the HOMO energy of Spiro-MeOTAD to lower binding energies compared to the pristine material. Therefore, the driving force to equalize the Fermi levels in both materials is different and, hence, a different band alignment could be formed.

A drop-casted film of a Spiro-MeOTAD:Li-TFSI composite was prepared from a blend of Spiro-MeOTAD dissolved in chloromethane (anhydrous, 99.8%) and Li-TFSI dissolved in cyclohexanone (>99%) solution. The blend consisted of 950 μl of 0.17 M (0.21 g/ml) Spiro-MeOTAD and 50 μl of 0.3 M (0.09 g/ml) Li-TFSI solutions. The drop-casting was performed in a glass cell as described in Section 8. A gold foil which was sputtered for 20 min prior the experiment was used as the substrate. The C1s, N1s and O1s spectra were taken with the same photon energies as in the previous interface experiment, the Li1s, F1s and S2p spectra with 106, 900 and 210 eV, respectively.

Core levels

Figure 10.7 shows the Au4f substrate emission before and after drop-casting. The Au4f emission is completely damped after the deposition, proving a dense Spiro-MeOTAD layer. The experiment was performed with a clean gold foil. No carbon, oxygen and nitrogen contaminations are visible in the gold detail spectra, labeled as "Au" in Figure 10.8.

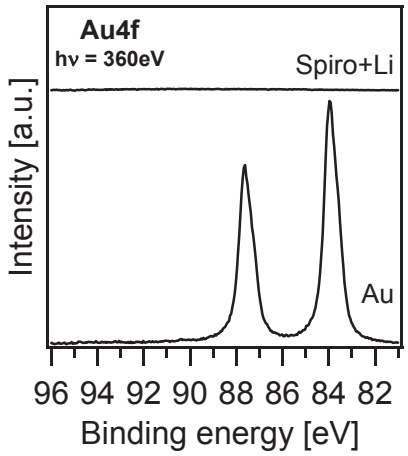

Figure 10.7: The Au4f substrate emissions recorded at a photon energy of 360 eV. The absence of the Au4f emission in the Spiro-MeOTAD:TFSI composite spectrum labeled as "Spiro+Li" proofs a dense layer.

After the drop-casting step, the evolving emissions can be attributed to Spiro-MeOTAD and Li-TFSI. The binding energy positions of the C1s (284.4 eV), N1s (399.6 eV), O1s (533.0 eV), Li1s (56.2 eV), F1s (689.3 eV) and S2p (169.3 eV) intensity maxima are comparable to those obtained for the TiO_2/Spiro-MeOTAD:Li-TFSI experiments shown in Subsection 8.2.2. The emission at ca. [50]eV in the Li1s gold spectrum is rather a feature of gold, similar to that emission in the valance band spectrum (see Figure 10.9), than a Li1s emission. The results are summarized in Table 10.1.

Table 10.1.: The core level binding energy positions of TiO_2/Spiro-MeOTAD:Li-TFSI and Au/Spiro-MeOTAD:Li-TFSI experiments: positions of the intensity maxima and used photon energies are given.

	C1s	N1s	O1s	Li1s	F1s	S2p
Substrate	**360 eV**	**450 eV**	**600 eV**	**106 eV**	**900 eV**	**210 eV**
TiO_2 (0.6M)	284.26 eV	399.45 eV	533.09 eV	56.19 eV	688.97 eV	169.30 eV
TiO_2 (1.2M)	284.42 eV	399.67 eV	533.16 eV	56.33 eV	688.93 eV	169.46 eV
Au (0.3M)	284.40 eV	399.60 eV	533.00 eV	56.18 eV	688.98 eV	169.31 eV

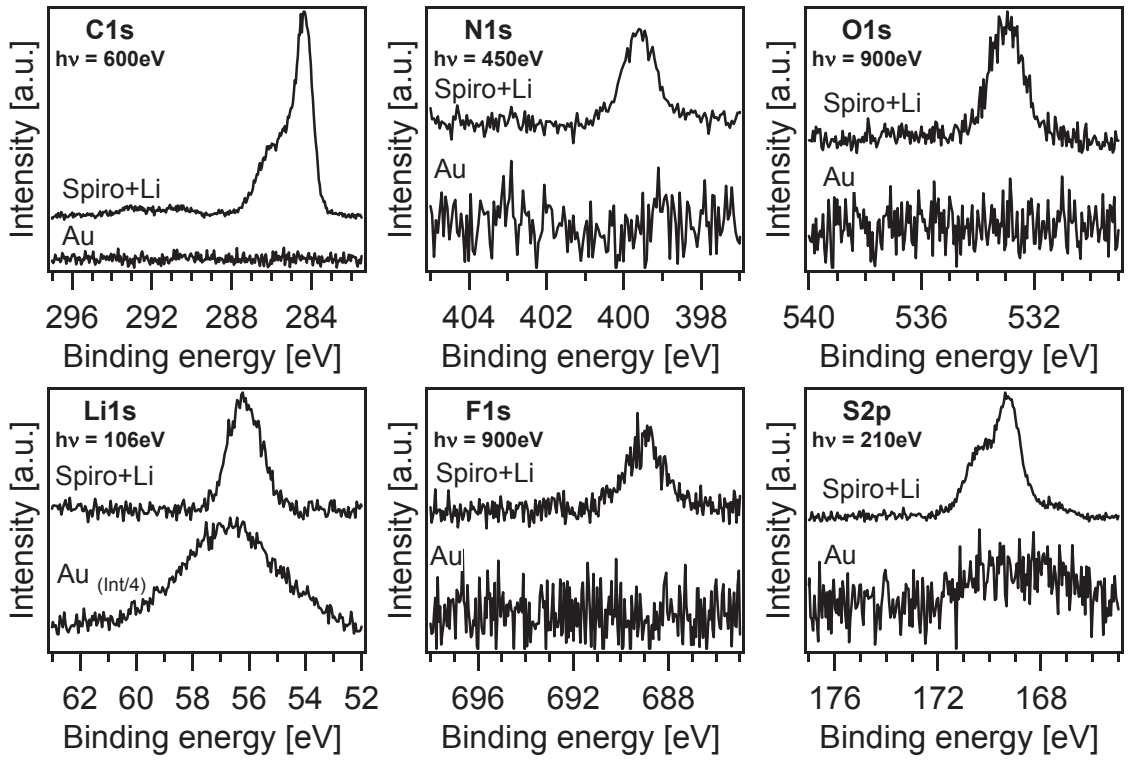

Figure 10.8.: The C1s, N1s, O1s, Li1s, F1s and S2p core level spectra of the Au / drop-casted Spiro-MeOTAD:Li-TFSI composite experiment: the Li1s, F1s and S2p can be attributed solely to the Li:TFSI salt, whereas the C1s, N1s and O1s emissions consist of both Li:TFSI and Spiro-MeOTAD. The gold substrate spectra are labeled as "Au" and the Spiro-MeOTAD:TFSI composite spectra as "Spiro+Li". The C1s spectra were recorded at a photon energy of 360 eV, N1s at 450 eV, O1s and F1s at 900 eV, Li1s at 106 eV and S2p at 210 eV.

Valence band - work function

The HOMO positions of Spiro-MeOTAD were fitted according to the procedure described in Subsection 8.2.2: the HOMO position is decomposed into two emissions originating from Spiro-MeOTAD and, additionally, one induced by the Li-TFSI dopant (10.9). The work function of Spiro-MeOTAD was determined to be 4.9 eV and, thus, 0.9 eV higher than the evaporated Spiro-MeOTAD in the previous section, whereas the work function of gold was the same (5.4 eV).

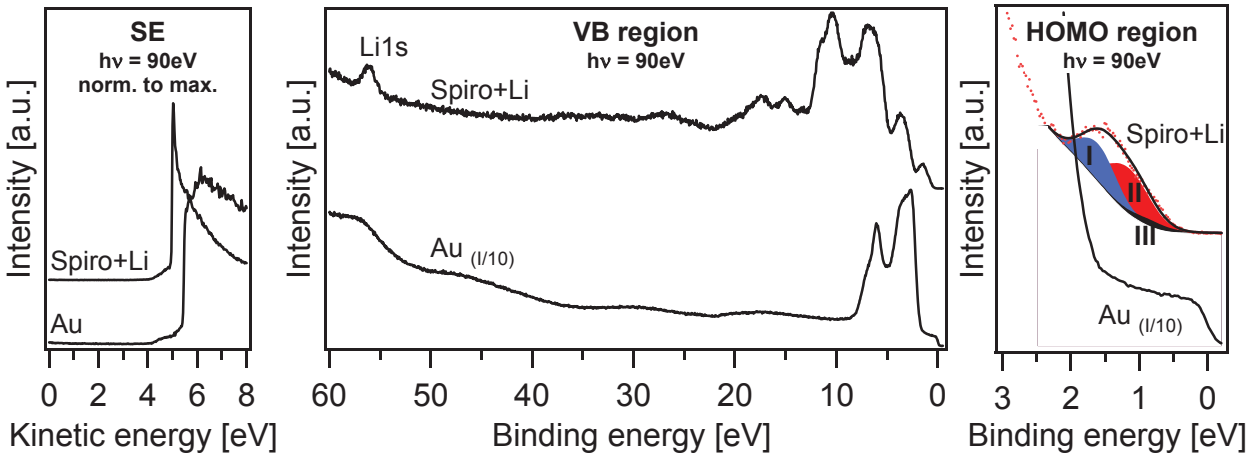

Figure 10.9.: The secondary electron emission edge, valence band and detailed HOMO region of the gold substrate and the Spiro-MeOTAD:TFSI composite: the HOMO emission was fitted as shown in Subsection 8.2.2. The derived values of the work functions are 5.4 for gold and 4.9 eV for Spiro-MeOTAD, respectively. The valence band, HOMO region spectra and secondary edge measurments were recorded at a photon energy of 90 eV.

Comparing the HOMO binding energy position of this drop-casting experiment to drop-casted Spiro-MeOTAD and other Spiro-MeOTAD composites with higher relative amounts of Li-TFSI in Subsection 8.2.2, the HOMO shift is not at its maximum (Table 10.2). Nevertheless, an additional shift due to band bending as a consequence of electron transfer to gold as observed in the interface experiment cannot be completely excluded.

Table 10.2.: The HOMO binding energy positions and work functions of drop-casted Spiro-MeOTAD, the TiO_2/Spiro-MeOTAD:Li-TFSI experiments with different Li-TFSI content (see Subsection 8.2.2) and the Au/Spiro-MeOTAD:Li-TFSI experiment: the position of the intensity maxima and the used photon energies are given.

Photon energy	HOMO 90 eV	HOMO-1 90 eV	$HOMO_{Li}$ 90 eV	Work function 90 eV
drop-casted	1.93 eV	2.37 eV		3.99 eV
Au	1.17 eV	1.61 eV	0.86 eV	4.93 eV
TiO_2 (0.6M)	0.94 eV	1.38 eV	0.63 eV	5.10 eV
TiO_2 (1.2M)	0.99 eV	1.43 eV	0.68 eV	5.02 eV

C1s and Lineup

The C1s emissions of Spiro-MeOTAD:LiTFSI and Spiro-MeOTAD are shown in Figure 10.10. The normalized spectra do not show a significant difference with a low C1s emission of Li-TFSI at ca. 293 eV (compared to the C1s emissions of the TiO_2/Spiro-MeOTAD:Li-TFSI experiments shown in Figure 8.44). Therefore, the oxidized species is assumed to be either too low to be visible or non-existent in the spectra. One reason for this could be that the charge which is transferred from Li to Spiro-MeOTAD is too

low to form a significant contribution in the spectra. This assumption is supported by the HOMO shift which is not at its maximum and hence less charges are transferred to Spiro-MeOTAD due to the relative low and insufficient Li-TFSI content.

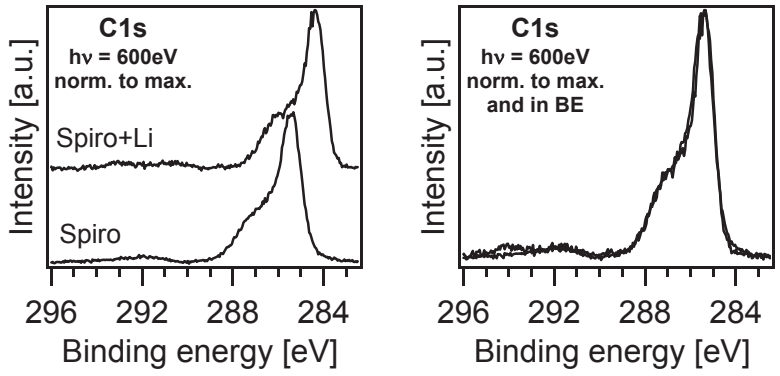

Figure 10.10.: The C1s emissions of Spiro-MeOTAD:LiTFSI and Spiro-MeOTAD recorded at a photon energy of 600 eV. Compared to the Spiro-MeOTAD:LiTFSI composites in Subsection 8.2.2, the C1s emission does not show a reduced component.

Figure 10.11 shows the line up of the thick Spiro-MeOTAD/Li:TFSI layer on gold and the assumed line up at the Au/Spiro-MeOTAD:Li-TFSI interface. For the latter one, a band bending of 0.5 eV is assumed. The band bending is chosen so that the offset of the HOMO of Spiro-MeOTAD and the Fermi level (0.65 eV) is the same as for the Au/Spiro-MeOTAD interface. Compared to pristine Spiro-MeOTAD, the assumed band bending in the doped Spiro-MeOTAD:Li-TFSI composite (0.5 eV) is smaller as the Fermi level is shifted toward the HOMO by doping. Moreover, the interface dipole vanishes in this line up, which can be another explanation for the non-existent oxidized species in the C1s spectra. Nevertheless, an oxidized species which forms due to an interface dipole is probably not visible in the spectra because the Spiro-MeOTAD:Li-TFSI layer is too thick to probe the Spiro-MeOTAD molecules right at the interface.

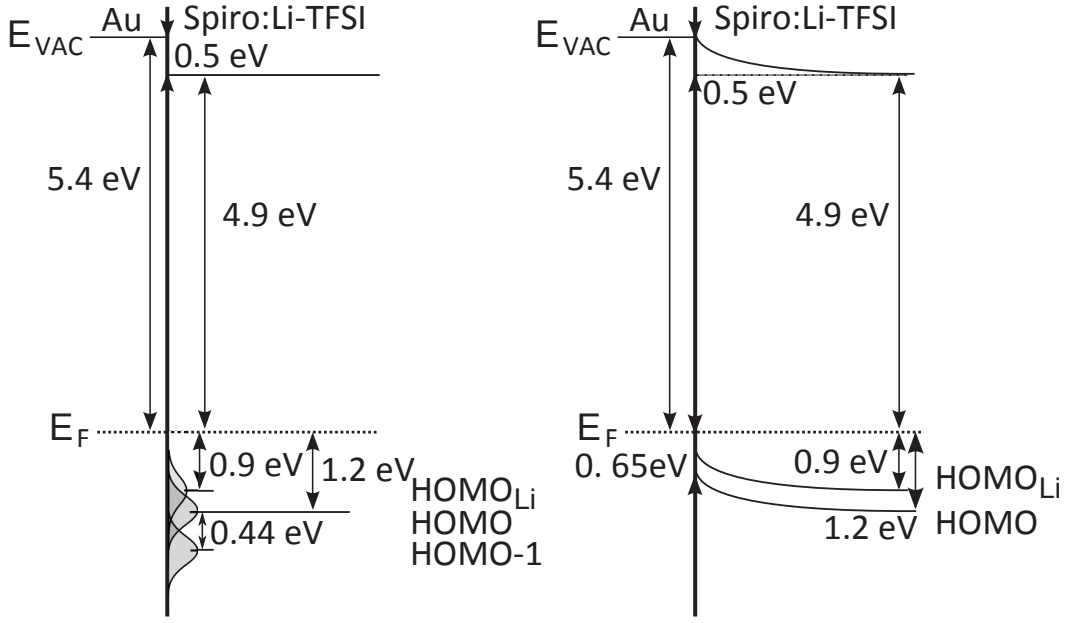

Figure 10.11.: The energetic line up of a thick drop-casted Spiro-MeOTAD:Li-TFSI layer on gold as it is deduced from the measurements (left) and the assumed line up at the Au/Spiro-MeOTAD:Li-TFSI interface (right). The work functions and the energetic positions of the HOMO emissions for a thick Spiro-MeOTAD:Li:TFSI layer on gold are deduced from the measurements shown in this section.

10.3 Summary and discussion

As expected, the Spiro-MeOTAD undergoes a band bending at the interface to gold, whereas the gold itself stays unaltered. Hereby, the work function difference of 1.4 eV is the sum of the band bending of 1.25 eV and a deduced dipole of 0.15 eV. The band bending was derived from the C1s core level shift of Spiro-MeOTAD which is similar to the N1s and O1s core level shift.
As already seen in Subsection 8.2.1, the transferred charges from Spiro-MeOTAD to WO_3 which acts as an electron acceptor causes an additional oxidized species in the C1s spectra recorded after the stepwise evaporation of Spiro-MeOTAD. During the interface experiment, one can locate this species right at the interface. In parallel, an additional species similar to the previous one can be identified in the Au/Spiro-MeOTAD interface experiment. In both cases a chemical reaction is excluded as the origin of the species. One difference is the smaller interface dipole in the case of the Au/Spiro-MeOTAD interface (0.15 eV) compared to the WO_3/Spiro-MeOTAD interface (1.00 eV), which contributes to the observed oxidized species and can explain the smaller intensity of the oxidized species in the C1s emission.

In contrast, no oxidized C1s species is visible in the C1s detail spectrum in the Au/drop-casted Spiro-MeOTAD experiment. Two possible explanations are given in this work. First, the Li-TFSI content of the Spiro-MeOTAD:Li-TFSI composite is too low that a significant oxidized species is formed (compare to Figure 8.49). Second, no interface dipole which can form an oxidized species is deduced from the assumed interface line up of Spiro-MeOTAD:Li-TFSI and gold. Hereby, a band bending toward the interface is assumed as the offset of the HOMO of Spiro-MeOTAD and the Fermi level (0.65 eV) is the same as for the Au/Spiro-MeOTAD interface. The measured work function difference of 0.5 eV is completely equalized by the band bending.
The HOMO fit was performed as described in Subsection 8.2.2: the HOMO position is decomposed into two emission originating from Spiro-MeOTAD (HOMO at 1.2 eV and HOMO-1 at 1.6 eV) and one induced by the Li-TFSI dopant ($HOMO_{Li}$ at 0.9 eV). Compared to the composites in that Subsection the shift is not at its maximum, which supports the given argument for the oxidized C1s species.

11 Summary

The solid-state dye-sensitized solar cells are one possibility to circumvent the problems of the dye-sensitized solar cell with liquid electrolytes that can degrade due to the evaporation of the solvent. In this work, the organic hole-conductor Spiro-MeOTAD, which is often used as a replacement for the liquid iodide/triiodide electrolyte in solid-state DSSCs, was investigated for the first time by SXPS in order to clarify its electronic properties. The industrial Spiro-MeOTAD films are typically manufactured by spin-coating. Because this technique was not experimentally applicable in the SoLIAS, drop-casting as a very similar method was chosen. It is, however, not suitable for interface experiments, where a stepwise deposition of very thin films in the Å range is required. As a consequence, these experiments are typically performed by PVD. Therefore, drop-casted and evaporated Spiro-MeOTAD films were first compared to ensure the comparability of the films produced by these methods. The measurements showed excellent agreement of core orbitals and valence band spectra, and the preparation of contamination free wet deposited films for SXPS characterization was successful. For the interface experiments between Spiro-MeOTAD and the different materials (TiO_2 electrode, dyes, dopants and the back contact material gold) Spiro-MeOTAD films were deposited stepwise via PVD. As one result, the energetic alignment of the materials at the different interfaces could be deduced. Moreover, the doping of Spiro-MeOTAD, wet chemically and via PVD, could be performed and compared in this way.
In general, the energetic alignment of materials is of high importance for solar cells. For the solid-state DSSC, the HOMO of Spiro-MeOTAD has to be aligned to the HOMO of the dye. In this work, metal-free perylene dyes (ID94, ID224 and ID504) obtained from the project partner BASF which are an alternative to the standard ruthenium complexes were investigated. Moreover, the Fermi level of the back contact material, in this case gold, has to match to the HOMO orbitals of Spiro-MeOTAD to guarantee an efficient hole extraction. Therefore, Spiro-MeOTAD was deposited via PVD and drop-casting on TiO_2 and gold substrates and the line up deduced from photoemission measurements. The TiO_2/Spiro-MeOTAD interface showed no band bending and thus no charge transfer, which would contribute to the losses in solid-state DSSCs. As expected, the energy levels of the undoped Spiro-MeOTAD shifted to lower binding energies toward the gold/Spiro-MeOTAD interface, which results in a band bending toward the interface. The band bending enhances the hole extraction into Spiro-MeOTAD and the drift of the holes towards the gold electrode.

Because of its low conductivity, Spiro-MeOTAD is usually p-doped for the use in solid-state DSSCs. In general, the mechanisms of the doping of organic molecules are not completely understood and still under discussion. Therefore, Spiro-MeOTAD was doped wet chemically with Li-TFSI which is widely used and via PVD with WO_3 as a model system and investigated. In both cases the maximum shift of the Fermi level towards the HOMO of Spiro-MeOTAD, which is the obtained doping maximum, was ca. 1.0 eV in the composites. An oxidized species in Spiro-MeOTAD was found in both experiments, right at the WO_3/Spiro-MeOTAD interface and in the WO_3:Spiro-MeOTAD composites as well as in the Spiro-MeOTAD:Li-TFSI composites. This species was a first proof of a charge transfer from the dopant to Spiro-MeOTAD and was attributed to the interface dipole between Spiro-MeOTAD and the dopants. Besides a shift of the Spiro-MeOTAD emissions, a reduced species in the dopant was found which also proofed the charge transfer from the respective dopant to Spiro-MeOTAD: a neutral Li-TFSI component in the Li-TFSI$^+$ and a reduced W^{5+} species in WO_3.

The influence of the different anchoring groups of the dyes ID94 and ID224 on the efficiencies of solid-state dye-sensitized solar cells as well as the influence of the additive ID662 on the dye ID504

concerning an improvement of the efficiency upon the additive incorporation were investigated in this work. The energetic lineup of the dyes to the TiO_2 substrate and to the hole conductor Spiro-MeOTAD were obtained by synchrotron-induced photoemission spectroscopy measurements. Hereby, the additive ID662 influenced the TiO_2/ID504 interface by quenching the TiO_2 gap-states and thus shifting the TiO_2 emissions by ca. 0.2 eV to lower binding energies compared to the interface without the additive. It is assumed that this effect also enlarges the open-circuit voltage as described in Subsection 9.1. The energetic line ups of the two dyes ID94 and ID224, which have the same structure except the anchoring group, to the TiO_2 substrates were the same. The dye ID94 docks via two Ti-O bonds to TiO_2 and the dye ID224 via one bond. Hereby, the first assumption was that the different docking mechanisms separate the dyes differently from each other, which should lead to less exciton quenching and thus a higher efficiency. However, the shape of the emissions of both dyes were the same, which does not support the assumption that either of the dye molecules are separated better than the other one.

The electronic properties, the anatase crystal phase and the denseness of the TiO_2 substrates, nanocrystalline and blocking layers, obtained from the projectpartner BASF and Bosch were investigated by REM, AFM, Raman, XRD and SXPS. SXPS measurements showed excellent agreement of the valence band distribution, gap-states and core levels of the two TiO_2 substrate types. Furthermore, varying efficiencies of cells using the same TiO_2 precursor material and the same recipe to prepare TiO_2 electrodes were obtained in different laboratories. Therefore, ex-situ heat treatments were performed on different ex-situ prepared nc-TiO_2 films. The films were systematically heated either using a hot plate or a heat gun. In both cases, the intensity of a contribution due to sodium observed as the Na2p core level increased after the heat treatment. The experiments clarified the source of the observed sodium which was the precursor material used for the TiO_2 electrodes. Consequently, the possible causes of the different efficiencies are the variations in the surface Na content, distribution, and chemical composition due to the variations in temperature treatment. Efficiency measurements on solid-state DSSCs performed by Bosch lead to the assumption that surface Na can improve the cell performance. These measurements were carried out on TiO_2 with different bulk Na contents and at a temperature of 150 °C.

12 Outlook

Printed electronics is a route to cost effective production of solar cells, light emitting diodes, thin film transistors, sensors, batteries, and displays. Photoelectron spectroscopy has proven to be a suitable method for the characterization of the electronic and chemical structure of semiconductors and semiconductor interfaces. The experiments in this work has also proven the applicability and equality of the two deposition methods, PVD and spin-coating, for Spiro-MeOTAD in terms of electronical properties. If other molecules which are stable during PVD and in solution show the same behavior, PVD can be used for modelling those molecules, as well. This enables one to perform interface experiments by stepwise deposition of the molecules and thus investigating the interface properties, which are not that easily accesable with drop-casting experiments.

The experiments on Spiro-MeOTAD/WO_3 and Spiro-MeOTAD/Li-TFSI composites were a further step towards the understanding of the doping mechanisms in organic semiconductors. As observed very high amounts of dopants are necessary, which was as shown by Mayer, Hein et al. is due to the formation of WO_3 clusters within the organic matrix and thus limiting the accessable amount of dopant [135]. Therefore, dopants are necessary which do not cluster in the organic matrix. Furthermore, as Spiro-MeOTAD is usually spin-coated, soluble dopants have to be found, like the investigated Li-TFSI.

The influence of the additive ID662 on the line up of the dye ID504 to the TiO_2 electrode was investigated in this work. Nevertheless, the additive could influence the line up of the dye to Spiro-MeOTAD, as well. Therefore, a ID662+ID504/Spiro-MeOTAD interface experiment should be performed. Furthermore, the investigation of ruthenium-free perylene dyes showed their possible application in the solid-state DSSC. In order to improve the efficiency of the solid-state DSSC, further work has to be done to improve the fitting of the HOMO and LUMO levels to the HOMO of Spiro-MeOTAD and the conduction band minimum of TiO_2.

In order to investigate the back contact of solid-state DSSCs in more detail, interface experiments between differently doped Spiro-MeOTAD and gold have to be performed. As the Spiro-MeOTAD:Li-TFSI cannot be codeposited, interface experiments with doped Spiro-MeOTAD films on which gold is evaporated are more practicable. In this work, WO_3/gold and Spiro-MeOTAD/gold interface experiments which are not shown were performed in the SoLIAS. Because the evaporation temperature of gold was approximately 1100 °C, residual molecules and other contaminations which are adsorbed to the UHV chamber walls, became desorbed due to the heating of the chamber by the gold source and hence were included in the deposited gold layer. Due to this the obtained spectra could not be used for analysis. Therefore, a clean UHV chamber is necessary to obtain pristine gold layers and good results.

Appendix

Table .1.: Additional information for Subsection 7.1.3: A detailed table of all SnO_2 and Anatase reference reflections and their indices, 2θ values and relative intensities (compare to Figure 7.3). Values are taken from the XRD-system library.

SnO_2			Anatase		
2 θ	**rel. Intensity**	**hkl**	**2 θ**	**rel. Intensity**	**hkl**
26.487	1.000	110	25.281	1.000	101
33.740	0.757	101	36.947	0.010	103
37.808	0.207	200	37.801	0.020	004
38.823	0.033	111	38.576	0.010	112
42.474	0.012	210	48.050	0.035	200
51.564	0.515	211	53.891	0.020	105
54.539	0.116	220	55.062	0.020	211
57.574	0.058	002	62.121	0.004	213
61.629	0.104	310	62.690	0.014	204
62.342	0.001	221	68.762	0.006	116
64.453	0.106	112	70.311	0.006	220
65.687	0.033	301	74.031	0.002	107
68.947	0.001	311	75.032	0.010	215
70.957	0.051	202	76.020	0.004	301
74.110	0.002	212	80.727	0.002	008
78.359	0.073	321	82.139	0.002	303
80.776	0.022	400	82.669	0.006	224
83.318	0.047	222	83.149	0.004	312
83.811	0.002	410			
86.829	0.021	330			
89.348	0.056	312			

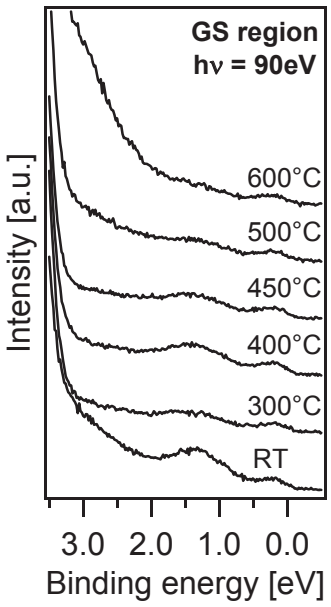

Figure .1: Additional information for Subsection 7.2.2: SXPS spectra of the nc-TiO_2 film in the course of hot plate heat treatment recorded at 90 eV: gap states region.

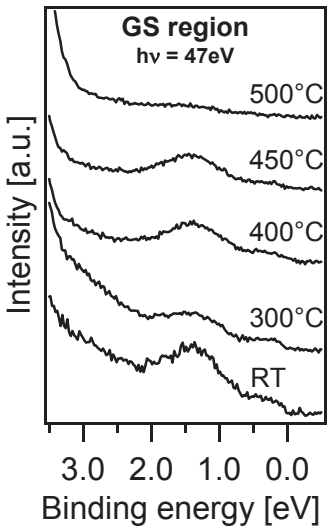

Figure .2: Additional information for Subsection 7.2.2: SXPS spectra of the nc-TiO_2 film in the course of heat gun heat treatment recorded at 90 eV: gap states region.

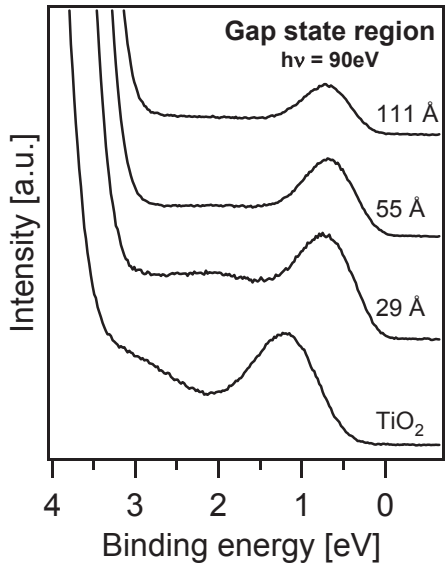

Figure .3: Additional information for Subsection 8.2.1: The spectra of the gap states region of the TiO_2 substrate (labeled as TiO_2) and WO_3 (labeled as 111 Å) deposited onto TiO_2, recorded at 90 eV photon energy. Both materials show gap states: TiO_2 at 1.2 eV and WO_3 at 0.8 eV.

Bibliography

[1] M. Grätzel, Nature **414**, 338 (2001).

[2] M. A. Green, K. Emery, Y. Hishikawa, W. Warta, and E. D. Dunlop, Progress in Photovoltaics **20**, 12 (2012).

[3] B. O'Regan and M. Grätzel, Nature **353**, 737 (1991).

[4] J. Moser, Monatshefte für Chemie **8**, 373 (1887).

[5] J. Desilvestro, M. Grätzel, L. Kavan, J. Moser, and J. Augustynski, Journal of the American Chemical Society **107**, 2988 (1985).

[6] M. Grätzel, Journal of Photochemistry and Photobiology C-Photochemistry Reviews **4**, 145 (2003).

[7] A. Hagfeldt and M. Grätzel, Chemical Reviews **95**, 49 (1995).

[8] H. Kuhn, The Journal of Chemical Physics **17**, 1198 (1949).

[9] J. Fabian, H. Nakazumi, and M. Matsuoka, Chemical Reviews **92**, 1197 (1992).

[10] M. Schwoerer and H. C. Wolf, *Organische Molekulare Festkörper* (Wiley-VCH Verlag GmbH & Co. KG, Berlin, 2005).

[11] K. Schwanitz, Dissertation, Technische Universität Darmstadt, 2008.

[12] L. M. Peter, Physical Chemistry Chemical Physics **9**, 2630 (2007).

[13] L. M. Peter, Journal of Physical Chemistry C **111**, 6601 (2007).

[14] I. Montanari, J. Nelson, and J. R. Durrant, Journal of Physical Chemistry B **106**, 12203 (2002).

[15] H. J. Snaith, Advanced Functional Materials **20**, 13 (2010).

[16] T. Hannappel, B. Burfeindt, W. Storck, and F. Willig, Journal of Physical Chemistry B **101**, 6799 (1997).

[17] N. A. Anderson and T. Lian, Coordination Chemistry Reviews **248**, 1231 (2004).

[18] M. Grätzel, Inorganic Chemistry **44**, 6841 (2005).

[19] Y. Tachibana, J. E. Moser, M. Grätzel, D. R. Klug, and J. R. Durrant, Journal of Physical Chemistry **100**, 20056 (1996).

[20] A. Hagfeldt and M. Grätzel, Accounts of Chemical Research **33**, 269 (2000).

[21] M. D. McGehee, Science **334**, 607 (2011).

[22] G. Boschloo and A. Hagfeldt, Accounts of Chemical Research **42**, 1819 (2009).

[23] S. M. Feldt, E. A. Gibson, E. Gabrielsson, L. Sun, G. Boschloo, and A. Hagfeldt, Journal of the American Chemical Society **132**, 16714 (2010).

[24] A. Yella, H. W. Lee, H. N. Tsao, C. Y. Yi, A. K. Chandiran, M. K. Nazeeruddin, E. W. G. Diau, C. Y. Yeh, S. M. Zakeeruddin, and M. Grätzel, Science **334**, 629 (2011).

[25] M. Grätzel, 27th European Photovoltaic Solar Energy Conference and Exhibition 2158 (2012).

[26] M. K. Wang, A. M. Anghel, B. Marsan, N. L. C. Ha, N. Pootrakulchote, S. M. Zakeeruddin, and M. Grätzel, Journal of the American Chemical Society **131**, 15976 (2009).

[27] Y. J. Wei, C. G. Liu, and L. P. Mo, Spectroscopy and Spectral Analysis **25**, 86 (2005).

[28] C. Li *et al.*, ChemSusChem **1**, 615 (2008).

[29] J. Salbeck, F. Weissörtel, and J. Bauer, Macromolecular Symposia **125**, 121 (1998).

[30] J. Salbeck, N. Yu, J. Bauer, F. Weissörtel, and H. Bestgen, Synthetic Metals **91**, 209 (1997).

[31] U. Bach, D. Lupo, P. Comte, J. E. Moser, F. Weissörtel, J. Salbeck, H. Spreitzer, and M. Grätzel, Nature **395**, 583 (1998).

[32] J. E. Kroeze, N. Hirata, L. Schmidt-Mende, C. Orizu, S. D. Ogier, K. Carr, M. Grätzel, and J. R. Durrant, Advanced Functional Materials **16**, 1832 (2006).

[33] J. H. Yum, P. Chen, M. Grätzel, and M. K. Nazeeruddin, ChemSusChem **1**, 699 (2008).

[34] L. Schmidt-Mende, U. Bach, R. Humphry-Baker, T. Horiuchi, H. Miura, S. Ito, S. Uchida, and M. Grätzel, Advanced Materials **17**, 813 (2005).

[35] L. Schmidt-Mende and M. Grätzel, Thin Solid Films **500**, 296 (2006).

[36] M. K. Wang *et al.*, Advanced Materials **20**, 4460 (2008).

[37] B. Peng, G. Jungmann, C. Jager, D. Haarer, H. W. Schmidt, and M. Thelakkat, Coordination Chemistry Reviews **248**, 1479 (2004).

[38] P. J. Cameron and L. M. Peter, Journal of Physical Chemistry B **107**, 14394 (2003).

[39] U. Bach, Y. Tachibana, J. E. Moser, S. A. Haque, J. R. Durrant, M. Grätzel, and D. R. Klug, Journal of the American Chemical Society **121**, 7445 (1999).

[40] H. J. Snaith and L. Schmidt-Mende, Advanced Materials **19**, 3187 (2007).

[41] I. K. Ding, N. Tetreault, J. Brillet, B. E. Hardin, E. H. Smith, S. J. Rosenthal, F. Sauvage, M. Grätzel, and M. D. McGehee, Advanced Functional Materials **19**, 2431 (2009).

[42] W. H. Howie, J. E. Harris, J. R. Jennings, and L. M. Peter, Solar Energy Materials and Solar Cells **91**, 424 (2007).

[43] C. S. Karthikeyan and M. Thelakkat, Inorganica Chimica Acta **361**, 635 (2008).

[44] S. A. Haque, T. Park, A. B. Holmes, and J. R. Durrant, ChemPhysChem **4**, 89 (2003).

[45] F. Fabregat-Santiago, J. Bisquert, L. Cevey, P. Chen, M. K. Wang, S. M. Zakeeruddin, and M. Grätzel, Journal of the American Chemical Society **131**, 558 (2009).

[46] J. R. Jennings and L. M. Peter, Journal of Physical Chemistry C **111**, 16100 (2007).

[47] J. Kruger, R. Plass, M. Grätzel, P. J. Cameron, and L. M. Peter, Journal of Physical Chemistry B **107**, 7536 (2003).

[48] H. J. Snaith and M. Grätzel, Advanced Materials **19**, 3643 (2007).

[49] H. J. Snaith and M. Grätzel, Applied Physics Letters **89**, 26114 (2006).

[50] Weissörtel, Dissertation, Universität Regensburg, 1999.

[51] R. Schmechel, Journal of Applied Physics **93**, 4653 (2003).

[52] L. G. Kaake, P. F. Barbara, and X. Y. Zhu, Journal of Physical Chemistry Letters **1**, 628 (2010).

[53] A. Schweig, U. Weidner, Hellwink.D, and W. Krapp, Angewandte Chemie-International Edition in English **12**, 310 (1973).

[54] N. Johansson, D. A. dosSantos, S. Guo, J. Cornil, M. Fahlman, J. Salbeck, H. Schenk, H. Arwin, J. L. Bredas, and W. R. Salanek, Journal of Chemical Physics **107**, 2542 (1997).

[55] A. Wold, Chemistry of Materials **5**, 280 (1993).

[56] L. Kavan, M. Grätzel, S. E. Gilbert, C. Klemenz, and H. J. Scheel, Journal of the American Chemical Society **118**, 6716 (1996).

[57] M. R. Hoffmann, S. T. Martin, W. Y. Choi, and D. W. Bahnemann, Chemical Reviews **95**, 69 (1995).

[58] C. J. Barbe, F. Arendse, P. Comte, M. Jirousek, F. Lenzmann, V. Shklover, and M. Grätzel, Journal of the American Ceramic Society **80**, 3157 (1997).

[59] C. Lin, F. Y. Tsai, M. H. Lee, C. H. Lee, T. C. Tien, L. P. Wang, and S. Y. Tsai, Journal of Materials Chemistry **19**, 2999 (2009).

[60] L. Kavan and M. Grätzel, Electrochimica Acta **40**, 643 (1995).

[61] S. D. Mo and W. Y. Ching, Physical Review B **51**, 13023 (1995).

[62] D. Bersani, P. P. Lottici, and X. Z. Ding, Applied Physics Letters **72**, 73 (1998).

[63] P. P. Lottici, D. Bersani, M. Braghini, and A. Montenero, Journal of Materials Science **28**, 177 (1993).

[64] U. Diebold, Surface Science Reports **48**, 53 (2003).

[65] L. Forro, O. Chauvet, D. Emin, L. Zuppiroli, H. Berger, and F. Levy, Journal of Applied Physics **75**, 633 (1994).

[66] S. Kambe, S. Nakade, Y. Wada, T. Kitamura, and S. Yanagida, Journal of Materials Chemistry **12**, 723 (2002).

[67] D. Cahen, G. Hodes, M. Grätzel, J. F. Guillemoles, and I. Riess, Journal of Physical Chemistry B **104**, 2053 (2000).

[68] B. A. Gregg, Coordination Chemistry Reviews **248**, 1215 (2004).

[69] N. G. Park, J. van de Lagemaat, and A. J. Frank, Journal of Physical Chemistry B **104**, 8989 (2000).

[70] G. H. Li, C. P. Richter, R. L. Milot, L. Cai, C. A. Schmuttenmaer, R. H. Crabtree, G. W. Brudvig, and V. S. Batista, Dalton Transactions 10078 (2009).

[71] R. Asahi, Y. Taga, W. Mannstadt, and A. J. Freeman, Physical Review B **61**, 7459 (2000).

[72] A. G. Thomas *et al.*, Physical Review B **75**, 035105 (2007).

[73] R. Heise, R. Courths, and S. Witzel, Solid State Communications **84**, 599 (1992).

[74] Z. M. Zhang, S. P. Jeng, and V. E. Henrich, Physical Review B **43**, 12004 (1991).

[75] M. Ramamoorthy, R. D. Kingsmith, and D. Vanderbilt, Physical Review B **49**, 7709 (1994).

[76] P. J. D. Lindan, N. M. Harrison, M. J. Gillan, and J. A. White, Physical Review B **55**, 15919 (1997).

[77] A. T. Paxton and L. Thien-Nga, Physical Review B **57**, 1579 (1998).

[78] G. M. Liu, W. Jaegermann, J. J. He, V. Sundstrom, and L. C. Sun, Journal of Physical Chemistry B **106**, 5814 (2002).

[79] A. G. Thomas, W. R. Flavell, A. R. Kumarasinghe, A. K. Mallick, D. Tsoutsou, G. C. Smith, R. Stockbauer, S. Patel, M. Grätzel, and R. Hengerer, Physical Review B **67**, 035110 .

[80] K. Westermark, A. Henningsson, H. Rensmo, S. Sodergren, H. Siegbahn, and A. Hagfeldt, Chemical Physics **285**, 157 (2002).

[81] K. Schwanitz, U. Weiler, R. Hunger, T. Mayer, and W. Jaegermann, Journal of Physical Chemistry C **111**, 849 (2007).

[82] K. Schwanitz, E. Mankel, R. Hunger, T. Mayer, and W. Jaegermann, Chimia **61**, 796 (2007).

[83] F. Nunzi, E. Mosconi, L. Storchi, E. Ronca, A. Selloni, M. Grätzel, and F. De Angelis, Energy & Environmental Science **6**, 1221 (2013).

[84] G. Schlichthorl, S. Y. Huang, J. Sprague, and A. J. Frank, Journal of Physical Chemistry B **101**, 8141 (1997).

[85] S. Yu, S. Ahmadi, C. H. Sun, P. Palmgren, F. Hennies, M. Zuleta, and M. Gothelid, Journal of Physical Chemistry C **114**, 2315 (2010).

[86] A. J. Frank, N. Kopidakis, and J. van de Lagemaat, Coordination Chemistry Reviews **248**, 1165 (2004).

[87] K. Zhu, N. Kopidakis, N. R. Neale, J. van de Lagemaat, and A. J. Frank, Journal of Physical Chemistry B **110**, 25174 (2006).

[88] T. P. I. Saragi, T. Spehr, A. Siebert, T. Fuhrmann-Lieker, and J. Salbeck, Chemical Reviews **107**, 1011 (2007).

[89] Y. Shirota and H. Kageyama, Chemical Reviews **107**, 953 (2007).

[90] K. Naito and A. Miura, Journal of Physical Chemistry **97**, 6240 (1993).

[91] K. Naito, Chemistry of Materials **6**, 2343 (1994).

[92] R. Pudzich, T. Fuhrmann-Lieker, and J. Salbeck, Emissive Materials: Nanomaterials **199**, 83 (2006).

[93] U. Bach, K. De Cloedt, H. Spreitzer, and M. Grätzel, Advanced Materials **12**, 1060 (2000).

[94] H. E. Simmons and T. Fukunaga, Journal of the American Chemical Society **89**, 5208 (1967).

[95] N. A. Vandantzig, D. H. Levy, C. Vigo, and P. Piotrowiak, Journal of Chemical Physics **103**, 4894 (1995).

[96] A. L. Shain, J. P. Ackerman, and M. W. Teague, Chemical Physics Letters **3**, 550 (1969).

[97] V. Prelog and D. Bedekovic, Helvetica Chimica Acta **62**, 2285 (1979).

[98] B. Schartel, S. Kruger, V. Wachtendorf, and M. Hennecke, Journal of Chemical Physics **112**, 9822 (2000).

[99] W. T. Yip, D. H. Levy, R. Kobetic, and P. Piotrowiak, Journal of Physical Chemistry A **103**, 10 (1999).

[100] D. Poplavskyy and J. Nelson, Journal of Applied Physics **93**, 341 (2003).

[101] H. Bassler, Physica Status Solidi B-Basic Research **175**, 15 (1993).

[102] O. Rana, R. Srivastava, R. Grover, M. Zulfequar, M. Husain, and M. N. Kamalasanan, Synthetic Metals **161**, 828 (2011).

[103] A. Kahn, W. Zhao, W. Y. Gao, H. Vazquez, and F. Flores, Chemical Physics **325**, 129 (2006).

[104] M. Pfeiffer, K. Leo, X. Zhou, J. S. Huang, M. Hofmann, A. Werner, and J. Blochwitz-Nimoth, Organic Electronics **4**, 89 (2003).

[105] C. K. Chan, W. Zhao, A. Kahn, and I. G. Hill, Applied Physics Letters **94**, 203306 (2009).

[106] B. Enright, G. Redmond, and D. Fitzmaurice, Journal of Physical Chemistry **98**, 6195 (1994).

[107] C. L. Olson, J. Nelson, and M. S. Islam, Journal of Physical Chemistry B **110**, 9995 (2006).

[108] G. Redmond and D. Fitzmaurice, Journal of Physical Chemistry **97**, 1426 (1993).

[109] S. E. Koops, B. C. O'Regan, P. R. F. Barnes, and J. R. Durrant, Journal of the American Chemical Society **131**, 4808 (2009).

[110] H. Wriedt, Journal of Phase Equilibria **10**, 368 (1989).

[111] T. Vogt, P. M. Woodward, and B. A. Hunter, Journal of Solid State Chemistry **144**, 209 (1999).

[112] K. Kosuge, *Chemistry of Non-Stoichiometric Compounds* (Oxford University Press, Oxford, 1994).

[113] E. Salje and K. Viswanathan, Acta Crystallographica Section A **A 31**, 356 (1975).

[114] D. Gogova, K. Gesheva, A. Szekeres, and M. Sendova-Vassileva, Physica Status Solidi a-Applied Research **176**, 969 (1999).

[115] A. Azens, M. Kitenbergs, and U. Kanders, Vacuum **46**, 745 (1995).

[116] L. Ottaviano, M. Rossi, and S. Santucci, Thin Solid Films **490**, 59 (2005).

[117] A. Antonaia, T. Polichetti, M. L. Addonizio, S. Aprea, C. Minarini, and A. Rubino, Thin Solid Films **354**, 73 (1999).

[118] K. J. Patel, C. J. Panchal, V. A. Kheraj, and M. S. Desai, Materials Chemistry and Physics **114**, 475 (2009).

[119] L. Weinhardt, M. Blum, M. Bar, C. Heske, B. Cole, B. Marsen, and E. L. Miller, Journal of Physical Chemistry C **112**, 3078 (2008).

[120] Y. Shigesato, A. Murayama, T. Kamimori, and K. Matsuhiro, Applied Surface Science **33-4**, 804 (1988).

[121] F. G. Bauke and J. Zauner, Physik in unserer Zeit **18**, 21 (1987).

[122] F. J. Himpsel, J. F. Morar, F. R. Mcfeely, R. A. Pollak, and G. Hollinger, Physical Review B **30**, 7236 (1984).

[123] A. Stashans and S. Lunell, International Journal of Quantum Chemistry **63**, 729 (1997).

[124] R. A. Dixon, J. J. Williams, D. Morris, J. Rebane, F. H. Jones, R. G. Egdell, and S. W. Downes, Surface Science **399**, 199 (1998).

[125] K. Mašek, S. Nemšák, M. Mravčáková, P. Blumentrit, T. Skála, M. Škoda, and V. Matolín, Journal of Physics: Conference Series **100**, 012008 (2008).

[126] K. Mašek, J. Libra, T. Skála, M. Cabala, V. Matolín, V. Cháb, and K. C. Prince, Surface Science **600**, 1624 (2006).

[127] X. Huang, H. J. Zhai, J. Li, and L. S. Wang, Journal of Physical Chemistry A **110**, 85 (2006).

[128] X. Huang, H. J. Zhai, B. Kiran, and L. S. Wang, Angewandte Chemie-International Edition **44**, 7251 (2005).

[129] M. Kroger, S. Hamwi, J. Meyer, T. Riedl, W. Kowalsky, and A. Kahn, Organic Electronics **10**, 932 (2009).

[130] S. D. Ha, J. Meyer, and A. Kahn, Physical Review B **82**, 155434 (2010).

[131] J. Meyer, S. Hamwi, S. Schmale, T. Winkler, H. H. Johannes, T. Riedl, and W. Kowalsky, Journal of Materials Chemistry **19**, 702 (2009).

[132] C. Hein, E. Mankel, T. Mayer, and W. Jaegermann, Physica Status Solidi a-Applications and Materials Science **206**, 2757 (2009).

[133] S. Olthof, W. Tress, R. Meerheim, B. Lussem, and K. Leo, Journal of Applied Physics **106**, 103711 (2009).

[134] S. Braun, W. R. Salaneck, and M. Fahlman, Advanced Materials **21**, 1450 (2009).

[135] T. Mayer, C. Hein, E. Mankel, W. Jaegermann, M. M. Muller, and H. J. Kleebe, Organic Electronics **13**, 1356 (2012).

[136] H. Ishii, N. Hayashi, E. Ito, Y. Washizu, K. Sugi, Y. Kimura, M. Niwano, Y. Ouchi, and K. Seki, Physica Status Solidi a-Applied Research **201**, 1075 (2004).

[137] J. H. Lee, H. M. Kim, K. B. Kim, and J. J. Kim, Organic Electronics **12**, 950 (2011).

[138] F. De Angelis, G. Vitillaro, L. Kavan, M. K. Nazeeruddin, and M. Grätzel, Journal of Physical Chemistry C **116**, 18124 (2012).

[139] M. K. Nazeeruddin, A. Kay, I. Rodicio, R. Humphrybaker, E. Muller, P. Liska, N. Vlachopoulos, and M. Grätzel, Journal of the American Chemical Society **115**, 6382 (1993).

[140] A. S. Polo, M. K. Itokazu, and N. Y. M. Iha, Coordination Chemistry Reviews **248**, 1343 (2004).

[141] K. Kalyanasundaram and M. Grätzel, Coordination Chemistry Reviews **177**, 347 (1998).

[142] A. Mishra, M. Fischer, and P. Bäuerle, Angewandte Chemie **121**, 2510 (2009).

[143] S. Ito *et al.*, Advanced Materials **18**, 1202 (2006).

[144] S. Ito, H. Miura, S. Uchida, M. Takata, K. Sumioka, P. Liska, P. Comte, P. Pechy, and M. Grätzel, Chemical Communications 5194 (2008).

[145] S. Hwang *et al.*, Chemical Communications 4887 (2007).

[146] T. Mayer, M. Lebedev, R. Hunger, and W. Jaegermann, Applied Surface Science **252**, 31 (2005).

[147] H. Hertz, Annalen der Physik **267**, 983 (1887).

[148] A. Einstein, Annalen der Physik **322**, 132 (1905).

[149] C. Nordling, E. Sokolowski, and K. Siegbahn, Physical Review **105**, 1676 (1957).

[150] S. Hagström, C. Nordling, and K. Siegbahn, Zeitschrift für Physik **178**, 439 (1964).

[151] K. Siegbahn *et al.*, *ESCA applied to free molecules* (North-Holland Pub Co, Amsterdam, 1969).

[152] J. Moulder, W. Stickle, P. Sobol, and K. Bomben, *Handbook of X-ray Photoelectron Spectroscopy: A Reference Book of Standard Spectra for Identification and Interpretation of XPS Data* (Perkin-Elmer Corporatioon, Waltham, 1995).

[153] B. Feuerbacher, B. Fitton, and R. Willis, *Photoemission and the Electronic Properties of Surfaces* (John Wiley & Sons Inc., New York, 1978).

[154] S. Tanuma, C. J. Powell, and D. R. Penn, Surface and Interface Analysis **21**, 165 (1994).

[155] M. L. M. Rocco, M. Haeming, D. R. Batchelor, R. Fink, A. Scholl, and E. Umbach, The Journal of Chemical Physics **129**, 074702 (2008).

[156] T. Rhodin and G. Ertl, *The nature of the surface chemical bond* (North-Holland Pub Co, Amsterdam, 1979).

[157] J. Yeh and I. Lindau, Atomic Data and Nuclear Data Tables **32**, 1 (1985).

[158] L. C. Davis and L. A. Feldkamp, Physical Review Letters **44**, 673 (1980).

[159] L. C. Davis and L. A. Feldkamp, Physical Review B **23**, 6239 (1981).

[160] L. C. Davis, Physical Review B **25**, 2912 (1982).

[161] L. C. Davis, Journal of Applied Physics **59**, R25 (1986).

[162] A. Kay, E. Arenholz, S. Mun, F. J. G. de Abajo, C. S. Fadley, R. Denecke, Z. Hussain, and M. A. Van Hove, Science **281**, 679 (1998).

[163] J. H. Richter, A. Henningsson, P. G. Karlsson, M. P. Andersson, P. Uvdal, H. Siegbahn, and A. Sandell, Physical Review B **71**, 235418 (2005).

[164] E. Bertel, R. Stockbauer, and T. E. Madey, Surface Science **141**, 355 (1984).

[165] C. Raman and K. Krishnan, Nature **121**, 501 (1928).

[166] R. McCreery, *Raman Spectroscopy for Chemical Analysis* (John Wiley & Sons Inc., New York, 2000).

[167] L. Reimer and G. Pfefferkorn, *Raster-Elektronenmikroskopie* (Springer Verlag, Berlin, 1977), Vol. 2.

[168] N. Geisse, AFM and Combined Optical Techniques.

[169] W. Bragg, Nature **90**, 410 (1912).

[170] W. F. Zhang, Y. L. He, M. S. Zhang, Z. Yin, and Q. Chen, Journal of Physics D-Applied Physics **33**, 912 (2000).

[171] W. Ma, Z. Lu, and M. Zhang, Applied Physics A-Materials Science & Processing **66**, 621 (1998).

[172] T. U. Kampen, G. Gavrila, H. Mendez, D. R. T. Zahn, A. R. Vearey-Roberts, D. A. Evans, J. Wells, I. McGovern, and W. Braun, Journal of Physics-Condensed Matter **15**, S2679 (2003).

[173] A. R. Kumarasinghe *et al.*, Journal of Chemical Physics **127**, 114703 (2007).

[174] R. Cervini, Y. B. Cheng, and G. Simon, Journal of Physics D-Applied Physics **37**, 13 (2004).

[175] P. Ravirajan, S. A. Haque, J. R. Durrant, D. Poplavskyy, D. D. C. Bradley, and J. Nelson, Journal of Applied Physics **95**, 1473 (2004).

[176] Q. B. Meng, K. Takahashi, X. T. Zhang, I. Sutanto, T. N. Rao, O. Sato, A. Fujishima, H. Watanabe, T. Nakamori, and M. Uragami, Langmuir **19**, 3572 (2003).

[177] T. Taguchi, X. T. Zhang, I. Sutanto, K. Tokuhiro, T. N. Rao, H. Watanabe, T. Nakamori, M. Uragami, and A. Fujishima, Chemical Communications 2480 (2003).

[178] J. Fritsche, A. Klein, and W. Jaegermann, Advanced Engineering Materials **7**, 914 (2005).

[179] T. Mayer, J. Lehmann, C. Pettenkofer, and W. Jaegermann, Chemical Physics Letters **198**, 621 (1992).

[180] J. N. Andersen, E. Lundgren, R. Nyholm, and M. Qvarford, Surface Science **289**, 307 (1993).

[181] R. D. Shannon and J. A. Pask, Journal of the American Ceramic Society **48**, 391 (1965).

[182] U. Balachandran and N. G. Eror, Journal of Solid State Chemistry **42**, 276 (1982).

[183] Q. H. Wu, A. Thissen, and W. Jaegermann, Applied Surface Science **252**, 1801 (2005).

[184] Q. H. Wu, A. Thissen, and W. Jaegermann, Solid State Ionics **167**, 155 (2004).

[185] A. Abrutis, V. Plausinaitiene, M. Skapas, C. Wiemer, W. Gawelda, J. Siegel, and S. Rushworth, Journal of Crystal Growth **311**, 362 (2009).

[186] R. Hunger, T. Schulmeyer, A. Klein, W. Jaegermann, M. V. Lebedev, K. Sakurai, and S. Niki, Thin Solid Films **480**, 218 (2005).

[187] C. Lim and D. E. Day, Journal of the American Ceramic Society **60**, 198 (1977).

[188] E. M. T. Njiokep and H. Mehrer, Solid State Ionics **177**, 2839 (2006).

[189] K. Benyamin, Solid State Ionics **73**, 303 (1994).

[190] M. S. Mattsson, G. A. Niklasson, and C. G. Granqvist, Journal of Applied Physics **81**, 2167 (1997).

[191] S. Lunell, A. Stashans, L. Ojamae, H. Lindstrom, and A. Hagfeldt, Journal of the American Chemical Society **119**, 7374 (1997).

[192] D. L. Liao and B. Q. Liao, Journal of Photochemistry and Photobiology a-Chemistry **187**, 363 (2007).

[193] S. Wendt *et al.*, Science **320**, 1755 (2008).

[194] V. Shklover, Y. E. Ovchinnikov, L. S. Braginsky, S. M. Zakeeruddin, and M. Grätzel, Chemistry of Materials **10**, 2533 (1998).

[195] O. Rana, R. Srivastava, R. Grover, G. Chauhan, S. S. Bawa, M. Zulfequar, M. Husain, and M. N. Kamalasanan, Japanese Journal of Applied Physics **50**, 061601 (2011).

[196] R. D. Deegan, O. Bakajin, T. F. Dupont, G. Huber, S. R. Nagel, and T. A. Witten, Nature **389**, 827 (1997).

[197] W. Jaegermann and T. Mayer, Solar Energy Materials and Solar Cells **83**, 371 (2004).

[198] D. A. Shirley, Physical Review B **5**, 4709 (1972).

[199] A. Decker, S. L. Suraru, O. Rubio-Pons, E. Mankel, M. Bockstedte, M. Thoss, F. Wurthner, T. Mayer, and W. Jaegermann, Journal of Physical Chemistry C **115**, 21139 (2011).

[200] B. Bröker *et al.*, Physical Review Letters **104**, 246805 (2010).

[201] E. Mankel, Dissertation, Technische Universität Darmstadt, 2010.

[202] L. Ottaviano, E. Maccallini, and S. Santucci, Surface Science **492**, L700 (2001).

[203] J. F. Morar, F. J. Himpsel, G. Hughes, J. L. Jordan, F. R. Mcfeely, and G. Hollinger, Journal of Vacuum Science & Technology a-Vacuum Surfaces and Films **3**, 1476 (1985).

[204] K. Mašek, P. Blumentrit, J. Beran, T. Skála, I. Píš, J. Libra, and V. Matolín, Surface and Interface Analysis **42**, 540 (2010).

[205] M. Prietsch, C. Laubschat, M. Domke, and G. Kaindl, Europhysics Letters **6**, 451 (1988).

[206] X. J. Feng, R. Hock, E. Mankel, D. Lingenfelser, B. Volker, T. Mayer, and W. Jaegermann, Journal of Physical Chemistry C **114**, 20049 (2010).

[207] A. Crispin *et al.*, Journal of Chemical Physics **116**, 8159 (2002).

[208] B. A. Gregg, S. G. Chen, and S. Ferrere, Journal of Physical Chemistry B **107**, 3019 (2003).

[209] Y. Chiba, A. Islam, Y. Watanabe, R. Komiya, N. Koide, and L. Y. Han, Japanese Journal of Applied Physics Part 2-Letters & Express Letters **45**, L638 (2006).

[210] P. Wang, S. M. Zakeeruddin, J. E. Moser, R. Humphry-Baker, P. Comte, V. Aranyos, A. Hagfeldt, M. K. Nazeeruddin, and M. Grätzel, Advanced Materials **16**, 1806 (2004).

[211] D. P. Hagberg, T. Edvinsson, T. Marinado, G. Boschloo, A. Hagfeldt, and L. C. Sun, Chemical Communications 2245 (2006).

[212] S. Kim, J. K. Lee, S. O. Kang, J. Ko, J. H. Yum, S. Fantacci, F. De Angelis, D. Di Censo, M. K. Nazeeruddin, and M. Grätzel, Journal of the American Chemical Society **128**, 16701 (2006).

[213] K. Hara, T. Sato, R. Katoh, A. Furube, Y. Ohga, A. Shinpo, S. Suga, K. Sayama, H. Sugihara, and H. Arakawa, Journal of Physical Chemistry B **107**, 597 (2003).

[214] T. Horiuchi, H. Miura, K. Sumioka, and S. Uchida, Journal of the American Chemical Society **126**, 12218 (2004).

[215] K. Westermark, A. Henningsson, H. Rensmo, S. Sodergren, H. Siegbahn, and A. Hagfeldt, Chemical Physics **285**, 157 (2002).

[216] A. K. Thakur, A. K. Mukherjee, D. M. G. Preethichandra, W. Takashima, and K. Kaneto, Journal of Applied Physics **101**, 104508 (2007).

[217] R. J. Bird and P. Swift, Journal of Electron Spectroscopy and Related Phenomena **21**, 227 (1980).

Curriculum vitae

Persönliche Daten

Name	René Pekkola (geb. Hock)
geboren	04.10.1981 in Erlenbach am Main

Schule

1988 - 1992	Grundschule Niedernberg
1992 - 2001	Hermann-Staudinger Gymnasium Erlenbach am Main

Zivildienst

2001 - 2002	Klinikum Erlenbach am Main

Ausbildung / Beruflicher Werdegang

2002 - 2008	Studium der Materialwissenschaft an der Technische Universität Darmstadt
2005 - 2006	Studentisches Austauschjahr an der Chalmers University of Technology Göteborg, Schweden
2008	Diplomarbeit an der Technischen Universität Darmstadt im Fachgebiet Dünne Schichten des Fachbereichs Material- und Geowissenschaften
2009 - 2012	Wissenschaftlicher Mitarbeiter an der Technischen Universität Darmstadt im Fachgebiet Oberflächenforschung des Fachbereichs Material- und Geowissenschaften
seit 2013	Entwicklungsingenieur bei MTS Sensor Technologie GmbH & Co. KG, Lüdenscheid

Publications and conference contributions

Publications

René Hock, Thomas Mayer, and Wolfram Jaegermann, *P-type doping of Spiro-MeOTAD with WO_3 and the Spiro-MeOTAD/WO_3 interface investigated by synchrotron induced photoelectron spectroscopy*, Journal of Physical Chemistry C 116 (2012), 18146–18154

Xianjin Feng, René Hock, Eric Mankel, Dominic Lingenfelser, Barbara Voĭker, Thomas Mayer, and Wolfram Jaegermann, *Processing Temperature and Surface Na Content of TiO2 Nanocrystallites in Films for Solid-State Dye-Sensitized Solar Cells*, Journal of Physical Chemistry C 114, 20049 (2010), 20049–20054

Conference contributions

René Hock, Thomas Mayer, Wolfram Jaegermann, *P-Doping of Organic Hole-Conductor using Metal-Oxides: Electronic Structure of Spiro-MeOTAD:WO_3 composites and Spiro-MeOTAD/WO_3 Interfaces*, Deutsche Tagung für Forschung mit Synchrotronstrahlung, Neutronen und Ionenstrahlen an Großgeräten 2010, Berlin, Germany

René Hock, Thomas Mayer, Wolfram Jaegermann, *P-Doping of Organic Hole-Conductor using Metal-Oxides: Electronic Structure of Spiro-MeOTAD:WO_3 composites and Spiro-MeOTAD/WO_3 interfaces as determined by SXPS*, European Materials Research Society Spring Meeting 2011, Nice, France

René Hock, Thomas Mayer, Wolfram Jaegermann, *Comparison of drop-casted and evaporated organic semiconductor films using SXPS*, Deutsche Tagung für Forschung mit Synchrotronstrahlung, Neutronen und Ionenstrahlen an Großgeräten 2011, Berlin, Germany

Julia Maibach, René Hock, Thomas Mayer, and Wolfram Jaegermann, *Combined study of interface and device properties of a solid state dye sensitized solar cell*, Frühjahrstagung der Deutschen Physikalischen Gesellschaft 2011, Dresden, Germany

René Hock, Thomas Mayer, Wolfram Jaegermann, *Synchrotron induced photoelectron spectroscopy of solution processed and evaporated Spiro-MeOTAD films. Electronic structure of Spiro-MeOTAD:WO_3 codeposits and Spiro-MeOTAD/WO_3 interfaces*, Materials Research Society Spring Meeting 2012, Darmstadt, Germany

René Hock, Thomas Mayer, Wolfram Jaegermann, *P-type doping of Spiro-MeOTAD with WO_3 and the Spiro-MeOTAD/WO_3 interface investigated by synchrotron induced photoelectron spectroscopy*, 27th European Photovoltaic Solar Energy Conference and Exhibition 2012, Frankfurt, Germany

Danksagung

An dieser Stelle möchte ich mich bei allen Personen herzlich bedanken, die zum Gelingen dieser Arbeit beigetragen haben. Besonderer Dank gilt hierbei:

Prof. Dr. Wolfram Jaegermann für die Ermöglichung dieser Dissertation und die sehr interessante Aufgabenstellung.

Prof. Dr.-Ing. Heinz von Seggern für die freundliche Übernahme der Zweitkorrektur.

Dr. Thomas Mayer für die Betreuung dieser Arbeit und der Bereitschaft über viele wissenschaftliche als auch nichtwissenschaftliche Dinge ausgiebig zu diskutieren.

Der BASF und Bosch für die Förderung des Projektes und den beteiligten Personen für die Messungen und wissenschaftlichen Diskussionen.

Xianjin Feng für die eineinhalb Jahre, die wir wunderbar zusammengearbeitet haben und in denen wir Freunde geworden sind. Aber auch dafür, dass er sich mit mir die Tage und Nächte bei BESSY um die Ohren geschlagen hat.

Meinen zwei ehemaligen Schreibtisch-Nachbarn Andreas und Philip "Vollborst" mit denen man nicht nur über wissenschaftliche Dinge sprechen konnte und die immer ein offenes Ohr für mich hatten.

Mehrdad Baghaie Yazdi für die GIXRD Messungen und die moralische Unterstützung während der Promotion.

Den Leuten bei BESSY in Berlin, insbesondere Wolfram Calvet, für die Instandhaltung der SoLIAS und der Strahlrohre und für die Unterstützung während den Messzeiten.

Dem Admin Team (Eric, Stefan, Andreas und Bastian) für die gute Zusammenarbeit auch in stressigen Zeiten.

Julia für die Hilfe bei den Versuchen, den Messungen und der Auswertung in der Zeit als mein HiWi und während der Diplomarbeit.

Der gesamten Arbeitsgruppe Oberflächenforschung, insbesondere der Organik Gruppe und der guten Seele der Gruppe Marga, für das sehr entspannte Arbeitsklima und die ständige Hilfsbereitschaft in allen Fragen.

Meiner Familie, ohne die ich niemals so weit gekommen wäre und ohne die ich niemals das alles erreicht hätte. Ich hoffe ich werde ein genauso guter Vater für unseren Sohn wie es mein Vater für mich war! Ich wünschte, du hättest das alles noch miterleben können!

Haluaisin kiittää vaimoani Oilia rakastavasta tuesta ja kannustuksesta. Sinun kanssasi voin nauraa ja hölmöillä, ja pahimmatkin asiat muuttuvat siedettäviksi.
Rakastan sua!